

UNIVERSITÀ DEGLI STUDI DI BARI
DIPARTIMENTO INTERATENEO DI FISICA
“Michelangelo Merlin”

DOTTORATO DI RICERCA IN FISICA XXVI CICLO
Settore Scientifico Disciplinare FIS-01



**Measurement of $\bar{\nu}_\mu$ CC interactions with the
ND280 detector of the T2K experiment**

Supervisor:

Prof. Vincenzo BERARDI
Dr.ssa Maria Gabriella CATANESI

Coordinatore:

Prof. Gaetano SCAMARCIO

Dottorando:

Lorenzo MAGALETTI

Contents

Introduction	12
1 The neutrino physics	14
1.1 The neutrino discovery	14
1.1.1 Parity violation in weak processes	17
1.2 The neutrino in the Standard Model	18
1.2.1 Electroweak Lagrangian	19
1.2.2 The neutrino mass in the SM	23
1.3 The neutrino oscillations	24
1.3.1 Neutrino oscillations in vacuum	25
1.3.2 Neutrino oscillations in the matter	28
1.4 Solar neutrinos	29
1.5 Atmospheric neutrinos	31
1.6 Reactor anti-neutrinos	34
1.7 Accelerator neutrino experiments	36
1.7.1 Short-Baseline (SBL) accelerator experiments	37
1.7.2 Long-Baseline (LBL) accelerator experiments	38
1.8 T2K oscillation results	38
1.8.1 ν_e appearance results	39
1.8.2 ν_μ disappearance results	41
1.9 Status of the art and future of the neutrino physics	41
2 The T2K experiment	45
2.1 Physics motivations	47
2.1.1 ν_e appearance	47
2.1.2 ν_μ disappearance	49
2.1.3 Oscillation analyses	50
2.1.4 The T2K physics goals in the next future	51
2.2 The neutrino beam	52
2.2.1 The off-axis method	53
2.2.2 The J-PARC accelerators	54
2.2.3 The neutrino beamline	55
2.2.4 The Muon Monitor and Emulsion Trackers	59
2.2.5 The neutrino flux simulation	59
2.3 The near detector complex	61
2.4 The on-axis detector: <i>INGRID</i>	64
2.5 The off-axis detector: <i>ND280</i>	65

2.5.1	The UA1/NOMAD magnet	66
2.5.2	Side Muon Range Detector (SMRD)	68
2.5.3	Electromagnetic Calorimeter (ECal)	69
2.5.4	The π^0 detector (P \emptyset D)	69
2.5.5	The Fine Grain Detectors (FGDs)	70
2.5.6	The Time Projection Chambers (TPCs)	71
2.6	The far detector Super-Kamiokande	73
3	Measurement of $\bar{\nu}_\mu$ CC interactions using the ND280 Tracker	77
3.1	The ND280 software overview	77
3.2	The calibration procedure	79
3.2.1	Calibration of the electronics	79
3.2.2	Physics calibration	79
3.3	Reconstruction	80
3.3.1	TPC reconstruction	80
3.3.2	Global reconstruction	81
3.4	The data sets	82
3.5	The selection criteria	84
3.6	The μ^+ identification in the ND280 Tracker	87
3.6.1	TPC PID and one TPC track multiplicity	88
3.6.2	TPC-ECal Matching and ECal PID	92
3.7	Final sample and selection summary	97
3.8	Analysis efficiency and purity	99
3.9	The likelihood fit	103
3.9.1	Likelihood description	103
3.9.2	Validation of the fit with toy MC	106
3.9.3	Fit result obtained for the nominal MC	106
4	Systematics uncertainties	110
4.1	Detector response uncertainties	111
4.1.1	Cluster efficiency	112
4.1.2	TPC tracking efficiency	112
4.1.3	TPC PID	113
4.1.4	TPC charge confusion	115
4.1.5	TPC momentum resolution	117
4.1.6	TPC momentum scale	118
4.1.7	Magnetic field distortions	120
4.1.8	FGD-TPC Matching	120
4.1.9	TPC-ECal Matching	120
4.1.10	ECal PID	121
4.1.11	Pion Secondary interactions	122
4.1.12	FGD Mass	124
4.1.13	Sand muon background	125
4.1.14	Cosmic rays background	125
4.1.15	Event pile up	125
4.2	Propagation of detector systematics	125
4.2.1	Efficiency like systematics	126

4.2.2	Reconstructed observable variation	127
4.2.3	Normalization systematic errors	128
4.3	The corrected Monte Carlo	128
4.4	Propagation of detector systematics in the corrected MC	128
4.5	Likelihood fit results	131
4.5.1	Fit results obtained for the corrected MC	132
4.5.2	Effect of detector systematics in the likelihood fit	134
4.6	Flux and cross section systematics	135
4.6.1	Compatibility of BANFF fit with the $\bar{\nu}_\mu$ beam data at ND280	136
4.6.2	Inclusion of flux and cross sections systematic errors	139
4.7	Summary and outlook	140
5	Conclusions	143
A	The muon anti-neutrino analysis with an anti-neutrino beam	145
A.1	$\bar{\nu}_\mu$ CC event selection	145
A.2	μ^+ selection efficiency and purity	147
A.3	Analysis results	148
A.4	Detector systematic errors	152
A.5	Summary and outlook	154

List of Figures

1.1	Schematic appearance of the electron spectrum in β -decay.	15
1.2	Electron proton elastic scattering.	15
1.3	Fermi's explanation of β -decay.	15
1.4	Determination of the number of light neutrino generations using the Z^0 decay by the ALEPH experiment	17
1.5	Charged Current (CC) neutrino interaction.	17
1.6	Neutral Current (NC) neutrino interaction.	17
1.7	The ^{60}Co experiment	18
1.8	Standard Model of elementary particles.	19
1.9	The oscillation probability	27
1.10	Neutral current (NC) neutrino interaction with the matter.	28
1.11	Charged Current (CC) neutrino interaction with matter.	28
1.12	Reactions and neutrino energies predicted by the SSM.	30
1.13	Key reactions in the SNO Experiment: CC and NC interactions	31
1.14	Key reactions in the SNO Experiment: ES reaction.	31
1.15	Atmospheric neutrinos.	32
1.16	Flight distances for atmospheric neutrinos.	32
1.17	The zenith angle distributions for fully contained 1-ring e -like and μ -like events at Super-Kamiokande	33
1.18	The KamLAND experiment results	35
1.19	The $\bar{\nu}_e$ survival probability observed by the KamLAND experiment	35
1.20	SBL exclusion curves	38
1.21	The 90% C.L. allowed regions and the best fitted atmospheric parameters measured by T2K superimposed to MINOS and SK measurements	39
1.22	The 68% and 90% C.L. allowed regions measured by T2K for $\sin^2 2\theta_{13}$, scanned over values of δ_{CP}	40
1.23	The 90% C.L. allowed regions for δ_{CP} measured by T2K	40
1.24	The allowed regions measured by T2K for the atmospheric parameters	41
1.25	Neutrino mass eigenstate composition	42
2.1	The neutrino beam journey in the T2K experiment	45
2.2	The muon neutrino survival and electron neutrino appearance probabilities at 295 km	46
2.3	Expected CCQE reaction of oscillated ν_e at Super-Kamiokande.	48
2.4	Total charged current ν inclusive cross sections as a function of neutrino energy	48
2.5	The cuts applied on M_{inv} and E_{ν}^{rec} at Super-Kamiokande	50
2.6	The ν_{μ} CCQE reaction.	50
2.7	Reconstructed neutrino energy spectrum at Super-Kamiokande	51

2.8	T2K sensitivity to δ_{CP} running w/ and w/o an anti-neutrino beam	52
2.9	T2K sensitivity to $\sin^2 \theta_{23}$ running w/ and w/o an anti-neutrino beam	52
2.10	A schematic cartoon of the T2K neutrino beam.	53
2.11	Expected neutrino energy as a function of the parent pion energy for different values of the off-axis angle.	54
2.12	Overview of the J-PARC accelerators and facilities	55
2.13	Overview of the T2K neutrino beamline.	56
2.14	Location of the primary beamline monitors.	56
2.15	Side view of the secondary beamline	57
2.16	Conceptual drawing of the target system of J-PARC neutrino beamline.	58
2.17	Muon monitor inside the support enclosure	60
2.18	The layout of the NA61/SHINE experiment at the CERN SPS	60
2.19	The prediction from the T2K beam simulation and fraction of accepted particles as a function of momentum and polar angle, after the track acceptance cuts and ToF-F acceptance cut	61
2.20	The ND280 and SK flux predictions	62
2.21	The T2K near detector complex	63
2.22	INGRID on-axis detector.	64
2.23	A schematic view of an INGRID standard module	65
2.24	A schematic view of the INGRID proton module	65
2.25	The INGRID event display	66
2.26	An exploded view of the ND280 off-axis detector.	67
2.27	The ND280 event display	67
2.28	View of SMRD scintillator counter components prior to assembly.	68
2.29	A schematic view of the P \emptyset D	70
2.30	View of an FGD with the front cover removed	71
2.31	Simplified cut-away drawing showing the main aspects of the TPC design.	72
2.32	Track reconstruction in a MicroMegas detector.	72
2.33	Energy loss in a T2K's TPC versus momentum	73
2.34	Diagram of the Super-Kamiokande Detector	74
2.35	Example of reconstructed T2K events in Super-Kamiokande	75
2.36	ΔT_0 distributions at Super-Kamiokande	75
3.1	The ND280 offline software suite [118].	78
3.2	Sketch of clustering method and pattern recognition algorithm	81
3.3	The good spill integrated POT delivered to T2K (January 2010 - May 2013).	82
3.4	Predicted 11b-v3.2 flux at ND280 and 11a nominal flux differences	83
3.5	$\bar{\nu}_\mu$ CC Inclusive interaction at the T2K energy peak.	84
3.6	Bunch structure of selected events for Run I (0000-6000) and Run IV (8895-9799)	85
3.7	Scheme of FGD1 and FGD2 fiducial volumes.	86
3.8	Sample after the pre-selection	87
3.9	Distribution of the TPC ionization loss as a function of the TPC momentum for the candidate lepton track starting in the FGD FV	88
3.10	The δ_i variable for different particle hypothesis	89
3.11	The likelihood computed in the muon hypothesis.	90
3.12	The TPC PID cuts and momentum spectra of rejected tracks	91
3.13	Momentum spectrum of the most energetic positive tracks after the TPC PID.	92

3.14	Feynman graph of $CC1\pi$ and DIS neutrino interactions	92
3.15	Momentum spectrum of the most energetic positive tracks rejected from the one TPC track selection.	93
3.16	Momentum spectrum of the most energetic positive tracks after the one TPC track selection.	93
3.17	Momentum spectrum of the most energetic positive tracks without TPC-ECal Matching	94
3.18	Momentum spectrum of the most energetic positive tracks with the TPC-ECal matching.	94
3.19	Momentum spectrum of the most energetic positive tracks with TPC-DsECal matching and TPC-BrECal matching	95
3.20	LLR discriminators shapes with the particle gun MC	96
3.21	LLR discriminators in Ds-ECal and Br-ECal	97
3.22	Event display of two selected events	98
3.23	μ^+ selection efficiency and purity	98
3.24	Momentum spectrum of the final selected sample	99
3.25	$\cos(\theta)$ spectrum of the final selected sample	100
3.26	Events failing the μ^+ selection.	100
3.27	$\bar{\nu}_\mu$ CC selection efficiency and purity versus the cut applied	102
3.28	Signal and background in the final sample	104
3.29	The momentum spectra of the four PDFs that are input to the fit.	105
3.30	The final sample. The MC is broken down in signal and background sources.	105
3.31	$(p, \cos\theta)$ spectrum of the selected sample	106
3.32	Fitted rescaling factors and pulls for each input to the fit	107
3.33	The effect of the fit on the kinematics distributions. Data/Mc ratios after the fit	108
3.34	Likelihood minimum and f contours for each backgrounds component versus signal.	109
4.1	Sketch of the sub-detectors relevant for this analysis with the corresponding associated systematic components	110
4.2	TPC tracking efficiency versus the number of horizontal clusters.	113
4.3	TPC muon pull for tracks with TPC momentum between 500 MeV/c and 2 GeV/c in the TPC2	114
4.4	Mean of the TPC muon pull in data and MC as a function of the TPC local momentum	114
4.5	Width of the TPC muon pull in data and MC as a function of the TPC local momentum	115
4.6	Truncated mean of positive tracks with momentum between 300 MeV/c and 500 MeV/c and momentum distribution for the tracks selected in the proton sample	115
4.7	Mean value of the pulls in the proton hypothesis as a function of the TPC local momentum	116
4.8	Width value of the pulls in the proton hypothesis as a function of the TPC local momentum	116
4.9	Charge confusion systematic error	117
4.10	Momentum resolution systematic error	118
4.11	Momentum distributions of stopping muons for each range in the FGD1	119
4.12	TPC-FGD matching efficiency systematic error	121
4.13	Reconstructed kinematics for the muon control sample in the downstream and barrel ECal	122
4.14	ECal matching efficiency as a function of the muon momentum	123

4.15	Difference of selection efficiency between data and MC for downstream ECal and barrel ECal	123
4.16	π^+ Absorption on Carbon-12	124
4.17	Comparison between nominal and corrected MC kinematic spectra.	129
4.18	Main contributes to the corrected MC	129
4.19	Comparison between nominal PDFs distributions (black) and corrected PDFs distributions (colored).	130
4.20	Effect on the momentum spectrum of the TPC proton PID systematic propagation .	130
4.21	Effect on the momentum spectrum of the TPC proton PID bias systematic propagation	131
4.22	Effect on the momentum spectrum of the momentum resolution systematic propagation	131
4.23	Data and corrected MC kinematic spectra before the likelihood fit	132
4.24	Data and corrected MC kinematic spectra after the likelihood fit	133
4.25	Likelihood minimum and f contours for each backgrounds component versus signal. .	134
4.26	Kinematic spectra of data, corrected MC and MC toys superimposed	135
4.27	Fitted value for $f_{\bar{\nu}_\mu}$ when all systematics are enabled.	135
4.28	The parameter correlations prior to (left) and after (right) the BANFF fit	137
4.29	Kinematic spectra of data, corrected MC and BANFF MC superimposed	138
4.30	Differences on momentum spectrum of the inputs to the fit between corrected MC and BANFF MC	138
4.31	Data and BANFF MC kinematic spectra after the likelihood fit	140
4.32	Likelihood minimum and f contours for each backgrounds component versus signal. .	141
4.33	Kinematic spectra of data, BANFF MC and MC toys superimposed	141
4.34	Fitted value for $f_{\bar{\nu}_\mu}$ based on flux and cross-section systematics after the BANFF fit.	142
4.35	Fitted value for $f_{\bar{\nu}_\mu}$ based on flux and cross-section systematics before the BANFF fit.	142
A.1	T2K sensitivity to δ_{CP} running w/ and w/o an anti-neutrino beam	146
A.2	T2K sensitivity to $\sin^2 \theta_{23}$ running w/ and w/o an anti-neutrino beam	147
A.3	Sample after the pre-selection	148
A.4	Expected fluxes in neutrino and anti-neutrino beam modes	149
A.5	Momentum spectrum of the most energetic positive tracks after the TPC PID. . . .	149
A.6	Momentum spectrum of the most energetic positive tracks rejected from the TPC PID.	149
A.7	Momentum spectrum of the most energetic positive tracks after the “one TPC track multiplicity” cut.	150
A.8	Momentum spectrum of the most energetic positive tracks rejected from the “one TPC track multiplicity” cut.	150
A.9	Momentum spectrum of the most energetic positive tracks after the ECal PID. . . .	151
A.10	μ^+ selection efficiency and purity	151
A.11	$\bar{\nu}_\mu$ CC selection efficiency and purity versus the cut applied	152
A.12	Kinematic spectra of the final sample in anti-neutrino mode	152
A.13	Comparison between nominal and corrected MC kinematic spectra.	154
A.14	Main contributes to the corrected MC	154
A.15	Effect on the momentum spectrum of the TPC proton PID systematic propagation .	155
A.16	Effect on the momentum spectrum of the TPC proton PID bias systematic propagation	155
A.17	Effect on the momentum spectrum of the momentum resolution systematic propagation	156
A.18	Kinematic spectra of data corrected MC and MC toys superimposed	156

List of Tables

1.1	Leptons masses	16
1.2	Eigenvalues coming from the Gell-Mann–Nishijima relation for leptons and quarks.	22
1.3	Eigenvalues of the weak isospin I , of its third component I_3 , of the hypercharge Y and of the charge $Q = I_3 + \frac{Y}{2}$ of the Higgs doublet.	22
1.4	The present status of neutrino oscillation parameters presented at TAUP 2013 conference	42
1.5	Results of the global 3ν oscillation analysis	43
2.1	Machine design parameters of the J-PARC MR for the fast extraction.	55
2.2	The horns dimensions.	58
2.3	Neutrino-producing decay modes considered in JNUBEAM and their branching ratio in percentage	61
2.4	Main parameters of the T2K MPPCs	63
3.1	Definition of T2K runs and the amount of data and MC POT used in the analysis	83
3.2	Central bunch time (in ns) for the different run periods	86
3.3	Reduction in the number of events selected in data and MC	101
3.4	Composition of the final selected sample broken down by final state particle type.	101
3.5	Composition of the final selected sample broken down by interaction type.	101
3.6	Composition of the final selected sample. The $\bar{\nu}_\mu$ component is broken down by neutrino parent type.	102
3.7	Composition of the final selected sample broken down by input to the fit.	103
3.8	Value of the parameters for best fit. The rescaling factor and absolute number of events are indicated for each component.	108
4.1	Pile-up correction and uncertainty for each data set.	126
4.2	Systematic error propagation model for each of the systematic errors considered.	126
4.3	Composition of the final selected sample broken down by input to the fit.	132
4.4	Value of the parameters for best fit for the corrected MC. The rescaling factor and absolute number of events are indicated for each component.	133
4.5	Summary of the effect of detector systematics in the fit.	134
4.6	Post-BANFF fit flux and cross section systematics central values	137
4.7	Composition of the final selected sample broken down by input to the fit.	139
4.8	Value of the parameters for best fit for the corrected MC. The rescaling factor and absolute number of events are indicated for each component.	139
5.1	Summary of the systematic errors in the $\bar{\nu}_\mu$ analysis.	144

A.1 Composition of the final selected sample broken down by final state particle type. . . 151
A.2 Composition of the final selected sample broken down by interaction type. 153
A.3 Composition of the final selected sample. The $\bar{\nu}_\mu$ component is broken down by
neutrino parent type. 153

Introduction

Neutrinos are fundamental particles of the universe. The neutrino oscillations are a quantum mechanical phenomenon whereby a neutrino created with a specific lepton flavor (e, μ, τ) changes flavor during its propagation. The observation of this phenomenon implies that neutrinos have non zero mass, contrary to the original Standard Model assumption of massless neutrinos. Thus, the discovery of neutrino oscillations is crucial to the development of the Standard Model and so far it is the only experimental result for physics beyond this theory. The evidence of this phenomenon has been confirmed by the latest measurements of the T2K experiment, which measured for the first time the transmutation of ν_μ in ν_e with a significance greater than 5σ . T2K is a long baseline neutrino oscillation experiment installed in Japan and designed to measure neutrino flavor oscillation using an off-axis neutrino beam, mainly composed of ν_μ , generated at J-PARC (Tokai-Mura), and measured at Super-Kamiokande (mount Kamioka). Through the neutrino flavor oscillations, T2K is sensitive to several parameters of the Pontecorvo-Maki-Nakagawa-Sakata oscillation matrix (PMNS matrix):

- the $\nu_\mu \rightarrow \nu_e$ appearance channel is sensitive to θ_{13} and δ_{CP} ;
- the $\nu_\mu \rightarrow \nu_\mu$ disappearance channel is sensitive to θ_{23} and Δm_{23}^2 .

A summary of the neutrino physics and an overview of the T2K experiment are presented in Chapters 1 and 2 respectively.

In order to precisely measure the oscillation parameters, it is fundamental to reduce as much as possible the systematic uncertainties. This thesis describes the measurement of the $\bar{\nu}_\mu$ component of the T2K beam through the identification of $\bar{\nu}_\mu$ Charged Current (CC) interactions in the near detector ND280 of the T2K experiment. This measure is mainly motivated by the fact that it helps to the reduction of the related systematic errors in the measurement of the oscillation parameters. In Chapter 3, I described the $\bar{\nu}_\mu$ analysis performed with all the data sets collected by T2K up to May 2013, corresponding to 6.63×10^{20} Proton On Target (POT). The event selection that I developed to identify $\bar{\nu}_\mu$ CC inclusive interactions in the ND280 tracker uses both TPC and ECal particle identification (PID) to obtain a final sample with a good purity. Than to precisely measure the number of $\bar{\nu}_\mu$ selected, I developed a likelihood fit in kinematic distributions. Chapter 4 is dedicated to the systematic uncertainties that affect the analysis. The systematic error sources can be divided into three categories: (1) detector, (2) flux and (3) cross section systematics. Detector systematics are due to discrepancies between data and Monte Carlo (MC) occurring in the event reconstruction, while flux and cross sections systematics are due to systematic errors of flux predictions and neutrino interaction models implemented in the MC sample. In particular, I evaluated the systematic error related to the proton identification in the TPC which is the highest detector systematic that affect the analysis. Finally, I measured the impact of these systematic uncertainty in the analysis. The conclusions with all the results obtained and their discussion are object of Chapter 5.

The Appendix A at the end of the thesis is a complement to this work, where it is described a MC based study that I have done to point out the ND280 potentiality in view of the anti-neutrino

pilot run planned from the T2K collaboration in 2014. In fact, as described in the appendix, T2K will increase its sensitivity to the δ_{CP} and θ_{23} octant sharing the data taking between neutrino and anti-neutrino beams from 2014.

Chapter 1

The neutrino physics

The neutrino physics is one of the most important field of particle physics. In the last century, neutrino experiments have largely contributed to improve our knowledge about the Standard Model and its parameters. Experiments like Sudbury Neutrino Observatory (SNO) with solar neutrino data, and Super-Kamiokande, with atmospheric neutrino data, confirmed the neutrino oscillation phenomenon, giving a clear evidence that neutrinos are not massless particles. The following sections will cover the development of neutrino physics starting from the neutrino discovery to the current and future generation of neutrino experiments. It will also be discussed the inclusion of neutrino masses in the Standard Model and the neutrino oscillation phenomenon.

1.1 The neutrino discovery

The hypothesis of neutrino was proposed by W. Pauli in December 1930 in the famous letter addressed to participants of a nuclear conference in Tübingen. At that time protons and electrons were considered as elementary particles and nuclei were considered as bound states of protons and electrons. In the framework of this last assumption there were two fundamental problems:

1. the problem of continuous β -decay spectra;
2. the problem of spin of some nuclei.

Indeed, in this framework, the β -decay of a nucleus (A, Z) , the process can occur via electron emission in the nuclear transition $(A, Z) \rightarrow (A, Z + 1) + e^-$. If (A, Z) decays in the rest frame, according to the conservation energy law, the energy of the emitted electron must be:

$$E_{e^-} = \frac{M_{(A,Z)}^2 - M_{(A,Z+1)}^2 + m_{e^-}^2}{2M_{(A,Z)}}. \quad (1.1)$$

If the process is well described by (1.1), the electron produced in the β -decay has a fixed energy. Instead, a continuous electron energy spectrum, peaked at energy $E_{e^-}^{\text{Max}}$ was experimentally observed, extremely close to the predicted E_{e^-} (Figure 1.1). Pauli was the first who understood that under the condition of energy-momentum conservation the only possibility to explain the continuous β -spectra was to assume that there existed a new, neutral particle which was emitted in the β -decay with the electron that was not detected in the experiment. According to this new framework, Pauli inferred that this particle should be: electrically neutral (in order to conserve charge), with spin 1/2

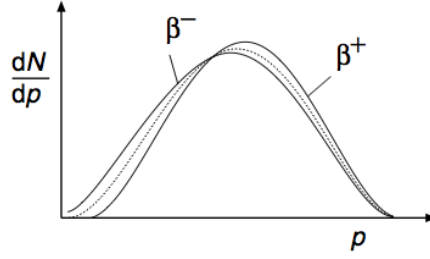


Figure 1.1: Schematic appearance of the electron spectrum in β -decay.

(in order to conserve angular momentum and to solve a problem¹ with some nuclei as $^{14}\text{N}_7$) and weakly interacting. Finally, it is needed that this new particle has a mass lighter than the electron mass, given the experimental observation of $E_{e^-}^{\text{Max}} \simeq E_{e^-}$. He called the new particle “*neutron*”. This idea was developed by E. Fermi in 1934 [1]. He built the first theory of the β -decay of nuclei, which was based on the Pauli assumption.

After the discovery of heavy neutron done by Chadwick in 1932 [2], Fermi proposed to call the light Pauli particle *neutrino* (from italian neutral, light). Fermi’s theory assumed that nuclei are bound states made of proton and neutrons. There was a problem to understand how an electron-neutrino pair was produced. By analogy with the electromagnetic interactions, Fermi explained the β -decay process as the electron-proton scattering (Feynman graph 1.2) with the assumption that the electron-neutrino pair is produced in the quantum transition of a neutron in a proton (Feynman graph 1.3).

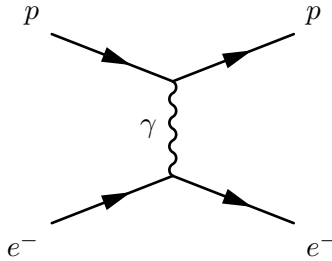


Figure 1.2: Electron proton elastic scattering.

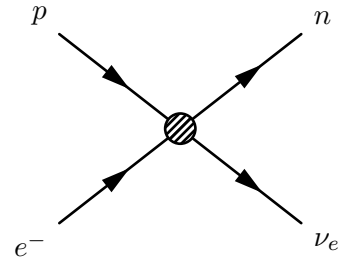


Figure 1.3: Fermi’s explanation of β -decay.

The simplest electromagnetic Hamiltonian which induces the quantum transition

$$p \rightarrow p + \gamma, \quad (1.2)$$

it has the form of the scalar product of the electromagnetic vector current for proton $\bar{p}(x)\gamma_\alpha p(x)$ and the vector electromagnetic field $A^\alpha(x)$:

$$\mathcal{H}^{EM}(x) = e \bar{p}(x)\gamma_\alpha p(x) A^\alpha(x). \quad (1.3)$$

¹ The nucleus $^{14}\text{N}_7$, from the point of view of the electron proton model, is a bound state of 14 protons and 7 electrons, i.e. his spin must be an half-integer. However, from the investigation of spectra of molecular nitrogen, experimental data confirmed that $^{14}\text{N}_7$ follows the Bose-Einstein statistics, in disagreement with the electron-proton model.

By analogy, Fermi assumed that the Hamiltonian of decay 1.3 was the scalar product of vector $\bar{p}(x)\gamma_\alpha n(x)$ and vector $\bar{e}(x)\gamma^\alpha\nu(x)$, which can be built from the electron and neutrino field

$$\mathcal{H}^\beta(x) = G_F \bar{p}(x)\gamma_\alpha n(x) \bar{e}(x)\gamma^\alpha\nu(x) + \text{h.c.}, \quad (1.4)$$

where G_F is a constant (the so called Fermi's constant). The fundamental difference between (1.3) and (1.4) is that (1.3) is the Hamiltonian of the interaction of two fermion fields (proton and proton) with a boson field, instead (1.4) is the Hamiltonian of the interaction of four fermions fields. As result of that, the coupling constant e and G_F have different dimension, $G_F \propto M^{-2}$, where M is the mass, and the charge e is dimensionless in the unit system $\hbar = c = 1$.

Today we know that β -decay occurs with the exchange of the intermediate boson W , and the Fermi theory is the low energy limit of this process.

The main proof of Fermi's theory and neutrino existence arrived in 1956, when Reines and Cowan using a nuclear reactor succeeded in detecting anti-neutrinos in the inverse β -decay process [3]:

$$\bar{\nu}_e + p \rightarrow e^+ + n. \quad (1.5)$$

The muon neutrino (ν_μ) was discovered in 1962 in the Brookhaven experiment of Lederman [4], which was the first experiment using a neutrino beam coming from pion decay, obtained by the bombardment of a Be target by protons with an energy of 15 GeV. The experimental result was that there is a kind of neutrino associated with the electron and a second kind of neutrino associated with muon. So the neutrino observed by Reines and Cowan experiment was an electron neutrino ν_e .

In 1975-77 in an experiment performed using an $e^+ - e^-$ collider at Stanford, the third lepton τ^\pm was discovered [5]. It was assumed the existence of a third type of neutrino ν_τ , later experimentally observed in 2001 by DONUT experiment at Fermilab [6]. The lepton sector framework is now completed with the three family

$$\left(\begin{array}{c} \nu_e \\ e \end{array} \right), \left(\begin{array}{c} \nu_\mu \\ \mu \end{array} \right), \left(\begin{array}{c} \nu_\tau \\ \tau \end{array} \right).$$

The leptons masses are shown in Table 1.1.

The Standard Model, that will be discussed in the section 1.2, requires three neutrino generations

Table 1.1: Leptons masses

Charged lepton	Mass (MeV)	Neutrino	Mass
e	0.511	ν_e	<15 eV
μ	105.658	ν_μ	<190 keV
τ	1776.84	ν_τ	<18.2 MeV

and their corresponding charged leptons, as proved by the LEP experiments at CERN ($N_\nu = 2.982 \pm 0.013$ [7] (see Figure 1.4)). Neutrinos are electrically neutral and colorless², so they do interact neither via electromagnetic interactions, nor via strong interactions. Neutrinos can only interact via weak interactions. There are two type of weak interactions: Charged Current (CC)

² Color is the charge associated to the strong interactions.

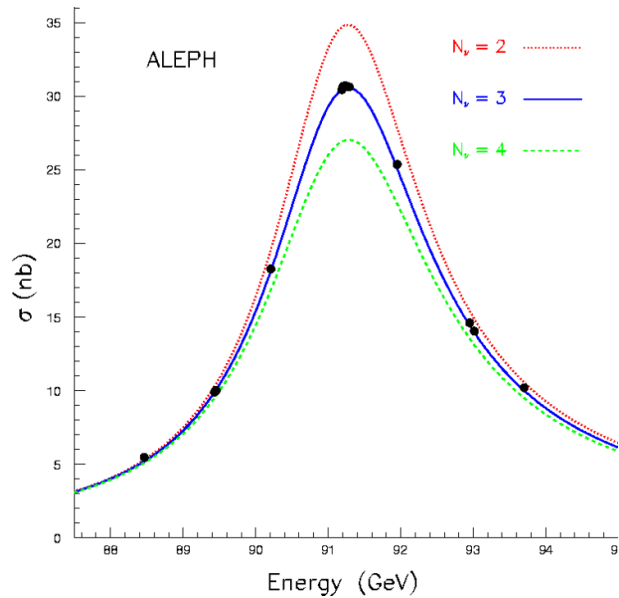


Figure 1.4: Determination of the number of light neutrino generations using the Z^0 decay by the ALEPH experiment. In the plot are showed the data (black markers with error bars) and three hypothesis on the number of neutrino generations (colored curves).

and neutral current (NC) interactions. In a charged current process, a neutrino (anti-neutrino) exchanges with the interacting particle a W^+ boson (W^-) and becomes his charged lepton partner l (Figure 1.5). Instead in a neutral current process, a neutrino (anti-neutrino) does not change after exchanging a Z^0 boson (Figure 1.6).

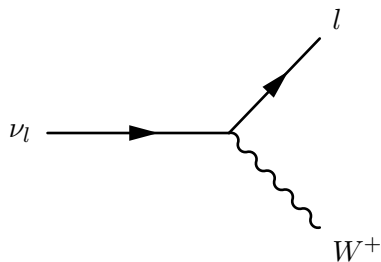


Figure 1.5: Charged Current (CC) neutrino interaction.

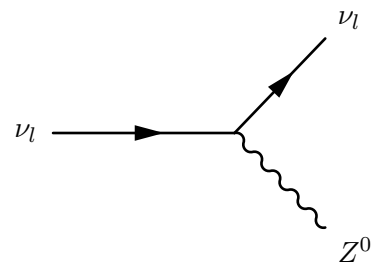


Figure 1.6: Neutral Current (NC) neutrino interaction.

1.1.1 Parity violation in weak processes

For many years physicists thought that the invariance under space inversion is a general law of nature valid for all interactions. The discovery of violation of parity in the β -decay and other weak processes was a great surprise. In the beginning, it looked that this discovery made the theory of the β -decay and other weak processes more complicated. In reality this discovery allowed building the correct theory of the neutrino and weak interaction. The results of the first experiments in

which large violation of parity in weak processes was observed were published by Wu et al. [8] and Lederman et al. [9] at the beginning of 1957. The most famous experiment was done by Wu, in which the β -transition of polarized cobalt nuclei ${}^{60}\text{Co} \rightarrow {}^{60}\text{Ni}^* + e^- + \bar{\nu}_e$ was investigated (Figure 1.7). The nuclear spin in a sample of ${}^{60}\text{Co}$ were aligned by an external magnetic field, and an

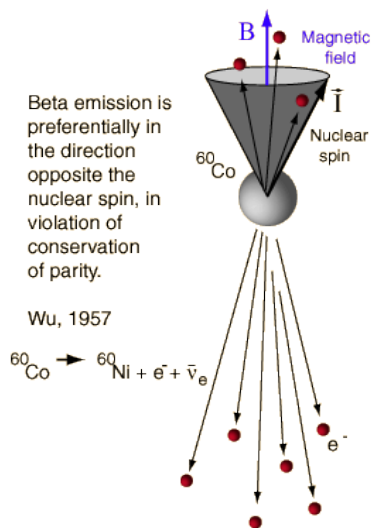


Figure 1.7: The ${}^{60}\text{Co}$ experiment: the electron is emitted preferentially opposite the direction of the spin of ${}^{60}\text{Co}$ nucleus.

asymmetry in the direction of the emitted electrons was observed. The asymmetry was found to change sign upon reversal of the magnetic field such that electrons prefer to be emitted opposite to that of the nuclear spin. The observed correlation between the nuclear spin and the electron momentum is explained with the conservation of angular momentum: indeed if the spin of ${}^{60}\text{Co}$ is $J = 5$, and the spin of ${}^{60}\text{Ni}^*$ is $J = 4$, to conserve the angular momentum, the J_z of the system $e^- + \bar{\nu}_e$ must be equal to one. This can happen only if $\bar{\nu}_e$ is right-handed $\bar{\nu}_R$ and e^- is left-handed e_L . In Lederman et al. experiment was observed a strong violation of the parity in the chain of decays $\pi^+ \rightarrow \mu^+ \nu_\mu$ and $\mu^+ \rightarrow e^+ \nu_e + \bar{\nu}_\mu$. Those observations were verified in many experiments confirming that only $\bar{\nu}_R$ and ν_L are involved in weak interactions. The absence of the “mirror image” states, $\bar{\nu}_L$ and ν_R , is a clear violation of parity invariance. Those experimental evidences are taken into account in the theory by the $V-A^3$ structure of the weak interactions and the unified theory of the electromagnetic and weak interaction (Standard Model).

1.2 The neutrino in the Standard Model

The Standard Model (SM) [10–12] describes the strong, electromagnetic and weak interactions of elementary particles in the framework of the quantum field theory. It is a gauge theory based on the local symmetry group $\text{SU}(3)_C \times \text{SU}(2)_L \times \text{U}(1)_Y$, where C, L and Y denote respectively color, left-handed chirality and weak hypercharge. There are two kinds of particles in the SM, fermions (particle with a half-integer spin) and gauge bosons (particles with a integer spin). Fermions obey

³ $V-A$ means Vector-Axial vector.

to the Pauli exclusion principle⁴ and each of them has an anti-particle with the same mass but opposite quantum numbers. They are divided in two families: *quarks* and *leptons*. Leptons do not interact via strong interactions, contrary to quarks. Instead, bosons obey to the Bose-Einstein statistic and they are able to mediate the strong, weak and electromagnetic interactions. The gauge group uniquely determines the interactions and the number of vector gauge bosons that correspond to the generators of the group. For the $SU(3)_C$ group there are eight generators $T_a = \frac{\lambda_a}{2}$, where λ_a are the Gell-Mann matrices, that correspond to eight massless *gluons* (gauge bosons), that mediate strong interactions; other four gauge bosons, of which three are massive (W^\pm and Z) and one is massless (γ , the *photon*), corresponding to the three generators of $SU(2)_L$ (the so called Pauli's matrices) and one of $U(1)_Y$, responsible for the electroweak interactions. The current knowledge of elementary particles is showed in Figure 1.8.

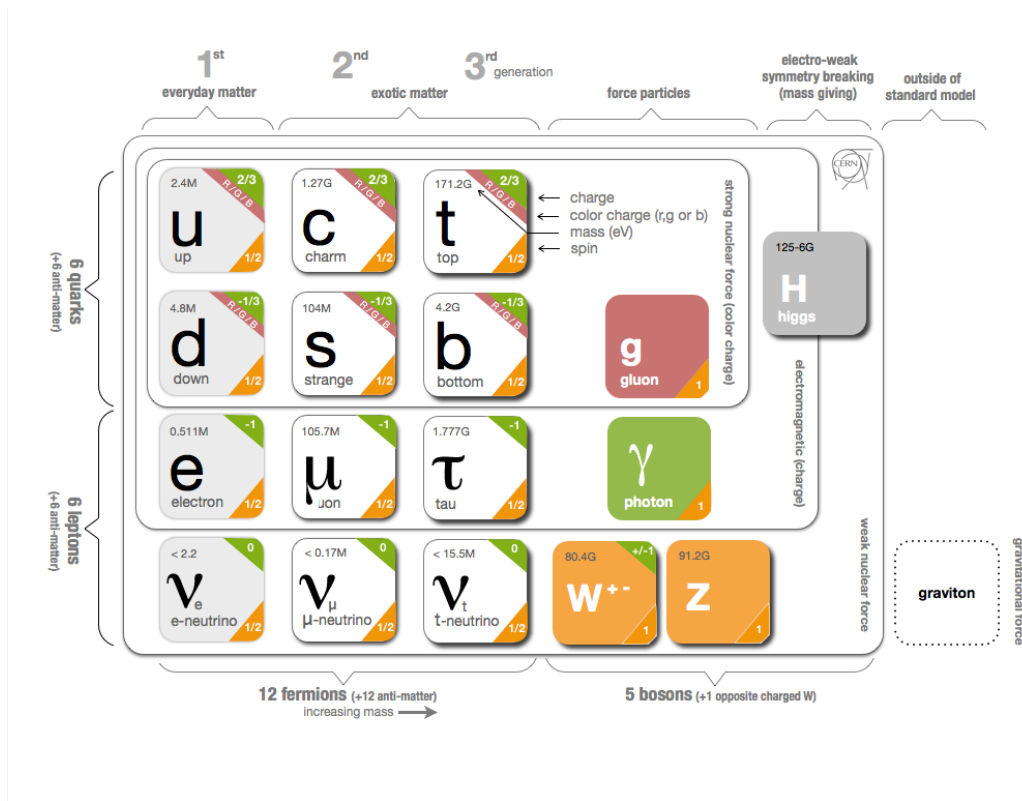


Figure 1.8: Standard Model of elementary particles.

1.2.1 Electroweak Lagrangian

The symmetry group $SU(2)_L$ is called *weak isospin*. The L indicates that the elements of this group have only the left-handed chiral components of the fermions fields (the right-handed chiral components are singlets under weak isospin transformations). In a two-dimensional representation,

⁴ The Pauli exclusion principle is a quantum mechanical principle that forbids two identical particles with half-integer spin to occupy the same quantum state simultaneously. So according to this principle, the total wave function for two identical particle with half-integer spin must be anti-symmetric with respect to exchange of particles.

the generators of the group are $I_a = \tau_a/2$, where τ_1 , τ_2 , and τ_3 are the three Pauli matrices⁵. The symmetry group $U(1)_Y$ is called *hypercharge*. It is generated by the hypercharge operator Y , which is related to the third component of weak isospin I_3 and charge Q by the Gell-Mann-Nishijima relation:

$$Q = I_3 + \frac{Y}{2}. \quad (1.6)$$

The Gell-Mann-Nishijima relation (1.6) implies the unification of weak and electromagnetic interactions. Indeed Q is the generator of $U(1)_{em}$ symmetry group of electromagnetic interactions. In order to have a local gauge invariance, three vector gauge boson fields A_a^μ ($a= 1, 2, 3$) associated with the three generators of $SU(2)_L$, I_a ($a= 1, 2, 3$), and one vector gauge boson field B^μ associated with the generator Y of the group $U(1)_Y$ are needed. The covariant derivative D_μ , which in gauge theories replace the standard derivative ∂_μ in the Lagrangian, is:

$$D_\mu = \partial_\mu + ig\underline{A}_\mu \cdot \underline{I} + ig'B_\mu \frac{Y}{2}, \quad (1.7)$$

where \underline{A}_μ and \underline{I} are written in vector notation:

$$\underline{A}_\mu \equiv (A_1^\mu, A_2^\mu, A_3^\mu), \quad \underline{I} \equiv (I_1, I_2, I_3), \quad (1.8)$$

with the scalar product:

$$\underline{A}^\mu \cdot \underline{I} \equiv \sum_{j=1}^3 A_j^\mu I_j. \quad (1.9)$$

The covariant derivative in the equation (1.7) contains two independent coupling constant: g associated with the group $SU(2)_L$ and g' associated with the group $U(1)_Y$. The next step is the choose of the representations of fermion field. Historically, this choice has been guided by the wisdom of previous experience, in particular the V - A theory of weak interactions and the two-component theory of the neutrino. The left-handed chiral components of the fermions field are grouped into *weak isospin doublets*. For simplicity lets consider only the first generation of leptons and quarks:

$$L_L \equiv \begin{pmatrix} \nu_{eL} \\ e_L \end{pmatrix}, \quad Q_L \equiv \begin{pmatrix} u_L \\ d_L \end{pmatrix}.$$

From this choice, the generator of $SU(2)_L$ group are fixed to be $I_a = \tau_a/2$, and the action of the hypercharge operator Y is fixed by the Gell-Mann-Nishijima relation (1.6). Hence, the left-handed lepton and quark doublets have, respectively hypercharge $Y = -1$ and $Y = 1/3$.

Parametrizing the elements g of the group of local $SU(2)_L \times U(1)_Y$ transformations with a set of 3+1 parameters $(\underline{\theta}(x), \eta(x))$ ⁶ which depend on space-time x

$$g(\underline{\theta}(x), \eta(x)) \in SU(2)_L \times U(1)_Y, \quad (1.10)$$

with the unitary representation of $g(\underline{\theta}(x), \eta(x))$

$$U(\underline{\theta}(x), \eta(x)) = e^{i\underline{\theta}(x) \cdot \underline{I} + i\eta(x) \frac{Y}{2}} = U(\underline{\theta}(x))U(\eta(x)), \quad (1.11)$$

⁵ The Pauli matrices τ_a are: $\tau_1 = \begin{pmatrix} 0 & 1 \\ 1 & 0 \end{pmatrix}$, $\tau_2 = \begin{pmatrix} 0 & -i \\ i & 0 \end{pmatrix}$ and $\tau_3 = \begin{pmatrix} 1 & 0 \\ 0 & -1 \end{pmatrix}$.

⁶ $\underline{\theta}(x) \equiv (\theta_1(x), \theta_2(x), \theta_3(x))$.

where $U(\underline{\theta}(x)) = e^{i\underline{\theta}(x)\cdot I}$ and $U(\eta(x)) = e^{i\eta(x)\frac{Y}{2}}$, the transformation of the left-handed fermion doublets under $g(\underline{\theta}(x), \eta(x))$ is given by:

$$L_L \xrightarrow{g(\underline{\theta}(x), \eta(x))} L'_L = U(\underline{\theta}(x), \eta(x))L_L = U_L^l(\underline{\theta}(x), \eta(x))L_L, \quad (1.12)$$

and the same for the quark isospin doublet Q_L :

$$Q_L \xrightarrow{g(\underline{\theta}(x), \eta(x))} Q'_L = U(\underline{\theta}(x), \eta(x))Q_L = U_L^q(\underline{\theta}(x), \eta(x))Q_L, \quad (1.13)$$

where $U_L^l(\underline{\theta}(x), \eta(x)) = e^{\frac{i}{2}\underline{\theta}(x)\cdot\tau - \frac{i}{2}\eta(x)}$ for leptons and $U_L^q(\underline{\theta}(x), \eta(x)) = e^{\frac{i}{2}\underline{\theta}(x)\cdot\tau - \frac{i}{6}\eta(x)}$. In the SM, it is assumed that neutrino fields have only the left-handed component. This assumption comes from the hypothesis of massless neutrino [13]. The right-handed components of the others fermions are

$$e_R, u_R, d_R.$$

Those components are assumed to be singlets under the weak isospin group transformation:

$$I f_R = 0 \quad (f = e, u, d). \quad (1.14)$$

From the Gell-Mann-Nishijima relation (1.6), e_R , u_R and d_R have respectively the hypercharge $Y = -2, 4/3, -2/3$. Then, the transformation of the right-handed components of the fermion fields under the transformation in (1.10) is given by:

$$f_R \xrightarrow{g(\underline{\theta}(x), \eta(x))} f'_R = U(\underline{\theta}(x), \eta(x))f_R = U_R^f(\eta(x))f_R \quad (f = e, u, d), \quad (1.15)$$

where:

$$U_R^e(\eta(x)) = e^{-i\eta(x)}, \quad U_R^u(\eta(x)) = e^{\frac{2}{3}i\eta(x)}, \quad U_R^d(\eta(x)) = e^{-\frac{1}{3}i\eta(x)}.$$

The values of the weak isospin, hypercharge, and electric charge of the fermion doublets and singlets are listed in Table 1.2.

In the SM, the masses of gauge bosons, as well as those of the fermions, are generated through the Higgs mechanism [14–16] implemented by the Higgs doublet

$$\phi(x) = \begin{pmatrix} \phi^+(x) \\ \phi^0(x) \end{pmatrix},$$

where $\phi^+(x)$ is a charged complex scalar field and $\phi^0(x)$ is a neutral complex scalar field. The gauge quantum numbers of the Higgs fields are listed in Table 1.3. The transformation of the Higgs doublet under an element $g(\underline{\theta}(x), \eta(x))$ of the gauge group (see equation (1.10)) is given by:

$$\Phi \xrightarrow{g(\underline{\theta}(x), \eta(x))} \Phi' = U(\underline{\theta}(x), \eta(x))\Phi = e^{\frac{i}{2}\underline{\theta}(x)\cdot\tau + \frac{i}{2}\eta(x)}\Phi. \quad (1.16)$$

Using the above transformation and the transformation of the covariant derivative in order to satisfy the gauge invariance

$$D_\mu \xrightarrow{g(\underline{\theta}(x), \eta(x))} D'_\mu = U(\underline{\theta}(x), \eta(x))D_\mu U^{-1}(\underline{\theta}(x), \eta(x)), \quad (1.17)$$

Table 1.2: Eigenvalues coming from the Gell-Mann–Nishijima relation for leptons and quarks.

		I	I_3	Y	Q
lepton doublet	$L_L \equiv \begin{pmatrix} \nu_{eL} \\ e_L \end{pmatrix}$	1/2	$\begin{matrix} 1/2 \\ -1/2 \end{matrix}$	-1	0
lepton singlet	e_R	0	0	-2	-1
quark doublet	$Q_L \equiv \begin{pmatrix} u_L \\ d_L \end{pmatrix}$	1/2	$\begin{matrix} 1/2 \\ -1/2 \end{matrix}$	1/3	$\begin{matrix} 2/3 \\ -1/3 \end{matrix}$
quark singlets	$\begin{matrix} u_R \\ d_R \end{matrix}$	0	0	$\begin{matrix} 4/3 \\ -2/3 \end{matrix}$	$\begin{matrix} 2/3 \\ -1/3 \end{matrix}$

Table 1.3: Eigenvalues of the weak isospin I , of its third component I_3 , of the hypercharge Y and of the charge $Q = I_3 + \frac{Y}{2}$ of the Higgs doublet.

		I	I_3	Y	Q
Higgs doublet	$\phi(x) \equiv \begin{pmatrix} \phi^+(x) \\ \phi^0(x) \end{pmatrix}$	1/2	$\begin{matrix} 1/2 \\ -1/2 \end{matrix}$	+1	$\begin{matrix} 1 \\ 0 \end{matrix}$

one can verify that the Higgs part of the SM Lagrangian

$$\mathcal{L}_{\text{Higgs}} = (D_\mu \Phi)^\dagger (D_\mu \Phi) - \mu^2 \Phi^\dagger \Phi - \lambda (\Phi^\dagger \Phi)^2, \quad (1.18)$$

is invariant under a gauge transformation $g(\underline{\theta}(x), \eta(x))$. In equation (1.18), the coefficient λ of the quartic self-couplings of the Higgs fields must be positive, $\lambda > 0$, in order to have a potential

$$V(\Phi) = \mu^2 \Phi^\dagger \Phi + \lambda (\Phi^\dagger \Phi)^2, \quad (1.19)$$

which is bounded from below. On the other hand, the squared mass-like coefficient μ^2 is assumed to be negative, $\mu^2 < 0$, in order to realize the spontaneous breaking of the symmetry:

$$\text{SU}(2)_L \times \text{U}(1)_Y \rightarrow \text{U}(1)_Q, \quad (1.20)$$

where $U(1)_Q$ is the gauge symmetry group of electromagnetic interactions, associated with the conservation of the electric charge, which is well known to be unbroken.

Defining

$$v \equiv \sqrt{-\frac{\mu^2}{\lambda}}, \quad (1.21)$$

and neglecting an irrelevant constant term $v^4/4$, the Higgs potential in equation (1.19) can be written as:

$$V(\Phi) = \lambda \left(\Phi^\dagger \Phi - \frac{v^2}{2} \right)^2. \quad (1.22)$$

From the above expression it is clear that the potential is minimum for

$$\Phi^\dagger \Phi = \frac{v^2}{2}. \quad (1.23)$$

In quantum field theory the minimum of the potential corresponds to the vacuum, which is the lowest energy state, and the quantized excitations of each field above the vacuum correspond to particle states. Fermion and vector boson fields, which carry nonzero spin, must have a zero value in the vacuum, in order to preserve the manifest invariance of Nature under spatial rotation. Also, charged scalar fields must have zero value in the vacuum, which is electrically neutral. On the other hand, neutral scalar fields, which do not have electric charge, can have a nonzero value in vacuum, which is called *vacuum expectation value* (VEV). From equation (1.23) it is clear that the Higgs fields have a nonzero VEV.

The electroweak SM Lagrangian is the most general re-normalizable Lagrangian invariant under the local symmetry group $SU(2)_L \times U(1)_Y$. For the first generation of leptons and quarks it is written as:

$$\begin{aligned} \mathcal{L}_{\text{electroweak}} = & i\bar{L}_L \not{D} L_L + i\bar{Q}_L \not{D} Q_L + \sum_{f=e,u,d} i\bar{f}_R \not{D} f_R \\ & - \frac{1}{4} A_{\mu\nu} A^{\mu\nu} - \frac{1}{4} B_{\mu\nu} B^{\mu\nu} \\ & + (D_\mu \Phi)^\dagger (D_\mu \Phi) - \mu^2 \Phi^\dagger \Phi - \lambda (\Phi^\dagger \Phi)^2 \\ & - y^e (\bar{L}_L \Phi e_R + \bar{e}_R \Phi^\dagger L_L) \\ & - y^d (\bar{Q}_L \Phi d_R + \bar{d}_R \Phi^\dagger Q_L) - y^u (\bar{Q}_L \tilde{\Phi} u_R + \bar{u}_R \tilde{\Phi}^\dagger L_L). \end{aligned} \quad (1.24)$$

The terms proportional to y^i with $i = e, d, u$ the so called Yukawa coupling, generate lepton and quark masses. It is important to note that since the left-handed and right-handed components of the fermion fields transform in a different way under the transformations of the gauge group (equations (1.12), (1.13) and (1.15)), the presence of mass terms proportional to

$$\bar{f} f = \bar{f}_L f_R + \bar{f}_R f_L \quad (f = e, u, d), \quad (1.25)$$

it is forbidden in the Lagrangian by the gauge symmetry.

1.2.2 The neutrino mass in the SM

From the last section is clear that in the SM, the mass of fermions arises as a result of the Higgs mechanism through the presence of Yukawa couplings of the fermion fields with the Higgs doublet.

As shown in the equation (1.24), a fermion mass term involve a coupling of left-handed and right-handed fields. The fermions mass terms can be derived using (1.23) in the equation (1.24):

$$m_l \bar{l}_L l_R + m_q \bar{q}_L q_R, \quad (1.26)$$

where $m_i = \frac{v}{\sqrt{2}} Y_i$, with $i = (l, q)$. In the formula (1.26) v is the vacuum expectation value of the Higgs field and Y_i is the Yukawa coupling, that assumes different values for the different fermions. From this derive that neutrinos are massless in the SM, because their fields do not have the right-handed component (Section 1.1.1). So they are fully described in the SM, by the Lagrangian term

$$\mathcal{L}_\nu = i \bar{\nu} \not{D} \nu, \quad (1.27)$$

that includes a kinetic term plus the gauge interaction with the massive vector bosons, $\bar{\nu} W_L$ and $\bar{\nu} Z \nu$. From the experimental point of view, this picture is favorite by experiments that can measure the mass of neutrinos directly (such as β -decay experiments), that so far have only been able to set upper limits on neutrino masses (Table 1.1). Nevertheless, even if a direct measurement does not exist yet, there is an indirect proof of the existence of a neutrino mass different from zero: the observation, in different experiments, of the phenomenon of the neutrino oscillations (discussed in the next Section 1.3). After the discovery of that phenomenon, it was necessary to include the neutrino mass term into the SM. The most natural and simple way to include this masses is to consider the neutrino as the other fermions, so with the addition in the SM of $SU(2)_L$ singlet right-handed neutrino. Adding this field, neutrino masses are provided, as for all the other fermions (equation (1.26)), by the Higgs mechanism:

$$m^i \bar{\nu}_L^i \nu_R^i, \quad (1.28)$$

where i is the neutrino generation. The right-handed neutrino fields are called *sterile* [17] because they do not participate in weak interactions (as well as strong and electromagnetic interactions, as all neutrino fields); their only interaction is gravitational. On the other hand, the normal left-handed neutrino fields that participate in weak interactions are usually called *active*. The number of sterile right-handed neutrino fields is not constrained by the theory, and the introduction of three right-handed neutrino fields, one for each generation, is not even the minimal extension of the SM, because the presence of only one right-handed neutrino field cannot be excluded.

1.3 The neutrino oscillations

Neutrino oscillations are a quantum mechanical phenomenon whereby a neutrino created with a specific lepton flavor (electron, muon or tau) can later be measured to have a different flavor. This phenomenon is very important in the particle physics because so far, is the first evidence of neutrino mass and lepton number violation. A great amount of evidences for neutrino oscillation has been collected from many sources, over a wide range of neutrino energies and with many different detector technologies. The first experimental indication of neutrino oscillation, was probably observed in 1968 by the Homestake experiment. This indication remained controversial for several years, up to 1998 and 2002, when Super-Kamiokande and SNO experiments respectively published their results. In this section an overview on the neutrino oscillation theory will be presented and in the next sections, the main experimental results obtained in the recent history will be reviewed.

1.3.1 Neutrino oscillations in vacuum

Neutrino oscillations were proposed by Bruno Pontecorvo [18, 19] in 1950 in analogy with the oscillation $K^0 \rightarrow \bar{K}^0$. At that time, only the first family of *active* neutrinos was known, the electron neutrino ν_e , so he suggested the possibility of having neutrino oscillation of the type $\nu_e \rightarrow \bar{\nu}_e$. The muon neutrino was discovered in 1962 in the Brookhaven experiment [4] and since then, it became clear that oscillations between different *active* neutrino flavors are possible if neutrinos are massive and mixed. In 1962 Maki, Nakagawa, and Sakata [20] considered for the first time a model with the mixing of different neutrino flavors. In principle if neutrino is not a massless particle, and the mass eigenstates do not correspond to flavor ones, than neutrinos can mix, exactly as it happens in the quark sector. The flavor states $|\nu_\alpha\rangle$, are superpositions of mass eigenstates $|\nu_k\rangle$:

$$|\nu_\alpha\rangle = \sum_k U_{\alpha k}^* |\nu_k\rangle \quad (\alpha = e, \mu, \tau) \quad (k = 1, 2, 3), \quad (1.29)$$

where the weight $U_{\alpha k}^*$ is the unitary mixing matrix. Neutrinos are produced via weak interactions as flavor eigenstates $|\nu_\alpha\rangle$, where they are created with the corresponding lepton partner α . The massive neutrino states $|\nu_k\rangle$ are eigenstates of the Hamiltonian:

$$\mathcal{H}|\nu_k\rangle = E_k|\nu_k\rangle, \quad (1.30)$$

with the energy eigenvalues

$$E_k = \sqrt{\vec{p}^2 + m_k^2}. \quad (1.31)$$

The Schrödinger equation is

$$i \frac{d}{dt} |\nu_k(t)\rangle = \mathcal{H} |\nu_k(t)\rangle, \quad (1.32)$$

that implies that the massive neutrino states evolve in time as plane waves:

$$|\nu_k(t)\rangle = e^{-iE_k t} |\nu_k\rangle. \quad (1.33)$$

Considering now a neutrino flavor state $|\nu_\alpha(t)\rangle$, which describes a neutrino created with a specific flavor α at time $t = 0$, from the equations (1.29) and (1.33), the time evolution of this state will be:

$$|\nu_\alpha(t)\rangle = \sum_k U_{\alpha k}^* e^{-iE_k t} |\nu_k\rangle, \quad (1.34)$$

such that $|\nu_\alpha(t = 0)\rangle = |\nu_\alpha\rangle$. Using the unitarity relation of the mixing matrix ($UU^\dagger = \mathbb{1} \iff \sum_\alpha U_{\alpha k}^* U_{\alpha j} = \delta_{ij}$), the massive neutrino states are equal to

$$|\nu_k\rangle = \sum_\alpha U_{\alpha k} |\nu_\alpha\rangle. \quad (1.35)$$

Using the equation (1.35) in (1.34) one obtains:

$$|\nu_\alpha(t)\rangle = \sum_{\beta=e,\mu,\tau} \left(\sum_k U_{\alpha k}^* e^{-iE_k t} U_{\beta k} \right) |\nu_\beta\rangle. \quad (1.36)$$

Hence, the superposition of the neutrino state $|\nu_\alpha(t)\rangle$, which is the pure flavor state given in equation (1.29) at $t = 0$, becomes a superposition of different flavor states at $t > 0$ (if the mixing matrix U

is not diagonal, i.e. neutrinos are mixed). The transition amplitude $\nu_\alpha \rightarrow \nu_\beta$ is:

$$A_{\nu_\alpha \rightarrow \nu_\beta}(t) \equiv \langle \nu_\beta | \nu_\alpha(t) \rangle = \sum_k U_{\alpha k}^* U_{\beta k} e^{-iE_k t}. \quad (1.37)$$

The transition probability is then given by

$$P_{\nu_\alpha \rightarrow \nu_\beta}(t) = |A_{\nu_\alpha \rightarrow \nu_\beta}(t)|^2 = \sum_{k,j} U_{\alpha k}^* U_{\beta k} U_{\alpha j} U_{\beta j}^* e^{-i(E_k - E_j)t}. \quad (1.38)$$

For ultra-relativistic neutrinos, the relation (1.31) can be approximated by:

$$E_k \simeq E + \frac{m_k^2}{2E}, \quad (1.39)$$

and in this case, the term in the exponential in (1.38) becomes:

$$E_k - E_j \simeq \frac{\Delta m_{kj}^2}{2E}, \quad (1.40)$$

where Δm_{kj}^2 is the squared-mass difference ($\Delta m_{kj}^2 = m_k^2 - m_j^2$) and $E = |\vec{p}|$ is the neutrino energy, neglecting the mass contribution. Therefore, the transition probability in (1.38) can be approximated as:

$$P_{\nu_\alpha \rightarrow \nu_\beta}(t) = \sum_{k,j} U_{\alpha k}^* U_{\beta k} U_{\alpha j} U_{\beta j}^* \exp\left(-i \frac{\Delta m_{kj}^2 t}{2E}\right). \quad (1.41)$$

In the neutrino oscillation experiments, the propagation in time t is not measured. What is known is the distance L from the neutrino source and the detector. Since ultra-relativistic neutrinos propagate almost at the speed of light, it is possible to approximate $t = L$, and (1.41) becomes:

$$P_{\nu_\alpha \rightarrow \nu_\beta}(L, E) = \sum_{k,j} U_{\alpha k}^* U_{\beta k} U_{\alpha j} U_{\beta j}^* \exp\left(-i \frac{\Delta m_{kj}^2 L}{2E}\right). \quad (1.42)$$

This expression shows that the source–detector distance L and the neutrino energy E are the quantities depending on the experiment which determine the phases of neutrino oscillations

$$\Phi_{kj} = -\frac{\Delta m_{kj}^2 L}{2E}. \quad (1.43)$$

Of course, the phases are determined also by the squared-mass differences Δm_{kj}^2 , which are physical constants. The amplitude of the oscillations is specified only by the elements of the mixing matrix U , which are constants of nature. Therefore measurements of neutrino oscillations allow the investigation of the squared-mass differences Δm_{kj}^2 and the elements of the mixing matrix U . It is possible to write the equation (1.42), using the properties of the complex exponential and the unitarity of the matrix U , as:

$$P_{\nu_\alpha \rightarrow \nu_\beta}(L, E) = \delta_{\alpha\beta} - 4 \sum_{k>j} \Re(W_{\alpha\beta}^{kj}) \sin^2\left(\frac{\Delta m_{kj}^2 L}{4E}\right) \pm 2 \sum_{k>j} \Im(W_{\alpha\beta}^{kj}) \sin\left(\frac{\Delta m_{kj}^2 L}{2E}\right), \quad (1.44)$$

where $W_{\alpha\beta}^{kj} = U_{\alpha k}^* U_{\beta k} U_{\alpha j} U_{\beta j}^*$, the sign \pm distinguish respectively neutrinos from anti-neutrinos and the imaginary part correspond to the CP violation term. So if the imaginary part of (1.44) is different from zero, is clear that $P(\nu_\alpha \rightarrow \nu_\beta) \neq P(\bar{\nu}_\alpha \rightarrow \bar{\nu}_\beta)$. In order to understand better the oscillation phenomenon, is useful to consider the simple case where only two neutrino generations exist. In this case the mixing matrix U can be written as a rotation in a real space:

$$U = \begin{pmatrix} \cos \theta & \sin \theta \\ -\sin \theta & \cos \theta \end{pmatrix}, \quad (1.45)$$

where the only parameter needed to describe the mixing is the angle θ . In this case, the probability of flavor change becomes

$$P_{\nu_\alpha \rightarrow \nu_\beta}(L, E) = \sin^2(2\theta) \sin^2 \left(\frac{1.27 \Delta m^2 [\text{eV}^2] L [\text{km}]}{E [\text{GeV}]} \right). \quad (1.46)$$

In the above equation $\sin^2(2\theta)$ is the maximum oscillation amplitude, $\frac{1.27 L [\text{km}]}{E [\text{GeV}]}$ are the controlled parameters by experiments, and $\Delta m^2 [\text{eV}^2]$ is the oscillation frequency. From the Figure 1.9 is clear that the best sensitivity to oscillation is when $L/E \sim 1/\Delta m^2$. In the case of $\alpha = \beta$, the *survival probability* $P_{\nu_\alpha \rightarrow \nu_\alpha}(L/E)$ is easily obtained by unitarity from the transition probability:

$$P_{\nu_\alpha \rightarrow \nu_\alpha}(L, E) = 1 - P_{\nu_\alpha \rightarrow \nu_\beta}(L, E) = 1 - \sin^2(2\theta) \sin^2 \left(\frac{1.27 \Delta m^2 [\text{eV}^2] L [\text{km}]}{E [\text{GeV}]} \right). \quad (1.47)$$

In the case of three neutrino generations, the unitary mixing matrix will be written as 3×3 matrix:

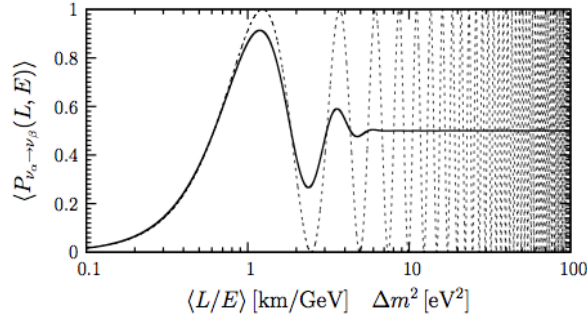


Figure 1.9: $P_{\nu_\alpha \rightarrow \nu_\beta}(L, E)$ for $\sin^2(2\theta) = 1$ as a function of $\langle L/E \rangle [\text{km/GeV}]$ $\Delta m^2 [\text{eV}^2]$.

$$U = \begin{pmatrix} 1 & 0 & 0 \\ 0 & +c_{23} & +s_{23} \\ 0 & -s_{23} & +c_{23} \end{pmatrix} \begin{pmatrix} +c_{13} & 0 & +s_{13}e^{-i\delta_{CP}} \\ 0 & 1 & 0 \\ -s_{13}e^{i\delta_{CP}} & 0 & +c_{13} \end{pmatrix} \begin{pmatrix} +c_{12} & +s_{12} & 0 \\ -s_{12} & +c_{12} & 0 \\ 0 & 0 & 1 \end{pmatrix} \quad (1.48)$$

$$= \begin{pmatrix} c_{12}c_{13} & s_{12}c_{13} & s_{13}e^{-i\delta_{CP}} \\ -s_{12}c_{23} - c_{12}s_{23}s_{13}e^{i\delta_{CP}} & c_{12}c_{23} - s_{12}s_{23}s_{13}e^{i\delta_{CP}} & s_{23}c_{13} \\ s_{12}s_{23} - c_{12}c_{23}s_{13}e^{i\delta_{CP}} & -c_{12}s_{23} - s_{12}c_{23}s_{13}e^{i\delta_{CP}} & c_{23}c_{13} \end{pmatrix},$$

where $c_{ij} = \cos \theta_{ij}$ and $s_{ij} = \sin \theta_{ij}$. In this case there are four parameters that describe the matrix: three angles θ_{12} , θ_{23} and θ_{13} and the CP violating phase δ_{CP} .

1.3.2 Neutrino oscillations in the matter

Neutrinos that travel in the matter (where matter can be earth, sun, etc ...) can scatter with the particles along their way, and this interactions are able to modify their propagation. Neutrinos can interact only weakly via a NC or CC process. A NC process (Figure 1.10) has the same amplitude for all neutrino flavors and cannot be observable on flavor oscillation since it will change an immeasurable phase to all neutrino states. A CC process (Figure 1.11), instead, involve only ν_e , because the ordinary matter contains electrons and not muons or taus. The result of this phenomenon is an oscillation probability different from (1.44) (valid in the vacuum) and it is known as the Mikheyev-Smirnov-Wolfenstein (MSW) effect [21, 22]. This means that ν_e acquires an extra energy due to CC

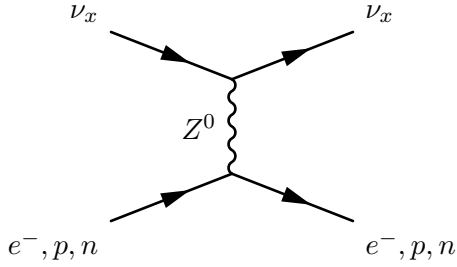


Figure 1.10: Neutral current (NC) neutrino interaction with the matter.

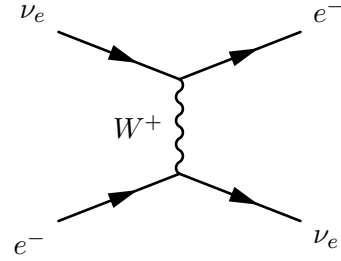


Figure 1.11: Charged Current (CC) neutrino interaction with matter.

interactions, generally called potential $V_{CC} = \pm\sqrt{2}G_F n_e$, where n_e is the electron number density, G_F is the Fermi's constant and the \pm is respectively for neutrinos and anti-neutrinos. In the simple two flavor case, the effective Hamiltonian in the flavor bases is:

$$\mathcal{H}_M = \frac{\Delta m^2}{4E} \begin{pmatrix} -\cos(2\theta_V) & \sin(2\theta_V) \\ \sin(2\theta_V) & \cos(2\theta_V) \end{pmatrix} + V_{CC} \begin{pmatrix} 1 & 0 \\ 0 & 0 \end{pmatrix}. \quad (1.49)$$

For example, the matter effect can be seen in the neutrino oscillation from the sun to the earth. This oscillation occurs between two flavor: ν_e produced from the sun oscillate in a state ν_x that is a linear combination of ν_μ and ν_τ . The Hamiltonian of this process can be written as:

$$\mathcal{H} = \mathcal{H}_V + \mathcal{H}_M(r) = \frac{\Delta m_\odot^2}{4E} \begin{pmatrix} -\cos(2\theta_\odot) & \sin(2\theta_\odot) \\ \sin(2\theta_\odot) & \cos(2\theta_\odot) \end{pmatrix} + V_{CC}(r) \begin{pmatrix} 1 & 0 \\ 0 & 0 \end{pmatrix}, \quad (1.50)$$

where \mathcal{H}_V is the Hamiltonian in the vacuum, $\mathcal{H}_M(r)$ contains the matter effect that depend from the sun radius r , because the electron number density n_e depends on r and the angle θ_\odot is the solar mixing angle, defined by the two neutrino mixing matrix of equation (1.45) with $\theta = \theta_\odot$. The splitting Δm_\odot^2 is $m_2^2 - m_1^2$, with the assumption that ν_2 is the heavier of the two mass eigenstates, so that Δm_\odot^2 is defined positive. From the equations (1.46), (1.47), with $\theta = \theta_\odot$, is clear that the two neutrino oscillation in the vacuum cannot distinguish between a mixing angle θ_\odot and an angle $\theta'_\odot = \pi/2 - \theta_\odot$. The problem is that this two mixing angle represents two different physical situations. If for example $\theta_\odot < \pi/4$, from the equation (1.45), the lighter mass eigenstate (defined

as ν_1) is more ν_e instead than ν_x , while if it is θ'_\odot , than this mass eigenstate is more ν_x than ν_e . So while neutrino propagation cannot discriminate between these two physical situations, neutrino propagation through the solar matter can do so. The neutrino interaction energy $V_{CC}(r)$ is defined positive [23]. The corresponding energy for anti-neutrinos is negative. Thus, the $\nu_e - \nu_e$ element of the solar \mathcal{H} , $-(\Delta m_\odot^2/4E) \cos 2\theta_\odot + V_{CC}(r)$, has different size if is θ_\odot or θ'_\odot . As a result, the flavor content of the neutrinos coming from the Sun can be different in the two cases [24]. Solar and long-baseline reactor neutrino data establish that the behavior of solar neutrinos is governed by a Large-Mixing-Angle (LMA) MSW effect. Is it possible now, as exercise, try to estimate the survival probability $P(\nu_e \rightarrow \nu_e)$ of electron neutrinos produced in the sun that arrives at the earth, looking just at electron neutrinos produced in the ^8B decay, which are at the high-energy tail of solar neutrino spectrum. At $r \simeq 0$ where the solar neutrinos are created, the electron density $n_e \simeq 6 \times 10^{25} \text{ eV}^2/\text{MeV}$. Thus, for Δm_\odot^2 in the favored region, around $8 \times 10^{-5} \text{ eV}^2$, and $E \simeq 6 - 7 \text{ MeV}$, \mathcal{H}_M dominates \mathcal{H}_V . So from the equation (1.50), in first approximation $\mathcal{H}(r \simeq 0)$ is diagonal. Since $V_{CC} > 0$, the neutrino will be in the heavier of the two mass eigenstate (ν_2). Now, under the conditions where the LMA-MSW effect occurs, the propagation of a neutrino from $r \simeq 0$ to the outer edge of the Sun is adiabatic. This assumption is realistic if n_e changes sufficiently slowly. Since the eigenvalues of $\mathcal{H}(r)$ do not cross at any r and the neutrino is born in the heavier eigenstate of the two in $r = 0$, it emerges from the Sun in the heavier of the two \mathcal{H}_V eigenstate [25], and so according to (1.45):

$$\nu_2 = \nu_e \sin \theta_\odot + \nu_x \cos \theta_\odot. \quad (1.51)$$

Since this is an eigenstate of the vacuum Hamiltonian, the neutrino remains in it all the way to the surface of the Earth. The probability of observing the neutrino as a ν_e on earth is then just the probability that ν_2 is a ν_e [26]:

$$P(\nu_e \rightarrow \nu_e) = \sin^2 \theta_\odot. \quad (1.52)$$

A $\theta_\odot < \pi/4$, means that follow the equation (1.52) the ν_e survival probability is less than 1/2. In contrast, when matter effects are negligible, the energy-averaged survival probability in two-neutrino oscillation cannot be less than 1/2 for any mixing angle [27].

1.4 Solar neutrinos

During the first half of the twentieth century, scientists became convinced that the Sun is a natural nuclear fusion reactor, powered by a proton-proton chain reaction which convert four hydrogen nuclei (protons) into helium (^4He), 2 electron neutrinos (ν_e) and two positrons (e^+). As said in the previous section, these neutrinos produced in this fusion process can escape the sun, because of their low cross section. While this theory was widely accepted there was no way of observing the sun's core and directly testing the hypothesis. In the late 1960's started a pioneering solar neutrino experiment by Davis, called the Homestake Experiment [28] (because the experiment took place in the Homestake Gold Mine). This experiment used a tank of 400 m³ of C_2Cl_4 to detect solar ν_e by inverse β -decay to check the Standard Solar Model (SSM) (Figure 1.12). It was observed that the flux was significantly smaller, about 1/3 respect to the prediction of the SSM. This deficit has been called "*the solar-neutrino problem*". At that time, three kind of explanation were proposed to solve this problem:

1. the SSM was wrong;
2. the Homestake experiment made wrong measurement;

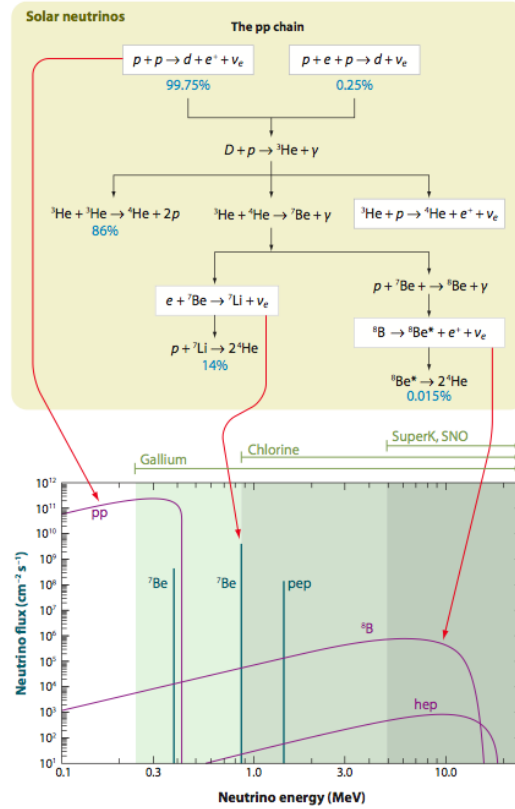


Figure 1.12: Reactions and neutrino energies predicted by the SSM.

3. the Standard Model was wrong about the neutrino mass.

The last explanation was the less substantiated from the scientific community, because the SM was deeply tested in the experiments the measurement of the Z^0 and W masses, etc. . . In the following years the first two hypothesis were ruled out, the first one (a wrong SSM) by the progress in the understanding of the Sun, and the second one (something wrong in the Homestake experiment) by the fact that several experiments, with different detection techniques, have measured the same deficit founded by Davis: Gallex [29], Sage [30], and GNO [31] detecting the inverse β -decay as Homestake and Kamiokande [32] and SuperKamiokande [33] detecting electrons coming from ν_e interactions with water Cherenkov. The only remaining possibility was the transformation of ν_e coming from the sun in something else, which is not detectable with the inverse β -decay. So conserving the total neutrino flux, the ν_e escaping from the sun change in a linear superposition of the three neutrino generations. The answer to the solar neutrino problem, was established in 2002 by the SNO (Sudbury Neutrino Observatory) experiment, able to proof that the total neutrino flux is conserved. This experiment used 1000 tons of ultra-pure heavy water (D_2O) contained in a spherical acrylic vessel surrounded by an ultra-pure H_2O shield cherenkov detector [34] able to detect not only CC ν_e interactions, but also NC interactions that involve any neutrino flavor with the Deuterium nuclei and Electron Elastic Scattering (ES) (Figure 1.13 and 1.14). The results of this experiment are the following:

$$\phi_{CC} = \phi_e = 1.68 \pm 0.06 \text{ (stat.)}_{-0.09}^{+0.08} \text{ (syst.)} \times 10^6 \frac{\nu}{\text{cm}^2\text{s}}, \quad (1.53)$$

$$\phi_{NC} = \phi_e + \phi_\mu + \phi_\tau = 4.94 \pm 0.21 \text{ (stat.)}_{-0.34}^{+0.38} \text{ (syst.)} \times 10^6 \frac{\nu}{\text{cm}^2\text{s}}. \quad (1.54)$$

The result (1.54) (that is a mixing-independent result) is in a good agreement with the expectation of the SSM [35] and the fact that (1.53) is only about 1/3 of (1.54), is the demonstration of neutrino oscillation phenomenon of electrons neutrinos coming from the sun that arrive on the earth in a mix of ν_e , ν_μ and ν_τ .



Figure 1.13: Key reactions in the SNO Experiment: CC (left) reaction of ν_e with Deuteron and NC (right) reaction of ν_x with Deuteron.

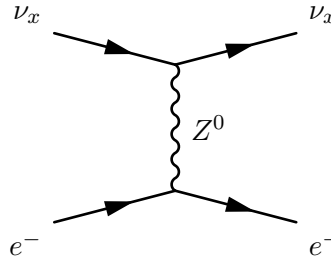


Figure 1.14: Key reactions in the SNO Experiment: ES reaction.

1.5 Atmospheric neutrinos

Neutrinos arrive on the earth not only from the sun, but also from the atmosphere. Indeed, cosmic rays, primarily protons, interact on the high atmosphere and produce a huge number of secondaries, in particular pions. Then pions decay in flight via the reaction $\pi^\pm \rightarrow \mu^\pm + \nu_\mu(\bar{\nu}_\mu)$. The produced muons again decay with the reaction $\mu^\pm \rightarrow e^\pm + \nu_e(\bar{\nu}_e) + \bar{\nu}_\mu(\nu_\mu)$ (Figure 1.15). The typical energy of these neutrinos starts at about hundred MeV up to several GeV. Since atmospheric neutrinos cannot be consider as solar neutrinos generated in a point like source at a fixed distance, they require a different technique to be detected. Neutrinos can be generated in each point of the atmosphere and thus neutrinos of the same energy born at the same time can travel very different distances before reaching the detector and this gives different oscillation probabilities (Figure 1.16). For this reason, to study the oscillation probability, the detector must be capable to recognize the direction of interacting neutrinos. The most common technique used is the water-Cherenkov detector. With

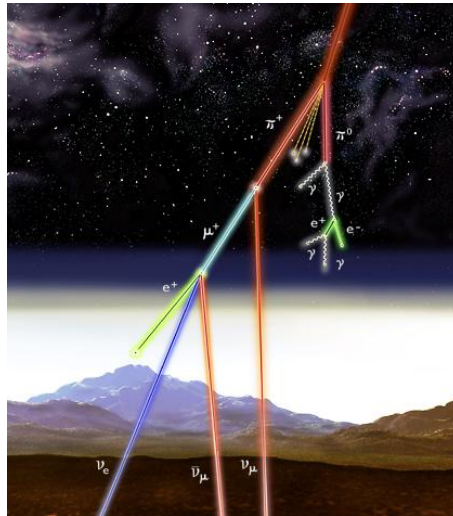


Figure 1.15: Atmospheric neutrinos.

this particular detector, if the energy of the lepton generated by the neutrino interaction is above the Cherenkov threshold (few MeV for electrons and hundreds MeV for muons), a cone of light is generated with the centre corresponding with the lepton trajectory. In these kinds of experiment, a typical water-Cherenkov detector is organized as a huge tank of water equipped with an array of phototubes on the inside walls used to record the Cherenkov light. In this way is possible to measure:

- if the generated lepton stops inside the detector: the amount of the Cherenkov light used to determine the energy of the lepton and neutrino that generate the lepton;
- the particle identification from the ring shape: electrons produce a more fuzzy rings than muons because electrons shower in the water.

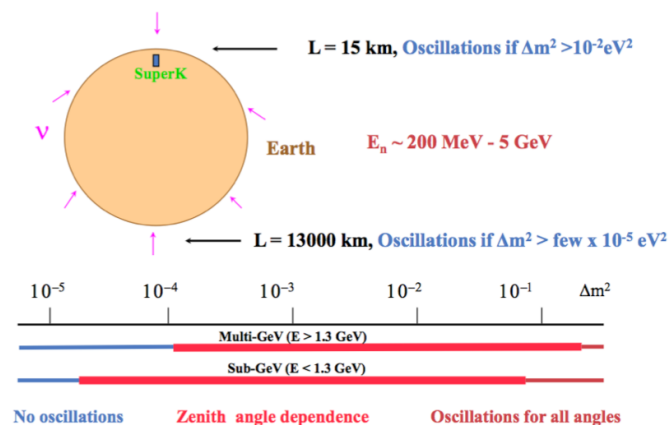


Figure 1.16: Flight distances for atmospheric neutrinos.

The first compelling evidence for the atmospheric neutrino oscillation was presented by the Super-Kamiokande Collaboration in 1998 [38]. The zenith-angle distributions of the μ -like events which

are mostly muon-neutrino and muon antineutrino initiated charged-current interactions, showed a clear deficit compared to the no-oscillation expectation. Note that a water Cherenkov detector cannot measure the charge of the final-state leptons, and therefore neutrino and antineutrino induced events cannot be discriminated. Neutrino events having their vertex in the 22.5 kton fiducial volume in Super-Kamiokande are classified into fully contained (FC) events and partially contained (PC) events. The FC events are required to have no activity in the anti-counter. Single-ring events have only one charged lepton which radiates Cherenkov light in the final state, and particle identification is particularly clean for single-ring FC events. All the PC events were assumed to be μ -like since the PC events comprise a 98% pure CC ν_μ sample. The Figure 1.17 shows the zenith-angle distributions of e -like and μ -like events from SK-I measurement [39]. $\cos\theta = 1$ corresponds to the zenith, while $\cos\theta = -1$ to the nadir. The experimental result that can be established from these plots is that ν_μ coming from the bottom ($\cos\theta = -1$), hence traversing the earth, are 1/2 of those coming from the top ($\cos\theta = 1$). The easiest explanation could be that neutrinos have interacted with the earth. But as shown, the asymmetry does not involve ν_e , and also is well known that the earth is practically transparent for neutrinos with energy lower than few GeV. The only explanation to this phenomenon is the oscillation of $\nu_\mu \leftrightarrow \nu_\tau$ and not $\nu_\mu \leftrightarrow \nu_e$, because was not observed an excess in the s -like events at $\cos\theta = -1$.

The Super-Kamiokande results provided a strong evidence of the existence of neutrino oscillations with a different Δm^2 from the solar neutrinos.

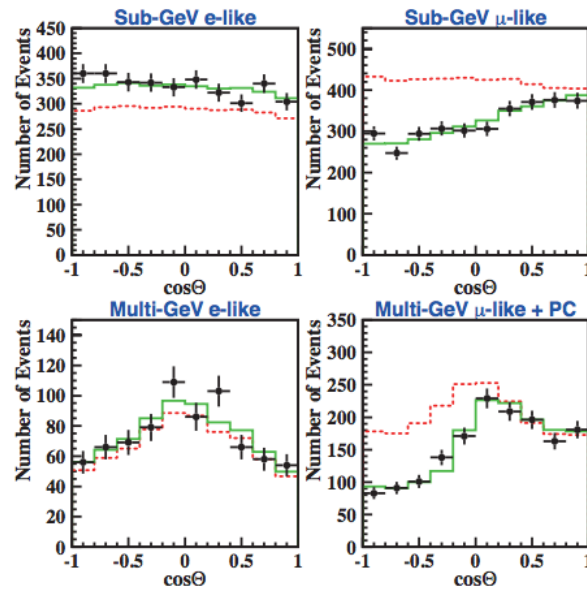


Figure 1.17: The zenith angle distributions for fully contained 1-ring e -like and μ -like events with visible energy < 1.33 GeV (sub-GeV) and > 1.33 GeV (multi-GeV). The dotted histograms show the non-oscillated Monte Carlo events, and the solid histograms show the best fit expectation for $\nu_\mu \rightarrow \nu_\tau$ oscillations.

1.6 Reactor anti-neutrinos

Fission reactors are copious sources of electron anti-neutrinos produced in the β -decay of neutron rich nuclei. The power of the reactor is mainly due to the fission of four isotopes ^{235}U , ^{138}U ($\sim 8\%$), ^{239}Pu ($\sim 30\%$) and ^{241}Pu ($\sim 6\%$). The electron anti-neutrinos are produced in the chain of β -decays of the fission products. Since, on average, each fission produces about 200 MeV, with release of about six $\bar{\nu}_e$'s, the electron anti-neutrino yield is about $2 \times 10^{20} \text{ s}^{-1}$ for each GW_{th} of thermal power. Typical modern light-water nuclear power plants have several reactor cores, each with a thermal power of the order of 3 GW_{th} . Thus, the total rate of anti-neutrino production of a typical nuclear power plant is very high. Unfortunately, however, since the anti-neutrino flux is isotropic, it decreases rapidly with distance. This is obviously a problem for neutrino oscillation experiments, which require an appropriate source–detector distance in order to reveal the oscillations. The anti-neutrinos produced have a typical energy of few MeV, which implies a relatively short oscillation length following the formula (1.46). Such a low energy also implies that **only $\bar{\nu}_e$ disappearance can be investigated in reactor experiments**, since the energy is not sufficient to produce, in a detector, muons or taus from a CC reaction. The NC interactions of oscillated $\bar{\nu}_\mu$ and $\bar{\nu}_\tau$ are too weak to be distinguished from the background. This means that reactor neutrino experiments are strongly dependent from MC simulation of the neutrino flux which must be understood with high precision (flux intensity, flux stability in time and energy spectrum). For this reason an oscillation measurement by appearance achievable with the accelerator experiments is needed to confirm reactor results.

In 2002 the first evidence of oscillation of reactor neutrinos was found by the KamLAND experiment [40]. KamLAND is a 1 kton ultra-pure liquid scintillator detector located at the old Kamiokande's site in Japan, and detects $\bar{\nu}_e$ coming from 16 reactors located at an average distance of 160 km. The inverse β -decay $\bar{\nu}_e + p \rightarrow e^+ + n$ is used and a delayed coincidence of the positron with a 2.2 MeV γ -ray from neutron capture on a proton is used to reduce the backgrounds. This experiment has a sensitive Δm^2 range down to $\sim 10^{-5} \text{ eV}^2$. Therefore, if the LMA solution is the real solution of the solar neutrino problem, KamLAND should observe reactor $\bar{\nu}_e$ disappearance, assuming CPT invariance. The first KamLAND results [40] (see Figure 1.18 on the left) showed that the ratio of observed to expected (assuming no $\bar{\nu}_e$ oscillations) number of events was:

$$\frac{N_{\text{obs}} - N_{\text{BG}}}{N_{\text{NoOsc}}} = 0.611 \pm 0.085 \text{ (stat.)} \pm 0.041 \text{ (syst.)}. \quad (1.55)$$

This result showed clear evidence of an event deficit expected from neutrino oscillations. A combined global solar + KamLAND analysis showed that the Large Mixing Angle is a unique solution to the solar neutrino problem with a C.L. $> 5\sigma$ [41] (see Figure 1.18 on the right). With increased statistics, KamLAND observed not only the distortion of the $\bar{\nu}_e$ spectrum, but also for the first time the periodic feature of the $\bar{\nu}_e$ survival probability expected from neutrino oscillations (see Figure 1.19). Another interesting result coming from a reactor experiment was published by CHOOZ collaboration [42] in 1999. At that time, CHOOZ produced the most significant limit on the neutrino mixing angle θ_{13} that was at that time the last mixing angle parameter to measure in the PMNS matrix. This experiment was located in France and used anti-neutrinos coming from two pressurized water reactors, which are able to provide a pure source ($> 99.9\%$) of $\bar{\nu}_e$. The average neutrino energy was approximately 3 MeV and the detector was roughly 1 km from the reactor. Neutrinos were observed via inverse β -decay in a detector divided in three regions:

- **region 1** (the innermost region): composed by 5 tons of scintillator doped with Gadolinium (Gd) in a plexiglass container (transparent to the scintillation light). The gadolinium quickly

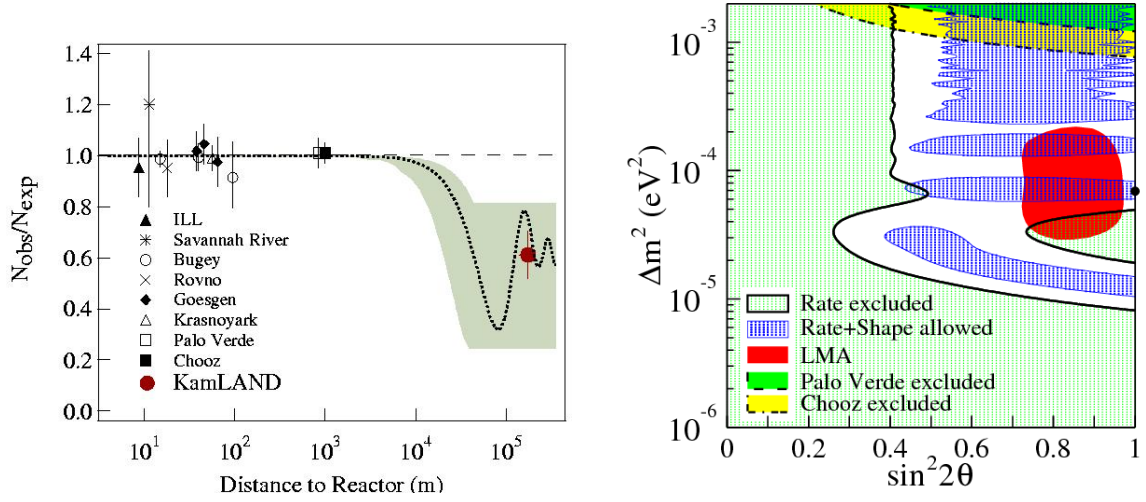


Figure 1.18: On the left, ratio of measured neutrinos over expected neutrinos versus the distance of different reactor anti-neutrino experiments. On the right, allowed zones for the oscillations parameters $\sin^2 \theta_{12}$ and Δm_{12}^2 measured by KamLAND. The red zone represent the best fit solution for combined KamLAND experimental data, solar neutrino experiments and LMA hypothesis.

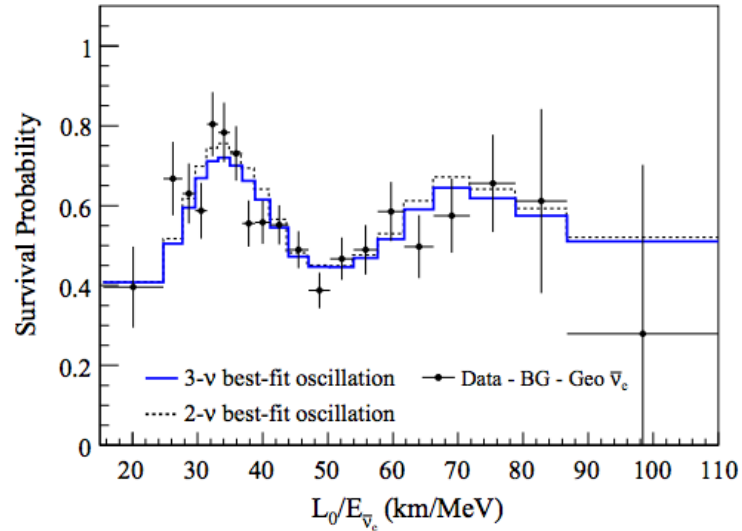


Figure 1.19: The ratio of the background and geoneutrino-subtracted $\bar{\nu}_e$ spectrum to the predicted one w/o oscillations (survival probability) as a function of L_0/E , where $L_0=180$ km.

captured the neutrons produced in the inverse beta decay;

- **region 2:** composed by 17 tons of undoped scintillators to capture the electromagnetic energy from the inverse beta decay ($\sim 99\%$) and the photons from the neutron capture in the Gd ($> 95\%$). The outer surface of region II contained 192 inward facing photomultiplier tubes (PMT) held in an opaque plastic structure;

- **region 3** (the outermost region): contained ninety tons of the same undoped scintillator as region 2 and vetoed cosmic ray events using 48 PMTs.

The CHOOZ experiment was designed to search for neutrino flavor oscillation in the mass mixing ranges of the Cosmic Ray Anomaly (CRA, discussed in the Section 1.5). In the case of SMA (Small Mixing Angle) solution ($\nu_\mu \leftrightarrow \nu_e$) a 50% reduction of $\bar{\nu}_e$ would be expected. The observation of no reduction of anti-neutrinos leaves the LMA scenario as the best explanation of the CRA. The upper limits measured was $\theta_{13} < 10^\circ$ for $\Delta m_{13}^2 = 3 \times 10^{-3}$ eV.

More recently, in 2012, three reactor experiments were able to measure the mixing angle θ_{13} : Daya Bay [43] in China, RENO [44] in South Korea and the evolution of CHOOZ, the Double-CHOOZ [45] experiment in France. They found:

$$\sin^2 2\theta_{13|\text{Daya Bay}} = 0.092 \pm 0.016 \text{ (stat.)} \pm 0.005 \text{ (syst.)}, \quad (1.56)$$

$$\sin^2 2\theta_{13|\text{RENO}} = 0.113 \pm 0.013 \text{ (stat.)} \pm 0.019 \text{ (syst.)}, \quad (1.57)$$

$$\sin^2 2\theta_{13|\text{Double-CHOOZ}} = 0.086 \pm 0.041 \text{ (stat.)} \pm 0.030 \text{ (syst.)}. \quad (1.58)$$

Reactor experiments give the cleaner θ_{13} measurement. In fact using the $\bar{\nu}_e \rightarrow \bar{\nu}_e$ disappearance channel, the oscillation probability depends only from the mixing angle θ_{13} and is independent from other oscillation parameters. The $P(\bar{\nu}_e \rightarrow \bar{\nu}_e)$ formula is:

$$P(\bar{\nu}_e \rightarrow \bar{\nu}_e) \approx 1 - \sin^2 2\theta_{13} \sin^2(1.27 \Delta m_{13}^2 L/E). \quad (1.59)$$

However this implies that reactor experiments are not sensitive to any other oscillation parameters except θ_{13} .

1.7 Accelerator neutrino experiments

The accelerator experiment can be classified according to the method of production of neutrino beam: pion decay in flight (DIF), muon decay at rest (DAR) and beam dump. The characteristics of each one of those neutrino beam are:

- **pion DIF**: these are the experiments with a neutrino beam composed mainly of muon neutrinos produced by the decay of pions and kaons initially produced by a proton beam hitting a target. The pions and kaons are allowed to decay in a decay tunnel of length of the order of 100 m. The beam is largely composed of ν_μ 's or $\bar{\nu}_\mu$'s, depending of the polarity of the horns which are able to focalize the desired pions and kaons and reject the remaining undesired particles. Some experiments that used the pion decay in flight technique to produce the neutrino beam are CHORUS [46] and NOMAD [47];
- **muon DAR**: these are lower energy experiments with a beam composed of muon anti-neutrinos coming from the muons decay. This $\bar{\nu}_\mu$'s have energy of the order of several tens of MeV and can be used for measure the oscillation $\bar{\nu}_\mu \rightarrow \bar{\nu}_e$. This kind of beam is frequently used in Short Base Line (SBL) experiments. Some experiments that used the muon decay at rest technique to produce the neutrino beam are LSND [48] and KARMEN [49];
- **beam dump**: also called *prompt* neutrino experiments. In this case a very high energy proton beam, of the order of hundred GeV, is completely stopped in a thick target, called the *beam*

dump, where the proton nucleon interactions generate heavy hadrons. The charmed heavy hadrons decay promptly with practically equal branching ratios into electrons and muons, emitting equal fluxes of electron and muon neutrinos with energies of the order of 10^2 GeV. Some experiments that used the beam dump technique to produce the neutrino beam are BEBC [50, 51] and CHARM [52].

In addition, the experiments with neutrino beams generated by pion decay in flight are further classified in three categories:

- **Wide Band (WB) beam:** these experiments have a high-intensity neutrino beam with a wide energy spectrum which can span one or two order of magnitude. This type of beam is convenient for investigating new oscillation signals in a wide range of values of Δm^2 ;
- **Narrow Band (NB) beam:** these experiments have a narrow energy spectrum, which is obtained with the selection neutrino parents (pions and kaons) momenta. The resulting intensity of the neutrino flux of a NB beam is reduced comparing with a WB beam obtained from the same proton beam. NB beams are convenient for precise measurements of Δm^2 ;
- **Off Axis (OA) beam:** these are experiments which use a high-intensity WB beam with the detector shifted by a small angle from the axis of the beam, where the neutrino energy is almost monochromatic.

Accelerator neutrino experiments, as reactor experiments, are mainly classified by the average value of the parameter L/E , which determine the sensitivity to Δm^2 . They can be divided accordingly to their typical neutrino source–detector distance L :

- **Short Base Line** accelerator neutrino experiments: $L \lesssim 1$ km.
- **Long Base Line** accelerator neutrino experiments: $L \gtrsim 10^3$ km.

1.7.1 Short-Baseline (SBL) accelerator experiments

Many of SBL accelerator experiments have been carried out in order to explore the exotic flavor transition channels, since they are sensitive to higher values of Δm^2 with respect to the atmospheric and solar ones. The typical Δm^2 sensitivity of a SBL experiment can be easily obtained from the formula (1.46):

- pion DIF: $L/E \lesssim 1$ km/GeV $\Rightarrow \Delta m^2 \gtrsim 1$ eV²;
- muon DAR: $L/E \lesssim 1$ m/MeV $\Rightarrow \Delta m^2 \gtrsim 1$ eV²;
- beam dump: $L/E \lesssim 10^{-2}$ m/MeV $\Rightarrow \Delta m^2 \gtrsim 10^2$ eV².

All the SBL accelerator experiments did not find any indication of neutrino oscillations except for the LSND (Liquid Scintillator Neutrino Detector) experiment at Los Alamos National Laboratory, which found a signal in the $\bar{\nu}_\mu \rightarrow \bar{\nu}_e$ channel [53] and a weaker signal in the channel $\nu_\mu \rightarrow \nu_e$ [54]. Experiments like CHORUS and NOMAD set an upper limit to the neutrino oscillation in the large Δm^2 region [55, 56]. Figure 1.20 shows the exclusion curves in the $\sin^2 2\theta$ - Δm^2 plane for $\nu_\mu \rightarrow \nu_\tau$ ($\bar{\nu}_\mu \rightarrow \bar{\nu}_\tau$) and $\nu_\mu \rightarrow \nu_e$ ($\bar{\nu}_\mu \rightarrow \bar{\nu}_e$) obtained by several SBL experiments [57].

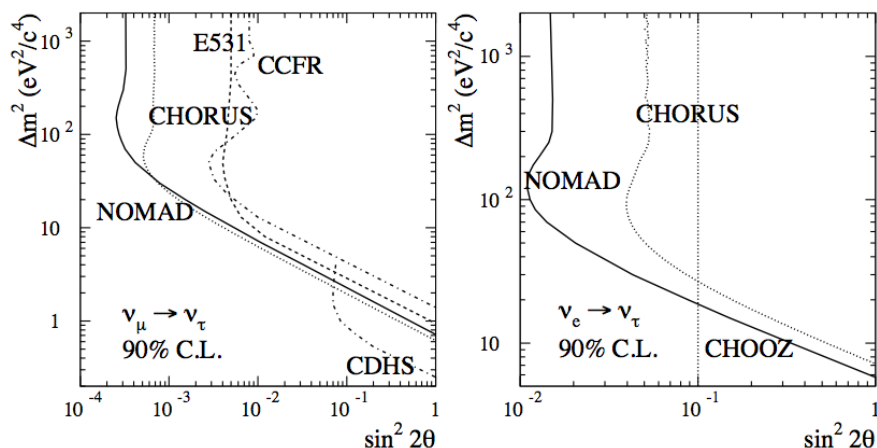


Figure 1.20: Right: Exclusion curves in the $\sin^2 2\theta$ - Δm^2 plane for $\nu_\mu \rightarrow \nu_\tau$ ($\bar{\nu}_\mu \rightarrow \bar{\nu}_\tau$). Left: Exclusion curves in the $\sin^2 2\theta$ - Δm^2 plane for $\nu_\mu \rightarrow \nu_e$ ($\bar{\nu}_\mu \rightarrow \bar{\nu}_e$).

1.7.2 Long-Baseline (LBL) accelerator experiments

These are experiments which have sources similar to SBL experiments, but the source–detector distance is about two or three orders of magnitude larger. These kind of experiments are very powerful in the study of neutrino oscillations parameters, in particular the atmospheric ones⁷ (Δm_{23}^2 and θ_{23}) and θ_{13} . Usually, neutrinos generated by the accelerator, are first measured in a near detector (before the oscillation) and then measured in a far detector (after the oscillation). The power of these technique is that if Δm^2 is known, with a well defined L/E is possible to produce a very intense beam having enough statistic to make a precise measurement of oscillation parameters. In the last years, several LBL experiments like K2K [58] and T2K [59] in Japan, MINOS [60] in USA and OPERA [61] in Italy, improved the knowledge of oscillation parameters measured by Super-Kamiokande using atmospheric neutrinos. In Figure 1.24 is shown the 90% C.L. allowed regions and the best fitted atmospheric parameters measured by T2K superimposed to MINOS and SK measurements.

1.8 T2K oscillation results

The subject of this thesis is the T2K experiment, so far the only LBL experiment using an OA neutrino beam (mainly composed by ν_μ). T2K is placed in Japan and is the evolution of the K2K experiment. T2K is able to measure θ_{13} and δ_{CP} oscillation parameters using the $\nu_\mu \rightarrow \nu_e$ appearance channel, and Δm_{23}^2 and θ_{23} oscillation parameters using the $\nu_\mu \rightarrow \nu_\mu$ disappearance channel.

⁷ The LBL accelerator experiments have a typical parameter $L/E \lesssim 10^3$ km/GeV which give sensitivity to $\Delta m^2 \gtrsim 10^{-3}$ eV².

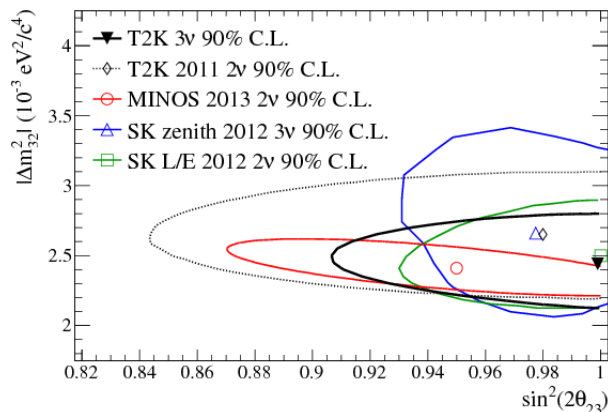


Figure 1.21: The 90% C.L. regions for $\sin^2(2\theta_{23})$ and $|\Delta m_{23}^2|$. The T2K 2011 [62], SK [63] and MINOS [64] 90% C.L. contours with different flavor assumptions are shown for comparison. [59].

1.8.1 ν_e appearance results

Already in 2011, with only the 4% of the total approved data, T2K was the first experiment in the world to give an indication of $\theta_{13} \neq 0$ with a significance of 2.5σ . The publication of this result reached more than 650 citation in less than two years and was recognized as one of the ten most important results in 2011 by the magazine *Physics World*. This result was then confirmed in the Summer 2013 at the EPS-HEP conference. T2K measured the $\sin^2 2\theta_{13} \neq 0$ with a significance of 7.3σ with only the 8.2% of the total approved data [66]. Since in the PMNS matrix the electron neutrino appearance signal depends on several parameters, the result is given assuming the neutrino oscillation scenario $|\Delta m_{23}^2| = 2.4 \times 10^{-3} \text{ eV}^2$, $\sin^2 \theta_{23} = 0.5$ and $\delta_{CP} = 0$:

$$\sin^2 2\theta_{13}|_{\text{T2K}} = 0.140_{-0.032}^{+0.038} \text{ (stat. + syst.)}, \quad (1.60)$$

$$\sin^2 2\theta_{13}|_{\text{T2K}} = 0.170_{-0.037}^{+0.045} \text{ (stat. + syst.)}, \quad (1.61)$$

for $\Delta m_{23}^2 > 0$ (normal hierarchy result (1.60)) and $\Delta m_{23}^2 < 0$ (inverted hierarchy result (1.61)). **For the first time the neutrino oscillation phenomenon is measured with a significance greater than 5σ in appearance mode.**

As said in Section 1.6 the reactor based measurement of $\sin^2 2\theta_{13}$ is independent from other oscillation parameters, while the T2K measurement is sensitive to δ_{CP} too. This aspect is clearly explained in Figure 1.22 where it is shown $\sin^2 2\theta_{13}$ scanned over different δ_{CP} values. As can be seen, the value of $\sin^2 2\theta_{13}$ measured from reactors is represented as a shaded yellow region, which is the $\pm\sigma$ range around the average value, without any dependence from the value of δ_{CP} . On the contrary the T2K measurement of $\sin^2 2\theta_{13}$ depends on the value of δ_{CP} . Combining the T2K results with the reactor measurement of $\sin^2 2\theta_{13}$, it is possible to give constraints on the value of δ_{CP} . Figure 1.23 shows **the first constraint of δ_{CP} obtained by T2K** [66]. At the moment, the data seems to prefer $\delta_{CP} = -\pi/2$. The same data excludes δ_{CP} between 0.19π and 0.80π ($-\pi$ and -0.97π , and -0.04π and π) with normal (inverted) hierarchy at 90% C.L.

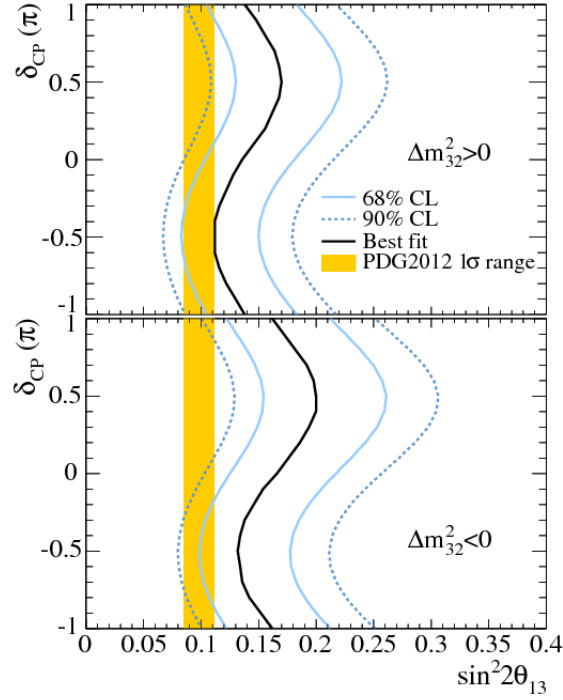


Figure 1.22: The 68% and 90% C.L. allowed regions for $\sin^2 2\theta_{13}$, scanned over values of δ_{CP} assuming normal hierarchy (top) and inverted hierarchy (bottom). The shaded region shows the average θ_{13} value from the PDG2012 [67].

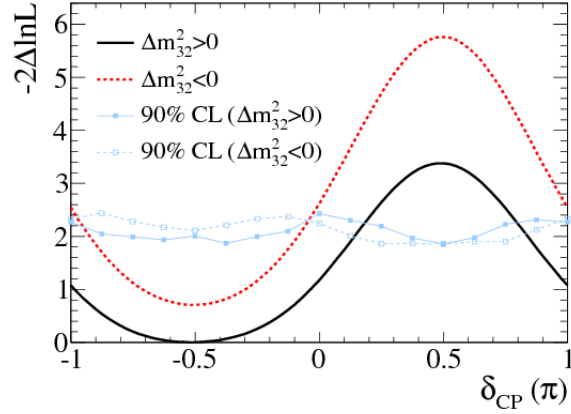


Figure 1.23: The $-2\Delta \ln \mathcal{L}$ value as a function of δ_{CP} for normal hierarchy (solid line) and inverted hierarchy (dotted line). The likelihood is marginalized over $\sin^2 2\theta_{13}$, $\sin^2 \theta_{23}$ and Δm_{32}^2 . The solid (dotted) line with markers corresponds to the 90% C.L. limits for normal (inverted) hierarchy, evaluated by using the Feldman-Cousins method. The δ_{CP} regions with values above the lines are excluded at $\sim 90\%$ C.L.

1.8.2 ν_μ disappearance results

T2K can also precisely measure the atmospheric parameters in the ν_μ disappearance channel. The best T2K fitted value of Δm_{23}^2 and $\sin^2 \theta_{23}$ are [59]:

$$\sin^2 \theta_{23}|_{\text{T2K}} = 0.514 \pm 0.082 \text{ (stat. + syst.)}, \quad (1.62)$$

$$|\Delta m_{23}^2|_{\text{T2K}} = 2.44_{-0.15}^{+0.17} \times 10^{-3} \text{ (stat. + syst.)}. \quad (1.63)$$

The disappearance result is obtained analyzing just 3.01×10^{20} POT of the total 6.63×10^{20} POT collected up to May 2013. Despite the limited amount of data collected until now, this is one of the most precise measurement of the atmospheric parameters, as can be seen from Figure 1.24 on the left.

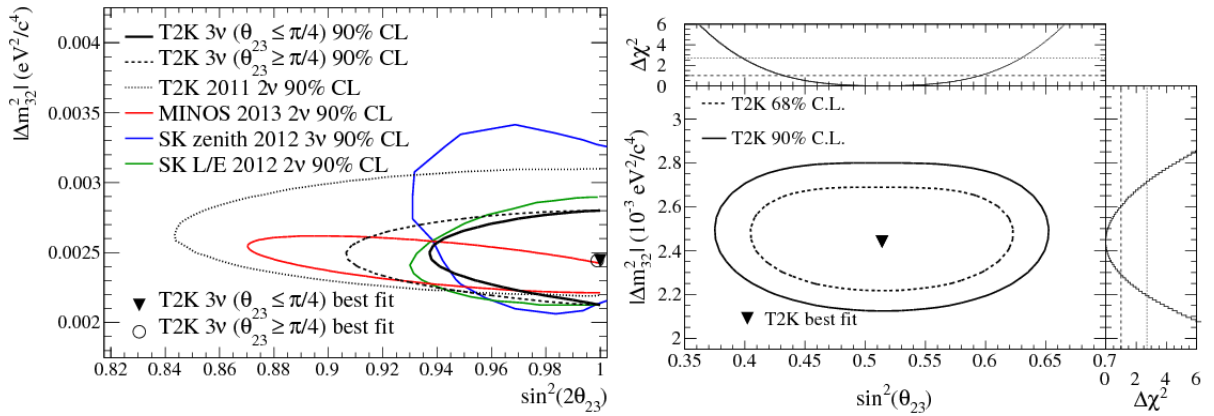


Figure 1.24: Right: The 90% C.L. contour regions for $\sin^2 \theta_{23}$ and Δm_{23}^2 are shown for octant 1 (solid) and octant 2 (dashed). The T2K 2011 [62], SK [63] and MINOS [64] 90% C.L. contours with different flavor assumptions are shown for comparison. Left: The 68% and 90% C.L. contour regions for $\sin^2 \theta_{23}$ and Δm_{23}^2 . The 1D profile likelihoods for each oscillation parameter separately are also shown. [59].

1.9 Status of the art and future of the neutrino physics

The neutrino oscillation phenomenon can be parametrized using six parameters: three angles, two mass differences and one CP violating phase. The current best knowledge of oscillation parameters [68, 69] is shown in Tables 1.4 and 1.5, while in Figure 1.25 it is summarized the neutrino mass eigenstate composition. As can be seen from Table 1.4, despite all the progress done in the understanding of neutrino oscillation physics in the last years, the picture is still not completed and the following unknowns need to be solved:

- **the CP violating phase δ_{CP} :** in the PMNS matrix, the phase δ_{CP} always appears in conjunction with the mixing angle θ_{13} . This means that the $\sin^2 2\theta_{13}$ different from zero opens the door to δ_{CP} search. T2K already started to look at δ_{CP} and currently reject at the 90% C.L. some values of δ_{CP} combining the T2K result with the world average value of θ_{13} from reactor experiments (see Section 1.8 for more details). Another powerful and elegant

Table 1.4: The present status of neutrino oscillation parameters presented at TAUP 2013 conference, derived from a global fit of the current neutrino oscillation data [68]. The results are shown with 1σ and 3σ uncertainties and for normal (NH) and inverted (IH) mass hierarchy.

Parameter	Best fit 1σ (3σ)
θ_{12}	$33.5^\circ_{-0.7^\circ}^{+0.8^\circ}$ ($+2.5^\circ$ -2.1°)
θ_{23} (NH)	$41.8^\circ_{-1.85^\circ}^{+9.2^\circ}$ ($+12.8^\circ$ -4.8°)
θ_{23} (IH)	$50.2^\circ_{-2.5^\circ}^{+1.7^\circ}$ ($+4.3^\circ$ -12.6°)
θ_{13}	$8.7^\circ_{-0.36^\circ}^{+0.47^\circ}$ ($+1.3^\circ$ -1.3°)
Δm_{12}^2	7.45 ± 0.18 ($+0.60$ -0.46) $\times 10^{-5}$ eV ²
Δm_{31}^2 (NH)	$2.42_{-0.06}^{+0.06}$ ($+0.21$ -0.18) $\times 10^{-3}$ eV ²
Δm_{32}^2 (IH)	$2.42_{-0.05}^{+0.07}$ ($+0.19$ -0.18) $\times 10^{-3}$ eV ²
δ_{CP} (NH)	$315^\circ_{-84^\circ}^{+36^\circ}$ ($+45^\circ$ -315°)
δ_{CP} (IH)	$270^\circ_{-68^\circ}^{+50^\circ}$ ($+90^\circ$ -270°)

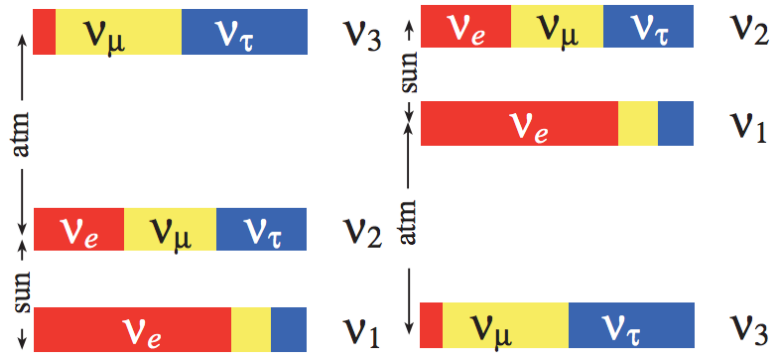


Figure 1.25: Neutrino mass eigenstate composition shown for normal (left) and inverted (right) mass hierarchy.

method to measure the CP violating phase in LBL experiments is the study of the differences between neutrino and anti-neutrino oscillation probabilities: $A_{CP} = \frac{P(\nu_\mu \rightarrow \nu_e) - P(\bar{\nu}_\mu \rightarrow \bar{\nu}_e)}{P(\nu_\mu \rightarrow \nu_e) + P(\bar{\nu}_\mu \rightarrow \bar{\nu}_e)}$;

Table 1.5: Results of the global 3ν oscillation analysis, in terms of best-fit values and allowed 1, 2 and 3σ ranges for the 3ν mass-mixing parameters [69]. Δm^2 is defined herein as $m_3^2 - (m_1^2 + m_2^2)/2$, with $+\Delta m^2$ for normal hierarchy (NH) and $-\Delta m^2$ for inverted hierarchy (IH). The CP violating phase is taken in the (cyclic) interval $\delta/\pi \in [0, 2]$. The $\sin^2 \theta_{23}$ (IH) and δ ranges are shown for both $\theta_{23} - \pi/4 < 0$ (left) and $\theta_{23} - \pi/4 > 0$ (right).

Parameter	Best fit	1σ range	2σ range	3σ range
$\sin^2 \theta_{12}/10^{-1}$	3.08	2.91 – 3.25	2.75 – 3.42	2.59 – 3.59
$\sin^2 \theta_{23}/10^{-1}$ (NH)	4.25	3.98 – 4.54	3.76 – 5.06	3.57 – 6.41
$\sin^2 \theta_{23}/10^{-1}$ (IH)	4.37	$4.08 - 4.96 \oplus 5.31 - 6.10$	3.84 – 6.37	3.63 – 6.59
$\sin^2 \theta_{13}/10^{-2}$ (NH)	2.34	2.16 – 2.56	1.97 – 2.76	1.77 – 2.97
$\sin^2 \theta_{13}/10^{-2}$ (IH)	2.39	2.18 – 2.60	1.98 – 2.80	1.78 – 3.00
$\delta m^2/10^{-5} \text{ eV}^2$	7.54	7.32 – 7.80	7.15 – 8.00	6.99 – 8.18
$\Delta m^2/10^{-3} \text{ eV}^2$ (NH)	2.44	2.38 – 2.52	2.30 – 2.59	2.22 – 2.66
$\Delta m^2/10^{-3} \text{ eV}^2$ (IH)	2.40	2.33 – 2.47	2.25 – 2.54	2.17 – 2.61
δ/π (NH)	1.39	1.12 – 1.72	$0.00 - 0.11 \oplus 0.88 - 2.00$	–
δ/π (IH)	1.35	0.96 – 1.59	$0.00 - 0.04 \oplus 0.65 - 2.00$	–

- **the mass hierarchy of neutrino eigenstate:** in cases where only two neutrino generations need be considered, neutrino oscillations in a vacuum are proportional to $\sin^2(1.27 \Delta m^2 L/E)$, and are therefore insensitive to the sign of Δm^2 . As a consequence, for θ_{23} (mixing between muon and tau neutrinos) it is not known whether mass state 2 is lighter or heavier than mass state 3. The mass hierarchy can be solved using the matter effect in the ν_e appearance channel. In fact the matter effect is sensitive to the sign of the mass difference $\Delta m_{13}^2 \simeq \Delta m_{23}^2$, because normal matter has a high electron density (not mu or tau density). LBL neutrino experiments with baselines of order 1000 km or more can therefore disentangle the mass hierarchy: electron neutrino appearance is enhanced for normal hierarchy ($m_1 < m_3$) but suppressed for inverted hierarchy ($m_1 > m_3$);
- **the octant of θ_{23} :** the octant of θ_{23} determine if the mass state ν_3 contains more ν_μ or ν_τ . This parameter can be measured combining reactor $\bar{\nu}_e$ disappearance and accelerator ν_μ disappearance and ν_e appearance analysis with neutrino and anti-neutrino mode flux.

Taking data both in neutrino and anti-neutrino beam mode T2K has the ability to increase its sensitivity to δ_{CP} and θ_{23} octant (see Appendix A for more details). For this reason, after the discovery of $\theta_{13} \neq 0$ at 7.3σ significance, T2K will be mainly focused on the measure of these unknown parameters.

Like T2K, also the LBL experiment at Fermilab NO ν A [70] is able to measure θ_{13} and δ_{CP} using both $\nu_{\mu} \rightarrow \nu_e$ and $\bar{\nu}_{\mu} \rightarrow \bar{\nu}_e$ appearance channels. In particular, since NO ν A has a baseline longer (810 km) with respect to the T2K one (295 km), can be sensitive to the mass hierarchy exploiting the matter effect.

In the future, a new generation of LBL experiments will focus on the measurement of these unknown parameters, especially δ_{CP} . The most important projects are: LAGUNA-LBNO [71] (Europe), LBNE [72] (USA) and the upgrade of T2K called T2HK [73] (Japan). Both LAGUNA and LBNE will use a baseline greater than 1000 km and Liquid Argon Time Projection Chambers as far detectors while T2HK will use the same T2K baseline (295 km, that means no matter effect with respect to LAGUNA and LBNE) and the evolution of SK, Hyper-Kamiokande [74] ($\times 25$ SK) as far detector.

In addition to the remaining unknown oscillation parameters, also the nature of the neutrino is a fundamental unknown to be determined. In fact, unlike the rest of the elementary fermions in the Standard Model, neutrinos have no electric charge (or any other fundamental charge that cannot be violated) and their lepton number can be violated without any consequence. This means that neutrinos can be either identical to their own anti-particles or different from their anti-particles. In the first case neutrinos are called Majorana particles [75], while in the second case they are called Dirac particles (as the rest of the elementary fermions in the Standard Model). The Dirac and Majorana nature of neutrinos is indistinguishable in any typical experiments with the exception of the neutrinoless double- β decay experiments⁸, like GERDA [76], CUORE [77], EXO [78], NEXT [79] and KamLAND-Zen [80]. There are many models implementing Dirac or Majorana mass terms or both in an extension of the Standard Model. One of them is called the *seesaw mechanism*, which add one heavy right handed neutrino per family. The right handed neutrino having a Majorana mass and the left handed neutrino being Dirac particles, with the possibility for the heavy neutrino to be sterile (i.e. they do not participate in weak interactions). The existence of sterile neutrinos can explain partially different anomalies observed in reactor and SBL experiments [81] and this is another important question that should be investigated in the future with dedicated experiments.

⁸ In a double beta decay, two neutrons in the nucleus are converted to protons, and two electrons and two electron anti-neutrinos are emitted, while If the neutrino is a Majorana particle (meaning that the anti-neutrino and the neutrino are the same particle), and at least one type of neutrino has non-zero mass, then it is possible for neutrino-less double beta decay to occur. In the simplest theoretical treatment of neutrino-less double beta decay (light neutrino exchange), in essence the two neutrinos annihilate each other, or equivalently, one nucleon absorbs the neutrino emitted by another nucleon of the nucleus. The signal of a neutrino-less double beta decay is a peak in the kinetic energy of the final state electrons. If neutrinos are present, part of the available energy is carried by them, so the spectrum is a continuous distribution. On the contrary, in the neutrino-less case the electrons have all the available energy of the decay.

Chapter 2

The T2K experiment

The T2K (Tokai-to-Kamioka) experiment is a second generation LBL neutrino oscillation experiment that probes physics beyond the Standard Model. T2K started to take data in 2010 [82] and uses a ν_μ beam produced using the new MW-class proton synchrotron at J-PARC¹. The neutrino beam is detected first in the near detector *ND280* and then travels 295 km to the far detector *Super-Kamiokande*.



Figure 2.1: The neutrino beam journey in the T2K experiment. The high intensity neutrino beam is produced at J-PARC (Tokai, Mito, Ibaraki Prefecture, Japan) and travel 295 km to the Super-Kamiokande detector (mount Kamioka, close to Hida, Gifu Prefecture, Japan).

Initially, the main goals of T2K were: (1) Discovery of $\nu_\mu \rightarrow \nu_e$ appearance by extending the search down to $\sin^2 2\theta_{\mu e} \simeq \frac{1}{2} \sin^2 2\theta_{13} = 0.006$, thereby probing that $\theta_{13} \neq 0$; (2) Precision measurement of oscillation parameters in the ν_μ disappearance down to $\delta(\Delta m_{32}^2) \sim 10^{-4} \text{ eV}^2$ and $\delta(\sin^2 2\theta_{23}) \sim 0.01$ ($\sim 1\%$ level); and (3) Search for sterile components in the ν_μ disappearance. Since, the primary physics goal, namely, discovery of $\nu_\mu \rightarrow \nu_e$ appearance has been realized at 7.3σ significance with just $\sim 8.2\%$ (6.63×10^{20} POT by May 2013) of the total approved data the T2K collaboration has updated the physics program for the 2014, as it will be discussed in Section 2.1.4, to measure the

¹ Japan Proton Accelerator Research Complex jointly constructed and operated by KEK and JAEA.

CP violation phase, running also with a $\bar{\nu}_\mu$ beam.

T2K adopts the off-axis method [83] to generate the narrowband neutrino beam using the proton synchrotron at J-PARC. In this method the neutrino beam is purposely directed at an angle with respect to the baseline connecting the proton target to the far detector, Super-Kamiokande. The off-axis angle is set at 2.5° so that the narrow-band ν_μ beam generated toward the far detector has a peak energy at ~ 0.6 GeV, such configuration maximizes the effect of the neutrino oscillation at 295 km and minimizes the background to electron-neutrino appearance detection (Figure 2.2). The angle can be reduced to 2.0° , allowing variation of the peak neutrino energy, if necessary. The J-PARC beamline can also provide to the experiment an anti-neutrino beam instead of a neutrino beam. As it will be shown in the Section 2.1.4, this aspect is very important to measure the δ_{CP} phase. The near detector complex is situated ~ 280 m far from the production target and

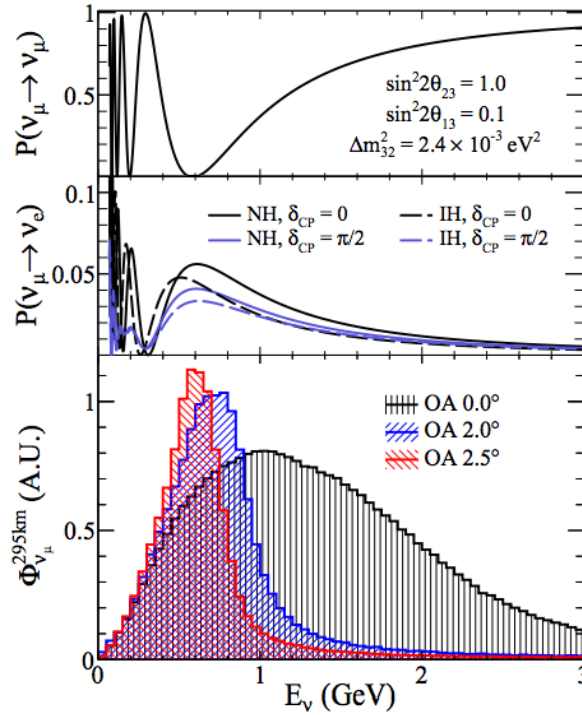


Figure 2.2: The muon neutrino survival probability (top) and electron neutrino appearance probability (middle) at 295 km, and the un-oscillated neutrino fluxes for different values of the off-axis angle (OA) (bottom). The appearance probability is shown for two values of the phase δ_{CP} , and for normal (NH) and inverted (IH) mass hierarchies.

houses on-axis and off-axis detectors. The on-axis detector (INGRID), composed by an array of iron/scintillator sandwiches, measures the neutrino beam direction and profile. Instead the off-axis detector, embedded in a magnetic field, measures the muon neutrino flux and energy spectrum, intrinsic ν_e and $\bar{\nu}_\mu$ contaminations in the beam towards the far detector, as well as the rates for exclusive neutrino reactions. These measurements are essential to characterize the signal and the background observed in the far detector. In addition, the near off-axis detector is able to measure different cross sections on carbon and water, to decrease systematic error from cross sections in the far detector. In this chapter it will be introduced the main physics measurements that T2K is able

to perform and each T2K components: the neutrino beam, the near detector complex and the far detector [84].

2.1 Physics motivations

As it was explained in Section 1.3, neutrino oscillations can be parametrized using 6 parameters: 3 angles, 2 mass differences and δ_{CP} . T2K is able to measure with high precision, three of those parameters: θ_{13} , θ_{23} and Δm_{23}^2 . Moreover, since θ_{13} is different from zero, the measure of δ_{CP} becomes accessible. From 2014 T2K will start to measure this oscillation parameter sharing data with a $\bar{\nu}_\mu$ beam and a ν_μ beam.

2.1.1 ν_e appearance

In a three neutrino flavor framework, the general expression of the transition probability $P(\nu_\mu \rightarrow \nu_e)$ can be derived from (1.48):

$$\begin{aligned}
P(\nu_\mu \rightarrow \nu_e) \simeq & \sin^2 \theta_{23} \sin^2 2\theta_{13} \sin^2 \frac{\Delta m_{13}^2 L}{4E} \\
& - \frac{\sin 2\theta_{12} \sin 2\theta_{23}}{2 \sin \theta_{13}} \sin \frac{\Delta m_{12}^2 L}{4E} \sin^2 2\theta_{13} \sin^2 \frac{\Delta m_{13}^2 L}{4E} \sin \delta_{CP} \\
& + (\text{CP even term, solar term, matter effect}).
\end{aligned} \tag{2.1}$$

For a $\theta_{13} = 8.7^{+0.47^\circ}_{-0.36^\circ}$ [68] the first term of the equation (2.1) dominates and, in a first approximation, it describes the appearance of ν_e in the ν_μ beam:

$$P(\nu_\mu \rightarrow \nu_e) \approx \sin^2 \theta_{23} \sin^2 2\theta_{13} \sin^2 \left(\frac{\Delta m_{13}^2 [\text{eV}^2] L [\text{km}^2]}{4E_\nu [\text{GeV}]} \right), \tag{2.2}$$

where $|\Delta m_{13}^2| \sim |\Delta m_{23}^2|$ (as $|\Delta m_{12}^2|$ is small compared to $|\Delta m_{23}^2|$), L is the length of the baseline (295 km in the case of T2K) and E_ν is the neutrino energy. From equation (2.2), the oscillation $\nu_\mu \rightarrow \nu_e$ is expected to be observed around the maximum of the ν_μ disappearance probability (Figure 2.2). In the measure of $\nu_\mu \rightarrow \nu_e$ oscillation, the matter effect can play an important role. As described in the Section 1.3.2, the matter effect can modify the propagation of ν_e and thus the observed oscillation parameters Δm_{13}^2 and θ_{13} . This modification can be parameterized by defining the adimensional ratio:

$$r = \frac{2\sqrt{2}G_F N_e E_\nu}{\Delta m_{13}^2} = \frac{N_e}{1.3N_A/\text{cm}^3} \frac{E_\nu}{10 \text{ GeV}} \frac{2 \times 10^{-3} \text{ eV}^2}{\Delta m_{13}^2}. \tag{2.3}$$

In T2K $r \simeq 4\%$. The modified oscillation parameters become:

$$\Delta m_M^2 = \Delta m_{13}^2 \sqrt{\sin^2 2\theta_{13} + (\cos 2\theta_{13} - r)} \tag{2.4}$$

and

$$\sin^2 2\theta_M = \frac{\sin^2 2\theta_{13}}{\sin^2 2\theta_{13} + (\cos 2\theta_{13} - r)^2}. \tag{2.5}$$

This implies a correction smaller than 10% to the vacuum solution. For this reason, if about 100 ν_e events are expected, the matter effect can be neglected since it is of the order of the statistical

error. In order to search the ν_e appearance at Super-Kamiokande, charged current quasi elastic (CCQE) interactions are used (Figure 2.3). The T2K neutrino beam has an energy peak around 0.6 GeV and in this region this kind of interaction is the dominant one (Figure 2.4). This means

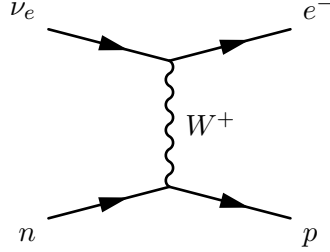


Figure 2.3: Expected CCQE reaction of oscillated ν_e at Super-Kamiokande.

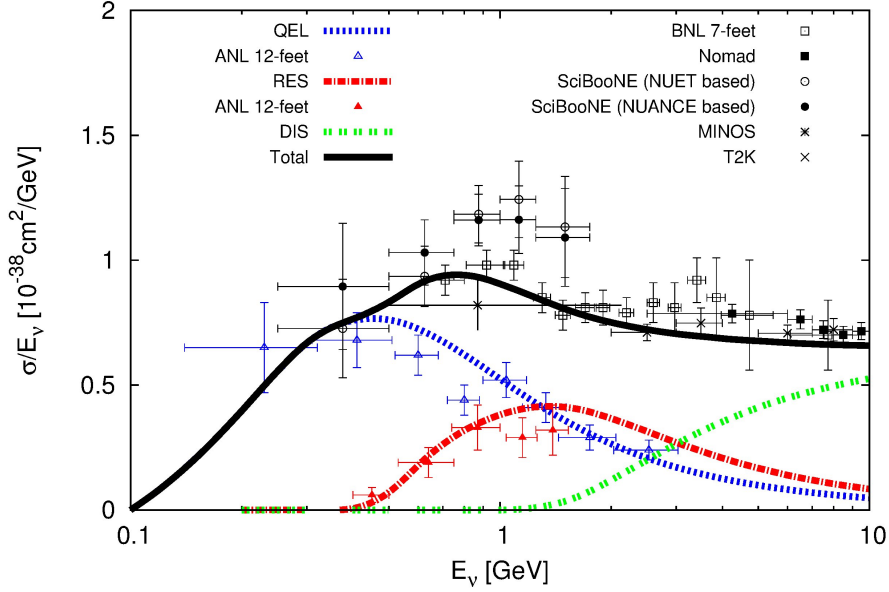


Figure 2.4: Total charged current ν inclusive cross sections as a function of neutrino energy. The T2K neutrino beam has a peak around 0.6 GeV that correspond to the low energy region in the plot. Below 1 GeV, the dominant contribution come from the blue curve, that represents the quasi elastic interactions (CCQE).

that assuming the target neutron is at rest, it is possible to reconstruct the neutrino energy only measuring the momentum and angle of the charged lepton produced via CCQE interaction. So the neutrino energy is given by

$$E_\nu = \frac{m_p^2 - (m_n - E_b)^2 - m_l^2 + 2(m_n - E_b)E_l}{2(m_n - E_B - E_l + p_l \cos \theta_l)}, \quad (2.6)$$

where m_n is the mass of the neutron, m_p the mass of the proton, $E_B = 27$ MeV is the binding energy of a nucleon inside the ^{16}O nucleus and p_l , m_l , E_l and θ_l are the momentum, the mass, the energy and the polar angle of the lepton produced by the neutrino interaction (in this case $l = e$) respectively.

As it will be explained in Section 2.6, Super-Kamiokande (SK) uses Cherenkov light and it can distinguish between muons coming from ν_μ interactions and electrons coming from ν_e interactions from the shape of the ring produced. The selection of ν_e events, fully explained in [66], requires:

1. the event must be fully contained (FC) in the SK inner detector (ID) and the reconstructed vertex be within the 22.5 kt fiducial volume (FCFV);
2. there must be only one reconstructed Cherenkov ring;
3. the ring must be electron-like;
4. the visible energy E_{vis} , must be greater than 100 MeV;
5. there must be no Michel electron (electron coming from the muon decay);
6. the event's invariant mass must be not compatible with π^0 mass;
7. the reconstructed neutrino energy E_ν^{rec} must be below 1250 MeV.

The E_{vis} cut removes low energy NC interactions and electrons from the decay of unseen muons and pions. An event can be tagged as event with a Michel electron if there is a time-delayed ID-PMT hit peak after the primary neutrino interaction. In order to reduce NC π^0 events, it is used a fitter able to reconstruct each event with a two photon ring hypothesis. The fitter searches for the direction and energy of the second ring which maximizes the likelihood based on the light pattern of the event. Figure 2.5 shows the invariant mass M_{inv} distribution of the two photon rings for data and simulation. Finally the E_ν^{rec} is applied since the signal at high energy is expected to be small for the atmospheric mass splitting, and the intrinsic ν_e background is dominant in this region.

2.1.2 ν_μ disappearance

One of the main goals of T2K is the precise measurement of the atmospheric parameters θ_{23} and Δm_{23}^2 . These parameters are measured in the ν_μ disappearance channel. The survival probability is given by:

$$\begin{aligned}
 P(\nu_\mu \rightarrow \nu_\mu) \simeq & 1 - 4 \cos^4 \theta_{13} \sin^2 2\theta_{23} [1 - \cos^2 \theta_{13} \\
 & \times \sin^2 \theta_{23}] \sin^2 \left(\frac{1.27 \Delta m_{23}^2 [\text{eV}^2] L [\text{km}]}{E_\nu [\text{GeV}]} \right).
 \end{aligned}
 \tag{2.7}$$

This equation means that measuring the neutrino energy spectrum at SK, a clear dip must be observed around 600 MeV according to the actual knowledge of Δm_{23}^2 . As for ν_e appearance, in this analysis charged current quasi elastic (CCQE) interactions are used (Figure 2.6). To do that, the single muon like (μ -like) ring events are selected. For these events, neglecting the Fermi motion, the neutrino energy E_ν can be reconstructed as (2.6) (with $l = \mu$). The latest T2K results in ν_μ disappearance are showed in Figure 2.7.

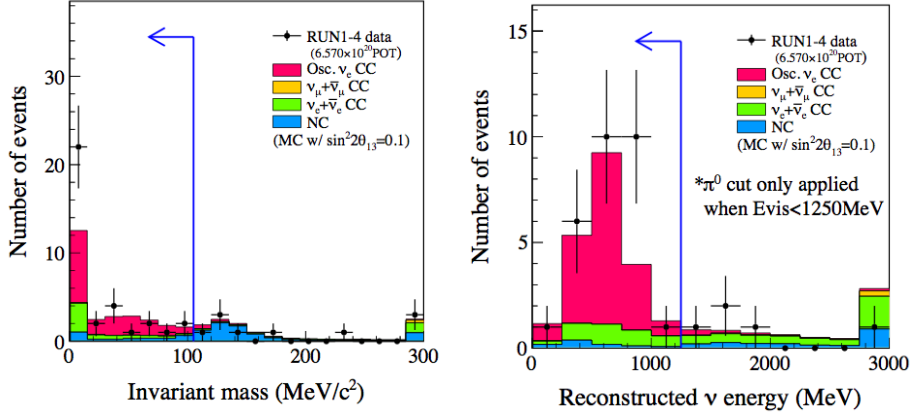


Figure 2.5: Left: Distribution of the invariant mass M_{inv} when each event is forced to be reconstructed as two photon rings. The arrows show the selection criterion $M_{\text{inv}} < 105 \text{ MeV}/c^2$. Right: Distribution of the reconstructed neutrino energy spectrum of the events which pass all ν_e appearance signal selection criteria with the exception of the energy cut. The arrow shows the selection criterion $E_{\nu}^{\text{rec}} < 1250 \text{ MeV}$.

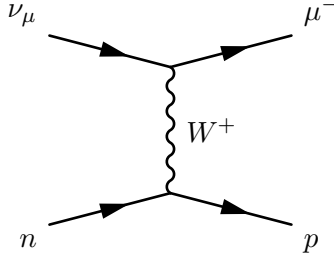


Figure 2.6: The ν_{μ} CCQE reaction.

2.1.3 Oscillation analyses

The ν_e appearance analysis and the ν_{μ} disappearance analysis are performed in T2K combining the measurements at the near and at the far detector. This strategy is common to the majority of the long baseline experiments that measure the neutrino flux in the far detector and compare it with the expected flux unmodified by the oscillation. This latter flux is measured in a near detector that intercepts the flux when the oscillation is still negligible. In an ideal world, if both detectors accept the same solid angle and if the detector efficiencies and systematic errors are the same, it is sufficient to measure the neutrino beam at the near detector in order to predict it at the far detector. In practice the near detector is different from the far in terms of acceptance, materials and responses and what is measured is the product of detector efficiencies (ϵ), the neutrino cross-section (σ) and the neutrino flux (Φ). For example in the case of ν_e appearance analysis, the number of expected events at SK is given by:

$$N_{\text{exp}}^{SK} = N_{\nu_{\mu}, \text{Data}}^{ND} \times \frac{N_{\nu_e, \text{MC}}^{SK}}{N_{\nu_{\mu}, \text{MC}}^{ND}}, \quad (2.8)$$

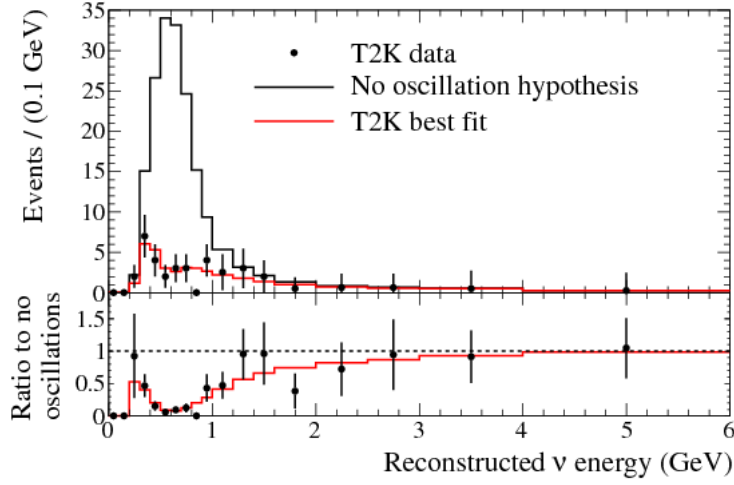


Figure 2.7: Reconstructed energy spectrum of data events compared with the expected spectra in the far detector w/o disappearance and with best fit $\nu_\mu \rightarrow \nu_\tau$ oscillation [59].

where

$$\frac{N_{\nu_e, \text{MC}}^{SK}}{N_{\nu_\mu, \text{MC}}^{ND}} = \frac{\int \Phi_{\nu_\mu}^{SK}(E_\nu) P_{\nu_\mu \rightarrow \nu_e}(E_\nu) \sigma(E_\nu) \epsilon_{SK}(E_\nu) dE_\nu}{\int \Phi_{\nu_\mu}^{ND}(E_\nu) \sigma(E_\nu) \epsilon_{ND}(E_\nu) dE_\nu} \frac{M^{SK}}{M^{ND}} \text{POT}^{SK}. \quad (2.9)$$

In the above equation, M^{SK} and M^{ND} are SK and ND280 masses, while MC means Monte Carlo simulation. In order to extrapolate the flux at the near and far detectors it is necessary to understand the beam and the detectors acceptances. In T2K this is done using a beam Monte Carlo simulation based on experimental data called JNUBEAM (see Section 2.2.5).

2.1.4 The T2K physics goals in the next future

Because the value of $\sin^2 2\theta_{13}$ has now been precisely measured from reactor experiments (via $\bar{\nu}_e$ disappearance) and T2K (via $\nu_\mu \rightarrow \nu_e$ appearance) and known to be relatively large, this is no longer the dominant uncertainty in neutrino oscillation measurements. As shown in this section, T2K $\nu_\mu \rightarrow \nu_e$ appearance measurement is sensitive to $\sin^2 2\theta_{13}$ and δ_{CP} , while the $\nu_\mu \rightarrow \nu_\mu$ disappearance measurement is sensitive to $\sin^2 2\theta_{23}$ and Δm_{23}^2 . Accordingly the T2K collaboration has updated the main physics goals that now are:

- observation of the $\bar{\nu}_e$ appearance in the $\bar{\nu}_\mu \rightarrow \bar{\nu}_e$ oscillation channel up to 3σ level of significance;
- initial measurement of CP violation in neutrinos up to 2.5σ level of significance;
- precision measurement of oscillation parameters in the ν_μ disappearance with precision of $\delta(\Delta m_{23}^2) \sim 10^{-4} \text{ eV}^2$ and $\delta(\sin^2 2\theta_{23}) \sim 0.01$ ($\sim 1\%$ level) and determination of θ_{23} octant, *i.e.* $\theta_{23} < 45^\circ, > 45^\circ$, at 90% C.L. if $|\theta_{23} - 45^\circ| > 4^\circ$;
- contribution to the determination of the mass hierarchy.

The first goal will be pursued running with an anti-neutrino beam, while the last three goals will be pursued by combined the analysis of ν_μ disappearance and ν_e appearance data, in neutrino and

anti-neutrino mode, and the data from other relevant experiments. An example of the achievable sensitivity is showed in Figures 2.8 and 2.9 [85].

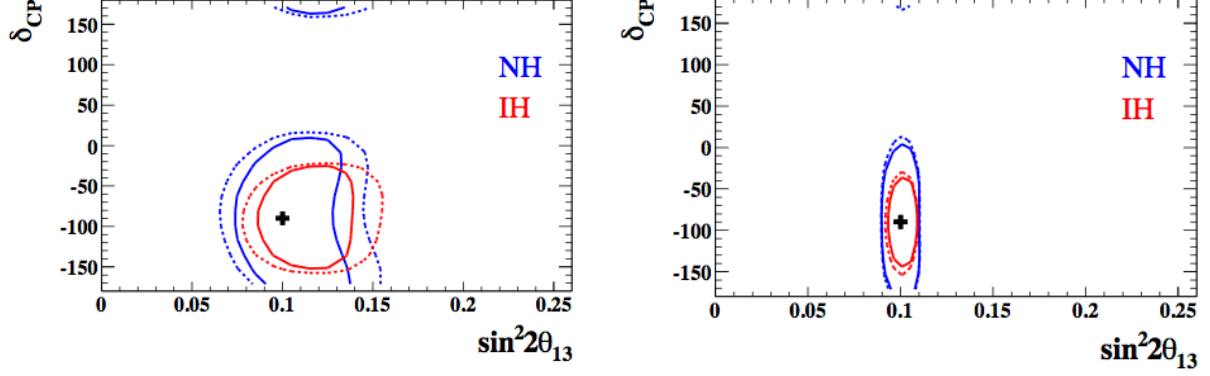


Figure 2.8: δ_{CP} versus $\sin^2 2\theta_{13}$ 90% C.L. allowed regions for 7.8×10^{21} POT. Contours are plotted assuming true $\sin^2 2\theta_{13} = 0.1$, $\delta_{CP} = -90^\circ$, $\sin^2 \theta_{23} = 0.5$, $\Delta m_{23}^2 = 2.4 \times 10^{-3} \text{ eV}^2$ and NH. Left: 50% $\nu - 50\%$ $\bar{\nu}$ -running mode, without ultimate reactor constraint. Right: 50% $\nu - 50\%$ $\bar{\nu}$ -running mode, with ultimate reactor constraint. The solid contours are with statistical error only, while the dashed contours include a conservative estimation of systematic errors.

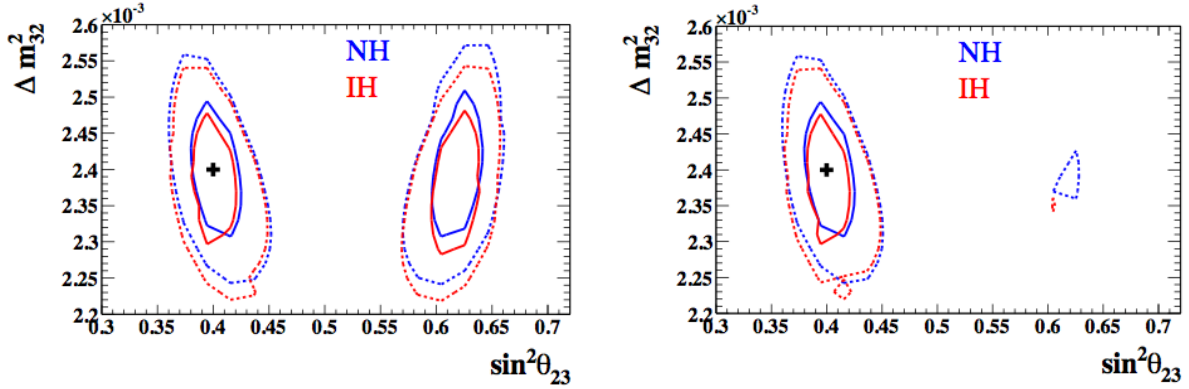


Figure 2.9: Δm_{32}^2 versus $\sin^2 \theta_{23}$ 90% C.L. allowed regions for 7.8×10^{21} POT. Contours are plotted assuming true $\sin^2 2\theta_{13} = 0.1$, $\delta_{CP} = 0^\circ$, $\sin^2 \theta_{23} = 0.4$, $\Delta m_{23}^2 = 2.4 \times 10^{-3} \text{ eV}^2$ and NH. Left: 50% $\nu - 50\%$ $\bar{\nu}$ -running mode, without ultimate reactor constraint. Right: 50% $\nu - 50\%$ $\bar{\nu}$ -running mode, with ultimate reactor constraint. The solid contours are with statistical error only, while the dashed contours include a conservative estimation of systematic errors.

2.2 The neutrino beam

The neutrino beam is obtained from the acceleration of protons. These protons are then extracted from the synchrotron and then hit the graphite target. The interaction of protons with the target produce a bunch of several mesons that are selected and focused by the horns and than decay

principally into muons and muon neutrinos in the decay tunnel. The beam dump stops the majority of no neutrino particles. The remaining high energy muons that managed to pass the beam dump are monitored by the muon monitor, which verifies the beam direction and its stability. A schematic description of the neutrino beam line and the near detectors is showed in Figure 2.10.

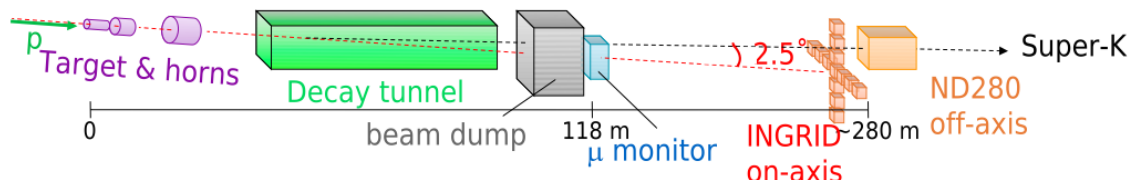


Figure 2.10: A schematic cartoon of the T2K neutrino beam.

2.2.1 The off-axis method

As showed in Figure 2.10, T2K uses an off-axis neutrino beam, originally introduced in [83]. The idea is to produce a neutrino beam from the two body decay of charged pions that is not directly directed to the detectors but is slightly misaligned (by few degrees) with respect to them. The advantages of an off-axis neutrino beam, is to have a more intense and narrower beam, centered at the interesting energy region to observe the oscillation signal (Figure 2.2). In addition cutting the high energy tail present in the “traditional” neutrino beam, it is possible to remove dangerous backgrounds like NC and non CCQE interactions. To understand better the off-axis mechanism, let us consider the ideal case where is possible to obtain a pure π^+ beam, produced by interactions of a proton beam with a graphite target. The pions will decay according the reaction $\pi^+ \rightarrow \mu^+ + \nu_\mu$. In the pion rest frame the neutrino has a maximal energy of:

$$E_{\nu, \text{Max}}^* = \frac{m_\pi^2 - m_\mu^2}{2m_\pi} = 29.8 \text{ MeV}, \quad (2.10)$$

where * indicates quantities in the pion rest frame. The neutrino 4-momentum for $|\vec{P}_\nu| \gg m_\nu$ will be in the pion rest frame

$$P_\nu = (E_\nu, E_\nu \sin \theta, 0, E_\nu \cos \theta), \quad (2.11)$$

where E_ν is the neutrino energy and θ is the angle of the neutrino relative to the direction of pion. The factor $\gamma = E_\pi/m_\pi$ is used to perform a Lorentz transformation between the pion rest frame and the laboratory frame. The 4-momentum neutrino can be related between frames using [86]:

$$(E_\nu, E_\nu \sin \theta, 0, E_\nu \cos \theta) = (\gamma E_\nu^*(1 + \beta \cos \theta^*), E_\nu^* \sin \theta^*, 0, \gamma E_\nu^*(\beta + \cos \theta^*)), \quad (2.12)$$

where $\beta = v_\pi/c$ and v_π is the magnitude of the pion velocity in the lab frame. The second and last components of the neutrino 4-momentum can be used to find a relation between angles in the two frames. Considering high energy pions with $\beta \sim 1$, the relationship is given by:

$$\tan \theta \simeq \frac{E_\nu^* \sin \theta^*}{E_\nu}. \quad (2.13)$$

² E_π and m_π are respectively the pion energy in the lab frame and his rest mass.

Since a pion has spin zero, its decay is isotropic in its rest frame. Moreover $\sin \theta^*$ is less than one in the lab frame, so there is a maximum value for the angle at which the neutrino with E_ν can be emitted. It is possible to compute this angle using (2.10):

$$\theta_{\text{Max}} \sim \frac{E_{\nu, \text{Max}}^*}{E_\nu} \sim \frac{30 \text{ MeV}}{E_\nu}. \quad (2.14)$$

So for a given angle θ , the equation (2.14) suggests that there is a maximum energy at which a neutrino can be emitted in this process (see Figure 2.11). For $\theta = 2.5^\circ$ (~ 43 mrad), this correspond to $E_\nu \lesssim 682$ MeV in the lab frame. A similar calculation can be applied to neutrinos coming from two body decay of Kaons.

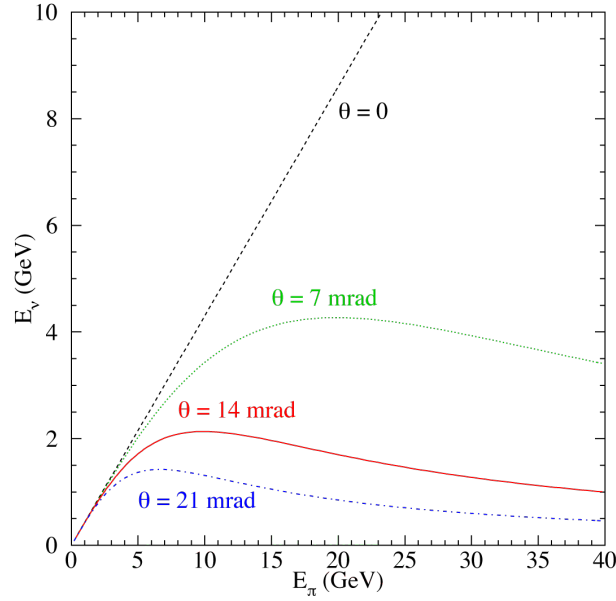


Figure 2.11: Expected neutrino energy as a function of the parent pion energy for different values of the off-axis angle.

2.2.2 The J-PARC accelerators

The J-PARC complex, consist of three accelerators:

1. the Linear Accelerator **LINAC** (acceleration stage up to 400 MeV);
2. the Rapid Cycle Synchrotron **RCS** (acceleration stage up to 3 GeV);
3. the Main Ring Synchrotron **MR** (acceleration stage up to 50 GeV).

An H^- beam is accelerated up to 400 MeV (181 MeV at present) by the LINAC, and is converted to an H^+ beam by charge-stripping foils at the RCS injection. The beam is accelerated up to 3 GeV by the RCS with a 25 Hz cycle. The harmonic number of the RCS is two, and there are two bunches in a cycle. About 5% of these bunches are supplied to the MR. The rest of the bunches are supplied to the muon and neutron beamline in the Material and Life Science Facility. The proton beam

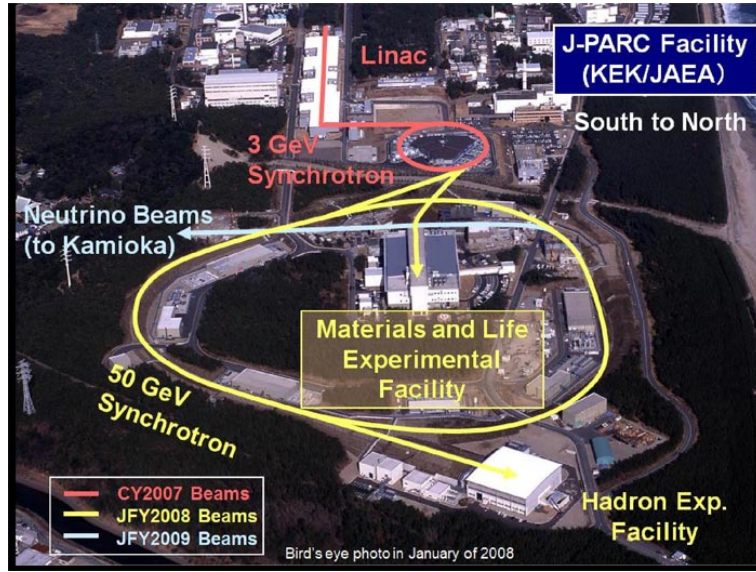


Figure 2.12: Overview of the J-PARC accelerators and facilities. The T2K neutrino beamline is colored in light blue.

injected into the MR is accelerated up to 30 GeV. The harmonic number of the MR is nine, and the number of bunches in the MR is eight (six before June 2010). After the acceleration up to 30 GeV the proton beam is extracted. There are two extraction point in the MR, the slow extraction point for the hadron beamline and the fast extraction point for the neutrino beamline. In the fast extraction mode, the eight circulating proton bunches are extracted within a single turn by a set of five kicker magnets. The time structure of the extracted proton beam is the key for discriminating various backgrounds, including cosmic rays, in the various neutrino detectors. The parameters of the J-PARC MR for the fast extraction are listed in Table 2.1.

Table 2.1: Machine design parameters of the J-PARC MR for the fast extraction.

Circumference	1567 m
Beam power	~ 750 kW
Beam kinetic energy	30 GeV
Beam intensity	$\sim 3 \times 10^{14}$ p/spill
Spill cycle	~ 0.5 Hz
Number of bunches	8/spill
RF frequency	1.67 – 1.72 MHz
Spill width	~ 5 μ s

2.2.3 The neutrino beamline

Each proton beam spill consists of eight proton bunches extracted from the MR to the T2K neutrino beamline, which produces the neutrino beam. The neutrino beamline is composed of two sequential

sections: the primary and secondary beamlines. In the primary beamline, the extracted proton beam is bent to point toward Kamioka. In the secondary beamline, the proton beam impinges on a target to produce secondary pions, which are focused by magnetic horns and decay into neutrinos. An overview of the neutrino beamline is shown in Figure 2.13.

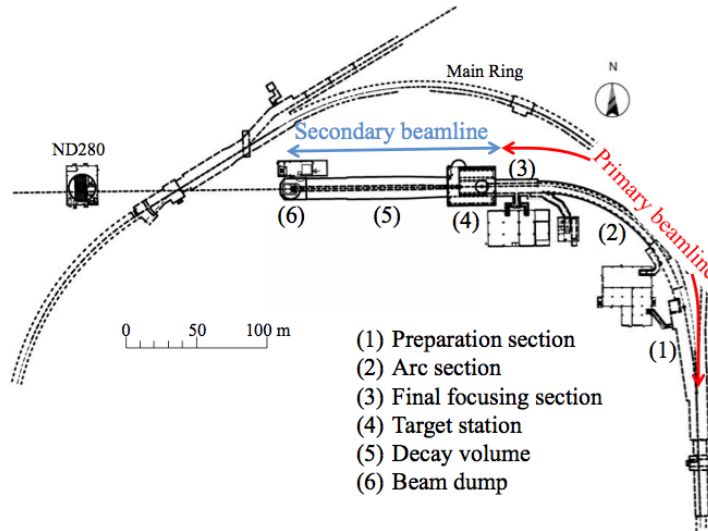


Figure 2.13: Overview of the T2K neutrino beamline.

Primary beamline

The primary beamline consists of the *preparation section* (54 m long), *arc section* (147 m) and *final focusing section* (37 m) (Figure 2.14).

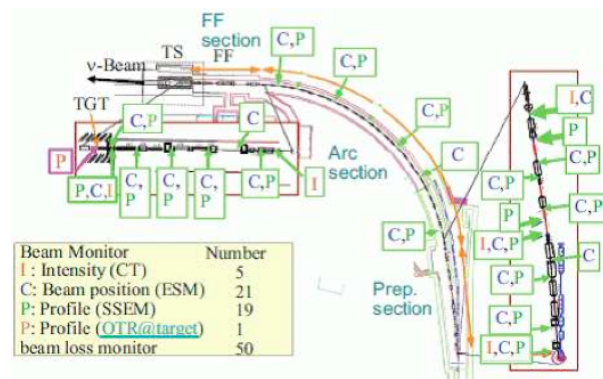


Figure 2.14: Location of the primary beamline monitors.

- In the preparation section, the extracted proton beam is tuned with a series of 11 normal conducting magnets (four steering, two dipole and five quadrupole magnets) so that the beam can be accepted by the arc section.

- In the arc section, the beam is bent toward the direction of Kamioka by 80.7° , with a 104 m radius of curvature, using 14 doublets of superconducting combined function magnets (SCFMs). There are also three pairs of horizontal and vertical superconducting steering magnets to correct the beam orbit.
- In the final focusing section, ten normal conducting magnets (four steering, two dipole and four quadrupole magnets) guide and focus the beam onto the target, while directing the beam downward by 3.637° with respect to the horizontal.

The proton beam needs to be well-tuned to ensure a stable neutrino beam production and is therefore equipped with a series of beam quality monitors. The beam intensity is monitored with an uncertainty of 2% on the absolute intensity and a fluctuation of 0.5% on the relative intensity by five current transformers (CTs), which are 50 turn toroidal coils with a ferromagnetic core.

The beam centre position is measured by a series of 21 electrostatic monitors (ESMs), with a precision of better than $450 \mu\text{m}$ by exploiting asymmetries in the electric field induced on four segmented cylindrical electrodes surrounding the proton beam orbit. The beam profile is monitored by 19 segmented secondary emission monitors (SSEMs). Each SSEM is made of three titanium foils, two of them horizontally and vertically stripped with a HV anode foil in the middle. The proton beam interacts with the foil material and thus produces secondary electrons which drift to the anode and give an indication of the beam profile with a systematic uncertainty of $200 \mu\text{m}$ on the beam width measurements. At various places along the primary beamline, 50 wire proportional counters filled with an Ar-CO₂ gas mixture are placed around the beam pipe to monitor beam losses. If the integrated signal during a spill exceeds a threshold value, the beam operation is instantly aborted.

Secondary beamline

The secondary beamline is separated from the primary beamline by a titanium-alloy beam window. The secondary beamline is placed in a volume of 1500 m^3 filled with helium gas (1 atm). It includes the *target station*, a 96 m long *decay pipe*, and a *beam dump* (Figure 2.15).

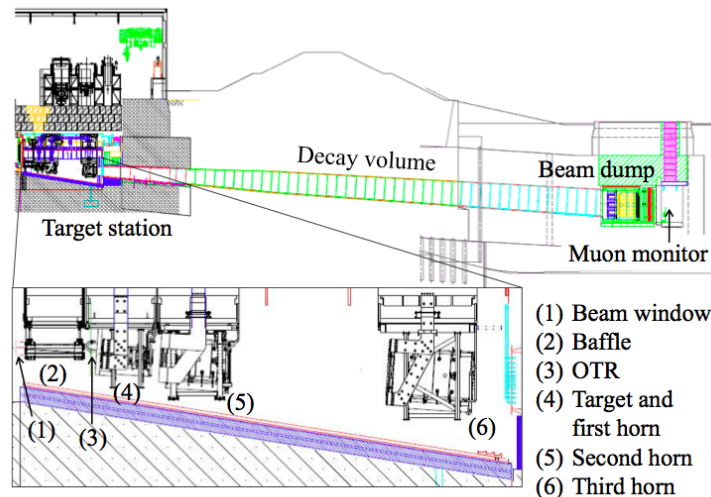


Figure 2.15: Side view of the secondary beamline. The length of the decay volume is $\sim 96 \text{ m}$.

- The target station** is located 12 m underground and contains: a baffle which is a collimator 1.7 m long graphite block with a hole of 30mm for the primary proton beam to pass through to protect the magnetic horns (Figure 2.16); an optical transition radiation monitor (OTR) [87] is used to monitor the proton beam profile just upstream of the target in the highly radioactive environment. A graphite target with a length of 91.4 cm, diameter of 2.6 cm and density equal to 1.8 g cm^{-3} follows the OTR. After the hit of protons with the target, mainly secondary pions are produced. These are collected and focused in the toroidal magnetic fields of the magnetic horns working at a pulsed current of 250 kA (320 kA in the future). When the horns are run with the operation current of 320 kA, the neutrino flux at Super-Kamiokande is increased by a factor of ~ 16 at the spectrum peak-energy ($\sim 0.6 \text{ GeV}$). The horns dimensions are listed on Table 2.2.

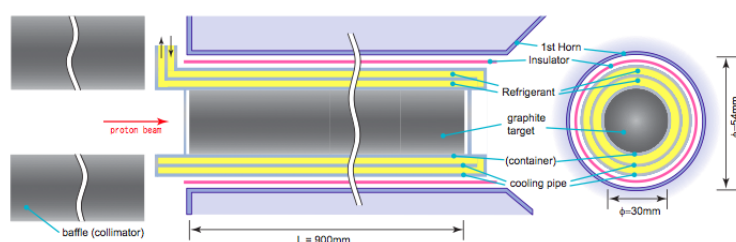


Figure 2.16: Conceptual drawing of the target system of J-PARC neutrino beamline.

Table 2.2: The horns dimensions.

	horn 1	horn 2	horn 3
Inner diameter	5.4 cm	8 cm	14 cm
Inner conductor thickness	3mm	3mm	3mm
Outside diameter	0.4 m	1m	1.4 m
Length	1.5 m	2m	2.5 m

- The decay volume** is a $\sim 96 \text{ m}$ long steel tunnel. This tunnel is filled with Helium (to minimize the interaction of particles with air) and here the secondary hadrons, mainly pions, produced from the target decay into muons and ν_μ . In which the secondary hadrons, mainly pions, decay into muons and muon neutrinos. The walls are made of iron plates equipped with a water cooling circuit to avoid the heat load from the secondary particles. In addition the entire tunnel is surrounded by concrete to shield the radiation. Its vertical dimension is made so that the neutrino beam direction can be off-axis by an angle between 2° and 3° . The length of the tunnel has been chosen long enough to have as many muon neutrino as possible but short enough to avoid as possible the decay of the muon into ν_e and $\bar{\nu}_\mu$. All the hadrons, as well as muons below $\sim 5 \text{ GeV}/c$, are stopped by the beam dump.
- The beam dump** is placed at the end of the decay volume. It consist of a core of 75 tons of graphite (1.7 g cm^{-3}), is 3.174 m long, 1.94 m wide and 4.69 m high and is surrounded by an helium vessel. Fifteen iron plates are placed outside the vessel and two inside, at the

downstream end of the graphite core, to give a total iron thickness of 2.40 m. The neutrinos pass through the beam dump and are used for physics experiments. Any muons above ~ 5 GeV/c that also pass through the beam dump are monitored to characterize the neutrino beam.

2.2.4 The Muon Monitor and Emulsion Trackers

The neutrino beam intensity and direction can be monitored on a bunch-by-bunch basis by measuring the profile distribution of muons. Since the muons are produced from the same parent particles as the neutrinos, the measurement of their properties also provides information about the neutrino beam. To reduce systematic uncertainties and assure the measurement at Super-Kamiokande, it is necessary to control the beam direction. The muon monitor [88, 89] is located just behind the beam dump. The muon monitor is designed to measure the neutrino beam direction with a precision better than 0.25 mrad, which corresponds to a 3 cm precision of the muon profile center. It is also required to monitor the stability of the neutrino beam intensity with a precision better than 3%. Based on the beamline simulation, for 3.3×10^{14} protons/spill and 320 kA horn current, is estimated to be 10^7 charged particles/cm²/bunch with a Gaussian like profile around the beam centre and approximately 1 m in width. The flux is composed of around 87% muons, with 13% of delta-rays. The muon monitor consists of two types of detector arrays (Figure 2.17):

- **ionization chambers** at 117.5 m from the target: it is a simple device to monitor the beam for a long run period and it is also suitable to cover the large area of the beam profile. It has a slow response and a weak signal over the unknown background coming from the beam dump;
- **silicon PIN photodiodes** at 118.7 m: they are used to overcome slow response and weak signals of the ionization chambers. They have a fast response and are less sensitive to the background because of the large and fast signal. Problems for the semiconductor may arise from the long term stability due to radiation damages.

Finally, a detector made of nuclear emulsion films is installed downstream the muon monitor. It is composed of two types of modules made to measure the flux and the momentum of the muons respectively. The flux is measured with a systematic uncertainty of 2%. The other module can measure the momentum of each particle by multiple Coulomb scattering with a precision of 28% at a muon energy of 2 GeV/c [90, 91].

2.2.5 The neutrino flux simulation

In order to predict the neutrino fluxes at near detectors and Super-Kamiokande, a neutrino beam MC simulation, called JNUBAEM, was developed by the T2K collaborators. The geometry of the baffle, target, three horn magnets, helium vessel, decay volume, beam dump and muon monitor is replicated in JNUBEAM according to the final drawings. JNUBAEM is also able to simulate the characteristics of the proton beam and the hadrons production cross sections. The simulation of the primary interaction of the 30 GeV protons with the graphite target is based on data from NA61/SHINE experiment³ [92–94] (Figure 2.19), which fully covers the kinematic region of interest for T2K (Figure 2.19). The NA61/SHINE measurements are crucial to reduce systematic errors, indeed for the 2010 analysis, the uncertainty on the neutrino flux was about 20% [99]. In 2011, the

³ NA61/SHINE (SPS Heavy Ion and Neutrino Experiment) at the CERN SPS pursues a rich physics program in various fields. The purpose of the NA61/SHINE measurements for T2K is to provide precise hadron production measurements at exactly the proton extraction energy of the MR, namely 30 GeV kinetic energy.



Figure 2.17: Muon monitor inside the support enclosure. The silicon PIN photodiode array is on the right side and the ionization chamber array is on the left side. The muon beam enters from the left side.

NA61 collaboration released the latest kaon cross section production, based on data taken in 2007. With this result was possible to reduce the uncertainty on the neutrino flux up to 10%. The hadronic

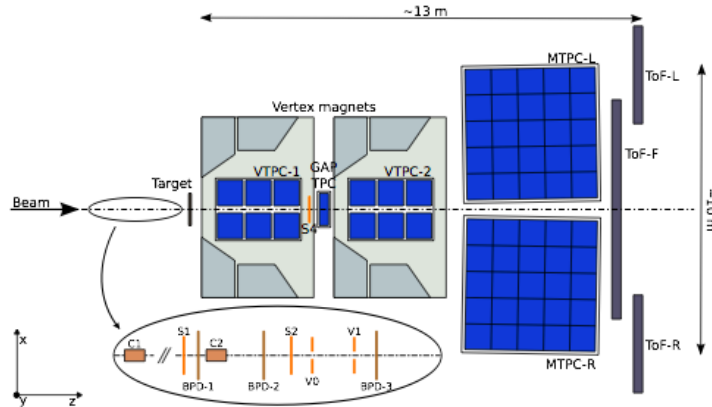


Figure 2.18: The layout of the NA61/SHINE experiment at the CERN SPS (top view, not to scale). The chosen right-handed coordinate system is shown on the plot. The incoming beam direction is along the z axis. The magnetic field bends charged particle trajectories in the x - z (horizontal) plane. The drift direction in the TPCs is along the y (vertical) axis [94].

interactions inside the target are simulated by FLUKA [95]. The particle transport is based on GEANT 3.21 [96]. The interactions outside the target are simulated using GEANT3/GCALOR [97], with the interaction cross sections tuned to experimental data. The secondaries particles and any un-interacted protons are tracked until they decay into neutrinos or are stopped at the beam dump. The particles considered in JNUBEAM as neutrino source and their decay modes are listed in the Table 2.3. The ν_e background in the beam, mainly comes from the decay $\pi^+ \rightarrow \mu^+ \nu_\mu$, $\mu^+ \rightarrow e^+ \bar{\nu}_\mu \nu_e$ and also from μ^+ produced in the K^+ and K_L^0 decay. The tracks of neutrinos are then extrapolated

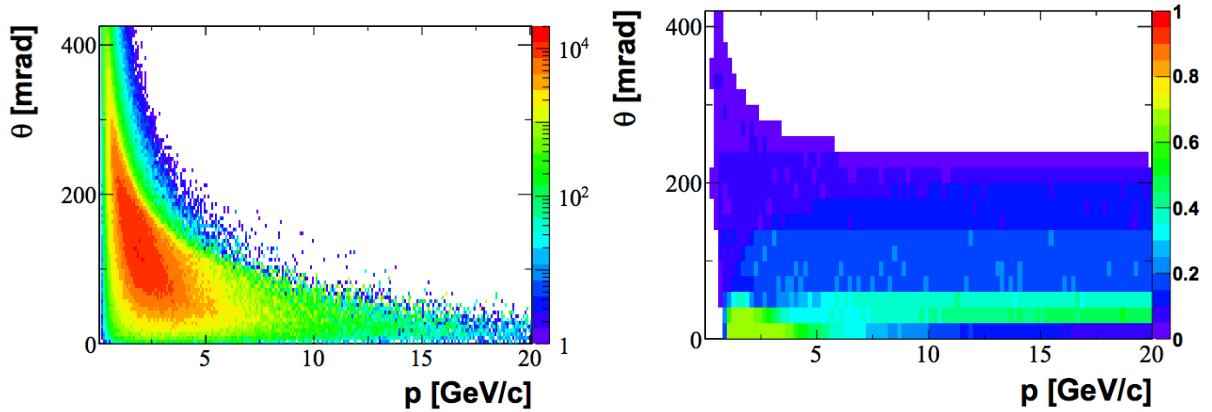


Figure 2.19: Left: The prediction from the T2K beam simulation: the (p, θ) distribution for π^+ weighted by the probability that their decay produces a muon neutrino passing through the SK detector. Right: Fraction of accepted particles as a function of momentum and polar angle, after the track acceptance cuts and ToF-F (see Figure 2.18) acceptance cut. The first polar angle bin, $[0,20]$ mrad, is fully covered by accepted particles up to 7.6 GeV/c [94].

Table 2.3: Neutrino-producing decay modes considered in JNUBEAM and their branching ratio in percentage. Decay modes for $\bar{\nu}_\mu$ and $\bar{\nu}_e$ are omitted in this Table. The π^- and K^- modes are charge conjugates of the π^+ and K^+ modes, respectively [98].

	π^+	K^+	K_L^0	μ^+	μ^-
ν_μ	$\mu^+\nu_\mu$	$\mu^+\nu_\mu, \pi^0\mu^+\nu_\mu$	$\pi^-\mu^+\nu_\mu$		$e^-\nu_\mu\bar{\nu}_e$
%	99.9877	63.55, 3.353	27.04		100
ν_e	$e^+\nu_e$	$\pi^0e^+\nu_e$	$\pi^-e^+\nu_e$	$e^+\bar{\nu}_\mu\nu_e$	
%	1.23×10^{-4}	5.07	40.55	100	

to near detectors and SK (Figure 2.20).

2.3 The near detector complex

The near detector complex is located at a distance of 280 m from the hadron production target. The near detectors are used to measure the neutrino energy spectrum, flavor content, and interaction rates of the un-oscillated beam, and to predict the neutrino interactions at Super-Kamiokande. The complex is composed by two detectors:

- **the on-axis detector INGRID** (Section 2.4): consists of 7+7 identical array of iron/scintillator detectors, arranged to form a “cross” configuration, and two diagonal modules positioned off the cross axes. The center of the cross corresponds to the neutrino beam center, defined as 0° with respect to the direction of the primary proton beamline. INGRID is able to measure the on-axis neutrino beam profile at the 280 m site;
- **the off-axis detector ND280** (Section 2.5): is a magnetized off-axis tracking detector.

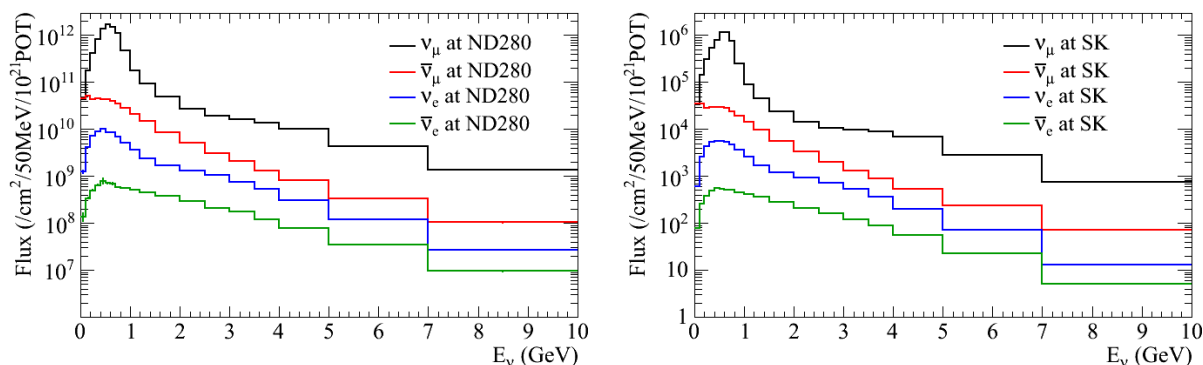


Figure 2.20: Left: The ND280 flux prediction for all neutrino flavors. Right: The SK flux prediction for all neutrino flavors.

The off-axis detector elements are contained inside the refurbished UA1⁴ magnet. Inside the upstream end of this magnet sits a π^0 detector (P \emptyset D) consisting of tracking planes of scintillating bars alternating with either water target/brass foil or lead foil. Downstream of the P \emptyset D there is the tracker, composed by three time projection chambers (TPCs) and two fine grained detectors (FGDs) consisting of layers of finely segmented scintillating bars. The tracker is designed to study measure charged current interactions in the FGDs. The P \emptyset D, TPCs, and FGDs are all surrounded by an electromagnetic calorimeter (ECal) for detecting electrons and photons to better constraint the ν_e contamination in the beam and the γ background, while the return yoke of the magnet is instrumented with scintillator to measure the ranges of muons (Side Muon Range Detectors, SMRD) that exit the sides of the off-axis detector.

All detectors in the near detector complex use the same coordinate convention: z is parallel to the nominal neutrino beam axis, and x and y are horizontal and vertical respectively. These detectors are housed in a pit inside the ND280 hall (Figure 2.21). The pit has a diameter of 17.5 m and a depth of 37 m, and has three floors:

- B1 floor: 24 m deep and houses the off-axis detector ND280;
- Service Stage (SS): 33 m deep and houses the horizontal modules of INGRID and the electronics of the off-axis detector;
- B2 floor: 37 m deep and houses the bottom modules of the vertical INGRID.

The ND280 off-axis detector, is located among the line between the average pion decay point and the far detector Super-Kamiokande, shifted by 2.5° respect to the proton beam direction, meaning an extrapolated on-axis beam passing diagonally in the center of INGRID. The facility design can accommodate off-axis angles in the range of between 2.0 and 2.5° .

Both detectors in the near detector complex make an extensive use of scintillator detectors, wavelength-shifting (WLS) fiber readout, with light from the fibers being detected by photo-sensors. The signal

⁴ The UA1 experiment was a high-energy physics experiment that ran at CERN's Super Proton Synchrotron (SPS) accelerator-collider from 1981 until 1993. The discovery of the W and Z bosons by this experiment and the UA2 experiment in 1983 led to the Nobel Prize for physics being awarded to Carlo Rubbia and Simon van der Meer in 1984.

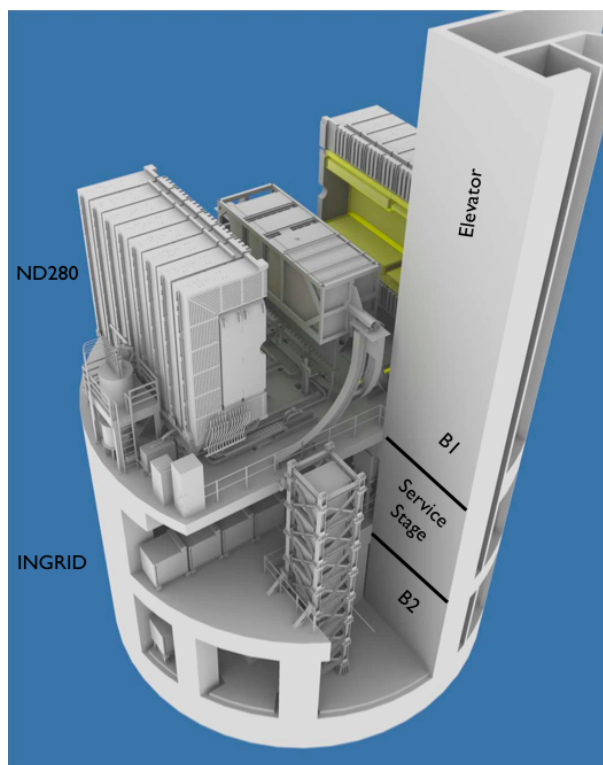


Figure 2.21: The near detector complex. The off-axis detector ND280 and the magnet are located on the upper level (B1); horizontal INGRID modules are located on the level below (SS); and the vertical INGRID modules span the bottom two levels (SS and B2). Note that the magnet in this Figure is open.

coming from the scintillated light is generally multiplied by multi-anodes Photo-Multipliers Tubes (PMTs). Although PMTs have been successfully used in other scintillator and WLS based neutrino experiments, Multi-Pixel Photon Counter (MPPCs) have been chosen as photo-sensor because of their ability to work in a magnetic field of 0.2 T and fit into a limited space inside the UA1 magnet too. Detailed information and the basic principles of operation of multi-pixel photodiodes can be found in the paper [100] and the main parameters of MPPCs are summarized in Table 2.4.

Table 2.4: Main parameters of the T2K MPPCs

Number of pixels	667
Active area	$1.3 \times 1.3 \text{ mm}^2$
Pixel size	$50 \times 50 \mu\text{m}^2$
Operational voltage	68-71 V
Gain	$\sim 10^6$
Photon detection efficiency at 525 nm	26-30%
Dark rate, threshold = 0.5 p.e., T = 25° C	$\leq 1.35 \text{ MHz}$

2.4 The on-axis detector: *INGRID*

INGRID (Interactive Neutrino GRID) is a neutrino detector centered on the neutrino beam axis and was designed to monitor directly the neutrino beam direction and intensity 280 m downstream of the target with sandwich type iron/scintillator calorimeters. Using the number of observed neutrino events in each module, the beam center is measured to a precision better than 10 cm that corresponds to 0.4 mrad precision at the near detector pit. The INGRID detector consists of 14 identical modules arranged as a cross of two identical groups along the horizontal and vertical axis, and two additional separate modules located at off-axis directions outside the main cross, as shown in the Figure 2.22. The detector samples the neutrino beam in a transverse section of $10\text{ m} \times 10\text{ m}$. The center of the INGRID cross, with two overlapping modules, corresponds to the neutrino beam center, defined as 0° with respect to the direction of the primary proton beamline. The purpose of the two off-axis modules is to check the axial symmetry of the neutrino beam. The 16 INGRID modules consist of

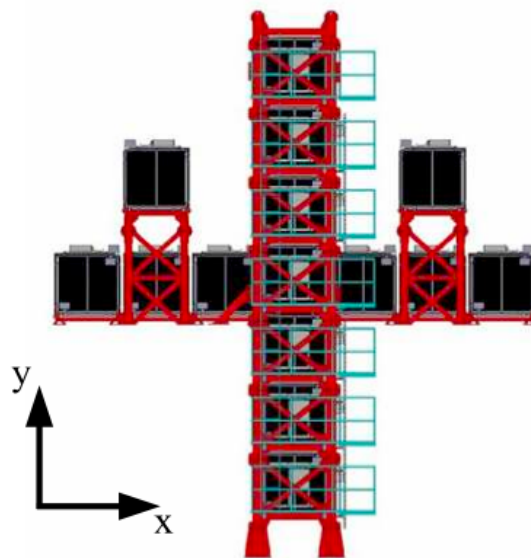


Figure 2.22: INGRID on-axis detector.

a sandwich structure of 9 iron plates and 11 tracking scintillator planes as shown in Figure 2.23. Each of the 11 tracking planes consists of 24 scintillator bars, in the horizontal direction glued to 24 perpendicular bars. Veto scintillator planes surround them, to reject interactions outside the module. The total iron mass serving as a neutrino target is 7.1 tons per module. The dimensions of the scintillator bars used for the tracking planes are $1.0\text{ cm} \times 5.0\text{ cm} \times 120.3\text{ cm}$. An extra module, called the Proton Module, different from the 16 standard modules, has been added in order to detect with good efficiency the muons together with the protons produced by the neutrino beam in INGRID. It consists of scintillator planes without any iron plate and surrounded by veto planes. A different size scintillator bar was used to improve tracking capabilities (finer grain scintillator). A schematic view of the Proton Module can be seen in Figure 2.24. It is placed in the pit in the center of the INGRID cross between the standard vertical and horizontal central modules. INGRID was calibrated using cosmic ray data taken on the surface and, during beam, in the ND280 pit. The mean light yield of each channel is measured to be larger than ten photoelectrons per 1 cm of

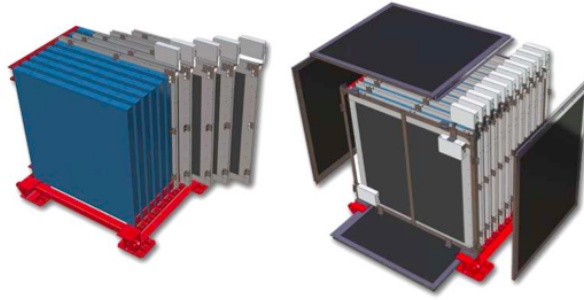


Figure 2.23: An INGRID module. The left image shows the tracking planes (blue) and iron plates. The right image shows veto planes (black).

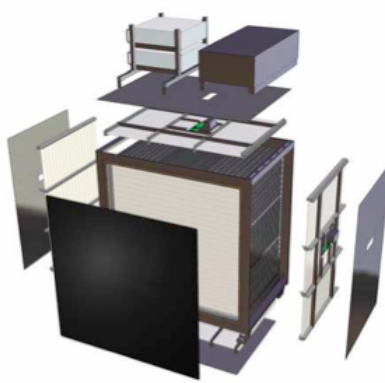


Figure 2.24: The Proton Module. Similar to the INGRID modules, but with finer grain scintillator and without the iron plates.

MIP tracks which satisfies our requirement. Furthermore the timing resolution of each channel is measured to be 3.2 ns. Typical neutrino events in the INGRID module and the Proton Module are shown in Figure 2.25.

2.5 The off-axis detector: *ND280*

The ND280 off-axis detector must satisfy several requirements:

- it must provide information to determine the ν_μ flux at the Super-Kamiokande detector;
- the ν_e contamination of the beam must be measured as a function of the neutrino energy. the beam ν_e background is expected to be approximately 1% of the ν_μ flux and creates a significant non-removable background for the ν_e appearance search;
- it must measure ν_μ interactions such that the backgrounds to the ν_e appearance search at Super-Kamiokande can be predicted. These backgrounds are dominated by neutral current single π^0 production;

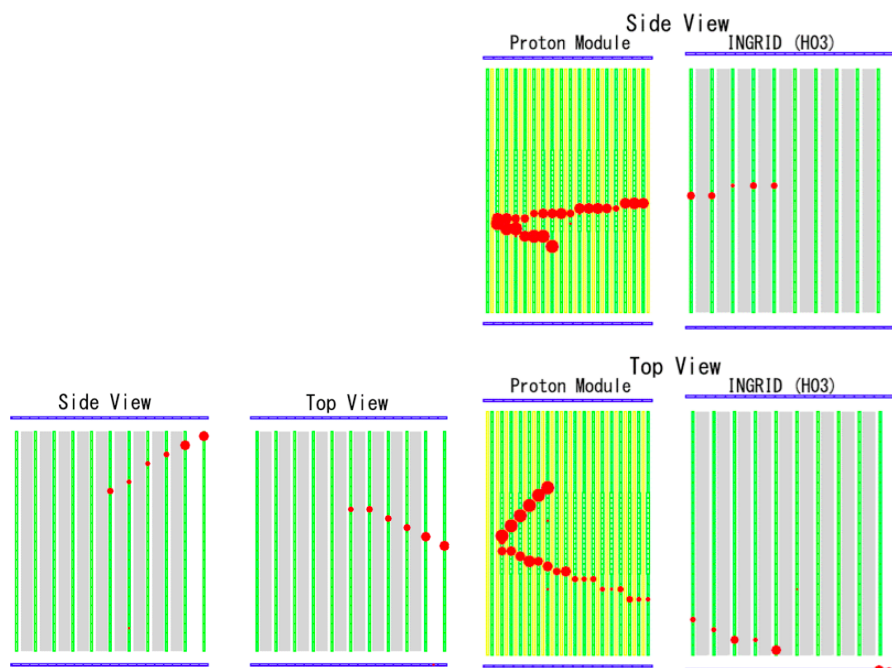


Figure 2.25: Left: A typical neutrino event in an INGRID module. A neutrino enters from the left and interacts within the module, producing charged particles. Right: A typical neutrino event in the Proton Module. A neutrino enters from the left and interacts within the module, producing charged particles whose tracks are shown as the red circles.

- it must measure inclusive and exclusive event rates.

To meet these goals the ND280 off-axis detector must have the capability to reconstruct exclusive event types such as ν_μ and ν_e charged current quasi-elastic, charged current inelastic, and neutral current events, particularly neutral current single π^0 events. The design of detector has been chosen to fulfill these requirements. The ND280 off-axis detector is shown in Figure 2.26. It consist of:

- the P \emptyset D, TPC/FGD sandwich (tracker) and the Downstream ECal, which are placed inside of a metal frame container, called the “basket”;
- an electromagnetic calorimeter (ECal) that surrounds the basket;
- the refurbished UA1/NOMAD magnet instrumented with scintillator to perform as a muon range detector (SMRD).

Figure 2.27 shows an event display of an event with a muon track entering into the P \emptyset D and continuing into the tracker (TPC and FGD) region. Multiple secondary particles are produced in the FGD, all of which are finally stopped in the ECal detectors.

2.5.1 The UA1/NOMAD magnet

The ND280 off-axis detector is built around the old CERN UA1/NOMAD [101, 102] which was refurbished at CERN and shipped to J-PARC in 2008. The magnet provide a dipole magnetic field

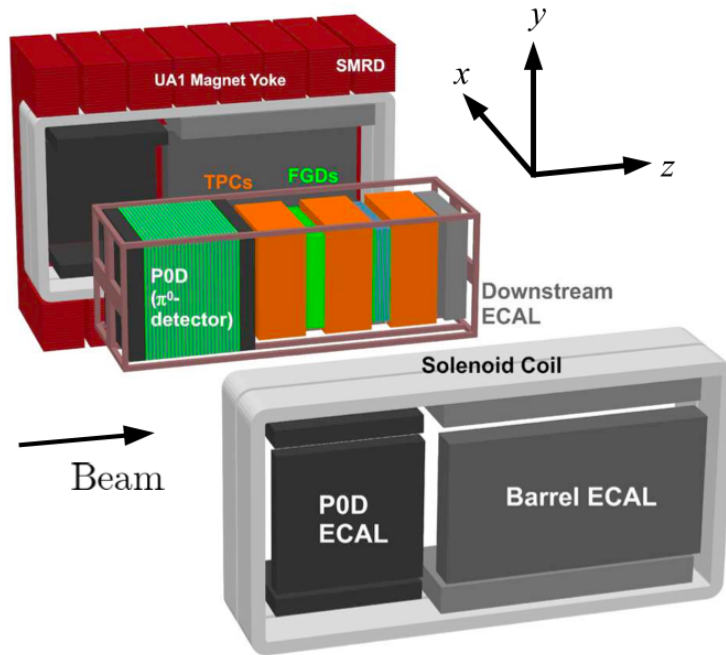


Figure 2.26: An exploded view of the ND280 off-axis detector.

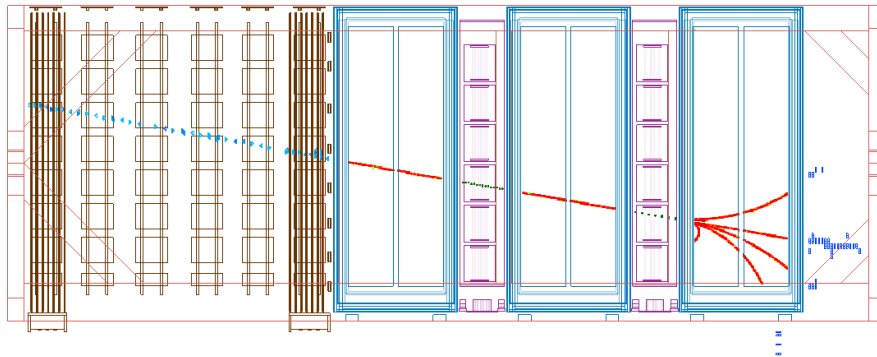


Figure 2.27: This event display shows an event with a muon track entering via the front face of the P0D detector, continuing to the tracker (TPC and FGD) region and producing secondary particles on the way. The secondary particles are then stopped in the ECAL detectors.

of 0.2 T, to measure momenta with good resolution and determine the sign of charged particles produced by neutrino interactions. It consists of water-cooled aluminum coils, which create the horizontally oriented dipole field, and a flux return yoke. The dimensions of the inner volume of the magnet are 7.0 m × 3.5 m × 3.6 m. The external dimensions are 7.6 m × 5.6 m × 6.1 m and the total weight of the yoke is 850 tons. The coils are made of aluminum bars with 5.45 cm × 5.45 cm square cross sections, with a central 23 mm diameter bore for water to flow. The coils are composed of individual “pancakes” which are connected hydraulically in parallel and electrically in series. It

consists of two mirror-symmetric halves. The coils are split into four elements, two for each half, and are mechanically supported by, but electrically insulated from, the return yoke. The two half yoke pieces each consist of eight C-shaped elements, made of low-carbon steel plates, which stand on movable carriages. Within the gaps of the magnet yokes SMRD modules are inserted.

2.5.2 Side Muon Range Detector (SMRD)

The SMRD performs multiple functions. Firstly, it records muons escaping with high angles with respect to the beam direction and measures their momenta. Secondly, it triggers on cosmic ray muons that enter or penetrate the ND280 detector. Thirdly, it helps identify beam-related event interactions in the surrounding cavity walls and the iron of the magnet. The SMRD consists of a total of 440 scintillator modules, which are inserted in the 1.7 cm air gaps between 4.8 cm thick steel plates which make up the UA1 magnet flux return yokes. It consists of 3-6 layers of scintillator modules on the top and bottom for all yokes. Pairs of yokes are labeled 1 through 8 from upstream to downstream. Due to the differently sized spaces for horizontal and vertical gaps, horizontal modules are composed of four scintillation counters and vertical modules consist of five scintillation counters. The scintillation counters consist of extruded polystyrene and dimethylacetamide with admixtures of POPOP and para-terphenyl. The surface of each scintillator counter features a white diffuse layer which acts as a reflector. An S-shaped groove, with a bending radius of 2.9 cm and a depth of 2.5 mm which deepens at the counter ends to 4 mm, has been machined into each scintillator in multiple passes to ensure good surface quality. A 1 mm diameter Kuraray Y11 double-clad WLS fiber exits both sides of the scintillator through a ferrule which is part of an endcap. The MPPCs are coupled to the polished WLS fiber ends through a snap-on mechanism. There are 4016 MPPCs connected to a miniature printed circuit (PCB), which are free to slide along the rails in the backside of the optical connector to allow for optimal WLS fiber and MPPC interconnection. The miniature PCBs couple the MPPC signals into mini-coaxial cables, which lead the signal to the custom-designed Trip-T front-end boards (TFBs) mounted on the vertical sections of the magnet yokes. The SMRD front-end electronics consists of 128 TFBs (Figure 2.28).

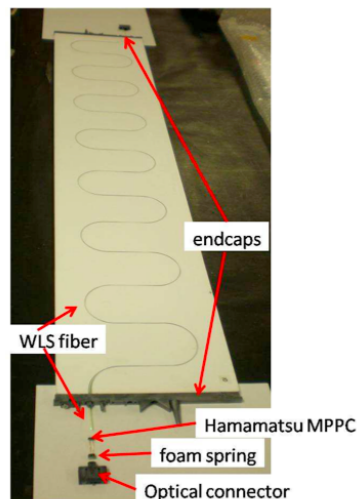


Figure 2.28: View of SMRD scintillator counter components prior to assembly.

2.5.3 Electromagnetic Calorimeter (ECal)

The ND280 ECal is a sampling electromagnetic calorimeter surrounding the inner detectors (P \emptyset D, TPCs and FGDs), used to measure the energy and direction of photons, primarily from π^0 production. It also helps to distinguish electrons, muons and pions in addition to the TPC dE/dx particle identification. It uses layers of plastic scintillator bars (made of doped 1% POP and 0.03% POPOP polystyrene with a TiO₂ reflective coating and a 1 mm in diameter WLS fiber inserted in a central hole) as active material with lead absorber sheets between layers. The bars have a 4 cm \times 1 cm cross section and vary in length depending on the module they belong to. The scintillation light from each bar is read out by one or two MPPCs depending on the length of the bar. It is composed by 13 independent modules of three different types: six Barrel-ECal modules (Br-ECal) surround the tracker volume on its four sides parallel to the z (beam) axis; one downstream module (Ds-ECal) covers the downstream exit of the tracker volume; and six P \emptyset D-ECal modules surround the P \emptyset D detector volume on its four sides parallel to the z axis. The Ds-ECal is located inside the basket carrying the inner sub-detectors of the off-axis detector. The other 12 ECal modules are mounted inside of the UA1 magnet. A drawing of a completed module is shown in Figure 2.26.

The Ds-ECal consists of 34 layers with 1.75 mm thick lead sheets corresponding to $10.6 X_0^5$ ($\sim 1 \lambda_I^6$). 50 bars of 2.04m length form a layer, and the orientation alternates between x and y in successive layers.

Limited by available space inside the UA1 magnet and structural considerations, the 6 Barrel-ECal modules surround the tracker. It is formed of 31 layers at each side corresponding to $9.7 X_0$. On the sides a layer of 3.84 m long bars (two-sided readout because of their length) in z -direction alternates with a layer of 2.36 m long bars in y -direction. On the top and bottom the z layers alternate with x layers of 1.52 m long bars.

The P \emptyset D-ECal has a reduced granularity in comparison with the others ECal modules and is made of six scintillator planes containing 2.34 m long bars always oriented in z -direction interleaved by 4 mm lead sheets. This because in the P \emptyset D region the photon conversion is happens mainly inside the P \emptyset D volume, and so the P \emptyset D-ECal is used as a veto for entering particles and tag muons and gammas that escape the P \emptyset D without being reconstructed.

2.5.4 The π^0 detector (P \emptyset D)

The primary goal of the P \emptyset D is to measure NC π^0 production ($\nu_\mu + N \rightarrow \nu_\mu + N' + \pi^0 + X$) on a water target (H₂O) with the same neutrino beam flux as reaches Super-Kamiokande. The P \emptyset D is made of four sections (so called Super-P \emptyset Dules): the “upstream ECal” followed by the “upstream water target”, the “central water target” and the “central ECal”, as shown in Figure 2.29. The combination of 134 2.2 m long vertical and 126 2.34 m long horizontal triangular scintillator bars form a P \emptyset D module, or P \emptyset Dule. Seven P \emptyset Dules alternate with 0.4 mm thick lead sheets in the case of the two ECal sections, and for the two water target sections 13 P \emptyset Dules are interleaved with 28 mm thick water bag layers followed by a 1.5 mm thick brass sheet. This design improves the containment of electromagnetic showers from photon conversion and provides a veto region before and after the water target to reject particles entering from outside the P \emptyset D. The doped polystyrene scintillator bars with a TiO₂ reflective layer have a central hole for WLS fibers (1 mm in diameter). The collected light is mirrored at one end of the bars and read out with MPPCs at the other end,

⁵ The X_0 is the radiation length which is defined to be the distance after which an electron has only $1/e$ of its initial energy remaining, where e is the Euler’s number.

⁶ The λ_I is the interaction length which is the mean free path of a particle before undergoing an interaction that is neither elastic nor quasi-elastic (diffractive), in a given medium.

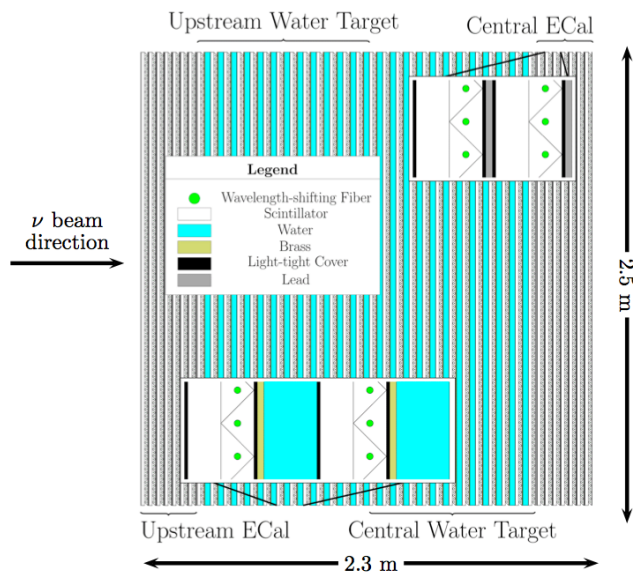


Figure 2.29: A schematic view of the π^0 detector. The beam is coming from the left and going right. Insets show details of the Water Target super-P ϕ Dule layers and Central ECal layers.

which transfer the signal to the TFBs. The signals from the overall 10,400 channels are sent to the ND280 DAQ system. The water bags can be filled or empty, which allows a subtraction method for the neutrino H_2O cross section determination. The total water mass is 1902 ± 16 kg, measured with two type of sensors. Binary level sensors (wet/ dry) and pressure sensors allowing to determine the water depth with a precision of 5 mm.

2.5.5 The Fine Grain Detectors (FGDs)

Two FGDs interleave the three TPCs, whose purpose is to provide target mass for neutrino interactions as well as tracking of charged particles coming from the interaction vertex. Moreover, the design of the first FGD being made of scintillators only and the other as a sandwich of scintillator and water allows a comparison of neutrino cross sections on carbon and water, complementary to the P ϕ D cross section. Each FGD (Figure 2.30) has outer dimensions of $2300 \text{ mm} \times 2400 \text{ mm} \times 365 \text{ mm}$ (width \times height \times depth in beam direction), and provides 1.1 tons of target material. The FGDs are constructed from $9.61 \text{ mm} \times 9.61 \text{ mm} \times 1864.3 \text{ mm}$ bars of extruded polystyrene scintillator, which are oriented perpendicular to the beam direction in either the x or y direction. The first FGD consists of 5760 scintillator bars, arranged into 30 layers of 192 bars each. The bars are orthogonally oriented in successive planes, such that each pair of orthogonal layers builds an XY module perpendicular to the neutrino beam. The second FGD is made of seven XY modules interleaved with 2.5 cm thick water layers at sub-atmospheric pressure⁷ (for a total of 2688 active scintillator bars and 15 cm total thickness of water). Each FGD is surrounded by a light tight dark box on which the readout electronics for the 42 so-called mini crates, which contain 4 front end boards each, are mounted.

⁷ The lower pressure with respect to the surrounding volume is a safety measure to avoid the water spilling over the electronics in a case of a leak.

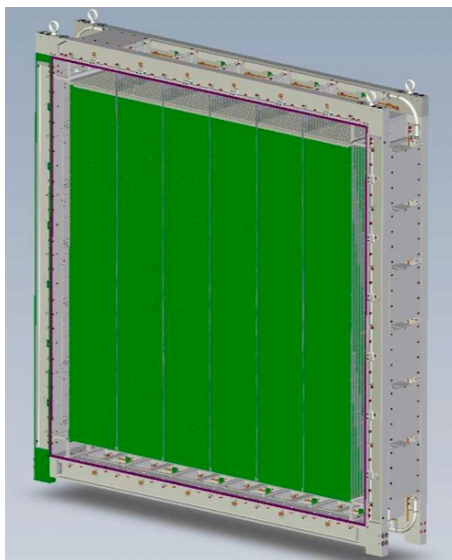


Figure 2.30: View of an FGD with the front cover removed. XY scintillator modules (green) hang perpendicular to the direction of the neutrino beam. Along the top, six mini-crates with electronics can be seen without their cooling lines, while on the right side the cooling lids covering the mini-crates are shown.

2.5.6 The Time Projection Chambers (TPCs)

The TPCs perform three key functions in the near detector. Firstly, with their excellent imaging capabilities in three dimensions, the number and orientations of charged particles traversing the detectors are easily determined and form the basis for selecting high purity samples of different types of neutrino interactions. Secondly, since they operate in a magnetic field, they are used to measure the momenta of charged particles produced by neutrino interactions elsewhere in the detector, and therefore determine the event rate as a function of neutrino energy for the neutrino beam, prior to oscillation. Finally, the amount of ionization left by each particle, when combined with the measured momentum, is a powerful tool for distinguishing different types of charged particles, and in particular allows the relative abundance of electron neutrinos in the beam to be determined.

Each of the three TPCs has outer dimension $2.3 \text{ m} \times 2.4 \text{ m} \times 1.0 \text{ m}$ and consists of an inner box with an argon-based drift gas ($\text{Ar}:\text{CF}_4:\text{iC}_4\text{H}_{10}$, 95:3:2) chosen for its high speed, low diffusion, and good performance with MicroMegas (micro-mesh gas detector) chambers [103]. The inner box is contained in an outer box that holds CO_2 as insulating gas. The inner volume is held under overpressure with respect to the outer gas volume which in turn is set to positive pressure with respect to the atmosphere to prevent impure gas from streaming in. The inner box panels were precisely machined to form an 11.5 mm pitch copper strip pattern. The TPCs are separated into two sides by a central cathode. The voltage on each strips and on the cathode is set in order to have an uniform electric field in the active drift volume of the TPC, roughly aligned with the magnetic field provided by the near detector magnet. A simplified drawing of the TPC design is shown in Figure 2.31. Ionization electrons, produced by charged particles, drift along the electric field towards the readout planes at the two ends of the TPC in positive and negative x -direction, where the charge is amplified by bulk MicroMegas detectors with a $7.0 \text{ mm} \times 9.8 \text{ mm}$ (vertical \times horizontal) pad segmentation ($48 \text{ rows} \times 36 \text{ columns}$). The signal produced by the charge amplification at the anode

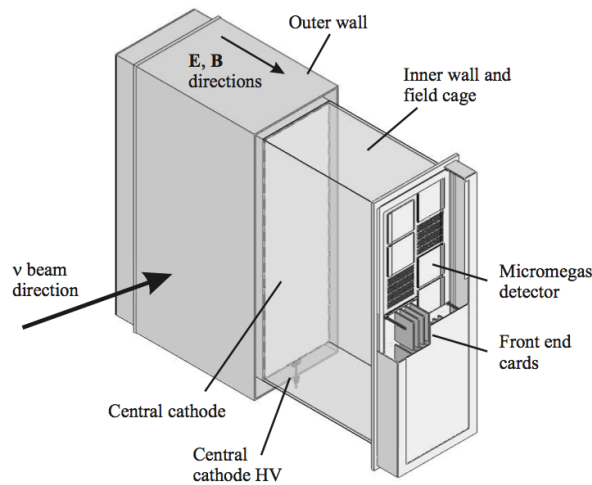


Figure 2.31: Simplified cut-away drawing showing the main aspects of the TPC design.

pads combined with the arrival time, allow a 3D imaging of charged particle trajectories within the TPC. Two vertical columns of six $342 \text{ mm} \times 359 \text{ mm}$ MicroMegas modules form a readout plane for a total of 72 MicroMegas modules (12 MicroMegas per each anode plane, 24 MicroMegas per each TPC). The columns are slightly offset in vertical direction such that the inactive regions between the modules in a single readout plane are not aligned (Figure 2.32). A calibration system uses diffuse light of a 266 nm laser to illuminate small aluminum discs which

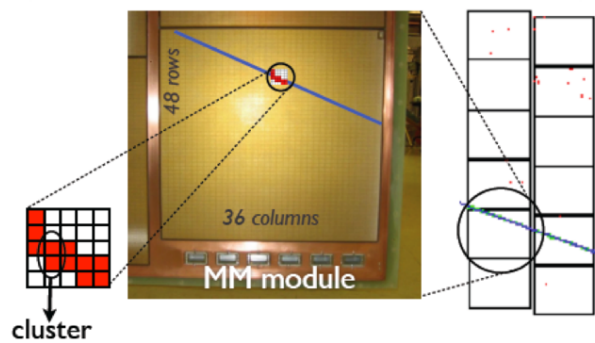


Figure 2.32: Track reconstruction in a MicroMegas detector.

are glued to the central cathode surface. The emerging photo electrons provide a control pattern which is used to precisely determine the electron drift velocity and to measure distortions because of inhomogeneous and misaligned electric and magnetic fields.

The TPC perform an excellent particle identification (PID), which uses a truncated mean of the energy loss (Figure 2.33) of a particle, taking into account the lowest 70% and rejecting the highest 30% of the energy loss Landau's tail. This value was optimized with the help of MC simulations and test beam studies. This results in an energy deposit resolution of about 7% for minimal ionizing particles (MIPs), while the point spatial resolution is determined to be 0.7 mm per column by comparison of the transverse coordinate from the global track fit to information obtained from

a single column of pads and the momentum resolution is less than 10% at 1GeV. More detailed information about the design, construction and the performance of the TPCs can be found in [104].

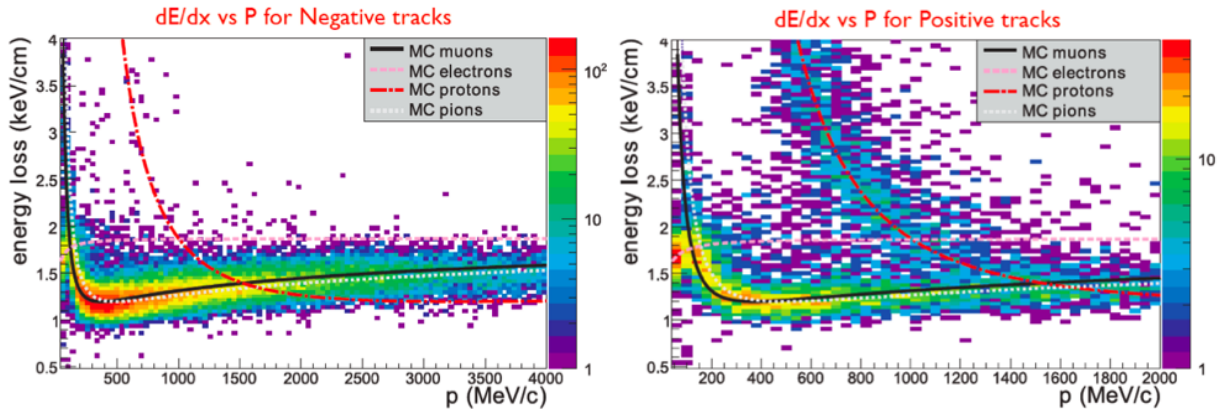


Figure 2.33: Energy loss in a T2K's TPC versus momentum for negative (left) and positive (right) charged particles.

2.6 The far detector Super-Kamiokande

The far detector, Super-Kamiokande (SK), is located in the Kamioka Observatory, and has been successfully taking data since 1996. The detector was also used as a far detector for the K2K experiment [105]. SK is the world's largest land-based water Cherenkov detector; it is a 50,000 tons water Cherenkov detector located at a depth of 1,000 m (2,700 meters water equivalent) in the Kamioka mine in Japan. During its four major running periods (SK I to SK IV) Super-Kamiokande contributed results in the field of flavor oscillations of atmospheric, solar and accelerator-produced neutrinos [38, 106–109], as well as setting the world-leading limits on the proton lifetime [110–112]. A schematic view of detector is shown in Figure 2.34. The cylindrical detector cavity is 41 m in height and 39 m in diameter, filled with 50,000 tons of pure water. The geometry of the SK detector consists of two major volumes, an inner and an outer detector which are separated by a cylindrical stainless steel structure. The inner detector (ID) is a cylindrical space 33.8 m in diameter and 36.2 m in height which currently houses along its inner walls 11,129 inward-facing 50 cm diameter PMTs. Each PMT has a 70.7 cm grid spacing for a 40% cathode surface coverage. Enclosing the ID is the outer detector (OD) which is a cylindrical space about 2 m thick radially and on the axis at both ends. The OD contains along its inner walls 1,885 outward-facing 20 cm diameter PMTs and is used as an anti-counter to identify entering/exiting particles to/from the ID.

The primary strategy to measure the flavor composition of the T2K neutrino beam at SK, and thereby observe the oscillation of ν_μ to either ν_e or ν_τ is to count charged current quasi-elastic (CCQE) interactions for muon and electron neutrinos, both of which produce leptons of their respective flavor. The relativistic charged particles, produced in these neutrino interactions, travel through the detector with a speed faster than the velocity of light in water. They thereby polarize water molecules rapidly turn back to their ground state and emit Cherenkov light, which is detected by the ID PMTs.

For both ν_μ and ν_e CCQE signals the starting position of the leptons is required to be fully contained in the fiducial volume, which is defined to be more than 2 m away from the ID wall for a total fiducial

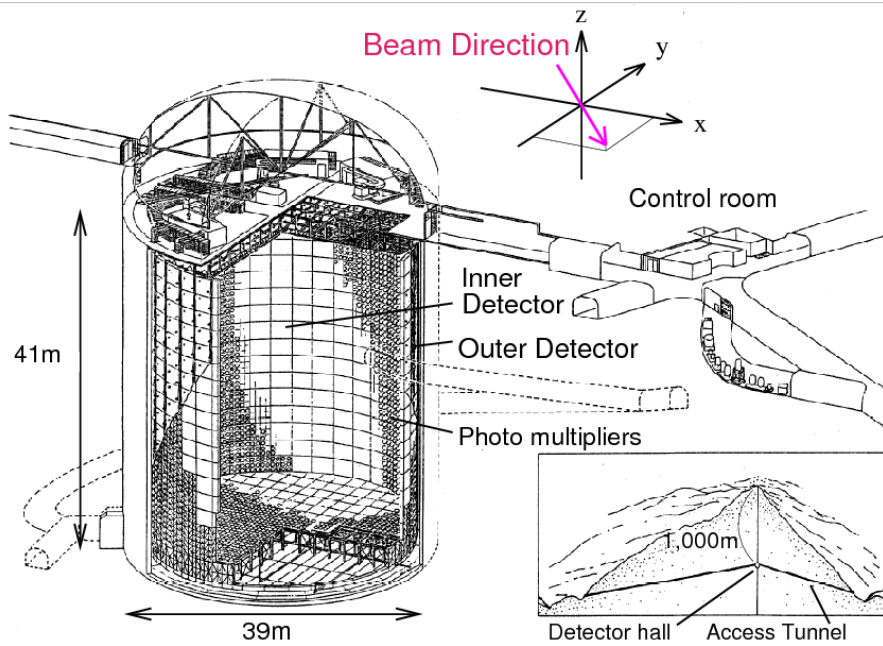


Figure 2.34: Diagram of the Super-Kamiokande Detector. The detector is mainly comprised of two segments, the inner and outer detectors. The boundary between the two segments is defined by a cylindrical scaffold used to mount photomultiplier tubes and optically separate the segments.

mass of 22,500 tons. The pulse height and timing information of the PMTs are fitted to reconstruct the vertex, direction, energy, and particle identification of the Cherenkov rings. A typical vertex, angular and energy resolution for 1 GeV muons is 30 cm, 3° and 3%, respectively. The typical ring shape, which is obtained from fully contained charged particles with an energy above the Cherenkov threshold, allows to infer the vertex position and the momentum of the charged particles. A very good discrimination between fuzzy electron like Cherenkov rings and sharp edged rings from muons enables to separate ν_e from ν_μ interactions. The fuzzy electron like ring is due to the multiple scattering which is more likely to occur for electrons than for muons because of the electron smaller mass and almost always an electron induce electromagnetic showers at the energies relevant to SK (Figure 2.35). A typical rejection factor to separate muons from electrons (or vice versa) is about 100 for a single Cherenkov ring event at 1 GeV. The electrons and muons are further separated by detecting decay electrons from the μ decays. A typical detection efficiency of decay electrons from stopping cosmic muons is roughly 80%. A 4π coverage around the interaction vertex provides an efficient π^0 detection. Interactions of neutrinos from the J-PARC accelerator are identified by synchronizing the timing between the beam extraction time at the accelerator and the trigger time at Super-Kamiokande using the Global Positioning System (GPS). A quantity ΔT_0 is defined, which is the timing between the beam extraction time at the accelerator and the trigger time at SK. In Figure 2.36 left, is shown the ΔT_0 of all Fully contained (FC), outer detector (OD) and low energy (LE) events within $\pm 500 \mu\text{s}$ of the beam arrival time; the spill duration is about $5 \mu\text{s}$. Instead, in Figure 2.36 right, is shown the ΔT_0 distribution of FC events within the spill window. The ΔT_0 of each event is corrected to account for the position of the neutrino interaction vertex and the photon propagation time from the interaction vertex to the PMTs. The far detector event timing clearly exhibits the eight bunch beam timing structure. The synchronization accuracy of the two

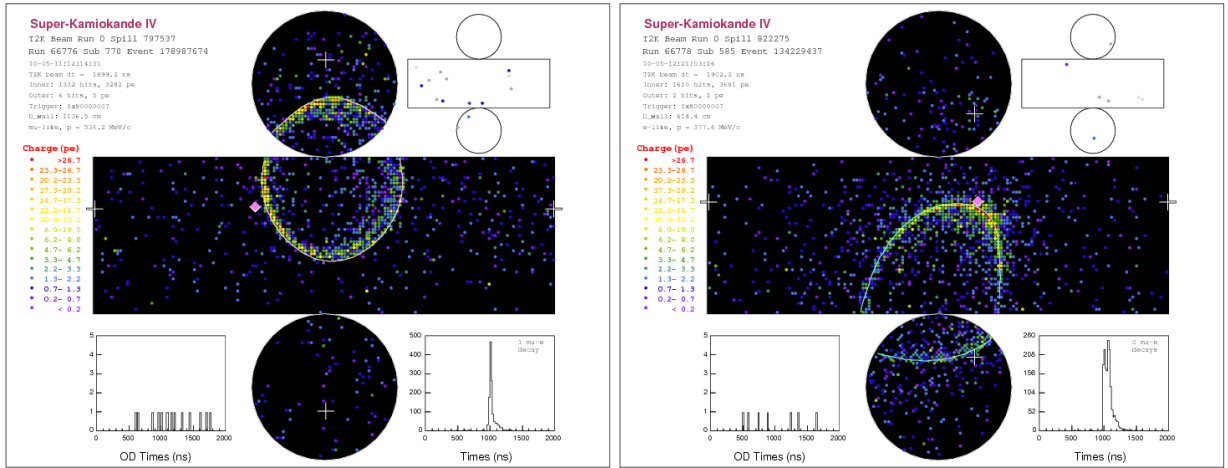


Figure 2.35: Example of reconstructed T2K events in Super-Kamiokande for a μ -like ring (left) and ν_e -like ring (right).

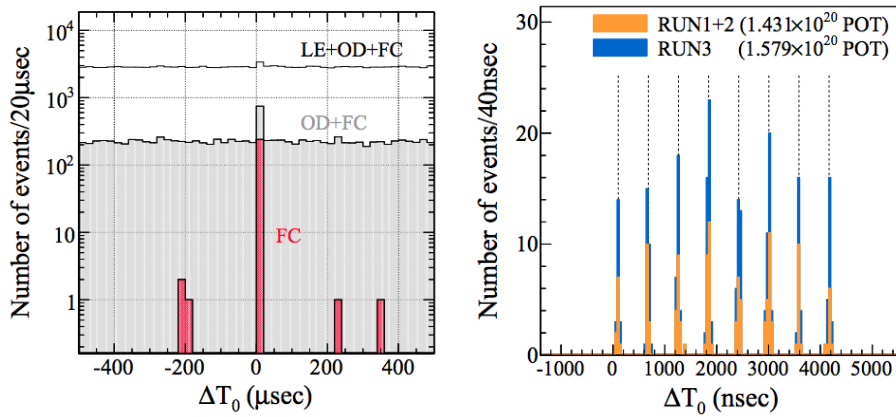


Figure 2.36: Left: ΔT_0 distribution of all FC, OD and LE events observed in the $\pm 500 \mu\text{s}$ T2K windows. Right: ΔT_0 distribution of FC events zoomed in on the spill time observed during T2K Run 1+2 and Run 3. The eight dotted vertical lines represent the 581 ns interval bunch center position fitted to the observed FC event times [113].

sites is demonstrated to be less than 200 ns. Because of this stringent time constraint, and the quiet environment of the deep Kamioka mine, a chance coincidence of any entering background is negligibly low. A typical chance coincidence rate of atmospheric neutrino events is 10^{-10} per spill, which is much smaller than the signal rate of about 3×10^{-3} per spill [114].

In 2008, the Super-Kamiokande collaboration completed an upgrade to the detector's readout electronics [115, 116] for the SK IV period, in which the T2K running period falls, to improve the data processing rate and the trigger method. The 550 new front end boards for the readout of the 13,014 PMTs allowed an increase of the order of a magnitude in the input pulse rate from 1.4 kHz per channel to 80 kHz per channel. In combination with new programmable software triggers, which are capable of implementing a coincidence trigger with the beam arrival time as in the case of T2K,

the setup improved Super-Kamiokande's ability to better accommodate a larger range of neutrino studies. The DAQ system records hit information in a 1 ms time window around the T2K beam arrival time and passes the data to a cluster of online PCs which organizes the PMT hit informations for later offline analysis.

Chapter 3

Measurement of $\bar{\nu}_\mu$ CC interactions using the ND280 Tracker

In this Chapter I will present the measure of the $\bar{\nu}_\mu$ beam component in ND280. The study of $\bar{\nu}_\mu$ interactions at ND280 is mainly motivated by the fact that it helps in the reduction of the related systematic errors in the oscillation analyses. In fact differently from the ND280 detector, the far detector SK is not immersed in a magnetic field and thus it cannot distinguish between μ^- and μ^+ coming from ν_μ and $\bar{\nu}_\mu$ charged current interactions respectively. The number of expected $\bar{\nu}_\mu$ one ring events at SK is very low in comparison with the ν_μ one ring events ($\sim 7\%$), however this implies a systematic uncertainty in the disappearance analysis. Up to now only the ND280 ν_μ sample is used to constrain flux and cross-section systematics at SK for the oscillation analyses. As a consequence the uncertainties related to $\bar{\nu}$ remain relatively large, in particular for the $\bar{\nu}/\nu$ cross section ratio and two main effects are foreseen:

- in the disappearance analysis, the one ring $\bar{\nu}_\mu$ background events at SK are weakly constraint by the ND280 ν_μ sample;
- a very large systematic error ($\sim 40\%$) has to be introduced for the $\bar{\nu}/\nu$ cross section ratio for the oscillation analyses [117].

The anti-neutrino sample selected in this analysis will be used to improve the ND280 constraint on $\bar{\nu}_\mu$ flux and cross section, and therefore the relative $\bar{\nu}$ systematic errors in the oscillation analyses will be reduced in the future. Finally, since in 2014 T2K will start the data taking in $\bar{\nu}_\mu$ flux mode (as discussed in Section 2.1.4), this topic will become one of the key ingredients of the analysis at ND280.

At the begin of this chapter, a general overview of the ND280 software (Section 3.1), calibration (Section 3.2) and reconstruction (Section 3.3) will be presented. The aim of these sections is to explain how the main variables used to select an event in the analysis are reconstructed and at which stage the calibration is applied. The anti-neutrino event selection will be detailed in Section 3.5 and finally, to extract information on the $\bar{\nu}_\mu$ component from the selected sample, a likelihood fit of signal and background in kinematic distributions will be performed.

3.1 The ND280 software overview

The ND280 software can be divided according to the role of its various packages. The relation between the different packages is shown in Figure 3.1. The ND280 software is able to process MC

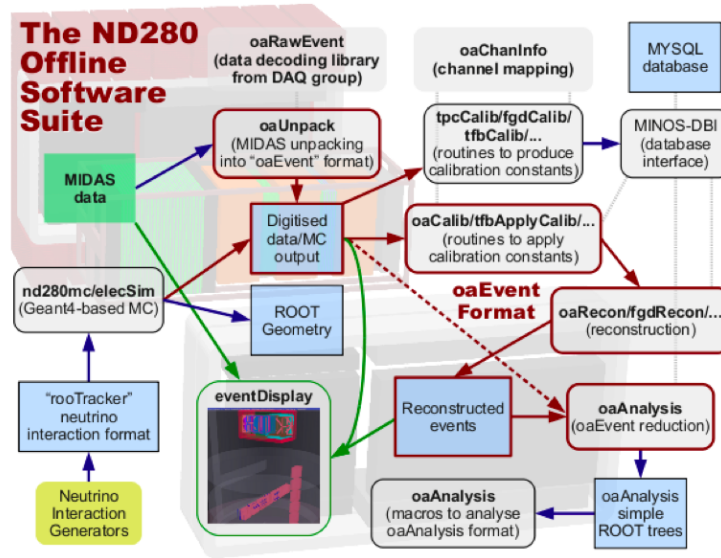


Figure 3.1: The ND280 offline software suite [118].

simulations as well as near detector measurements. The first stage of MC processing mainly consist in transforming the true simulated information into a format comparable to that of a measurement. This implies the incorporation of the detector and the electronic readout response. This first stage of the MC processing is the so called *event simulation*, and can be summarized as follows:

1. neutrino flux simulation at the near and far detector locations (JNUBEAM) is the input for the neutrino generator;
2. neutrino interaction generation (NEUT/GENIE) produces the interaction vertex in ND280;
3. all the particles coming from the interaction vertex are simulated by the package `nd280mc` (based on GEANT4);
4. the electronic and digitization of the detector response are simulated by `elecSim`.

The neutrino event generation is interfaced to the neutrino beam flux simulation. Therefore, the MC has a complete knowledge of the flux at different positions inside the near detector site. The simulation of neutrino interactions is done using two different neutrino event generators (NEUT and GENIE) [119, 120]. The particles coming from the neutrino interaction vertex are then propagated using GEANT4 [121] in the near detector (`nd280mc`) and a dedicated package simulates the response of the active detector components and readout electronics (`elecSim`). For data, the first stage consist in the conversion of the raw data output (MIDAS format) into the ROOT [122] event format, described in [118]. At this stage, the only difference between data and MC is that MC has in addition the MC truth information¹. Calibration and reconstruction are then applied similarly to both samples. It is worth noting that calibration not only affects real data but also the events simulated by MC methods. In order to be as close as possible to real data, the effect of the calibration is simulated.

¹ The MC truth is the knowledge of generated values of physical parameters, used as input for the detailed simulation of the detector response, and stored as part of the simulated event data.

3.2 The calibration procedure

The calibration procedure is divided in two steps: the first step involve the *electronics calibration* and consist in the normalization of all electronics channels to the same zero and scale, whereas the second step is a *physical calibration* and is dedicated to the adjustment of physical parameters as ADC/MeV conversion. It leads finally to the best possible reconstruction of the particle trajectories and their energy deposition, which is crucial for the determination of their type. The calibration includes calibration data (clusters, tracks, etc . . .), calibration algorithms and calibration constants. The ND280 software provides three type of calibration algorithms:

- algorithms computing the calibration constants: packages for each sub-detector like `tpcCalib`, `fgdCalib` and so on;
- algorithms that apply the calibration constants: the calibration constants are then applied by algorithms belonging to each sub-detector reconstruction package (`oaCalib`, `tpcRecon`, . . .);
- algorithms that “de-calibrate” the MC data in order to simulate the effect of the real detector: these algorithms are able to simulate for example the geometrical misalignment, the magnetic field inhomogeneities, the electronic response at the event simulation level. These algorithms are distributed among `nd280mc` and `elecSim`.

3.2.1 Calibration of the electronics

Each electronics channel i of ND280 provides uncalibrated signal Q_{raw}^i at time t_{raw}^i not sufficient to reconstruct the event. In order to extract the appropriate information from the received signals, all electronic channels in same sub-detector must refer to the same reference system, with the same zero and scale. For example, in the simplest case of a linear response, the calibrated signals, for each electronics channel i , are:

$$Q^i = \alpha^i(Q_{\text{raw}}^i - Q_0^i) \quad (3.1)$$

and

$$t^i = \beta^i(t_{\text{raw}}^i - t_0^i), \quad (3.2)$$

where Q_0^i is the channel pedestal, t_0^i is the starting time of the pulse, and α^i and β^i are appropriate scaling constants.

3.2.2 Physics calibration

This calibration step is different for each sub-detector, and includes the energy calibration (ADC/MeV conversion), charge attenuation, spatial distortions, magnetic field corrections and geometrical alignment. As a consequence, the physics calibrations can affect the charge, the time and also the position of the hit. The energy calibration of the TPC, for example, is done by using the Test Bench procedure, the spatial distortion by the use of the laser, the drift velocity by the use of the laser and monitoring chamber and finally the signal attenuation is done by using the monitoring chamber together with cosmic data [104]. In particular, in the energy calibration procedure, the raw information coming from the Test Bench is reprocessed using the calibration package where the different corrections are applied to the gain. The calibrated values are then stored to the database and applied afterwards to each MicroMegas pad by the reconstruction package of the TPC (`tpcRecon`). Applying the energy calibration procedure it is possible to achieve a dE/dx resolution in each TPC

of $\sim 8\%$ for particle between $500 < p < 600$ MeV/c which is better than the required 10% resolution goal that allows to distinguish muons electrons and protons at more than three σ around the T2K energy peak.

The calibration is very important for the online software, since most of the calibration data (cosmic and laser runs) are taken in parallel with the physics data. The evolution in time of the calibration constants is crucial to ensure the quality of the data and therefore some of these are computed online and monitored during the data taking.

3.3 Reconstruction

The event reconstruction can be divided into:

- *local* reconstruction: each sub-detector (TPC, FGD, etc. . .) develops its own reconstruction algorithm;
- *global* reconstruction: all the *local* reconstructed objects² are combined.

A brief description of the TPC reconstruction and of *global* reconstruction [123] will be presented in this section. At the end of the reconstruction process the high level informations are extracted by the `oaAnalysis` package and made available for the physics analyses.

3.3.1 TPC reconstruction

The first step in the TPC reconstruction, as mentioned in the Section 3.2.2, consists in the application of the gain calibration constants and the removal of dead and noisy channels. The result of this process is the waveform that represents the charge collected in a single pad as a function of time. The next step is the search for clusters of waveforms in the same row of a MicroMegas (Figure 3.2 on the left). Clusters are then joined into tracks using a pattern recognition algorithm. The pattern recognition is applied to TPC blocks independently, where the TPC blocks are the area defined by each MicroMegas (Figure 3.2 on the right). Prior to the track kinematics reconstruction, the drift distance has to be reconstructed to be able to predict the size of the electron cloud due to the transverse and longitudinal diffusion. This is achieved by determining the time at which the track was created (t_0 of the track) via a matching with clusters in the fast detectors, FGD, P \emptyset D and ECAL. The x -coordinate is then reconstructed as:

$$x = (t - t_0)v_d. \quad (3.3)$$

The reconstructed tracks are then matched to tracks in other TPC blocks and refitted to improve the accuracy of the track parameters. At the end of the pattern algorithm, the calculation of the ionization energy deposited in the TPC is computed to perform the particle identification (PID). After the calculation of the ionization energy deposited in the TPC, the reconstruction of the track kinematics is done using a single TPC likelihood fit with helix parameterization. From this fit, the main variables used to select the charged current events are obtained. They are the absolute x , y and z coordinates, the direction of the track and its curvature ρ . From the curvature, the reconstructed momentum p and charge q can be computed:

$$p = \frac{0.3 \times B}{\rho} \sqrt{\frac{1 + t_x^2 + t_y^2}{1 + t_y^2}}, \quad (3.4)$$

² From now on the term object will be used when referring to track and/or shower.

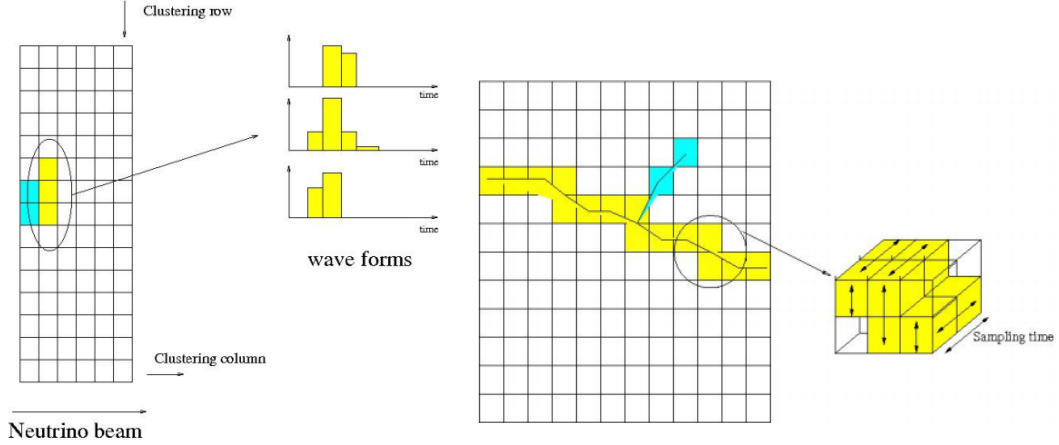


Figure 3.2: Right: Sketch of clustering method. Left: Sketch of pattern recognition algorithm.

$$q = \rho/|p|, \quad (3.5)$$

where the momentum p is in MeV, the fitted curvature ρ is in mm^{-1} , B is the mean amplitude of the magnetic field in Tesla, and t_x and t_y are the tangents of the projected angle in the XZ and YZ plane respectively. The transverse momentum to the magnetic field is defined for $t_x = 0$.

3.3.2 Global reconstruction

The final output from the local sub-detector reconstruction is a list of either track-like or shower-like objects. If the objects are identified as tracks then they will be fitted again with the RECPACK³ *Kalman Filter* [124]. Instead, if the objects are identified as showers then no changes will be necessary. The *global* reconstruction proceeds as follow:

1. Try to match each Tracker object (FGD-TPC matched tracks) to adjacent detectors through the computation of a matching χ_{match}^2 ⁴:
 - if the matching χ_{match}^2 is less than a certain cut-off value (200 for objects containing P \emptyset D or SMRD and 100 for object containing ECal) and the time difference between the objects is acceptable (within 300 ns of each other), then the two objects are matched together;
 - if two objects are matched together, then the objects are fitted again using the RecPack *Kalman Filter* [124];

³ RECPAC is an external reconstruction toolkit, which provides a series of standardized fitting, propagation and matching routines.

⁴ For example, if the two objects are two trajectories, the matching is done by extrapolating both trajectories on the same input surface. The goodness is given in both cases by the matching χ^2 divided by the number of degrees of freedom (ndof) of the matched vector, where the matching χ^2 is given by:

$$\chi_{\text{match}}^2 = (v_1 - v_2)(C_1 + C_2)^{-1}(v_1 - v_2)^T \quad (3.6)$$

and ndof is the number of meaningful parameters in both v_1 and v_2 . When matching two trajectories v_1 and v_2 are the extrapolated state vectors of the two trajectories and C_1 and C_2 are the covariance matrices of v_1 and v_2 respectively.

- only pairs of objects are combined at the same time. Therefore, a third object would be match to the merged object in the next iteration.
2. *Step 1* is repeated, but starting with all the $P\emptyset D$ objects that were not used in *Step 1*.
 3. *Step 1* is repeated, but starting with all the ECal objects that weren't used in *Step 1*.
 4. ...

3.4 The data sets

The anti-neutrino analysis is performed with all ND280 data taken from January 2010 until May 2013. During this period the proton beam power on the target has steadily increased and reached 220 kW continuous operation with a world record of 1.2×10^{14} protons per pulse. The total neutrino beam exposure corresponds to a total integrated 6.63×10^{20} protons on target (POT) (Figure 3.3). Of 6.63×10^{20} POT data collected, 90% of these ($\sim 5.9 \times 10^{20}$) passed the beam and ND280 data



Figure 3.3: The good spill integrated POT delivered to T2K (January 2010 - May 2013).

quality checks and is used in the analysis.

The MC sample used is approximately 10 times the data POT for each T2K run and is divided according to the $P\emptyset D$ status (water in/water out) and the beam power. A detailed summary of the data sets (data and MC samples) used in the analysis is shown in Table 3.1. The data and MC samples are both based on the ND280 production 5 (Prod5) obtained with the ND280 software version v10r11p21 (and v10r11p23). In each plot of this thesis *the MC is normalized to the data POT*.

The MC sample is produced with the so called “11a nominal” beam flux that is the nominal neutrino flux expected at ND280. During the data taking, the beam group released improved version of the neutrino flux based on the observed flux for each T2K run. The last flux release is the “11b-v3.2”, and in Figure 3.4 are shown the differences respect to the expected nominal flux. In the anti-neutrino analysis, to take into account the last flux release, the MC is re-weighted on the 11b-v3.2 tuned flux.

Table 3.1: Definition of T2K runs and the amount of data and MC POT used in the analysis. The beam power (beama = 50 kW, beamb = 120 kW, beamc = 178 kW) used in the MC files and whether they had water or air in the P \emptyset D is also shown in the Table. The barrel ECAL is not used in run 1 as it was not installed until the shutdown between runs 1 and 2.

T2K run	ND280 runs	Data POT	MC POT	MC water status	MC beam power
Run I	4165-5115	1.67×10^{19}	3.86×10^{20}	water	beama
Run II (water)	6462-7663	4.28×10^{19}	5.56×10^{20}	water	beamb
Run II (air)	7664-7754	3.55×10^{19}	4.62×10^{20}	air	beamb
Run III b	8309-8453	2.14×10^{19}	2.27×10^{20}	air	beamc
Run III c	8550-8753	13.48×10^{19}	13.72×10^{20}	air	beamc
Run IV (water)	8995-9422	16.25×10^{19}	23.46×10^{20}	water	beamc
Run IV (air)	9423-9798	17.62×10^{19}	9.04×10^{20}	air	beamc
Total		$\sim 5.9 \times 10^{20}$	$\sim 6.2 \times 10^{21}$		

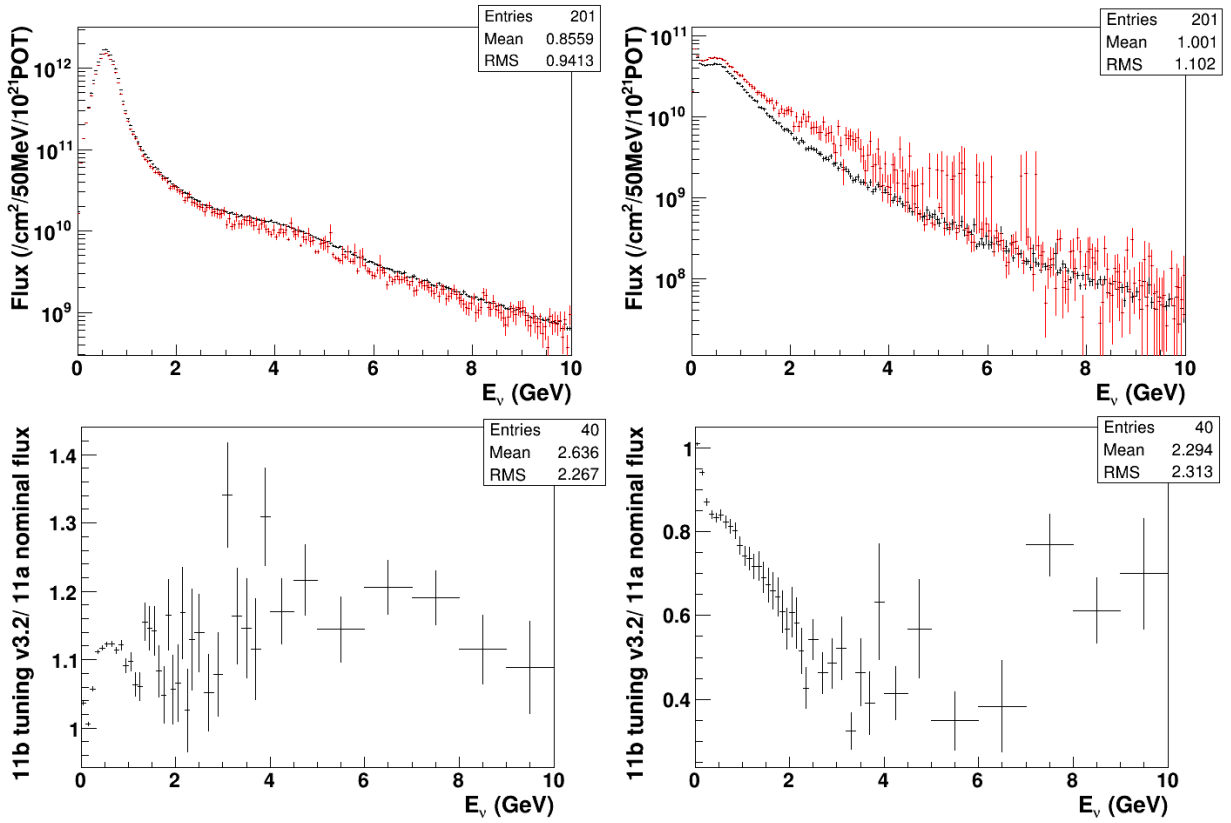


Figure 3.4: Top: Predicted 11b-v3.2 flux at ND280 (black) and 11a nominal flux (red) for ν_μ (left) and $\bar{\nu}_\mu$ (right). Bottom: Ratio of the 11b-v3.2 tuned flux to the 11a nominal flux at ND280 for ν_μ (left) and $\bar{\nu}_\mu$ (right).

3.5 The selection criteria

$\bar{\nu}_\mu$ CC interactions (Figure 3.5) can be selected by identifying the μ^+ produced in the final state. At the T2K energy peak (~ 600 MeV), in $\bar{\nu}_\mu$ CC interactions the μ^+ is, in 95% of the cases, the reconstructed track with the highest momentum. Nevertheless the selection of $\bar{\nu}_\mu$ CC interactions in ND280 is difficult due to the small fraction of $\bar{\nu}_\mu$ in the T2K beam. This component is expected to be of the order of 4% of the total neutrino flux, and to select it, a large amount of ν_μ CC interactions must be rejected. For this reason a fundamental tool for this analysis is the particle

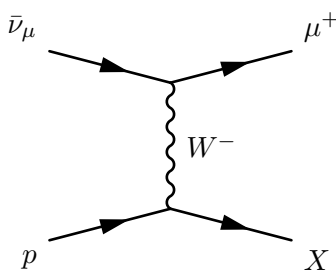


Figure 3.5: $\bar{\nu}_\mu$ CC Inclusive interaction at the T2K energy peak.

identification (PID) because combining TPC and ECal PID is possible to reject over the 98% of the ν_μ background.

The selection criteria can be divided in two fundamental steps. The first step, called *pre-selection*, simply consists in the selection of the positive tracks with the highest momentum produced by neutrino (anti-neutrino) interactions in the FGDs fiducial volumes and is driven by the following goals:

- reject the large background due to sand muons, produced by neutrino interactions in the sand or the concrete walls of the ND280 pit;
- reject the background from neutrino interactions in the magnet, producing tracks that enter the basket from the sides.

The second step consists in the selection of the μ^+ coming from $\bar{\nu}_\mu$ CC interactions and to achieve this purpose, the main goals are:

- reject as much as possible the positive pions coming from the neutrino CCnonQE interactions;
- reject as much as possible the highest momentum protons coming from the neutrino CC inclusive interactions;
- reject the low energy electromagnetic background (e^+ and e^- pairs coming from γ conversions);
- achieve a good purity retaining a high efficiency.

Thus the criteria to select $\bar{\nu}_\mu$ candidates events are the following:

- *pre-selection of the most energetic positive track in the tracker:*

1. **event quality:** use only events associated to beam trigger and compatible with one of the 8 (6 for Run I) bunches (see Figure 3.6). To do this selection the mean and the width of each bunch were measured and tracks in the event are accepted only if they are within 4σ (using $\sigma = 15$ ns) from the center of one of the bunches (see Table 3.2);
 2. **track selection:** select the most energetic positive track of the event entering the TPC. The analysis refers to this track as the lepton candidate;
 3. **FGDs FV:** request the start position of the lepton candidate to be in the FGDs Fiducial Volumes⁵ (FV) (Figure 3.7);
 4. **TPC Quality:** the selected track must have more than 18 reconstructed horizontal clusters⁶ in the TPC to reject short tracks for which the reconstruction is less reliable;
 5. **backwards-going tracks and TPC1 veto:** remove mis-reconstructed events entering the FGD1 FV from the upstream edge of the detector.
- **selection of $\bar{\nu}_\mu$ interactions candidates through the μ^+ identification:**
 1. **TPC PID:** The TPC particle identification (PID) criteria are applied to the most energetic positive track that satisfies the *pre-selection*;
 2. **one TPC track multiplicity:** Only events with one TPC-FGD matched track are selected in order to reject as much as possible the background coming from ν_μ CCnonQE interactions;
 3. **ECal Matching:** The selected track must enter the ECal;
 4. **ECal PID:** the ECal particle identification (PID) is applied to the selected track in order to enhance the μ^+ purity of the sample rejecting as much as possible showering pions and protons.

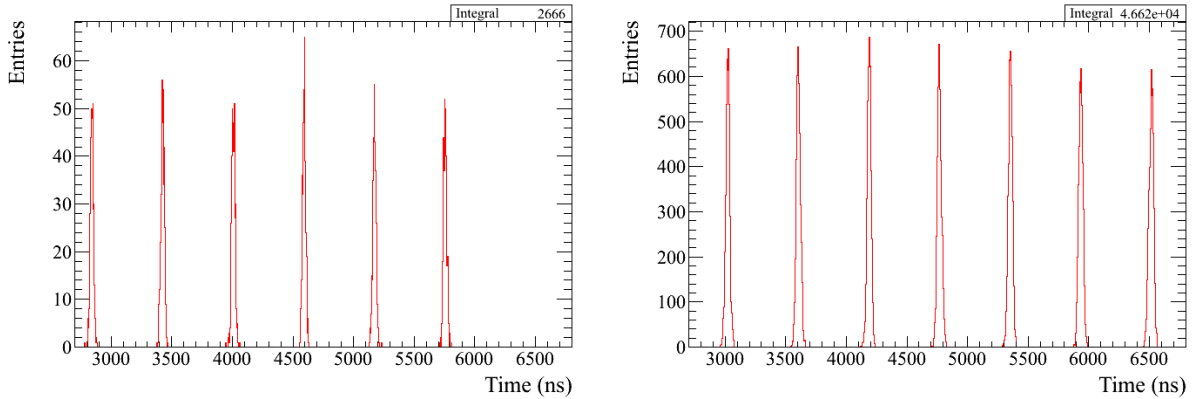


Figure 3.6: Bunch structure of selected events for Run I (0000-6000) (left) and Run IV (8895-9799) (right).

The sample after the *pre-selection* is shown in Figure 3.8. At this stage, the momentum spectrum of the highest momentum positive tracks shows, as expected, a well defined peak around 600 MeV/c

⁵ The FGDs fiducial volumes dimensions are: $|x| < 874.51$ mm, $|y - 55| < 874.51$ mm, and $136.875 < z < 446.955$ mm (FGD1) and $1474.045 < z < 1806.955$ mm (FGD2).

⁶ A horizontal cluster is a cluster in a MicroMegas column.

Table 3.2: Central bunch time (in ns) for the different run periods. For Run I MC, only the first 6 bunches are filled.

ND280 runs	Bunch 1	Bunch 2	Bunch 3	Bunch 4	Bunch 5	Bunch 6	Bunch 7	Bunch 8
0000-6000	2839.70	3423.50	4005.40	4588.60	5172.20	5754.60	N/A	N/A
6000-7000	2853.95	3444.15	4030.41	4620.34	5180.28	5770.12	6343.77	6924.67
7000-8000	3019.11	3597.74	4180.73	4763.93	5346.49	5927.83	6508.5	7093.56
8000-8550	3024.22	3606.11	4188.01	4769.90	5351.79	5933.68	6515.58	7097.47
8550-8800	3013.55	3597.55	4178.24	4758.78	5338.21	5927.31	6505.71	7086.80
8895-9799	3014.69	3600.57	4178.89	4764.24	5342.35	5931.73	6506.37	7090.15
Monte Carlo	2750.20	3332.00	3914.70	4497.00	5078.40	5659.70	6243.40	6824.20

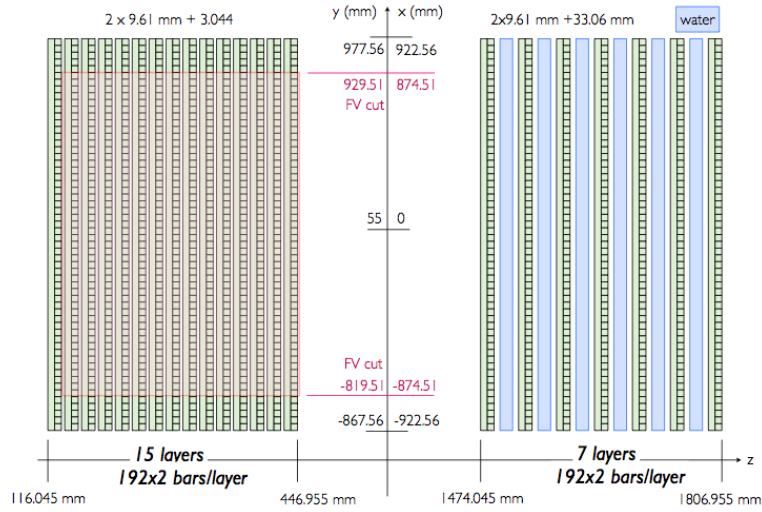


Figure 3.7: Scheme of FGD1 and FGD2 fiducial volumes.

coming from the ν_μ beam interactions. It is important to notice the presence of a peak below 300 MeV/c, mainly composed by μ^- and e^- that are clearly mis-identified as positive tracks. This happens when there are “backwards” tracks⁷, because if T_{start} and T_{stop} are very close, the reconstruction is not able to distinguish between the start and the end point of the track and flips the charge. However (see Figure 3.8 top-right) μ^- and e^- are tagged as Out Of Fiducial Volume (OOFV) because they are not generated in the FGDs FV. They are rather generated either in the ECal or in Magnet going then backward and stopping in FGDs FV. If rejecting OOFV e^- is possible via the PID, I must remark that some of mis-reconstructed μ^- will in any case remain in the final sample.

⁷ Are called “backwards” tracks all the tracks with an opposite direction respect to the beam direction.

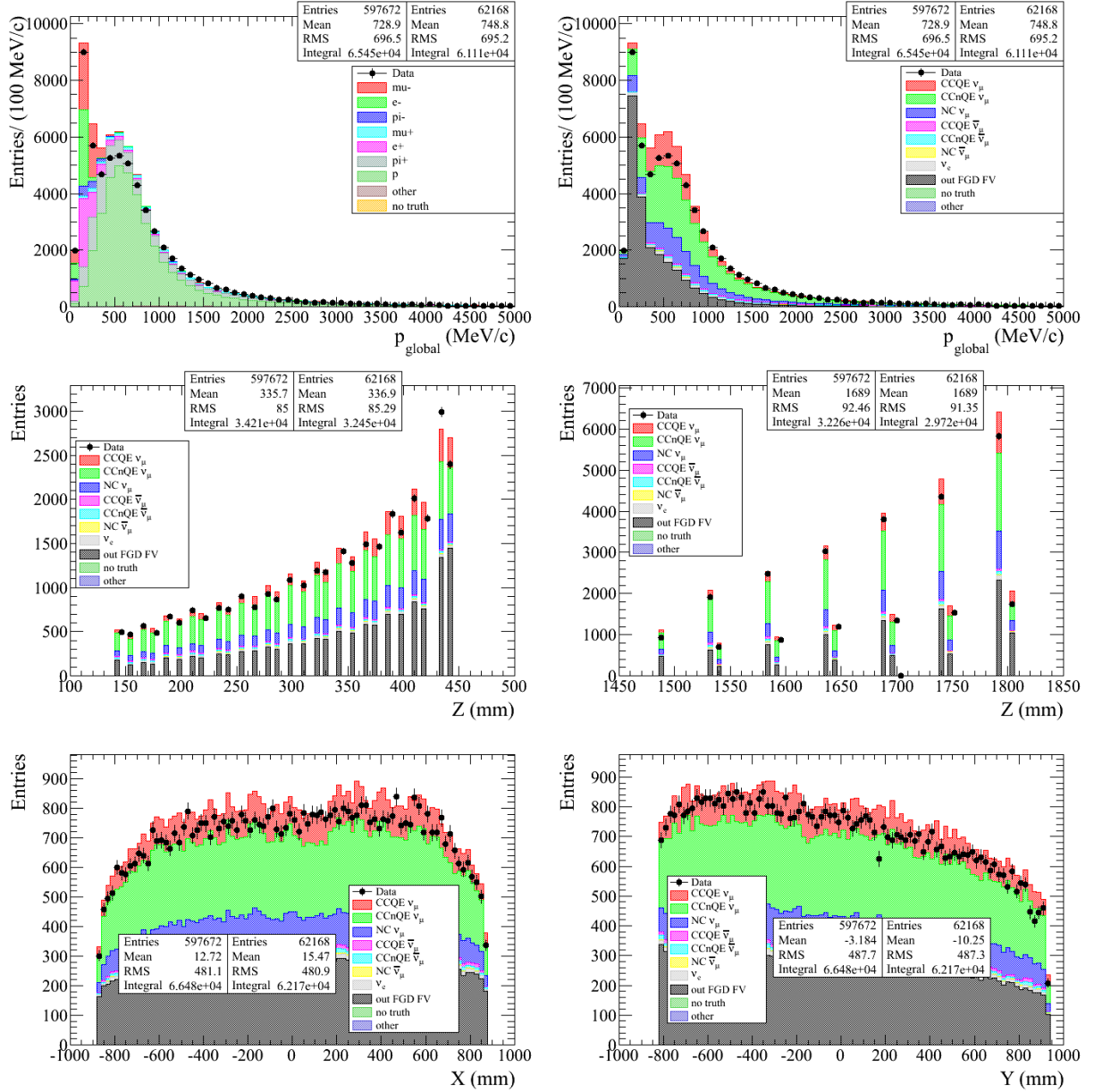


Figure 3.8: Sample after the *pre-selection*. Top: the momentum spectrum of the most energetic positive tracks. The MC sample is stacked and broken down according to final state particle type (left) and kind of reaction (right). Middle: the z coordinate of the reconstructed neutrino interaction point in FGD1 (left) and FGD2 (right). Bottom: the x (left) and y (right) coordinate of the reconstructed neutrino interaction point.

3.6 The μ^+ identification in the ND280 Tracker

The *pre-selection* leads to the result showed in Figure 3.8 that is a clean sample of neutrino (anti-neutrino) events in both FGDs FV, dominated by ν_μ interactions with either a pion or a proton in the final state identified as the most energetic positive track. As said before, the main challenge of

this analysis is then to select μ^+ coming from the $\bar{\nu}_\mu$ CC interactions, reducing as much as possible the ν_μ background. This result can be achieved by using a PID selection in the ND280 Tracker, and combining the information coming from the TPC and the ECal. In this way, since the TPC PID alone is not able to select μ^+ with an adequate purity, it is necessary to exploit the differences between MIP and shower particles (electrons and hadrons) to distinguish μ^+ from protons, pions and electrons. In this section will be discussed both the TPC and the ECal PID and how these tools are used in the anti-neutrino analysis.

3.6.1 TPC PID and one TPC track multiplicity

The PID in the TPC is based on the measurement of the truncated mean of the ionization loss (C_T), by the charged particles crossing the TPC gas. The TPC PID performances have been detailed in [125, 126] and TPC PID is used in all the ND280 tracker based analyses to select muons, electrons or protons. The distributions of the truncated mean versus the reconstructed momentum in the TPCs for negative and positive tracks starting in the FGDs FV are shown in Figure 3.9. To perform

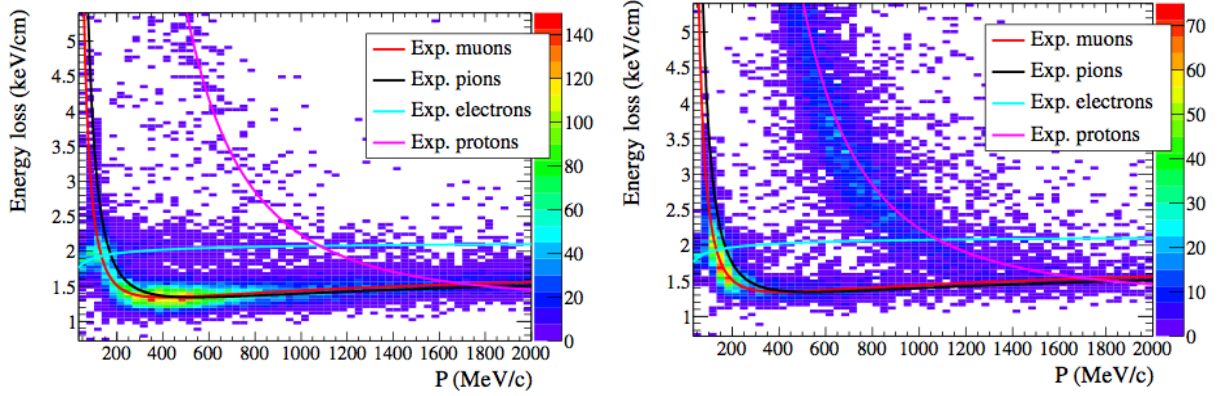


Figure 3.9: Distribution of the TPC ionization loss as a function of the TPC momentum for the candidate lepton track starting in the FGD FV, with superimposed the expected curves for muons, electrons and protons for negative (left) and positive (right) tracks [127].

the TPC PID, a pull value is computed as follow [125]:

$$\delta_i = \frac{C_T^{\text{meas}} - C_T^{\text{exp}}(i)}{\sigma^{\text{exp}}(i)}, \quad (3.7)$$

where $i = (\mu, e, \pi, p)$, $C_T^{\text{exp}}(i)$ is the expected energy loss for the particle i ⁸ and $\sigma^{\text{exp}}(i)$ is the deposited energy resolution. The $\delta(i)$ is computed for each TPC segment of the global track (e.g. if the track crosses one TPC is computed one $\delta(i)$, if the track goes through two TPC two $\delta(i)$ are computed). The δ_i variable for $i = (\mu, \pi, p, e)$ after the *pre-selection* is shown in Figure 3.10. Moreover, using the δ_i distributions, the following likelihood can be defined:

⁸ The parametrization of the expected energy loss is given in [125] and is

$$C_T^{\text{exp}} = \frac{785 \text{ ADC}}{\beta^{2.308}} \times 6.047 - \beta^{2.308} - \log 0.00064 + \frac{1}{(\beta\gamma)^{1.359}}. \quad (3.8)$$

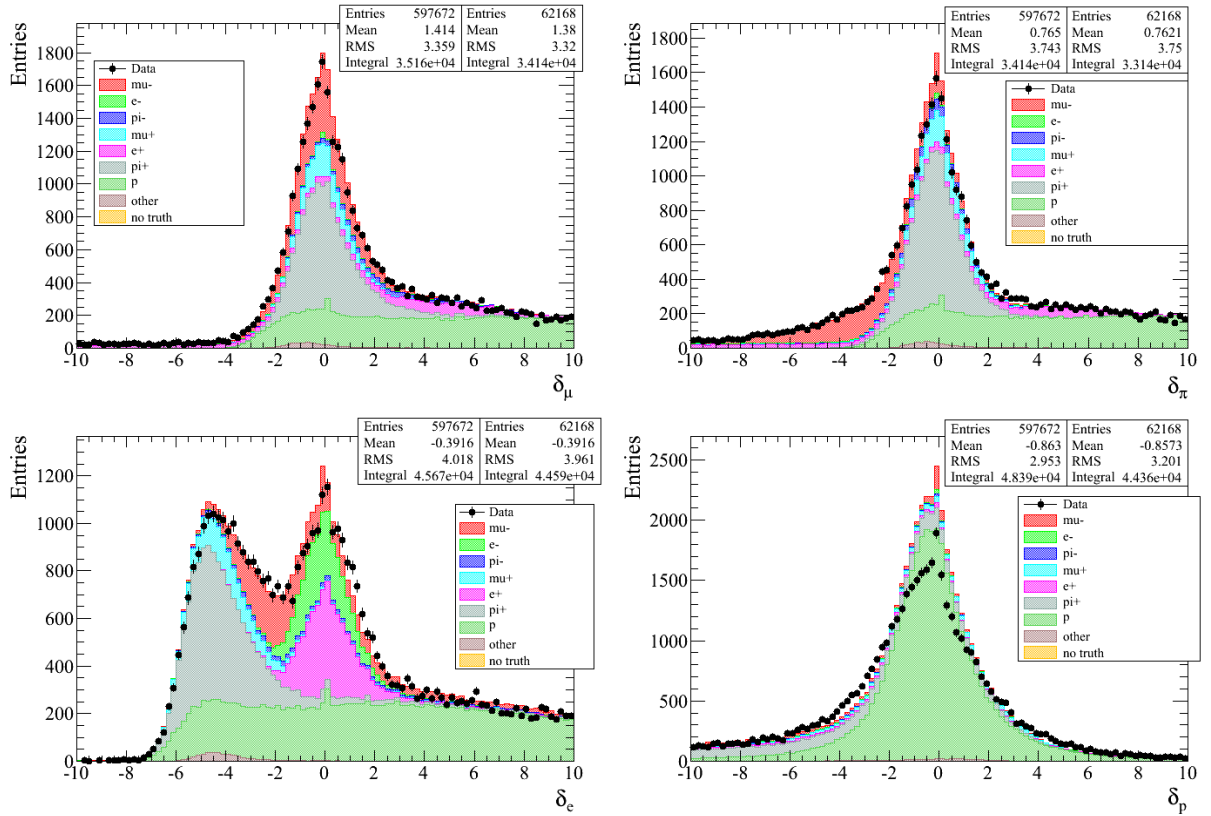


Figure 3.10: δ_i variable for different particle hypothesis: μ (top-left), π (top-right), e (bottom-left), p (bottom-right).

$$\mathcal{L}_i = \frac{P_i}{P_\mu + P_e + P_p + P_\pi} \quad (i = \mu, e, \pi, p), \quad (3.9)$$

where the probability density functions are

$$P_i = \frac{1}{\sqrt{2\pi}\sigma(i)} \exp\left[-\sum_j^{\text{TPC}_j} \frac{\delta_j(i)^2}{2}\right] \quad (i = \mu, e, \pi, p) \quad (3.10)$$

and where j covers the number of TPC segments contained in the global track. An example of \mathcal{L}_μ after the *pre-selection* is shown in Figure 3.11.

Pulls and likelihoods can be used for selecting tracks of a certain flavor. If μ^+ are selected correctly, the δ_μ distribution obtained will be a gaussian centered around zero with a sigma around one. On the contrary, if there are tracks that are not muons in the sample, the difference between the measured energy loss and the expected one will be bigger causing a change in the pull shape. Nevertheless, μ and π are indistinguishable because they have similar energy loss and the TPC C_T resolution⁹ is not good enough to evaluate this difference. Furthermore, in the momentum region above 800 MeV/c, where the energy loss by protons and muons is the same, protons can be mis-identified as

⁹ The C_T resolution computed for the TPCs used in the anti-neutrino analysis is about 7% for the TPC2 and 8% for TPC3.

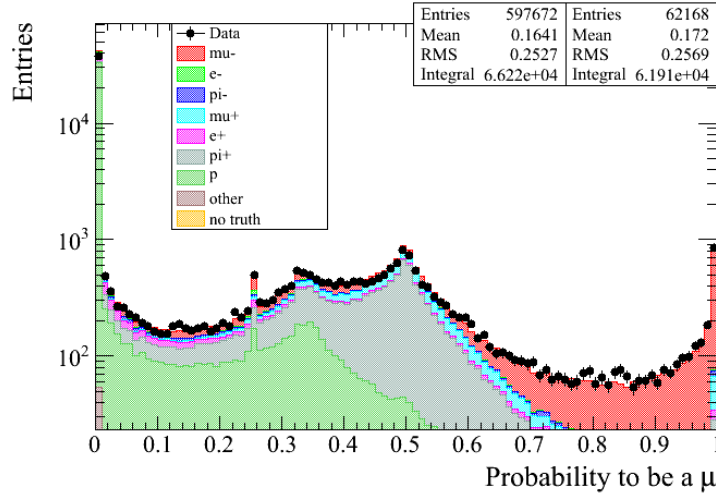


Figure 3.11: The likelihood computed in the muon hypothesis.

muon. In these two cases, the TPC PID will be not efficient enough because also pions and protons will have as muons a value of δ_μ centered around zero with a sigma around one (see Figure 3.12, bottom). The case of the likelihood is slightly more complicated, although the cuts done on the likelihood or on the pull distribution give similar results. The advantage of using the likelihood over the pull, is that the likelihood gives a nice framework for combine PID informations coming from more than one TPC.

In the anti-neutrino analysis, the TPC PID is performed as follows using the likelihoods:

$$\mathcal{L}_{MIP} = \frac{\mathcal{L}_\mu + \mathcal{L}_\pi}{1 - \mathcal{L}_p} > 0.9 \quad \text{if } p < 500 \text{ MeV}/c, \quad (3.11)$$

$$0.1 < \mathcal{L}_\mu < 0.7. \quad (3.12)$$

The first cut (3.11) (shown in Figure 3.12, top-left) is used to reject the background coming from e^\pm . The second cut (3.12) (shown in Figure 3.12, top-right) rejects, when possible, the background coming from protons and from the mis-reconstructed μ^- . The most energetic tracks that fail these two cuts are shown in the center of Figure 3.12. The TPC PID cuts are optimized in order to achieve the best possible μ^+ purity with the lower loss in the selection efficiency. The momentum spectrum of the most energetic positive tracks after the TPC PID is shown in the Figure 3.13 for MC broken down by final state particle and kind of reaction. Looking at Figure 3.13 I can state that:

- in the momentum region above 800 MeV/c there is a significant difference between data and MC. This is probably due to the TPC PID for protons that unfortunately is not so good as the muons end electrons. As a consequence, the TPC proton PID will be the larger contribution to systematic error affecting my analysis (see Section 4.1.3 for further details);
- the low energy peak visible at the end of the *pre-selection* (Figure 3.8) is almost completely discarded;
- there is still a large amount of pions and protons, coming from ν_μ CC non Quasi Elastic

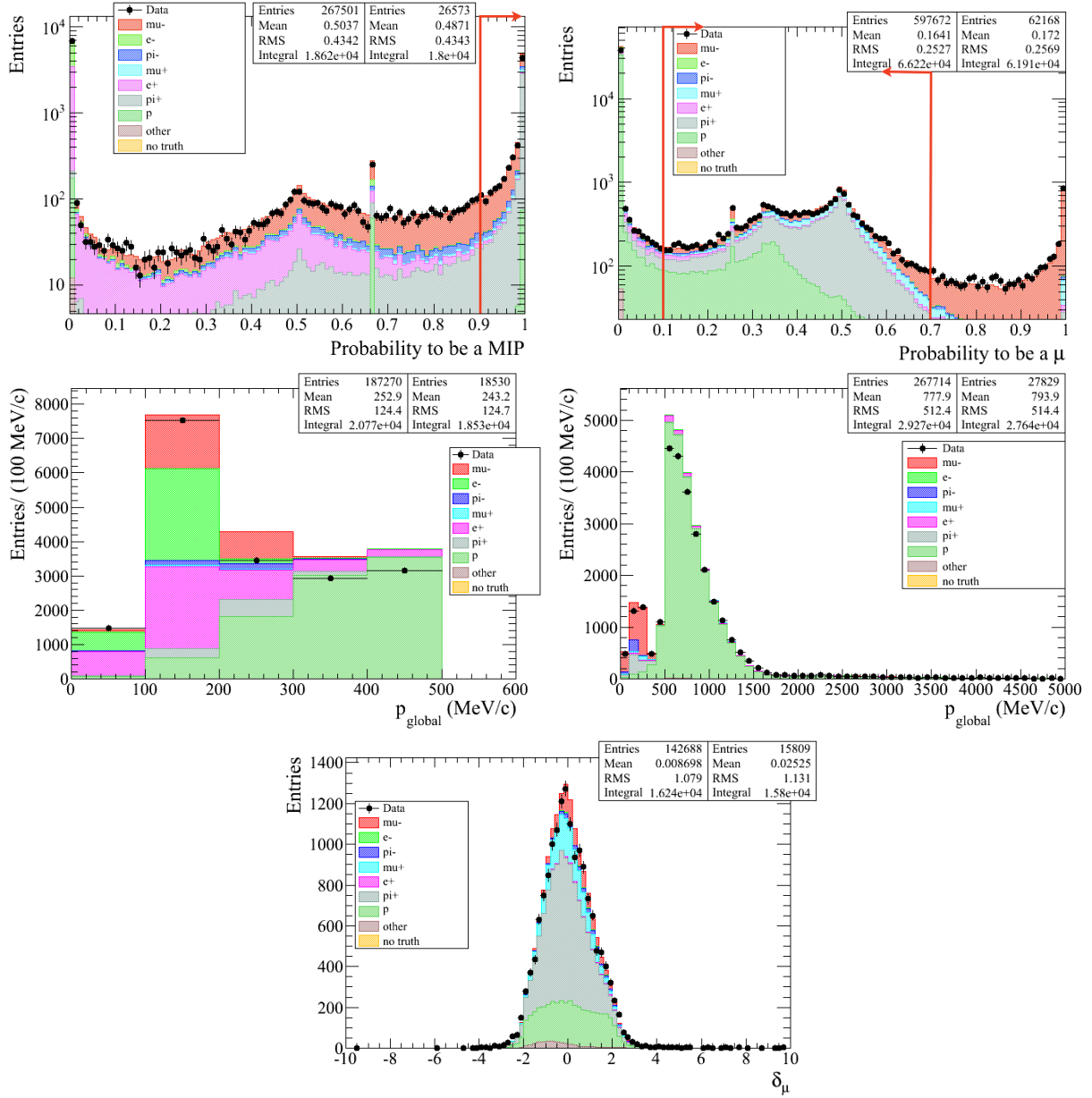


Figure 3.12: Top left: the \mathcal{L}_{MIP} plotted for tracks with $p < 500$ MeV/c. Top right: the \mathcal{L}_μ variable is plotted for all tracks selected. The cuts applied on this variables are shown with the red arrow. Middle left: most energetic positive tracks rejected by the cut (3.11). Middle right: most energetic positive tracks rejected by the cut (3.12). Bottom: the δ_μ distribution after the cuts (3.11) and (3.12).

interactions (CCnonQE) that is CC1 π , Deep Inelastic Scattering (DIS), etc... Such reactions produce a final state characterized by more than one charged particle that can enter the TPC as shown in 3.14.

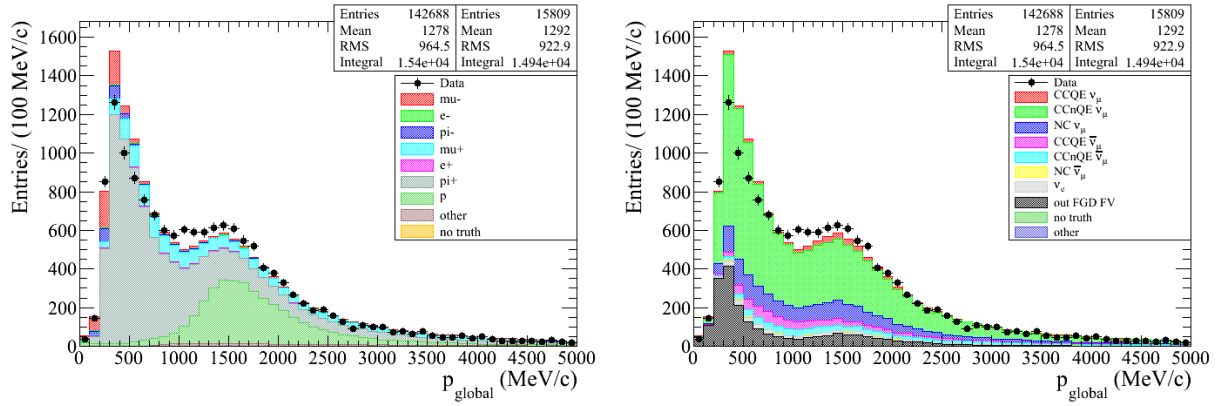


Figure 3.13: Momentum spectrum of the most energetic positive tracks after the TPC PID.


 Figure 3.14: Left: CC1 π interaction. Right: DIS interaction. In both cases, more than one positive charged particle in the final state are produced.

To enhance the $\bar{\nu}_\mu$ sample and reject as much background coming from ν_μ CCnonQE interactions as possible, only events with one track crossing the TPCs are selected. By this way, the μ^+ candidate becomes the only track in the TPC and all the events with higher multiplicity of tracks (compatible with CC1 π and DIS reactions) are rejected (see Figure 3.15). The price to pay is the rejection of some $\bar{\nu}_\mu$ CCnQE interactions too. However this is the only chance to achieve an acceptable purity of $\bar{\nu}_\mu$ interactions in the selected sample. The momentum spectrum of the most energetic positive tracks after this selection is shown in Figure 3.16. As expected, the background coming from ν_μ CCnonQE is strongly reduced but the μ^+ purity of the selected sample is still not satisfactorily (around 25%). With the help of the ECal some of the remaining protons and pions can be rejected.

3.6.2 TPC-ECal Matching and ECal PID

The tracker ECals provide PID independent from the TPCs that can be used in anti-neutrino analysis to identify and reject the background coming from showering protons and pions. Since, as shown at the end of the previous section, the sole application of TPC PID causes the μ^+ purity of the selected sample to be low, in my analysis I take into account only tracks with the TPC-ECal matching¹⁰. The momentum spectrum of the most energetic positive tracks without TPC-ECal matching is shown in Figure 3.17. The largest amount of tracks with no ECal matching is concentrated in the low energy region. The main reason is that the majority of tracks below 300 MeV/c cannot reach the ECal. It is also important to notice that there are more tracks with vertex

¹⁰Tracks with the TPC-ECal matching are TPC's tracks which enter the ECal.

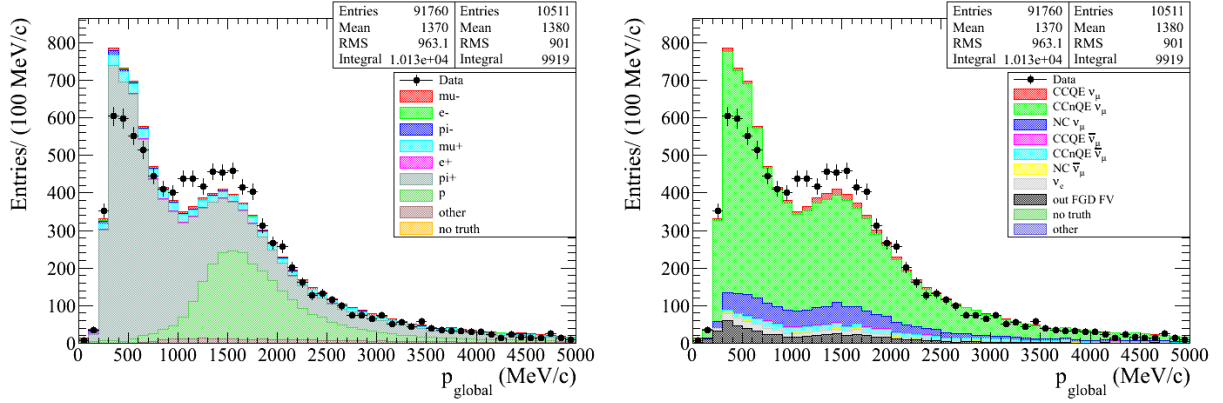


Figure 3.15: Momentum spectrum of the most energetic positive tracks rejected from the one TPC track selection.

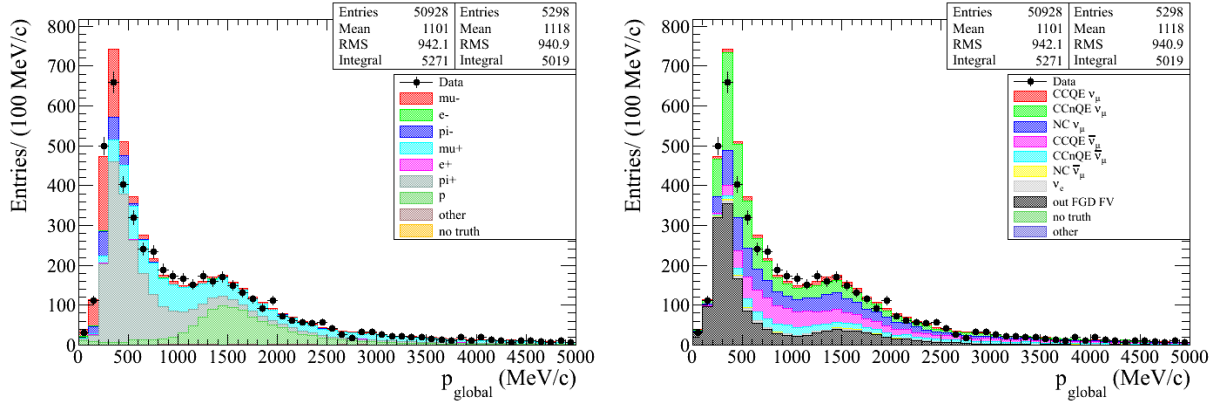


Figure 3.16: Momentum spectrum of the most energetic positive tracks after the one TPC track selection.

in FGD1 with no matching (Figure 3.17, bottom-left) than tracks with vertex in FGD2 with no matching (Figure 3.17, bottom-right). This can be explained by the fact that tracks with vertex in FGD1 have more probability to enter the barrel ECal (BrECal) than downstream ECal (DsECal), while tracks with the vertex in FGD2 mainly enter the DsECal and, as it will be shown in the Section 4.1.9, the DsECal has a better matching efficiency respect to the BrECal. The momentum spectrum of the most energetic positive tracks with ECal matching is shown in Figure 3.18. In Figure 3.19 it is also shown the selected sample for each ECal module (TPC-DsECal and TPC-BrECal matching). To perform the ECal PID, two discriminators [128] are used:

- MIP-EM LLR: discriminator designed to separate e^\pm/γ from μ^\pm ;
- MIP-PION LLR: discriminator designed to separate showering π^\pm from μ^\pm .

These discriminators are formed using the Log Likelihood Ratio (LLR) method. For each ECal cluster, the following variables are computed based on the cluster charge distribution and the shape of the cluster, they are:

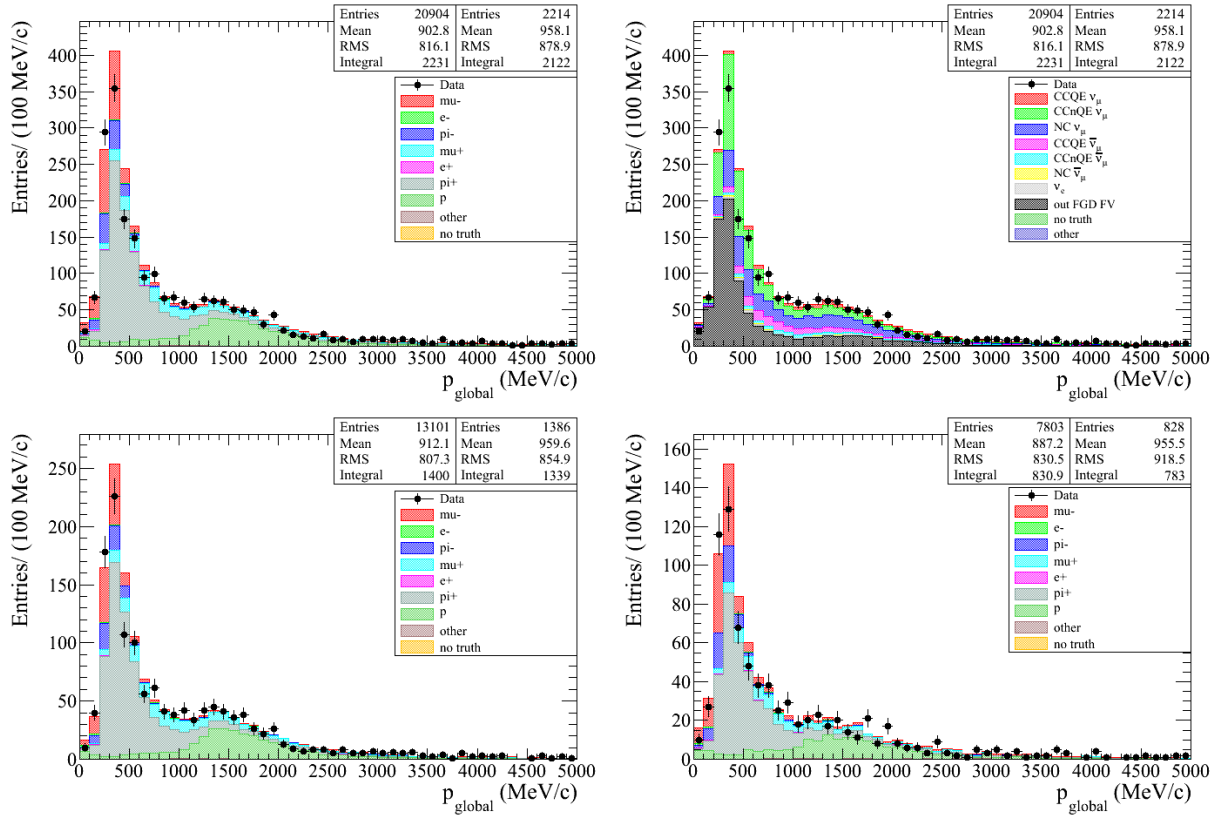


Figure 3.17: Top: Momentum spectrum of the most energetic positive tracks without TPC-ECal Matching. Bottom: the sample of tracks without the TPC-ECal matching is divided in tracks with vertex in FGD1 (left) and tracks with vertex in FGD2 (right).

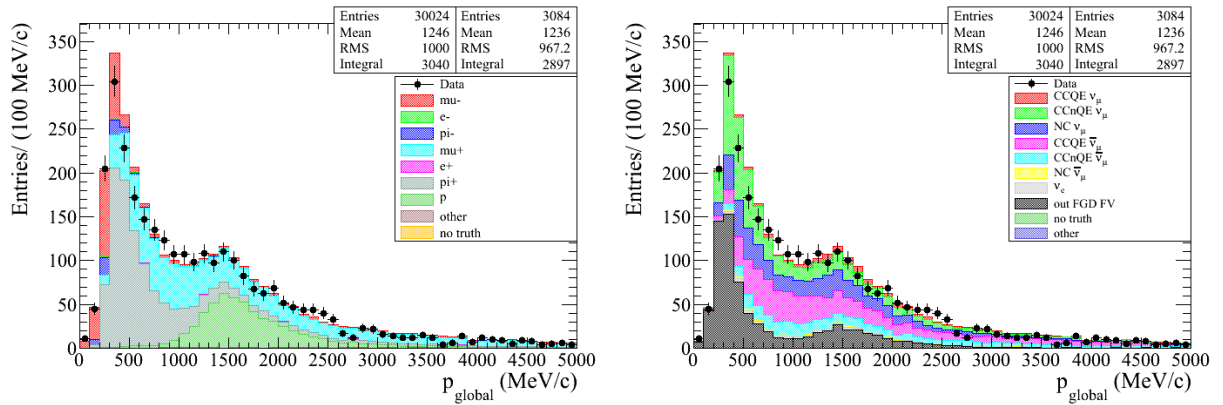


Figure 3.18: Momentum spectrum of the most energetic positive tracks with the TPC-ECal matching.

- *Circularity*: gives a measure of how round a cluster is. This variable separates short-and-fat (shower-like) clusters from long-and-thin (track-like) clusters.

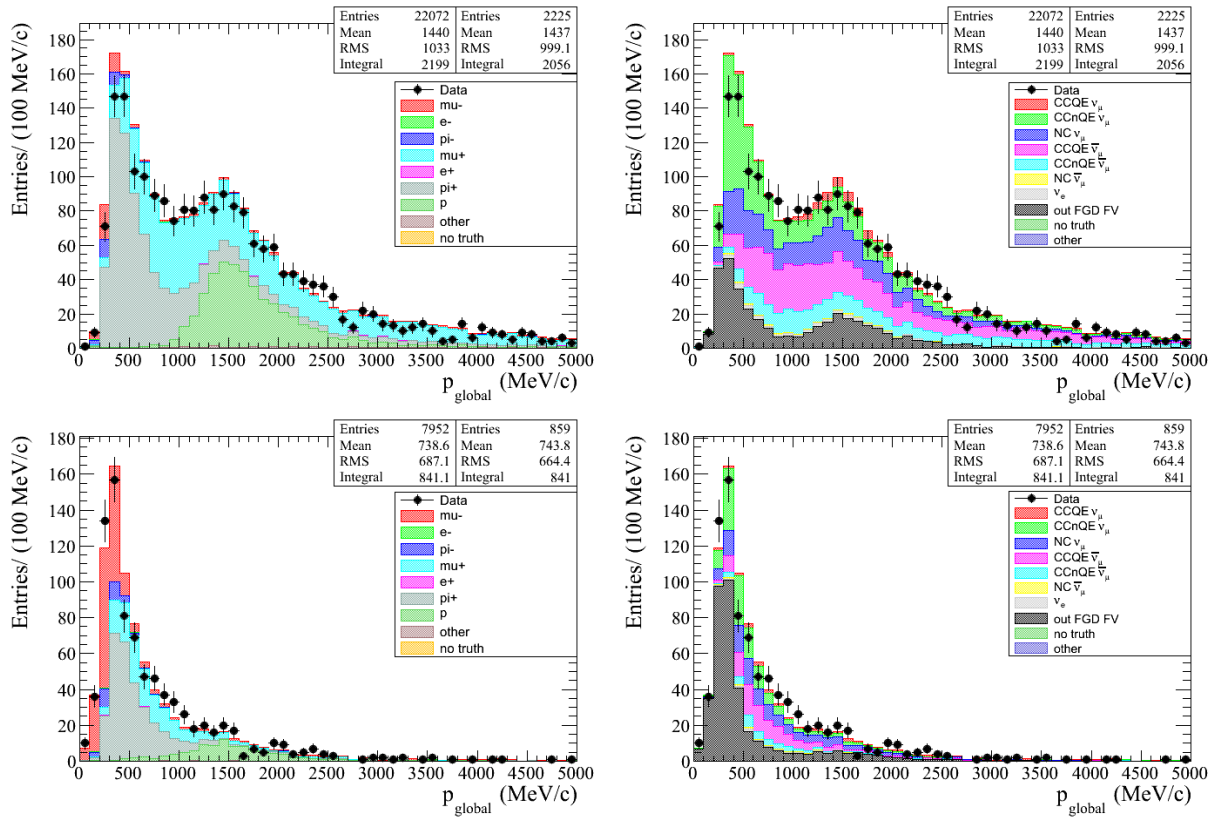


Figure 3.19: Top: Momentum spectrum of the most energetic positive tracks with the TPC-DsEcal matching. Bottom: Momentum spectrum of the most energetic positive tracks with the TPC-BrEcal matching.

- *QRMS*: is the standard deviation of the hit charges in the cluster. The hit charges in the cluster is divided by the mean of the hit charges to produce a dimensionless quantity that is independent of the overall charge scale. Electromagnetic showers tend to have larger QRMS than MIP-like muons.
- The total charge in each ECal layer is computed. The *Truncated Max Ratio* is the ratio of charge in the highest and lowest charge layers. Before computing the change per layer, the highest and lowest charge hits are removed to reduce the sensitivity to noise or saturated channels.
- *Front Back Ratio*: is a measure of the dE/dx along a track. It is defined as the total charge in the back quarter divided by the total charge in the front quarter. It is sensitive the the dE/dx profile of stopping tracks. But also discriminates electrons from muons as showering tend to deposit most of their charge at the front end of a cluster.

Particle gun MC¹¹ is used to generate probability density function (PDFs) for each particle type and variable. The likelihood ratio $\lambda(x)$ is defined as:

$$\lambda(x) = \frac{P(\vec{x}|H_0)}{P(\vec{x}|H_1)}, \quad (3.13)$$

where \vec{x} are the set of low level variables and H_0 and H_1 the two hypothesis (MIP, showering electrons or MIP, showering pions). The log likelihood is:

$$\ln |\lambda(x)| = \ln |P(\vec{x}|H_0)| - \ln |P(\vec{x}|H_1)|. \quad (3.14)$$

If the simplifying assumption that all input variables are independent is made, the PDF can be factorized:

$$|P(\vec{x}|H_0)| = \prod_i^N |P(x_i|H_0)|. \quad (3.15)$$

The resulting MIP-EM LLR and MIP-PION LLR are shown in Figure 3.21. As can be seen from

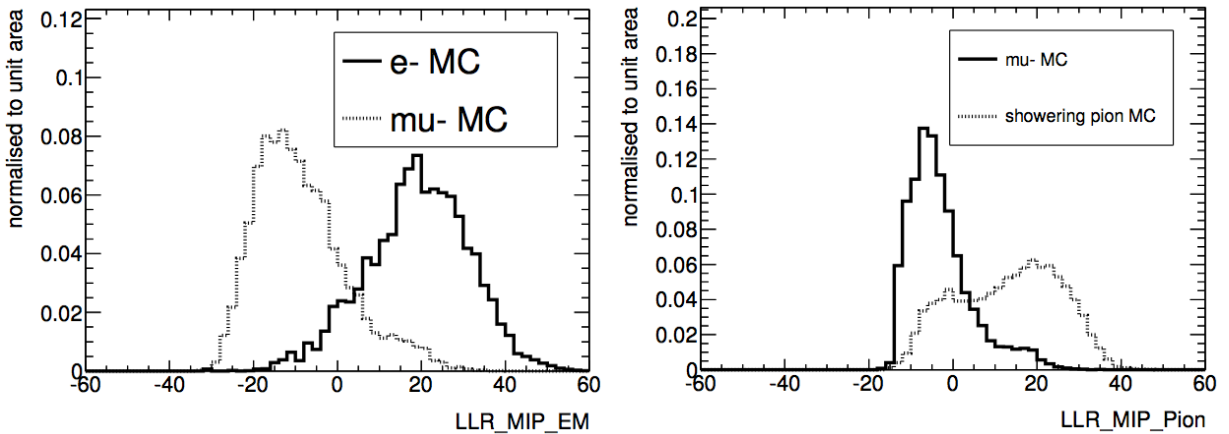


Figure 3.20: LLR discriminators shapes with the particle gun MC: MIP-EM LLR (left) and MIP-PION LLR (right).

these plots, two peaks are expected: a peak at $\lambda(x) < 0$ for MIP particles and a peak at $\lambda(x) > 0$ for showering particles. In my analysis the cuts applied on these two discriminators are:

$$\text{MIP-EM LLR} < -10 \quad (3.16)$$

$$\text{MIP-PION LLR} < -5 \quad (3.17)$$

and are shown in Figure 3.21. As for the TPC PID, these cuts are optimized to improve as much as possible the μ^+ purity.

¹¹The particle gun is a MC tool used to study the detector response to a specific kind of particles.

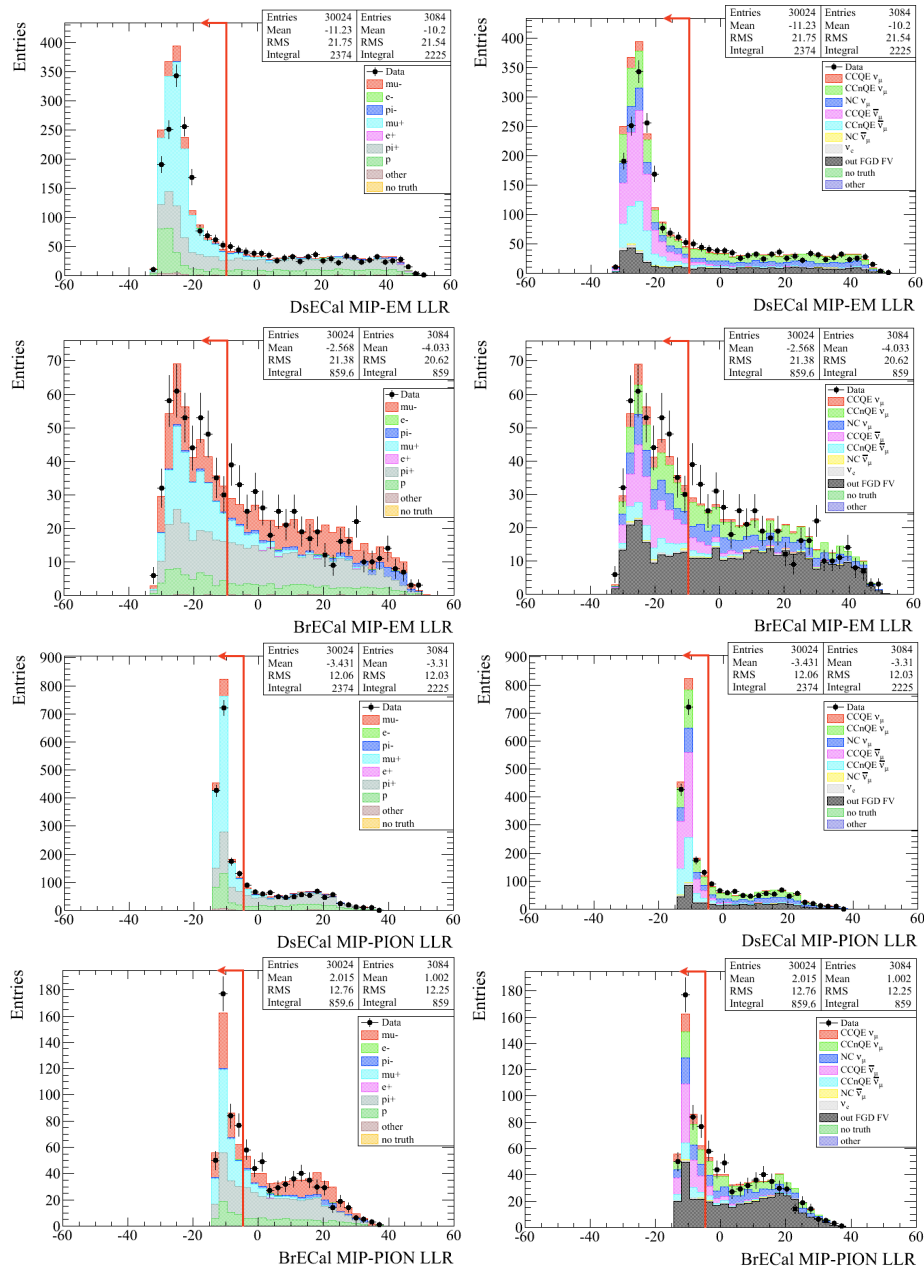


Figure 3.21: LLR discriminators (in Ds-ECal and Br-ECal) for the selected sample of highest energy positive tracks.

3.7 Final sample and selection summary

Figure 3.22 shows the event display of two Run IV events which pass the complete selection criteria. The anti-muon selection developed yield a sample that is 53% pure μ^+ with and an efficiency of $\sim 50\%$, where the efficiency is relative to the μ^+ contained in the sample at the end of the *pre-*

selection:

$$\text{efficiency} = \frac{\text{selected } \mu^+}{\mu^+ \text{ contained in the sample after the pre-selection}}, \quad (3.18)$$

$$\text{purity} = \frac{\text{selected } \mu^+}{\text{all selected particles}}. \quad (3.19)$$

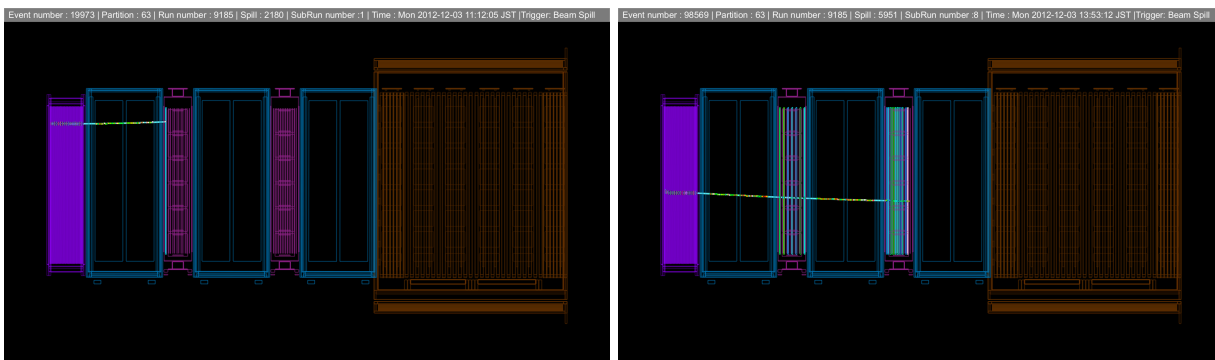


Figure 3.22: Event display of the ND280 basket plus the P0D ECal. Left: data event that pass the selection with the vertex in FGD2. Right: data event that pass the selection with the vertex in FGD1.

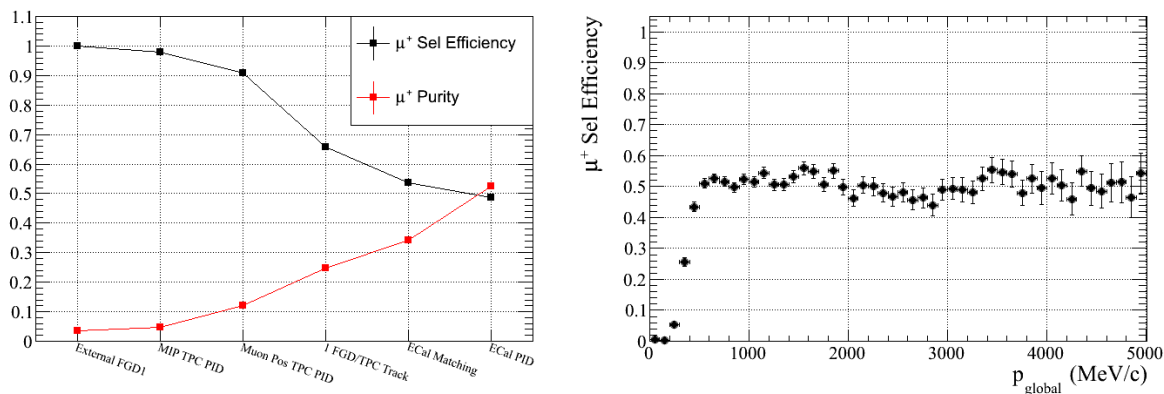


Figure 3.23: Left: Efficiency and purity vs cuts applied in the μ^+ selection. Right: μ^+ selection efficiency versus momentum.

In the Figure 3.23 is shown the effect of the μ^+ selection and is possible to figure out that:

- the efficiency is strongly reduced by the one TPC track multiplicity cut. This is due to the rejection of μ^+ coming from $\bar{\nu}_\mu$ CCnonQE interactions;
- the effect of the selection on the μ^+ momentum spectrum is almost flat above 500 MeV/c except in the region below 500 MeV/c where there are few μ^+ and the TPC-ECal matching is not efficient.

The kinematic spectra of the final selected sample are shown in Figure 3.24 and 3.25. The mean value of data/MC ratio for the momentum spectrum in the range $0 < p < 5$ GeV is:

$$\overline{\text{data}/\text{MC}}_{0 < p < 5 \text{ GeV}} = 0.95 \quad (3.20)$$

and for $0 < \cos(\theta) < 1$ I have:

$$\overline{\text{data}/\text{MC}}_{0 < \cos(\theta) < 1} = 0.93. \quad (3.21)$$

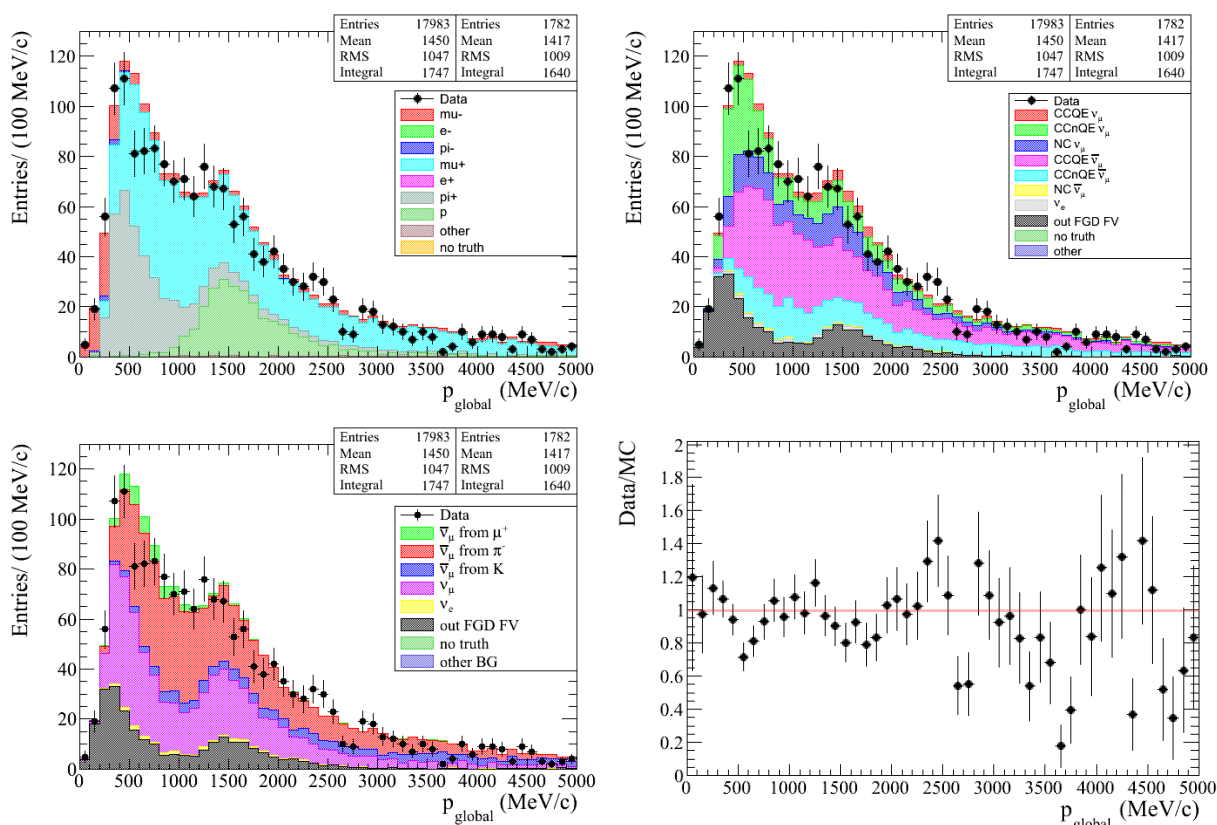


Figure 3.24: The final selected sample. The MC is broken down according to final state particle (top-left), kind of reaction (top-right) and neutrino parent (bottom-left). In the plot on the bottom-right the data/MC ratio is shown for the momentum spectrum.

With the selection criteria developed, it is possible to reject more than 98% of the background observed after the *pre-selection* (see Figure 3.26). In Table 3.3 is shown the events reduction in both data and MC. It is important to notice how the relative ratio of events surviving each cut agrees very well between data and MC.

3.8 Analysis efficiency and purity

Figures 3.24 and 3.25 show the kinematic spectra of the $\bar{\nu}_\mu$ CC sample. In these plots, the MC is broken down by the final state particle type, the neutrino interaction type and neutrino parent type

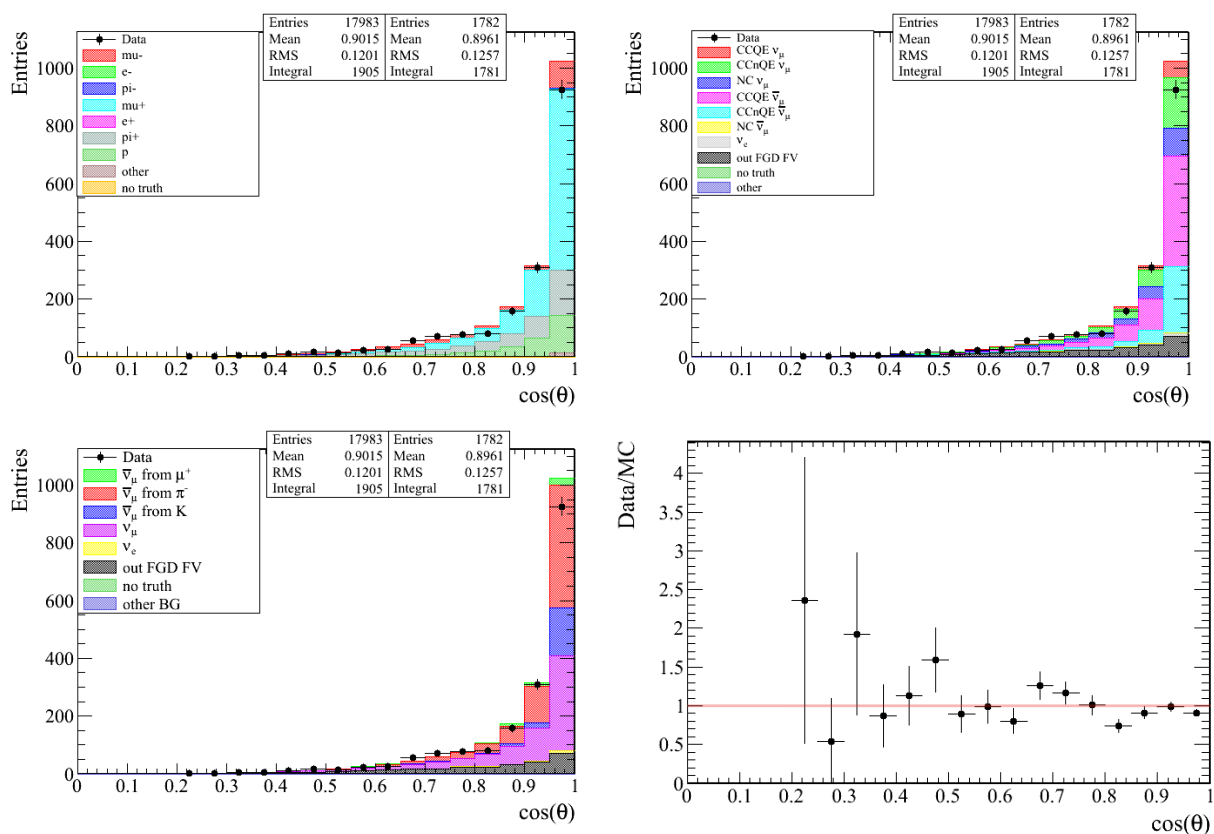


Figure 3.25: The final selected sample. The MC is broken down according to final state particle (top-left), kind of reaction (top-right) and neutrino parent (bottom-left). In the plot on the bottom-right the data/MC ratio is shown for the $\cos(\theta)$ spectrum.

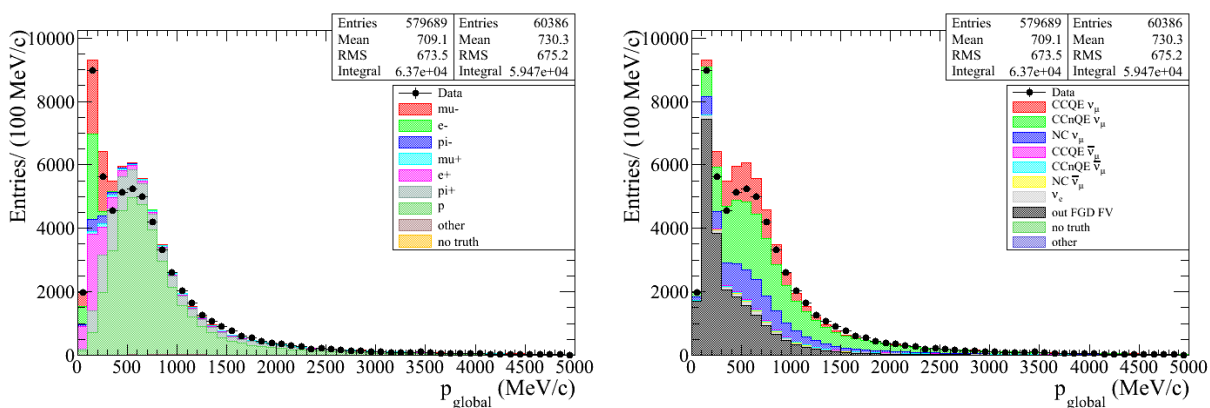


Figure 3.26: Events failing the μ^+ selection.

and the composition of the sample is detailed respectively in Tables 3.4, 3.5 and 3.6.

With the developed selection criteria it is possible to obtain a 50% pure final sample of $\bar{\nu}_\mu$ CC inclusive interactions (33.2% of $\bar{\nu}_\mu$ CCQE + 17% of $\bar{\nu}_\mu$ CCnonQE). It should be noted that these

Table 3.3: Reduction in the number of events selected in data and MC. The MC numbers are scaled to the data POT.

Cut	Events		Relative ratio %	
	Data	MC	Data	MC
<i>pre-selection</i>	62168	66470	100.0	100.0
TPC PID: $\mathcal{L}_{MIP} > 0.9$	43638	45690	70.2	68.7
TPC PID: $0.1 < \mathcal{L}_\mu < 0.7$	15809	16242	36.2	35.5
1 TPC Track multiplicity	5298	5528	33.5	34
TPC-ECal matching	3084	3234	58.2	58.5
ECal PID	1782	1906	57.8	58.9

Table 3.4: Composition of the final selected sample broken down by final state particle type.

Category	Composition (%)	MC expected events
μ^-	10.4	198.2
e^-	0.02	0.46
π^-	0.34	6.1
μ^+	52.6	1002
e^+	0	0
π^+	21.15	403
p	14.71	280.4
other	0.8	15.4

Table 3.5: Composition of the final selected sample broken down by interaction type.

Category	Composition (%)	MC expected events
$\bar{\nu}_\mu$ CCQE	33.2	632.8
$\bar{\nu}_\mu$ CCnonQE	17	323.3
$\bar{\nu}_\mu$ NC	0.38	7.3
ν_μ CCQE	5.5	104.3
ν_μ CCnonQE	17	324.6
ν_μ NC	11.4	218
ν_e	1	20.4
Out FGDs FV	14.4	275

numbers are based on the NEUT reaction code and not on the particles that are ejected from the nucleus (Final State Interaction).

The $\bar{\nu}_\mu$ selected come from the decay of μ^+ , π^- and K in the decay tunnel. $\bar{\nu}_\mu$ coming from μ^+ are produced by the same π^+ producing the ν_μ beam and will mainly populate the low energy region. $\bar{\nu}_\mu$ coming from π^- and K , instead, will mainly populate the high energy region because π^- and K are directly produced by the proton beam interactions with the target. As described in the Table 3.6, the $\bar{\nu}_\mu$ selected come mainly from π^- ($\sim 74\%$) and K (~ 20.7) and a few percent from

Table 3.6: Composition of the final selected sample. The $\bar{\nu}_\mu$ component is broken down by neutrino parent type.

Category	Composition (%)	MC expected events
$\bar{\nu}_\mu$ from μ^+	2.7	51.3
$\bar{\nu}_\mu$ from π^-	37.37	712.1
$\bar{\nu}_\mu$ from K	10.5	200
ν_μ	34	546.8
ν_e	1.1	20.4
Out FGDs FV	14.4	275

μ^+ . The fact that in the selected sample there are few $\bar{\nu}_\mu$ coming from μ^+ is an important aspect, because it is an indication that there are also few ν_e produced from the μ^+ decay, which are one of the backgrounds in the ν_e appearance analysis.

Finally, in Figure 3.27 are shown the overall efficiency and purity achieved by the selection for the $\bar{\nu}_\mu$ CC signal. In this case, also the reconstruction efficiency is taken into account, so the efficiency and purity are defined as follow:

$$\text{efficiency} = \frac{\text{selected true CC } \bar{\nu}_\mu \text{ interactions with true vertex in FGD FV}}{\text{all true CC } \bar{\nu}_\mu \text{ interactions with true vertex in FGD FV}}, \quad (3.22)$$

$$\text{purity} = \frac{\text{selected true CC } \bar{\nu}_\mu \text{ interactions with true vertex in FGD FV}}{\text{all selected reactions}}. \quad (3.23)$$

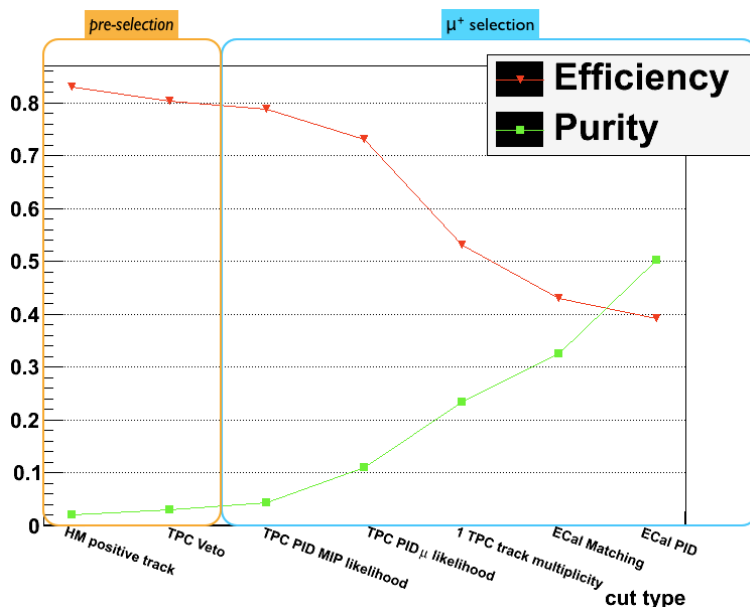


Figure 3.27: $\bar{\nu}_\mu$ CC selection efficiency and purity versus the cut applied. In this plot the are distinguished the *pre-selection* and the μ^+ selection.

The largest drop in the selection efficiency is due to the “1 TPC multiplicity track cut” that as explained reject with ν_μ CCnonQE interactions also $\bar{\nu}_\mu$ CCnonQE interactions.

3.9 The likelihood fit

To precisely measure the number of $\bar{\nu}_\mu$ selected with this analysis, it has been developed a likelihood fit on kinematics distributions. This method is based on the assumption that the MC correctly reproduces the shapes of signal and backgrounds and by fitting the MC to data, a rescaling factor for each component can be found. Notice that the variations in the shape of signal and background are not included in this section: detector, flux and cross-section systematics can vary the shape of both signal and background. These effect will be introduced in the likelihood fit in the next chapter, to achieve the final result. In this section it will be shown the description of the likelihood, the validation of the fit with toy MC and the effect of likelihood fit on the “nominal” MC.

3.9.1 Likelihood description

In Figure 3.28, the momentum spectrum of the final sample is divided between signal and background. The $\bar{\nu}_\mu$ signal, is composed by 65.7% CCQE, 33.5% of CCnonQE and less then 1% of NC interactions. The background is composed mainly of ν_μ and out of FGD FV interactions and its momentum distribution has a shape with two peaks: one around 600 MeV/c due to pions and another one around 1.5 GeV/c due to protons. Moreover, also a non negligible fraction of muons (mainly coming from out of FGDs FV interactions) is visible below 300 MeV/c.

To extract the rescaling factors, one possibility is to perform the fit directly on signal and background. In this case, since the background is composed by different sources (μ , π and p) with different kinematic spectra, it is possible to disentangle it, and fit simultaneously the signal and each background component. In this way the fit will give a better constraint on background sources and signal. Following the latter method, the PDF shapes input to the fit are (see Figure 3.29):

- $\bar{\nu}_\mu$ signal: the signal that is measured;
- background from μ : the background coming from out of FGDs FV interactions and high energy μ^- which the magnetic field cannot bend enough to allow the charge identification from the TPC;
- background from π : produced by π^+ from ν_μ CCnonQE interactions;
- background from p : as for pions also protons comes mainly from ν_μ interactions.

Table 3.7: Composition of the final selected sample broken down by input to the fit.

Category	Composition (%)	MC expected events
Signal $\bar{\nu}_\mu$	51.1	960.3
Background from μ	11.8	221.2
Background from π	21.5	404.4
Background from p	15.6	292.2

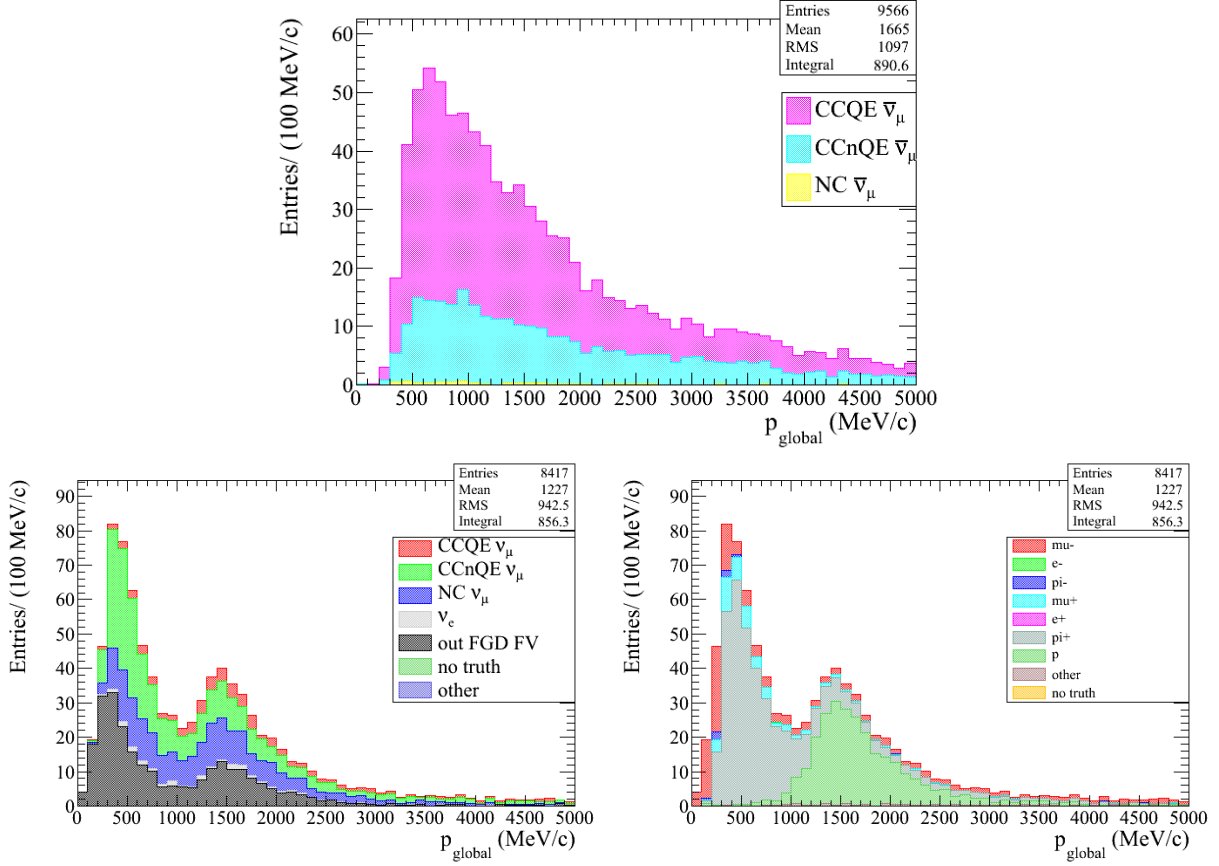


Figure 3.28: The final sample MC. Top: The MC signal is broken down by reaction type. Bottom: the MC background is broken down by reaction type and final state particle type.

The kinematics spectra for data and MC with the MC broken down by input to the fit are shown in Figure 3.30 and are detailed in Table 3.7.

The fit is performed in $(p, \cos \theta)$. The number of expected events in each bin can be written as:

$$F(p, \cos \theta) = f(\bar{\nu}_\mu)g_{\bar{\nu}_\mu}(p, \cos \theta) + \sum_i f(BG_i)g_{BG_i}(p, \cos \theta) \quad (i = \mu, \pi, p), \quad (3.24)$$

where $g_i(p, \cos \theta)$ are the PDF shapes for different components i , and $f(i)$ is the rescaling factor that will be minimized over in the fit to re-weight the MC.

The momentum and the $\cos \theta$ ranges, respectively $p \in [0, 30]$ GeV/c and $\cos \theta \in [-1, 1]$, are chosen to be the wider possible to cover all the phase space. To adopt these wide ranges in $(p, \cos \theta)$, the binning choice becomes very important, in order to avoid bins with a small number of expected events as this can bias the analysis due to Poissonian fluctuation. The criteria followed to find the most appropriate binning are:

- finer binning around the beam energy peak;
- at least 10 events per bin, because low statistic samples may show biases in the fit values.

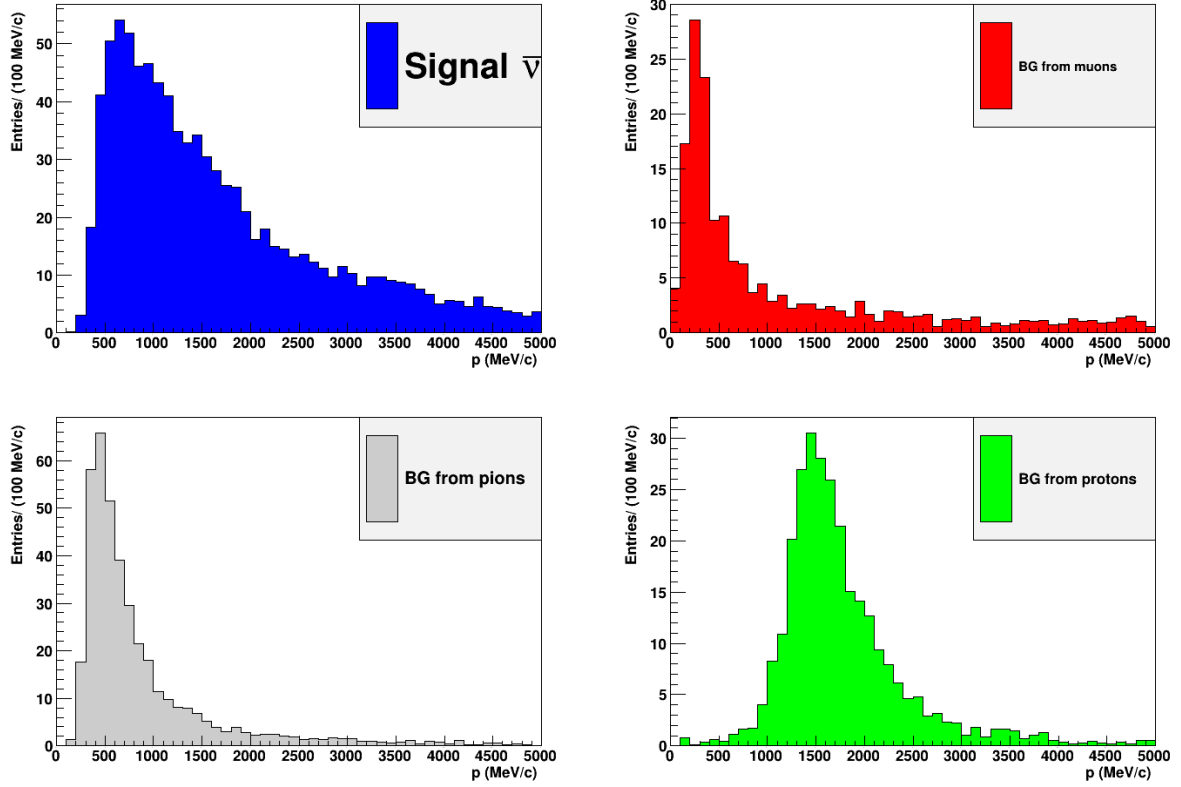


Figure 3.29: The momentum spectra of the four PDFs that are input to the fit.

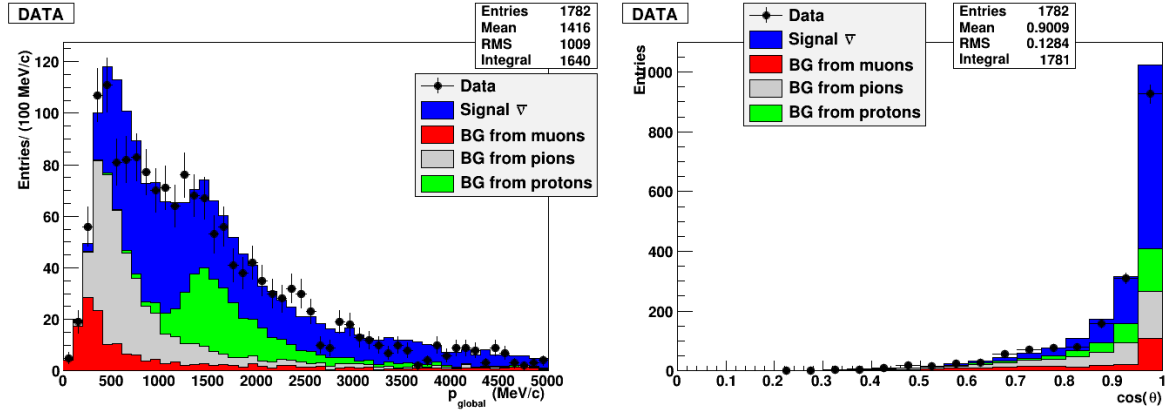


Figure 3.30: The final sample. The MC is broken down in signal and background sources.

Taking into account these two criteria, the selected binning is:

$$p = \{0, 400, 500, 600, 700, 800, 1000, 1250, 1500, 2000, 30000\}, \quad (3.25)$$

$$\cos\theta = \{-1, 0.8, 0.9, 0.95, 1\}.$$

The $(p, \cos\theta)$ final samples for data and MC with the new binning, are shown in Figure 3.31. The

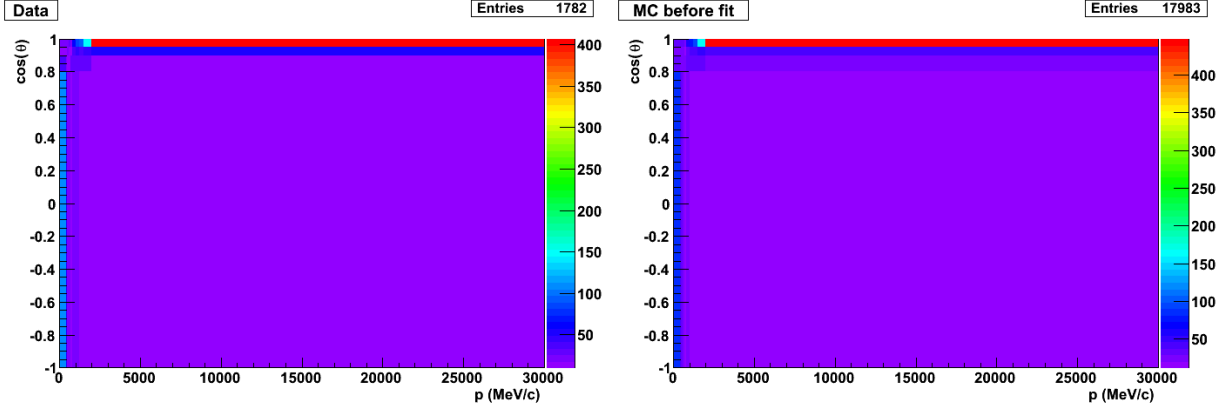


Figure 3.31: $(p, \cos\theta)$ spectrum of the selected sample for data (left) and MC (right).

log likelihood ratio is then:

$$-2 \log \mathcal{L}_{\bar{\nu}_\mu} = 2 \times \left\{ \sum_{i=1}^{10} \sum_{j=1}^4 F_{i,j} - n_{i,j}^{\text{data}} + n_{i,j}^{\text{data}} \times \log \left(\frac{n_{i,j}^{\text{data}}}{F_{i,j}} \right) \right\}, \quad (3.26)$$

where $F_{i,j}$ is the MC expectation in the bin $\{i, j\}$ and $n_{i,j}^{\text{data}}$ is the number of data entries in the bin $\{i, j\}$.

3.9.2 Validation of the fit with toy MC

In Figure 3.31, on the right it is shown the MC spectrum in $(p, \cos\theta)$ of the final sample selected before the fit. In order to validate the fit, the likelihood fit is performed on 1000 MC toys with the same POT as data and the amount of background and signal expected from the MC. Each of these toys is re-weighted by a well defined rescaling factor f_{set} . Then the MC spectrum is fitted 1000 times on each MC toy and the f_{fitted} is then evaluated. The goodness of the fit machinery is measured using the pull, defined as:

$$\text{pull} = \frac{f_{\text{fitted}} - f_{\text{set}}}{\sigma_{\text{fitted}}} \quad (3.27)$$

If the fit is not biased, the pull should have a mean value compatible with 0 and a sigma compatible with 1. In Figure 3.32 are shown the results of f_{fitted} and pulls obtained for each component setting the $f_{\text{set}} = 1$. As can be seen from these plots, only the pull computed for the background coming from protons has a sigma slightly lower than one. This means that the fit is underestimating the statistical error for this component. This is due to the binning chosen that is too large in the momentum region above 1 GeV/c where the protons background is concentrated.

3.9.3 Fit result obtained for the nominal MC

Using the likelihood defined in Section 3.9.1 the MC spectrum (Figure 3.31 right) is fitted on data spectrum (Figure 3.31 left). The obtained results are shown in Table 3.8. The fit results lead to a reduction of the signal and backgrounds coming from protons and pions, while the component coming from muons is increased. This result is in agreement with what was shown in the plot with

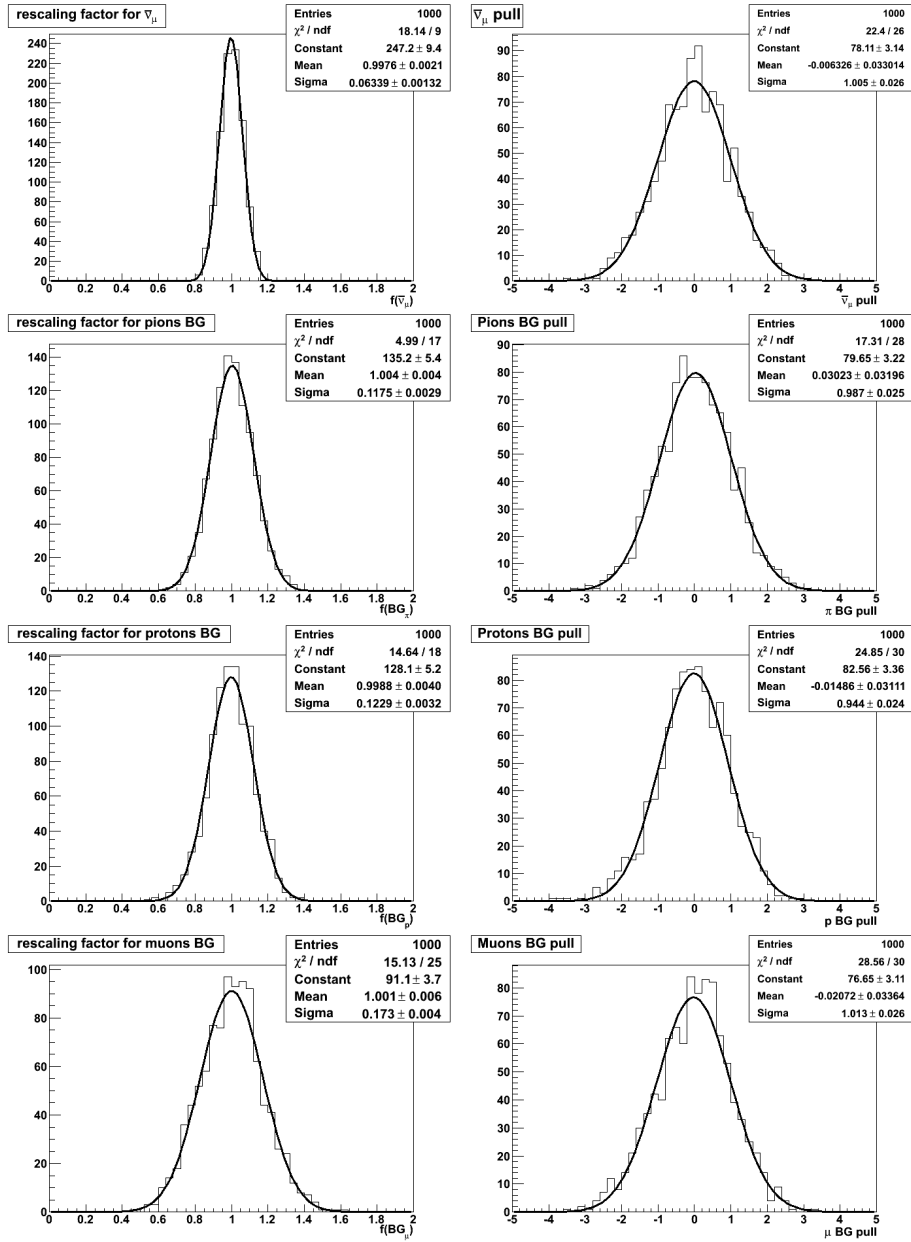


Figure 3.32: Fitted rescaling factors (left) and pulls (right) for each input to the fit for $f_{\text{set}} = 1$.

the data/MC ratio (Figure 3.24). In that plot in the low energy region the ratio data/MC is greater than 1 and this imply an increase of the muons background by the fit. On the contrary around 600 MeV/c and 1.5 GeV/c the ratio data/MC is lower than 1 and as a consequence the pion and proton background are reduced by the fit. The number of $\bar{\nu}_\mu$ events obtained with the fit is in a good agreement (inside 1σ) with the ones predicted by the nominal MC. The overall effect of the fit on the kinematics distributions and the data/MC ratios after the fit are shown in Figure 3.33. Finally in the Figure 3.34 are shown the global minimum of the likelihood found and the f contours. The contours shows an anti-correlation between the signal and either pion or proton background while,

Table 3.8: Value of the parameters for best fit. The rescaling factor and absolute number of events are indicated for each component.

	f	N_{events}
$f_{\bar{\nu}_\mu}$	0.94 ± 0.06	908.5 ± 62
f_{BG_μ}	1.36 ± 0.17	300.4 ± 38
f_{BG_π}	0.74 ± 0.11	298.7 ± 46.8
f_{BG_p}	0.86 ± 0.12	251.4 ± 36.5

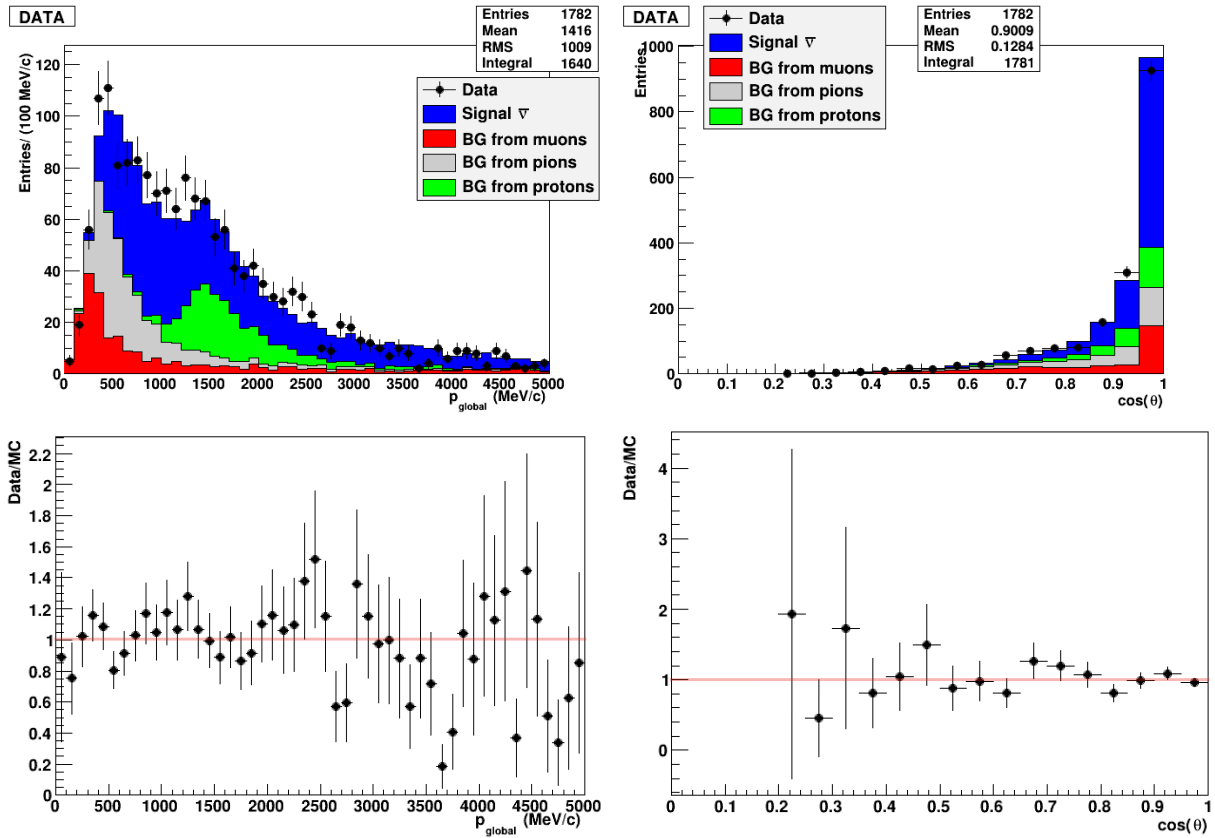


Figure 3.33: Top: The effect of the fit on the kinematics distributions. Bottom: Data/Mc ratios after the fit.

the signal and the muon background are independent each other. This happens because there is no signal in the low energy region.

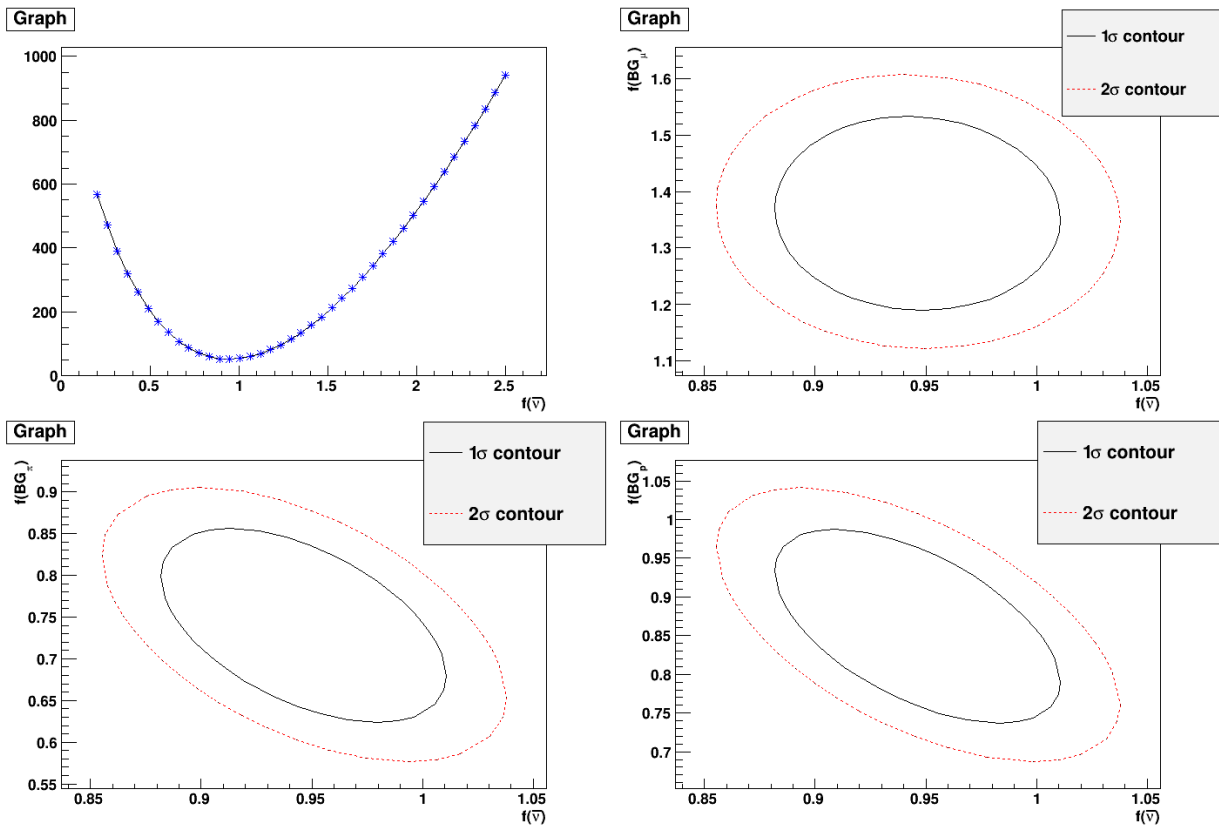


Figure 3.34: Likelihood minimum and f contours for each backgrounds component versus signal.

Chapter 4

Systematics uncertainties

In this Chapter I will present a summary of the systematic errors that affect the $\bar{\nu}_\mu$ analysis and their evaluation. The systematic uncertainties can be divided in three categories:

- detector uncertainties;
- cross section uncertainties;
- flux uncertainties.

The detector uncertainties, are due to discrepancies between data and MC occurring in the event reconstruction. The relevant ones for the $\bar{\nu}_\mu$ analysis are shown in Figure 4.1. Every source of

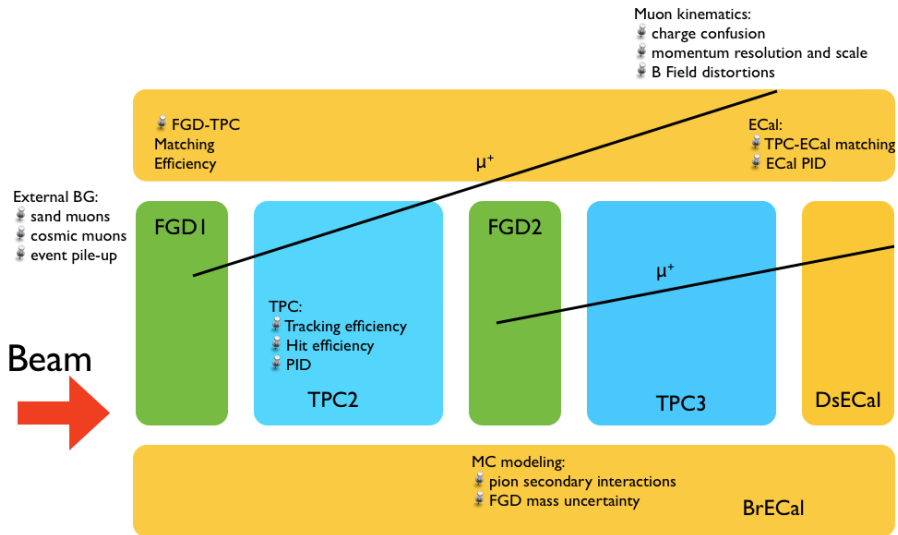


Figure 4.1: Sketch of the sub-detectors relevant for this analysis with the corresponding associated systematic components

detector systematics is evaluated independently and its effect on the selected sample will be shown. Finally the nominal MC will be corrected by taking into account all the relevant systematics and a new likelihood fit will be performed on the corrected MC. The same strategy will be used for

cross-section and flux uncertainties. As said in Section 3.1, the MC used is based on JNUBEAM flux simulation and NEUT cross section models whose predictions introduce a relative systematic error in the analysis that can be evaluated. It will be also shown how the flux and cross sections constraint provided by the ND280 ν_μ sample, can reduce these two systematic errors in the $\bar{\nu}_\mu$ analysis.

4.1 Detector response uncertainties

In this Section will be briefly introduced each detector systematic source relevant for this analysis and how their contribution is estimated. The majority of these are in common with other ND280 analyses and for this reason a group of people in T2K is involved in their evaluation. In particular, I evaluated the systematic error relative to the TPC PID for protons, that is the main systematic source for the $\bar{\nu}_\mu$ analysis. An extensive discussion on all the detector systematics errors is available in [127] and in [129]. The detector uncertainties can be divided as follow:

1. **TPC reconstruction:**

- TPC cluster efficiency;
- TPC tracking efficiency;
- TPC PID.

2. **Muon kinematics reconstruction:**

- TPC charge confusion;
- TPC momentum resolution;
- TPC momentum scale;
- magnetic field distortion.

3. **Tracker reconstruction:**

- FGD-TPC matching efficiency.

4. **Tracker-ECal reconstruction:**

- TPC-ECal matching;
- ECal PID.

5. **MC modeling:**

- pion secondary interactions;
- FGD mass uncertainty.

6. **External background:**

- sand muons;
- cosmic rays;
- event pile-up.

4.1.1 Cluster efficiency

A cluster in the TPC is defined as a collection of contiguous MicroMegas pads with charge above threshold (hit). Depending on the polar angle θ of the track, a cluster will have several hits in the same column (for tracks with $\theta \sim 90^\circ$) or in the same row (for tracks with $\theta \sim 0^\circ$). Given the beam direction (nearly horizontal), most clusters will contain several hits in the same row and in different columns. The TPC cluster efficiency is defined as the probability to find a reconstructed cluster at a given column where the particle should have produced one. A different cluster efficiency between data and MC induces a systematic error in the $\bar{\nu}_\mu$ selection criteria, mainly in the *pre-selection* when the “TPC Track quality” cut is applied. The TPC cluster efficiency is expected to be the dominant source of systematic error induced by this cut, since the effects of mis-alignment¹ and pattern recognition are expected to be small. The cluster efficiency should be driven by the amount of deposited charge in a given pad column. It is therefore natural to assume that the efficiency could be different (lower in principle) in the outermost columns due to the border effects. A particle longitudinally crossing the TPC should ideally produce 72 clusters (one per pad column) out of which 4 would be in the outermost columns (2 per MicroMegas module). It was found that the nominal MC has $\sim 3\%$ higher efficiency for outer columns and a 0.1% higher efficiency for inner columns than data.

In the case of the $\bar{\nu}_\mu$ analysis, as the TPC-ECal matching is always required in the selection criteria, two possibilities are foreseen:

- TPC-DsECal matching: the particle cross longitudinally the TPC to reach the DsECal and should produce ~ 72 clusters;
- TPC-BrECal matching: the particle is bent in the TPC by the magnetic field and should produce enough clusters to reach the BrECal.

In both these two possibilities a number larger than 17-18 TPC clusters is needed to match an ECal module. For this reason this systematic error is negligible in the $\bar{\nu}_\mu$ analysis.

4.1.2 TPC tracking efficiency

The TPC tracking efficiency describes the efficiency for the TPC reconstruction algorithm to successfully reconstruct a TPC track, and is measured on a track level basis. The efficiency for finding tracks is estimated as a function of track length, momentum, and angle using muon-like tracks induced by neutrino interactions. The TPC reconstruction efficiency is very high (statistically compatible with 100%) and shows no dependency on the number of nodes² for tracks with 16 nodes or more, for both data and MC (Figure 4.2). The efficiency starts to drop but remains above 97% for tracks with more than 10 horizontal clusters and the data and MC efficiencies are still consistent within the statistics uncertainties. The TPC track-finding efficiency for all angle, momenta, and track length is about $99.8^{+0.2}_{-0.4}\%$ for both data and MC and the relative systematic error is expected to be small.

¹ Tracks with few clusters normally cross only one MicroMegas module (except tracks crossing the cathode, but the contribution from this kind of tracks is expected to be small).

² In the ND280 reconstruction jargon a TPC node corresponds to a cluster in a MicroMegas column.

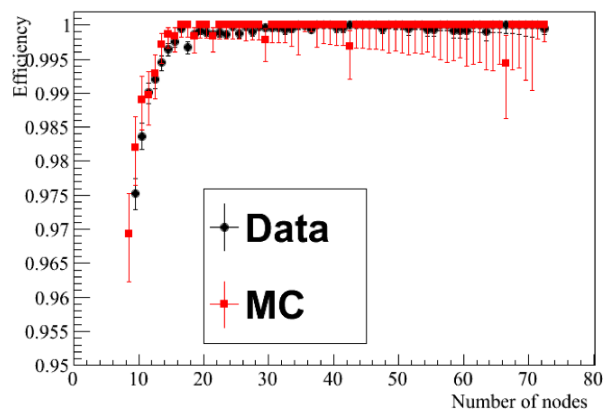


Figure 4.2: TPC tracking efficiency versus the number of horizontal clusters.

4.1.3 TPC PID

In the $\bar{\nu}_\mu$ analysis, the TPC PID is performed via likelihood, using the pull variable δ_i , defined in Section 3.6.1. Differences between data and MC in the δ_i can induce a systematic error when the TPC PID is performed in the μ^+ selection. For the $\bar{\nu}_\mu$ analysis, TPC PID systematics for muons that are selected as lepton candidates, and for protons that are partially rejected during the μ^+ selection, are of interest. Pions have an energy loss similar to that of muons and systematics for them are considered the same as those computed for the muons. Finally, since in $\bar{\nu}_\mu$ analysis it is expected a negligible fraction of electrons, their TPC PID systematics is neglected. It is important to notice that differently from the rest of the analysis, in this section, I use TPC momentum instead of global momentum³.

TPC PID systematics for muons and pions

The TPC PID systematics for the muons is computed from the difference between data and MC for a sample of sand muons⁴. An example of pulls computed according to a muon hypothesis from data and MC tracks with a TPC local momentum between 500 MeV/c and 2 GeV/c is shown in Figure 4.3. The distributions of Figure 4.3 are then grouped in momentum bins and fitted with a Gaussian distribution. In Figure 4.4 the mean of the pulls for data and MC in the sand muons sample as a function of the TPC momentum are shown. There are differences between data and MC, but the effect of these differences on the analysis is small. The width of the Gaussian distribution for the same bins is shown in Figure 4.5. Below 1 GeV/c the agreement between data and MC is good, while above 1 GeV/c the width in the MC are narrower than the one observed in the data suggesting a larger systematic error for particles with $p > 1$ GeV/c.

³ The TPC momentum comes from the TPC local reconstruction (see Section 3.3.1) and is the momentum measured by the TPC, while the global momentum comes from the global reconstruction (see Section 3.3.2) and in addition to the momentum computed in the TPC, takes into account also the energy lost by the particle in the other detectors. As a consequence, the TPC local momentum is always lower respect to the global momentum.

⁴ The so called sand muons are muons detected at ND280 coming from ν_μ interactions with the walls of the pit in the ND280 hall. Usually these muons have a high energy and cross each one of the 3 TPCs

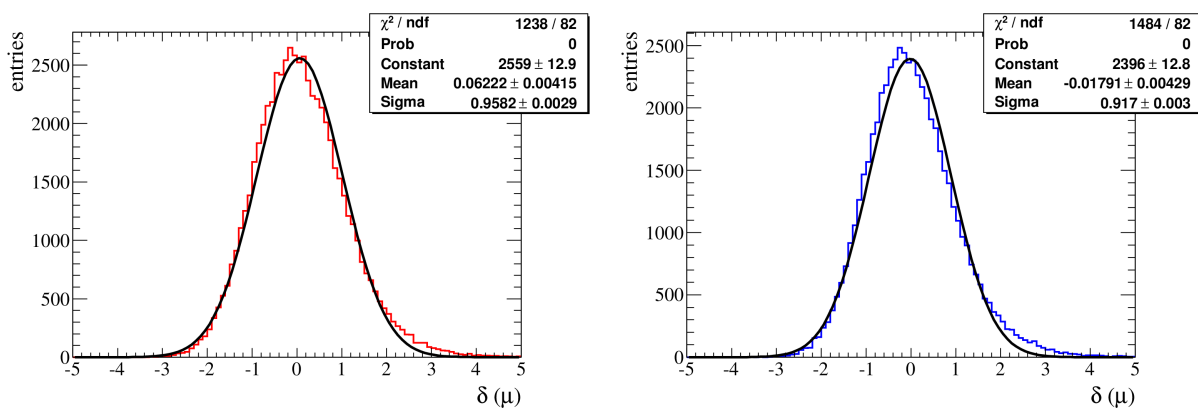


Figure 4.3: TPC muon pull in data (left) and MC (right) for tracks with TPC momentum between 500 MeV/c and 2 GeV/c in the TPC2.

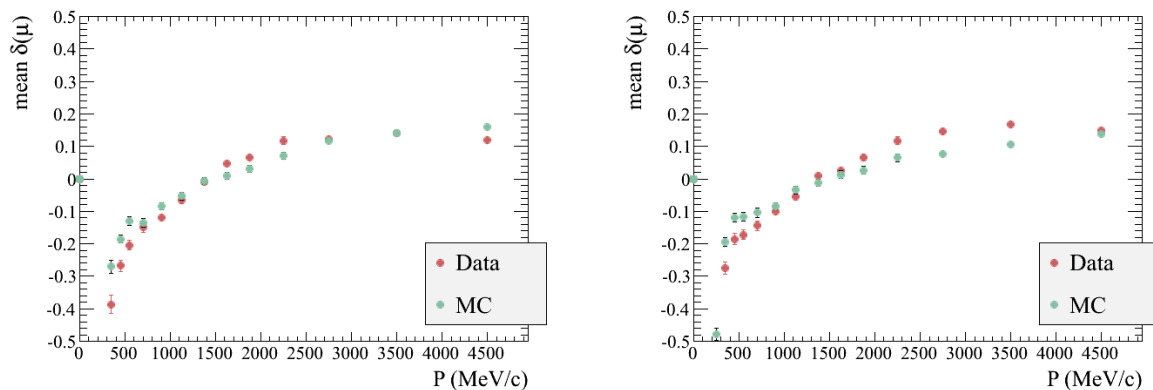


Figure 4.4: Mean of the TPC muon pull in data and MC as a function of the TPC local momentum for tracks in the TPC2 (left) and TPC3 (right).

TPC PID systematics for protons

The same approach is used to evaluate the TPC PID systematics for protons using a proton sample instead of a muon sample. The selection of the proton sample is based on the selection of the most energetic positive tracks, with vertex in the FGDs FV. The selected track to be considered in the proton sample should have both a large amount of deposited charge in the TPCs (see Figure 4.6 on the left) and TPC momentum between 300 MeV and 1.1 GeV (that is the momentum range where using the dE/dx is possible to identify protons from muons and pions). In this way it is possible to select a 98% pure proton sample as shown in Figure 4.6 on the right. In this plot the proton momentum shows a large scaling factor between data and MC. This is mainly due to the big uncertainty in the proton production cross section model implemented in the MC.

The mean value and width of the pull δ_p are calculated for both data and MC in TPC momentum bins of 100 MeV/c, independently for TPC2 and TPC3 (see Figures 4.7 and 4.8). Also, in this case two systematic error sources have been considered: the difference in the mean value and the smearing of proton pull distribution between data and MC. As it can be seen, the mean value of

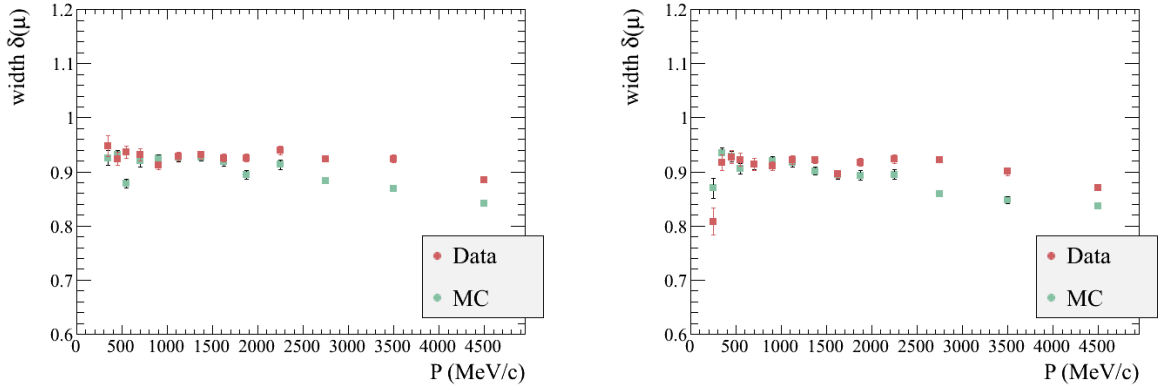


Figure 4.5: Width of the TPC muon pull in data and MC as a function of the TPC local momentum for tracks in the TPC2 (left) and TPC3 (right).

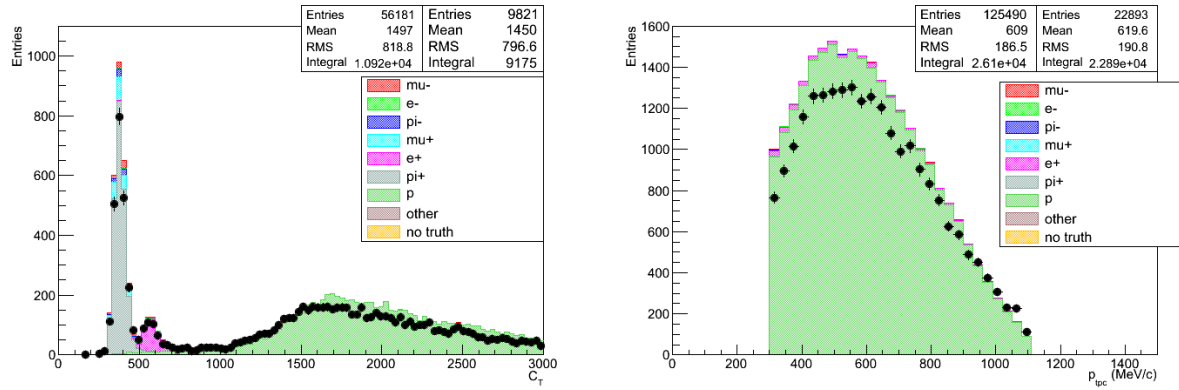


Figure 4.6: Left: Truncated mean of positive tracks with momentum between 300 MeV/c and 500 MeV/c. Protons have higher value of C_T than muons and pions. Right: Momentum distribution for the tracks selected in the proton sample.

proton pull for data is always lower with respect to MC. The same behavior is found for TPC2 and TPC3, and it is more striking for low momentum bins, where the deposited charge is larger. For a C_T resolution of around 7% for TPC2 and 8% for TPC3, the difference data-MC is about 5% in the TPC momentum region between 300 MeV/c and 600 MeV/c and becomes lower at higher momenta bins. As for muons, the width in the MC is slightly narrower than data. Since the TPC PID cut to select μ^+ is optimized using the MC, these differences in δ_p between data and MC cause a worse rejection of protons in data compared to the MC. This explains the strange behavior of data and MC in Figure 3.13 and suggests to take into account a big effect of the TPC proton PID systematic in the $\bar{\nu}_\mu$ analysis.

4.1.4 TPC charge confusion

As it is well known, through the curvature of the track, the TPC can identify the charge of the crossing particle. Nevertheless sometimes the charge of the particle can be mis-identified from

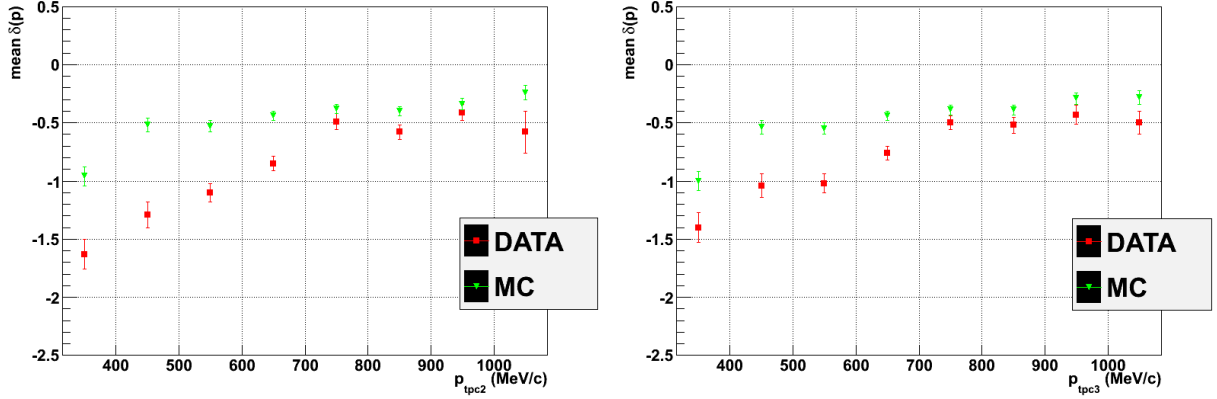


Figure 4.7: Mean value of the pulls in the proton hypothesis as a function of the TPC local momentum for data and MC in TPC2 (left) and TPC3 (right).

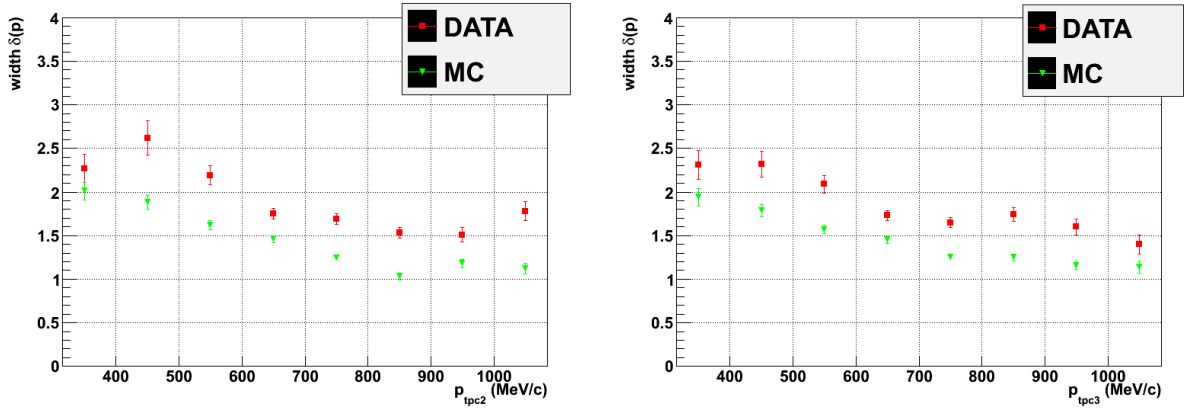


Figure 4.8: Width value of the pulls in the proton hypothesis as a function of the TPC local momentum for data and MC in TPC2 (left) and TPC3 (right).

the TPC and a positive charge can be confused with a negative charge and vice versa. A TPC charge mis-identification in data and MC induces a systematic error in the selection of the most energetic positive track. The charge mis-identification is evaluated using a statistical approach. Since this phenomenon depends only from the TPC performances, the evaluation of the charge mis-identification is performed using a sample of forward going tracks that pass through each one of the three TPC, to reduce as much as possible the contamination of the backwards going tracks that enlarge the charge mis-identification. The charge mis-identification probability P_{CM} and the probability of having all the same reconstructed charges in each one of the three TPCs, P_{same} , are related by:

$$\begin{aligned}
 P_{same} &= (1 - P_{CM})^3 + P_{CM}^3 = 1 + 3P_{CM}^2 - 3P_{CM} \Rightarrow \\
 \Rightarrow P_{CM} &= \frac{1}{2} \times (1 - \sqrt{1/3(4P_{same} - 1)}).
 \end{aligned}
 \tag{4.1}$$

This relationship is exact only under two assumptions:

- there is no mis-match: the three TPC segments of the track belong to the same particle,
- the charge mis-identification in each TPC have the same value.

For the used sample, these hypothesis are very light and will not have a big impact. Furthermore, a parallel MC truth study is used to cross-check the statistical approach:

- statistical estimation of the charge mis-identification: calculated both for data and MC and taken as the official results;
- MC truth validation: direct comparison of the reconstructed and true charge to compute the charge mis-identification only in the MC.

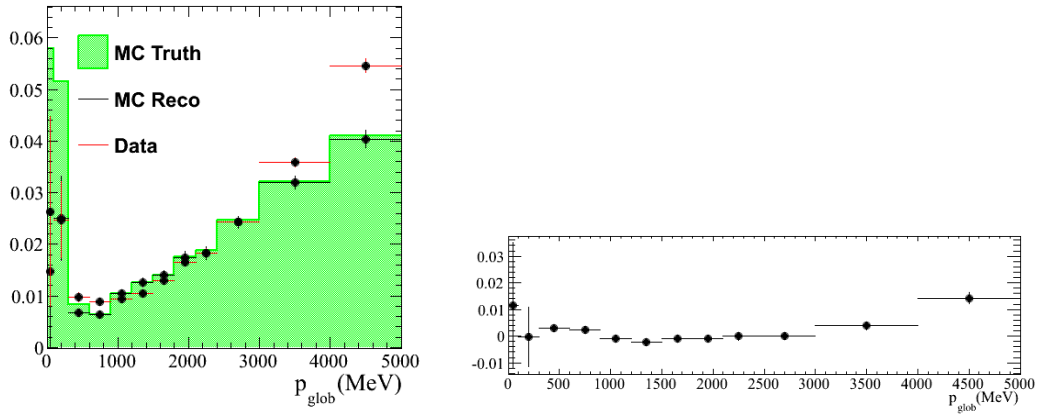


Figure 4.9: Left: Probability of charge mis-identification versus global momentum. Right: Absolute difference between data and MC of the P_{CM} .

The results are shown in Figure 4.9 on the left. The expected constant rising with the momentum is observed, since the straighter the track is, smaller is the corresponding sagitta. When the sagitta becomes more or less equal to the spatial resolution ($600 \mu\text{m}$ for MIP particles between $300 < p < 600 \text{ MeV}/c$ with a drift distance of 300 mm) become impossible or very difficult to measure it. The low energy region is populated mainly by remaining low quality reconstructed tracks, mis-matched tracks and backward-going tracks. As can be seen from the Figure 4.9 on the right the effect of this systematic on the $\bar{\nu}_\mu$ analysis is small.

4.1.5 TPC momentum resolution

The TPC momentum resolution systematic error is evaluated from tracks crossing at least two TPCs to compute the difference between the momentum reconstructed in data and MC, using the two TPC segments of the same track. Using the inverse of the transverse momentum with respect to the magnetic field lines $1/p_t$, the distribution of this difference between the first and second TPC, corrected by energy loss in the intermediate FGD, $\Delta 1/p_t$ is approximately Gaussian, with mean close to 0 and standard deviation $\sigma_{\Delta 1/p_t}$, having as main contributors the intrinsic resolutions of the TPCs involved, σ_{1/p_t} . Figure 4.10 shows $\sigma_{\Delta 1/p_t}$ as a function of p_t , x -coordinate and $\cos\theta_y$

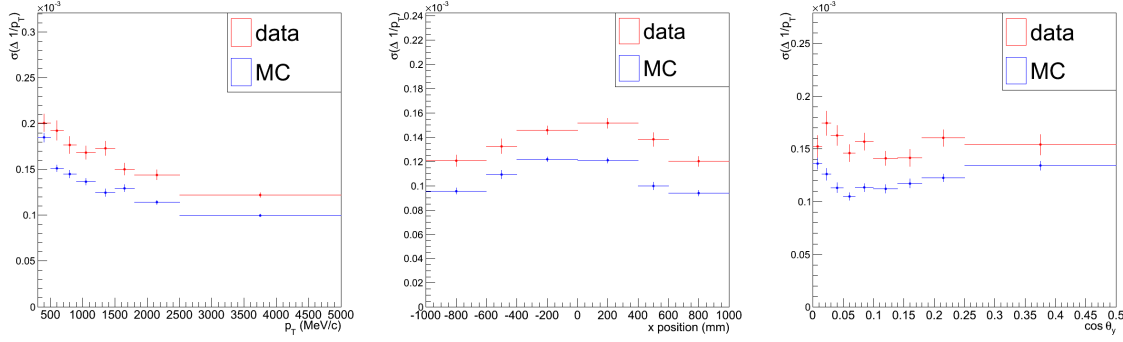


Figure 4.10: $\sigma_{\Delta 1/p_t}$ as a function of p_t (right), x -coordinate (middle) and $\cos \theta_y$ (left).

at TPC2 entrance, for data and MC. Since the momentum measurement comes from global tracks⁵ (containing several FGDs and TPCs), the same study is extended to those tracks. In this case the comparison is not done between two independent TPCs but between two different momentum measurements for the same track using different combination of detectors in the Kalman filter fit. Similar plots to the ones in Figure 4.10 can be found with this method.

In order to obtain the difference in resolution between data and MC, the MC can be smeared track by track by a factor α , which is the fractional difference in resolution between data and MC, as defined in this equation:

$$\sigma_{1/p_t}^{\text{data}} = (1 + \alpha) \sigma_{1/p_t}^{\text{MC}}, \quad (4.2)$$

where $\sigma_{1/p_t}^{\text{data}}$ and $\sigma_{1/p_t}^{\text{MC}}$ are the intrinsic $1/p_t$ resolutions in data and MC respectively. α can be found by numerical minimization of the matching χ^2 between data and MC. The smearing factor found is around 32% both for TPC and global resolution. As a consequence a big effect from this systematic is expected in the $\bar{\nu}_\mu$ analysis.

4.1.6 TPC momentum scale

The so called momentum scale is the systematic bias on the momentum measurement in the TPCs due mainly to the limited knowledge of the magnetic field. Differences in momentum scale between data and MC introduce a systematic bias in the momentum spectrum of the μ^+ candidate. The relation between the momentum and the magnetic field is given by:

$$p_t = \frac{0.3B}{\rho}, \quad (4.3)$$

where p_t is given in MeV, B in Tesla and ρ , that is the curvature, in mm^{-1} . The TPC momentum scale systematic is obtained from the magnetic field measurement [130]. The obtained data-MC differences are than cross checked using cosmic rays data and MC sample stopping in the FGD. Indeed, using cosmic rays stopping in FGD is possible to compare TPC momentum with the particle range in the FGD which is calculated by the track end position and its direction. Results are binned in 5 cm steps of particle range. If there is a relative data/MC momentum bias, a shift in momentum would be expected for a given range in FGD.

⁵ A global track, is a track object coming from the global reconstruction (see Section 3.3.2).

Figure 4.11 shows the momentum distributions for each range in the FGD1. A Gaussian fit is

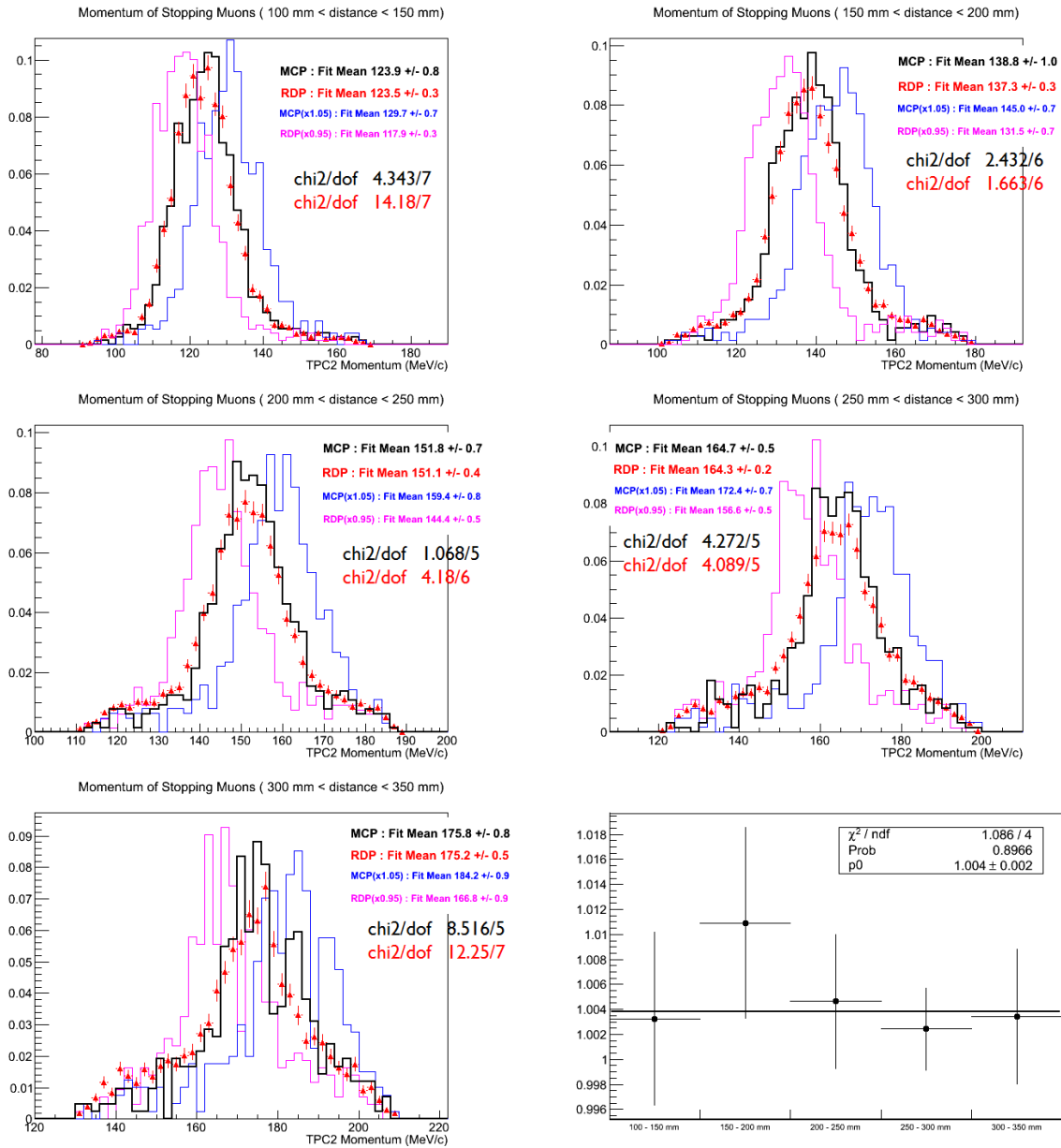


Figure 4.11: Momentum distributions of stopping muons for each range in the FGD1. A simple Gaussian fit at around the peak is performed to determine its position. The last plot shows the ratio of the momentum means of data and MC and fit with a straight line.

performed around the peak to determine its position. For all the cases, the data (red) and the nominal MC (black) agree well. On the contrary the $\pm 5\%$ shifted MC samples (pink and blue) clearly do not agree with data. In the last plot of Figure 4.11 it is also shown the ratio of the momentum means in data and MC and a fit with a straight line. To be conservative a systematic error of 5% is considered in the $\bar{\nu}_\mu$ analysis.

4.1.7 Magnetic field distortions

Particles entering a TPC create a cloud of primary ionization. Electrons from the ionization drift along the direction of the electric field lines towards the detector readout plane. In an ideal TPC the magnetic and electric fields orientated parallel to each other and drift electrons experience no deflection in directions transverse to the drift direction. However due to imperfections in the magnetic and electric fields, the path of the drift electrons can be distorted. The magnetic field distortion systematic is based on data and MC differences founded in a dedicated study of magnetic field distortions in the TPCs [131]. As for the TPC momentum scale, also in this case an error of $\sim 5\%$ in the $\bar{\nu}_\mu$ analysis is considered.

4.1.8 FGD-TPC Matching

An event will only be correctly associated to the fiducial volume if the reconstructed TPC track is matched to the corresponding FGD hits. A track may fail to associate with FGD hits for various reasons. If the track is mis-reconstructed, it is possible that the extrapolated track may simply miss the FGD hits. An error in T_0 calculation used to determine the x coordinates of TPC hits would also cause a track to be shifted in x and possibly miss the hits. A control sample of through-going muons is used to evaluate the matching efficiency. For example a sample of events with long tracks in TPC1 and TPC2 is used for the FGD1-TPC matching efficiency. The assumption is that if there are tracks in TPC1 and TPC2, they are probably a long track that also crossed FGD1; by checking for the presence of a TPC2-FGD1 reconstructed track the FGD1-TPC matching can be calculated. The measured efficiencies are shown in Figure 4.12. The figures show that for momentum > 200 MeV/c the TPC-FGD matching efficiency is very high and agrees well for data and MC. Below 200 MeV/c the matching efficiency is substantially reduced and there is a larger data/MC difference. As a consequence, the effect of this systematic error on the $\bar{\nu}_\mu$ analysis is expected to be low.

4.1.9 TPC-ECal Matching

The data-MC discrepancy in the TPC-ECal matching is very important for the $\bar{\nu}_\mu$ analysis, since only tracks with the ECal matching are used in the final sample. A different ECal matching efficiency between data and MC can introduce a systematic bias in the selection criteria. The efficiency of the TPC-ECal matching is defined as:

$$\frac{\text{Number of tracks entering the ECal with an ECal object attached}}{\text{Total number of tracks entering the ECal}}, \quad (4.4)$$

where the ECal object can be either a track or a shower. For this study, are used data and MC samples of muons obtained selecting through-going tracks from interactions upstream of the ND280 tracker that appear to enter an ECal module, with separate selections for the Downstream ECal and Barrel ECal (see Figure 4.13). The sample of muons that enter the downstream ECal has a μ purity of 92.2% while the sample of muons that enter the barrel ECal has a μ purity of 88.7%.

The efficiency of matching to an ECal object is shown in Figure 4.14 as a function of the track's momentum. Since in the low momentum region few tracks have the TPC-ECal matching, in these plots the matching efficiency is shown only for momenta greater than 300 MeV/c. The integrated efficiency for the downstream ECal is $\sim 94\%$ for both data and MC while the integrated efficiency for the barrel ECal is a bit lower for data (68%) than MC (70%). However the 2% disagreement in data and MC for the barrel ECal matching efficiency will introduce a small systematic error on the $\bar{\nu}_\mu$ analysis, since a small amount of tracks of the selected sample enter the barrel ECal.

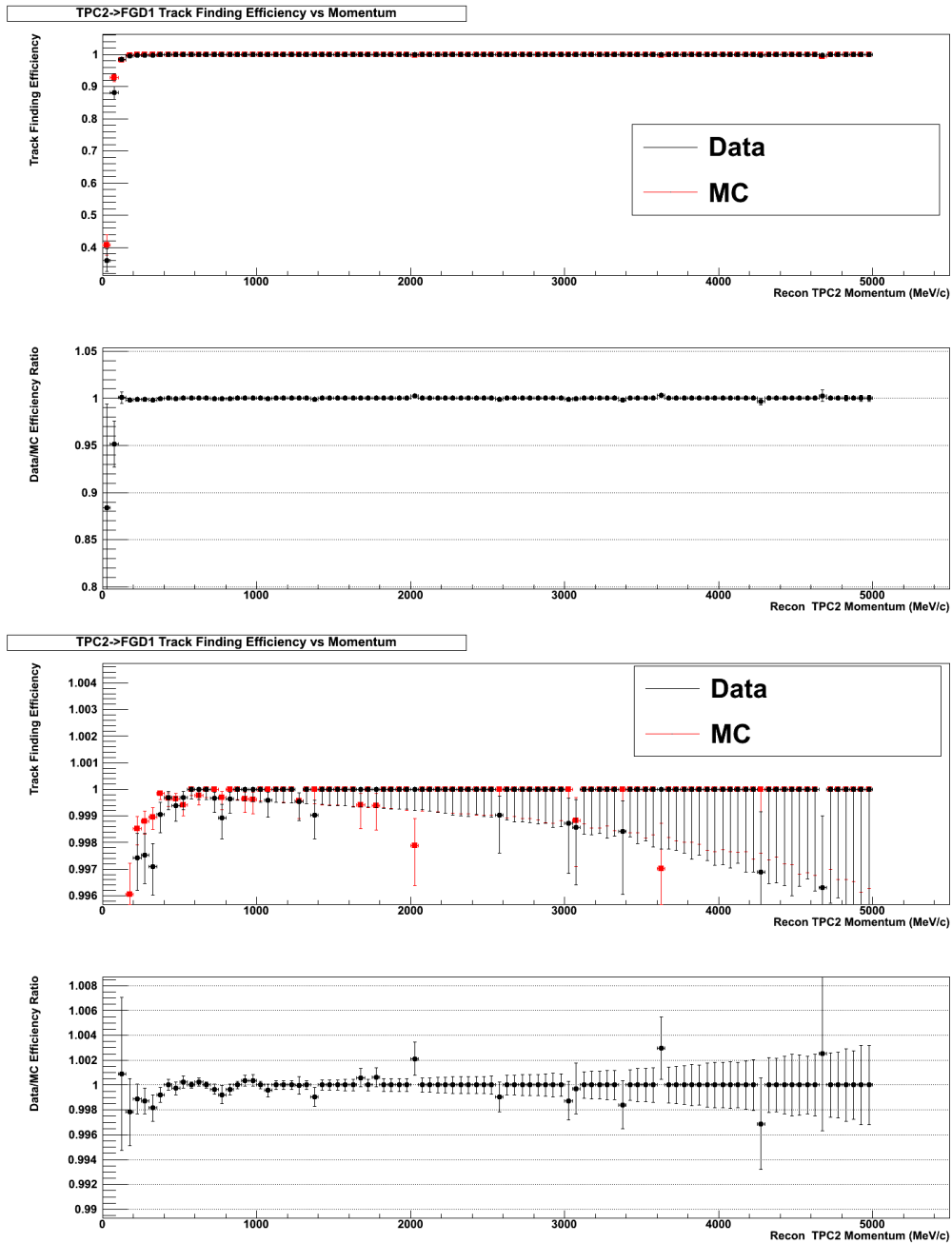


Figure 4.12: First plot: TPC-FGD matching efficiency vs TPC2 momentum for data (black) and MC (red). Second plot: ratio of the data over MC efficiency. Third plot: TPC-FGD matching efficiency vs TPC2 momentum for data (black) and MC (red) zoomed in on high efficiency region. Fourth plot: ratio of the data over MC efficiency zoomed in on high efficiency region.

4.1.10 ECal PID

The systematic uncertainty due to the ECal PID selection is estimated by comparing the muon selection efficiency in data and MC using the same high purity muon control sample showed in

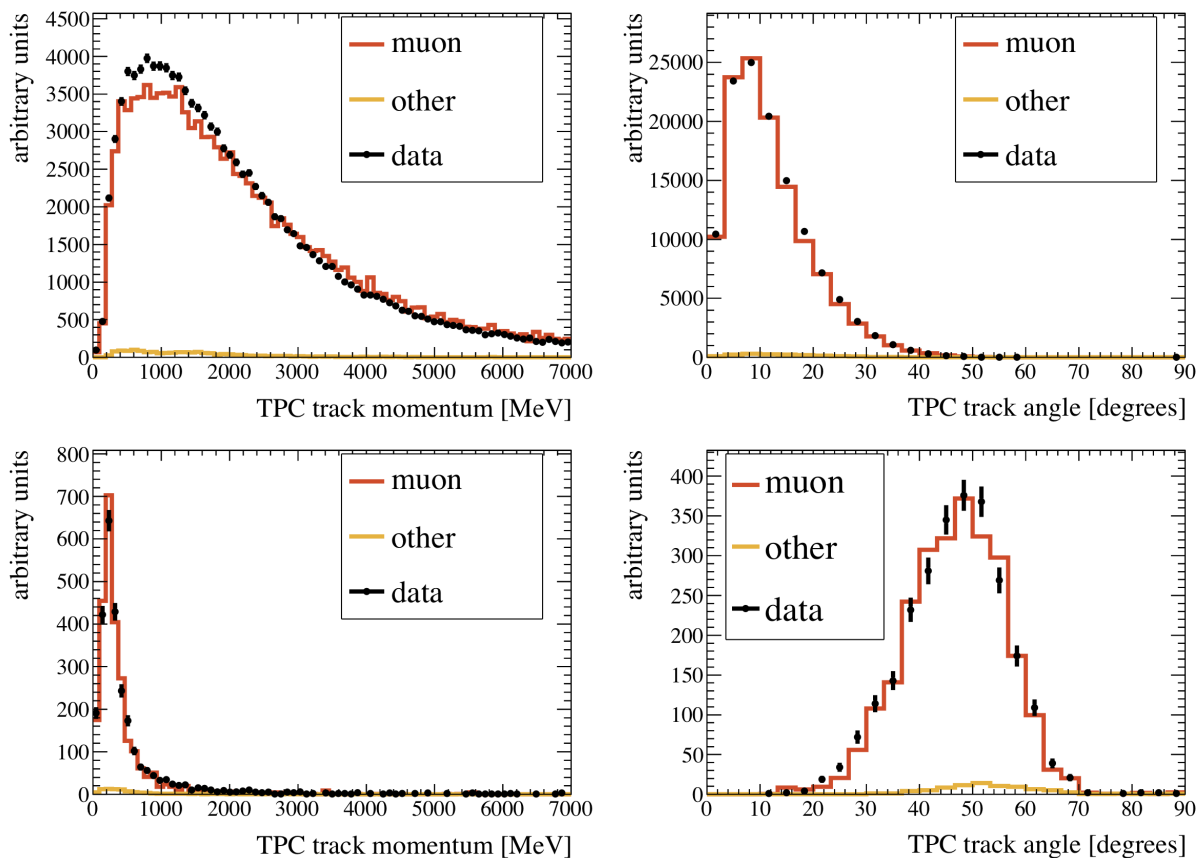


Figure 4.13: Reconstructed kinematics for the muon control sample in the downstream (top) and barrel (bottom) ECal. The momentum shown is the reconstructed TPC momentum extrapolated to the entry point of the ECal. The angle shown is the angle of incidence of the TPC track on the respective ECal.

Section 4.1.9. The selection efficiency as a function of the cut applied on the ECals PID variables is shown in the Figure 4.15. In the $\bar{\nu}_\mu$ analysis, two ECal PID variables are used, and the cuts applied are:

- LLR MIP-EM < -10
- LLR MIP-PION < -5

in both downstream and barrel ECals. As can be seen from Figure 4.15 the expected systematic error in the region between $-10 < \text{ECal PID} < -5$ is $\sim 1\%$ ($-0.9 \pm 0.1\%$) for muons entering the downstream ECal and $\sim 1.5\%$ ($-1.1 \pm 0.3\%$) for muons entering the barrel ECal.

4.1.11 Pion Secondary interactions

A “pion secondary interaction” is an interaction that a pion undergoes outside of the nucleus that it was produced in. These processes are modelled in Geant4, however the model has been found to differ significantly from the available external data (see Figure 4.16). In addition, the uncertainty in

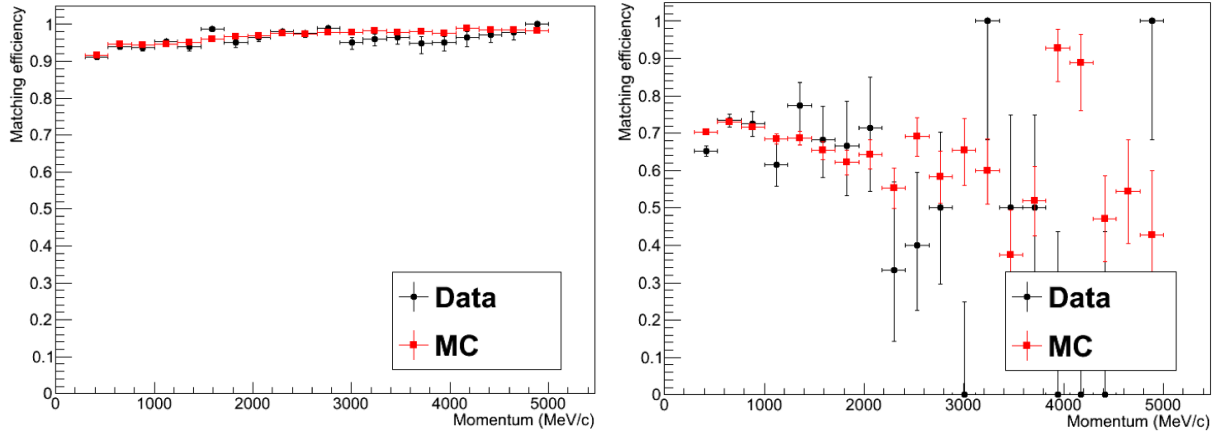


Figure 4.14: Left: Downstream ECal matching efficiency as a function of the muon momentum for data (black) and MC (red). Right: Barrel ECal matching efficiency as a function of the muon momentum for data (black) and MC (red).

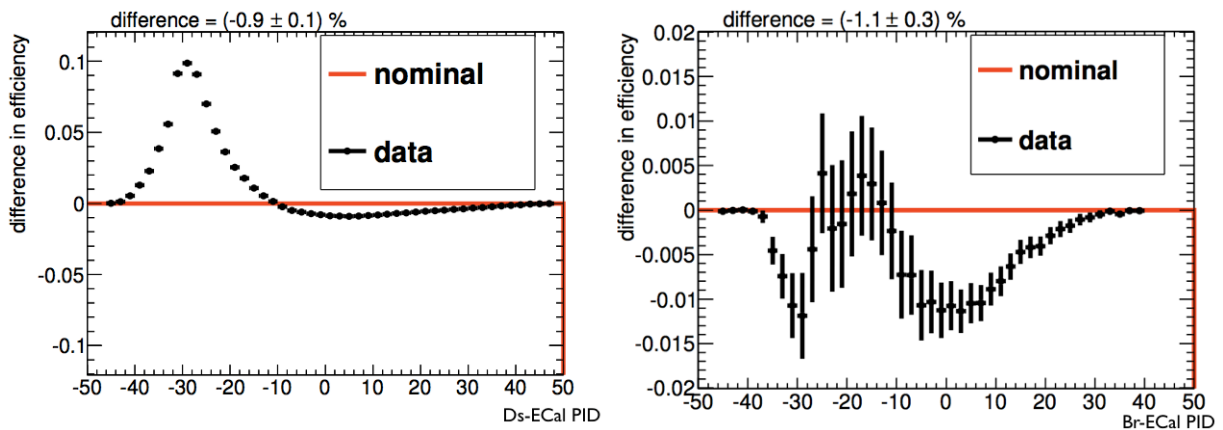


Figure 4.15: Difference of selection efficiency between data and MC for downstream ECal (right) and barrel ECal (left).

the external data needs to be taken into account. There are several different secondary interaction types. They are defined by the particles that exit the nucleus and that the pion interacts with. Only the three most significant types were considered. They are:

- **absorption:** The incident pion is completely absorbed by the nucleus, and there are no pions produced in the interaction;
- **charge exchange:** The incident pion interacts with the nucleus to produce a π^0 (and no other pions);
- **quasi-elastic scattering:** The pion interacts inelastically with the nucleus, and one pion of the same charge exits the interaction (amongst other non-pion particles).

Absorption and charge exchange have the ability to cause a charged pion to disappear before it could be detected while the quasi-elastic scatters, which has a large cross section at the pion momenta seen at ND280, has the following effects on the analysis:

- from the perspective of the reconstruction, they create a sudden change in direction and momentum of the pion, which could complicate reconstruction;
- the outgoing pion will be of lower momentum, and therefore may have a higher absorption cross section.

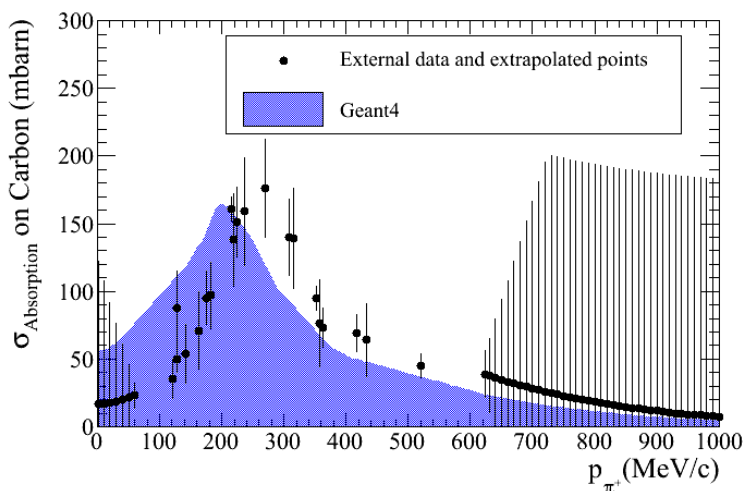


Figure 4.16: A comparison of the π^+ Absorption on Carbon-12 data and extrapolations (black) with the Geant4 cross section (blue). The extrapolated data points begin when the points get much denser, below and above the data region. The range of 1000 - 8000 MeV is not shown, in order to better show the extrapolation in the low energy region, which is more significant to this study.

Absorption, Charge Exchange and Quasi-Elastic scattering mainly affect an event selection that provides two or more tracks crossing the TPC in the final state of which one of these is identified as a pion. Since in the $\bar{\nu}_\mu$ analysis are selected events with only one track crossing the TPCs, this kind of systematic error will have a very low impact on the analysis.

4.1.12 FGD Mass

If the actual density of material in FGDs is different from the MC value, this will result in a normalization error in the number of simulated neutrino interactions. For this reason, the contents of the FGD's XY scintillator modules, in units of g/cm^2 , broken down by element, have been evaluated [132]. This measure is based on the measured geometry of the scintillator bars and the measured amounts of glue and G10 included in the module construction. The dominant component of the mass is carbon, which is known to roughly $\sim 0.5\%$ accuracy. The final results are in agreement with measured weights of the final machined modules and with the weights of raw scintillator bars, to within uncertainties, therefore no rescaling of the MC output is necessary on account of detector density. The uncertainty on the total FGD XY module mass is 0.67%.

4.1.13 Sand muon background

The default MC simulation used for ND280 contains only interactions that occur within the magnet. In order to estimate the contribution of events produced outside of the magnet, most notably from the pit wall and sand upstream of the detector, a separate sand interaction MC has been developed [133]. Among the particles produced by the neutrinos in the pit walls and surrounding sand, those which entered the magnet are simulated and reconstructed in the same way as in standard MC. The size of sand MC sample corresponds to $\sim 2.6 \times 10^{20}$ POT, which represents 44% of data taken during Runs 1-4. The expected contamination of sand muons in the $\bar{\nu}_\mu$ analysis is $\sim 0.5\%$.

The rates of sand interactions in data and sand simulation are compared using the tracks entering through the upstream wall of the PØD. The resulting data/MC discrepancy is about 10% and it is included as a systematic uncertainty to the predicted numbers of sand events in the final sample.

4.1.14 Cosmic rays background

The cosmic rays background to the selected sample has been studied using the dedicated cosmic muon MC simulation [134]. Additionally, a number of runs taken with the beam trigger when the neutrino beam was off (“empty spill” data), is used to compare the rates of cosmic events in MC and data. The predicted number of the cosmic rays passing the selection is $\sim 0.64 \pm 0.08$ and can be neglected.

The tracks crossing the TPC1 volume can also produce a false veto signal for neutrino (anti-neutrino) events. The probability of such events is calculated using the “empty spill” data sample. The obtained rate of cosmic events with a segment in TPC1 is 458 ± 28 Hz, which corresponds to the probability equal to 0.0055%. Also this error is very small compared to others and it is neglected.

4.1.15 Event pile up

There are a number of categories of possible pile up, but only the effect of sand muons is significant for this analysis. Events are rejected if there is activity in TPC1 since in most cases, the TPC1 activity is due to tracks from interactions upstream of the detector (sand muons) or outside the tracker fiducial volume. A study done on the events rejected due to the TPC1 veto indicates that the majority are not true CC interactions. Since sand muons are not included in the standard simulation, the MC does not include the effect of events that are rejected due to coincidence with a sand muon and a correction based on the sand muon MC must be made. The correction is evaluated for each data set (Run 1, 2, 3b, 3c, 4) separately for PØD filled or not with water. The evaluated corrections are shown in Table 4.1.

Another source of pile up is the probability to have two simultaneous CC anti-neutrino events in the same bunch. This probability can be derived from the square of the number of selected anti-neutrino events per bunch. The highest value, obtained for anti-neutrinos from the Run 4 data sample is 4.12×10^{-7} which means that this pile up effect is negligible in the $\bar{\nu}_\mu$ analysis.

4.2 Propagation of detector systematics

Each systematic error shown in the previous sections is propagated through the nominal MC, to take into account its effect on the $\bar{\nu}_\mu$ analysis. The systematic error propagation is based on several models depending on the nature of the systematic uncertainty [129]. In all cases, the nominal MC sample is modified or re-weighted. The full selection is then applied again on the newly modified observables. The propagation model applied to each of the systematic errors is shown in Table 4.2

Sample	TPC1/bunch (%)			C_{pileup}	σ_{pileup}
	Data	MC	Sand		
Run 1 - Water In	1.08	0.49	0.51	0.0051	0.00086
Run 2 - Water In	1.75	0.84	0.80	0.0080	0.0011
Run 2 - Water Out	2.07	0.94	0.99	0.0099	0.0014
Run 3b - Water Out	1.83	0.90	0.96	0.0096	0.00096
Run 3c - Water Out	2.24	1.01	1.08	0.011	0.0015
Run 4 - Water In	2.49	1.14	1.20	0.012	0.0016
Run 4 - Water Out	2.70	1.35	1.30	0.013	0.0013

Table 4.1: Pile-up correction and uncertainty for each data set.

and described in the following sub-sections.

Table 4.2: Systematic error propagation model for each of the systematic errors considered.

Systematic error	Implementation model	Probability Density Function
TPC Cluster efficiency	Efficiency like systematics	Gauss
TPC tracking efficiency	Efficiency like systematics	Gauss
TPC PID	Reconstructed observable variation	Gauss
TPC charge confusion	Efficiency like systematics	Gauss
TPC momentum resolution	Reconstructed observable variation	Gauss
TPC momentum scale	Reconstructed observable variation	Gauss
Magnetic field distortion	Reconstructed observable variation	Flat
FGD-TPC matching efficiency	Efficiency like systematics	Gauss
TPC-ECal matching	Reconstructed observable variation	Flat
ECal PID	Reconstructed observable variation	Flat
Pion secondary interactions	Efficiency like systematics	Gauss
FGD mass uncertainty	Normalization systematics	Gauss
sand muons	Efficiency like systematics	Gauss
event pile-up	Normalization systematics	Gauss

4.2.1 Efficiency like systematics

An event is properly reconstructed if there is a true MC object associated to the reconstructed track. If this happens, the event is weighted according to the relative efficiency formula:

$$\text{Weight} = \frac{(\epsilon + \delta(\Delta\epsilon))}{\epsilon}. \quad (4.5)$$

But, when the reconstructed variable differs from the true one (like wrong charge association) or the true MC object is not associated to a reconstructed one, the event is weighted according to the

relative inefficiency formula:

$$\text{Weight} = \frac{(1 - \epsilon - \delta(\Delta\epsilon))}{(1 - \epsilon)}, \quad (4.6)$$

where ϵ is the true efficiency of the association, $\Delta\epsilon$ is the systematic error in the efficiency and δ the toy random variable that follows the corresponding probability density function, normally a normal distribution. For example, the estimated TPC tracking efficiency is $99.8_{-0.4}^{+0.2}\%$, this means that $\epsilon = 0.998$ and $\Delta\epsilon = 0.002$.

The efficiency type is a very delicate systematic. The way it is computed in the systematic error evaluation is based on studies comparing data and MC predictions with control samples and not using the reconstructed to true association. The efficiency type systematics do not require repeating the selection: the error propagation takes place uniquely through the event weights in order to give to the event more or less contribution to the selection.

4.2.2 Reconstructed observable variation

This model is applied to the particle identification and momentum reconstruction variables. As shown in the previous sections, those observables might show different resolution in data and MC or a small bias causing the migration of events between bins in kinematic distributions. The procedure to take into account these differences consists in smearing these observables before applying the event selection on the new smeared observables. This type of systematic error propagation is performed in different ways depending on the properties of the error. They can be grouped in four classes:

1. when the true MC observable is known (i.e. the momentum), it is rescaled by the difference of the reconstructed observable with respect to the true one:

$$\text{Obs}_{\text{reco}}^{\text{new}} = \text{Obs}_{\text{true}} + (\text{Obs}_{\text{reco}}^{\text{old}} - \text{Obs}_{\text{true}}) \frac{\sigma_{\text{new}}}{\sigma_{\text{old}}}, \quad (4.7)$$

where

$$\sigma_{\text{new}} = \sqrt{\sigma_{\text{old}}^2 + \delta^2(\Delta\sigma^2)} \quad (4.8)$$

and σ_{old} is the nominal observable dispersion in MC, $\Delta\sigma$ is the systematic error associated and δ is a random variable following the corresponding probability density function (normally a normal distribution). The momentum resolution error is treated this way.

2. to correct the observable for a specific particle, for example the ionization for one type of particle, the true MC particle associated to the track is identified and it is applied the corresponding correction, normally a bias smeared with a normally distributed random variable:

$$\text{Obs}_{\text{reco}}^{\text{new}} = \text{Obs}_{\text{reco}}^{\text{old}} + \delta(\Delta\text{Obs}_{\text{reco}}), \quad (4.9)$$

where δ is the random variable, and $\Delta\text{Obs}_{\text{reco}}$ is the systematic bias to apply to the observable. This propagation is applied to the TPC ionization systematics.

3. when there is a simple scale of an observable, like the momentum scale due to the magnetic field calibration, the observable is corrected to the value with an scale factor that varies according to the expected error:

$$\text{Obs}_{\text{reco}}^{\text{new}} = \text{Obs}_{\text{reco}}^{\text{old}} + (1 + \delta(\Delta\text{Scale})), \quad (4.10)$$

where δ is the random variable, and ΔScale is the error on the scale to propagate.

- when there are 2 possible values of the observable, like in the case of the residual TPC magnetic field distortions, the observable is computed by weighting the two results with a random variable following a flat distribution:

$$\text{Obs}_{\text{reco}}^{\text{new}} = \text{Obs}_{\text{reco}}^{\text{nominal}} + (\text{Obs}_{\text{reco}}^{\text{alternate}} - \text{Obs}_{\text{reco}}^{\text{nominal}}) \cdot \delta, \quad (4.11)$$

where δ is the random variable, $\text{Obs}_{\text{reco}}^{\text{nominal}}$ is the nominal observable and $\text{Obs}_{\text{reco}}^{\text{alternate}}$ the alternate result with other reconstruction criteria.

4.2.3 Normalization systematics errors

These are systematic errors associated to the total event normalization. The pile up systematic error or the FGD mass systematics are good examples of this type. For this case the event is re-weighted according to the variation suggested by the systematic error evaluation:

$$\text{Weight} = (1 + \delta(\Delta\text{Norm})), \quad (4.12)$$

where ΔNorm is the systematic error in the normalization and δ a random variable to propagate the variations. This systematic error is propagated to all the events in the case of the pile up errors, while for the FGD mass uncertainty is propagated only to the sub-sample of events with the true MC vertex in the FGD.

4.3 The corrected Monte Carlo

The MC sample obtained correcting the nominal MC by the central value of each detector systematic error will be called “*corrected*” MC. This can be done using the method presented in Section 4.2 and setting $\delta = 0$. The goal of this procedure is to build an improved MC sample based on the understood data-nominal MC differences. In Figure 4.17 it is shown the comparison at the end of the event selection between the old nominal MC and the new corrected MC. As it can be seen, the corrected MC shows a different shape of kinematic spectra with respect to the nominal one. The differences in momentum shape are mainly due to the combined effects of the largest systematics for my analysis: TPC proton PID and momentum resolution (see Figure 4.18).

To understand how signal and backgrounds are altered taking into account the systematics, the corrected MC can be divided in four PDFs (see Figure 4.17) that are input to the likelihood fit (see Section 3.9). A significant difference can be seen in the PDF of proton background. This corrected distribution shows an increased peak and a shift to lower momentum respect to the nominal one. It is clear that these differences are mainly due to the TPC proton PID systematics.

From now on, **the corrected MC will be the reference MC sample.**

4.4 Propagation of detector systematics in the corrected MC

The effect of the propagation of each detector systematic error can be easily obtained by throwing a random value δ in the corresponding PDF, as discussed in the Section 4.2. For example (see Table 4.2) for the TPC PID systematic, the “Reconstructed observable variation” is used as implementation model (more precisely the formula (4.9)) and the systematic propagation is done throwing a random value δ in a normal distribution centered in zero with a σ equal to one. This means that, if δ is

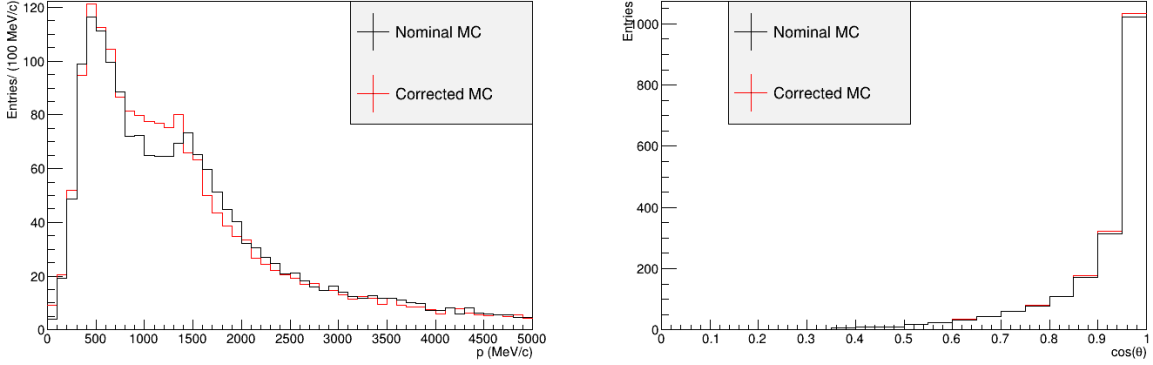


Figure 4.17: Comparison between nominal and corrected MC kinematic spectra.

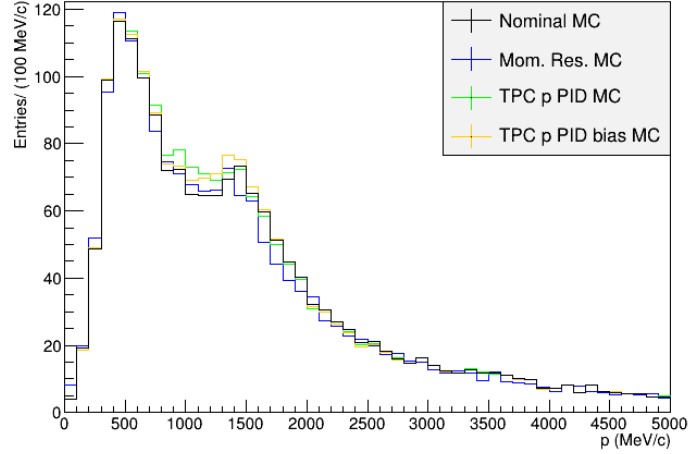


Figure 4.18: Comparison between nominal (black) and corrected MC kinematic spectra. In the corrected MC are propagated only: momentum resolution systematic (blue), TPC proton PID systematic (green) and TPC proton PID bias systematic (orange). The data-MC difference in the mean of pull distribution δ_p is identified as TPC proton PID systematic while the data-MC difference in the width of pull distribution δ_p is identified as TPC proton PID bias systematic.

set to ± 1 ($\pm\sigma$ of the normal distribution) the TPC proton PID systematic will be propagated around the nominal value of the pull δ_p (which is $\text{Obs}_{\text{reco}}^{\text{old}}$ in the formula (4.9)) in the corrected MC of $\pm\Delta\text{Obs}_{\text{reco}}$, which is the uncertainty of the TPC proton PID systematic. The result of this procedure consists in two MC toys shown together with the corrected MC in Figure 4.23 on the left. As can be seen, a variation of $\pm\sigma$ of this systematic introduce a relative error of $\sim 10\%$ in the region between $0.8 < p < 1.3$ GeV/c. It is also important to notice that since the systematic errors are not gaussian, their propagation leads to a result that is not symmetric around the nominal value in the corrected MC, as can be seen from the plot on the left in the Figure 4.23. The impact of TPC proton PID bias and momentum resolution systematics is also shown in Figures 4.21 and 4.22 respectively. In the case of TPC proton PID bias systematic a relative error of $\sim 8\%$ is introduced

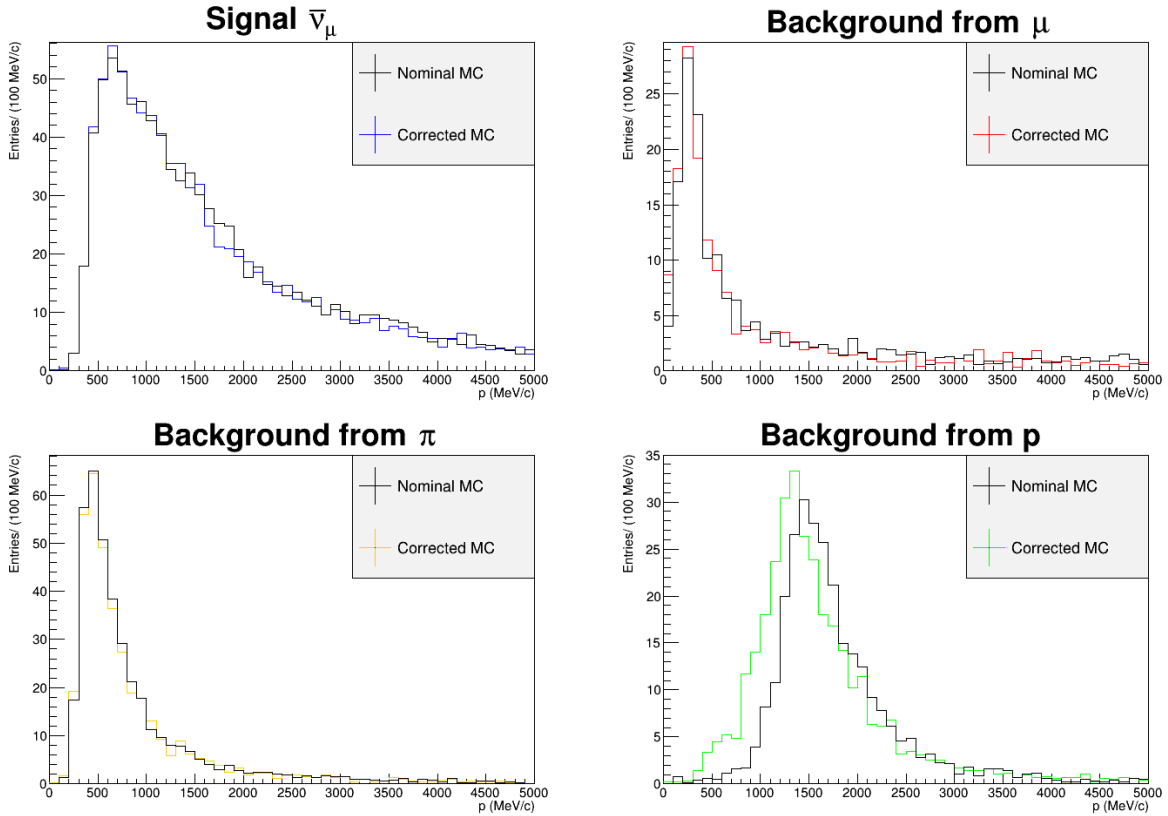


Figure 4.19: Comparison between nominal PDFs distributions (black) and corrected PDFs distributions (colored).

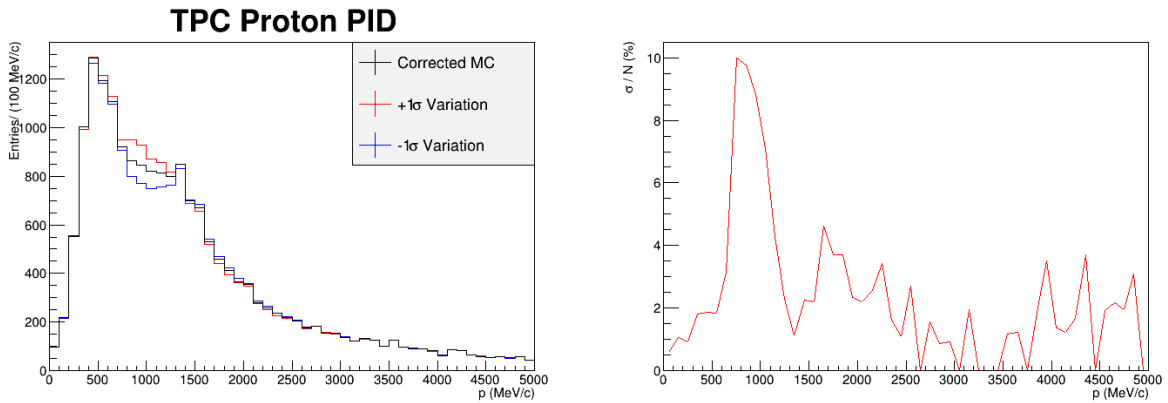


Figure 4.20: Left: Effect on the momentum spectrum of the TPC proton PID systematic propagation with a variation of $\pm\sigma$ respect to the nominal value of the pull δ_p in the corrected MC. Right: relative systematic error introduced in the analysis.

in the analysis, while in the case of momentum resolution systematic above 2 GeV/c the relative error is huge and exceed the 30%. However, as will be shown in the next section, this is not an issue

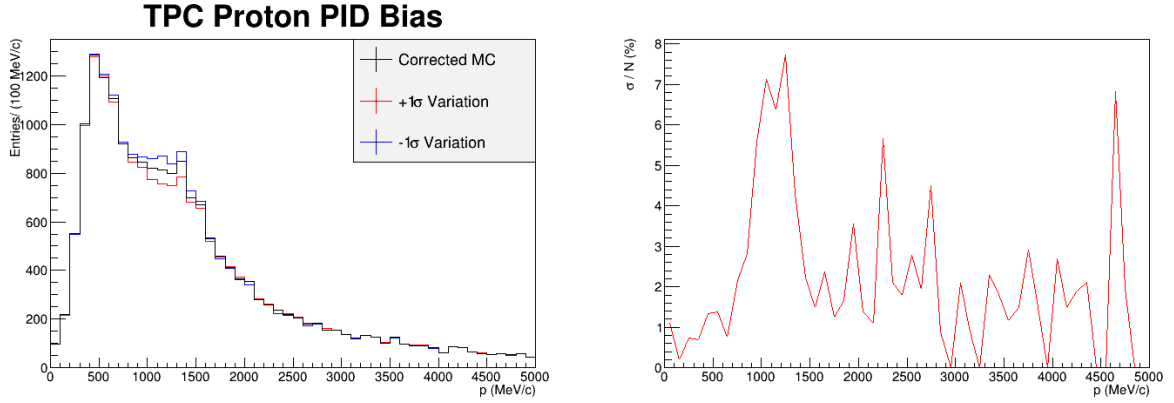


Figure 4.21: Left: Effect on the momentum spectrum of the TPC proton PID bias systematic propagation with a variation of $\pm\sigma$ respect to the nominal value of the pull δ_p in the corrected MC. Right: relative systematic error introduced in the analysis.

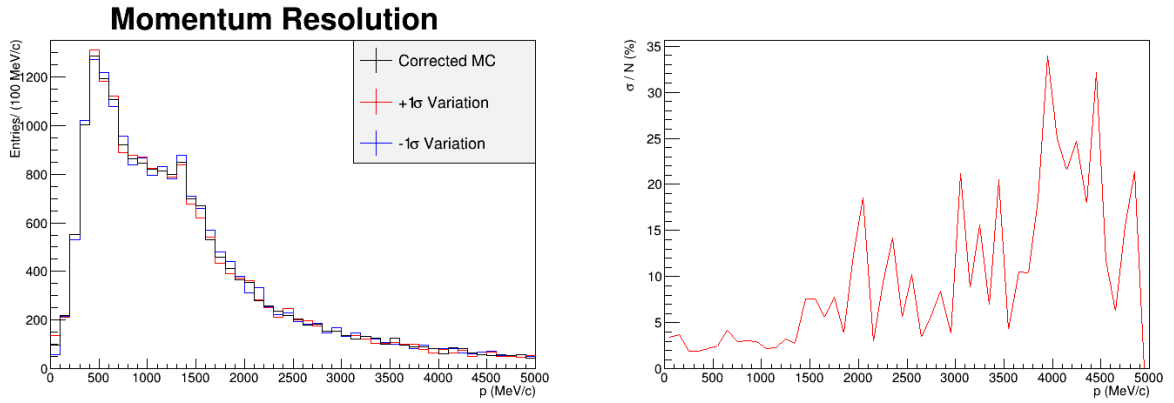


Figure 4.22: Left: Effect on the momentum spectrum of the momentum resolution systematic propagation with a variation of $\pm\sigma$ respect to the nominal value of the momentum in the corrected MC. Right: relative systematic error introduced in the analysis.

because the likelihood fit mainly works in the region below 2 GeV, where there are more data.

4.5 Likelihood fit results

To estimate the effect of the detector systematics in the likelihood fit I performed one thousand fit on one thousand MC toys where all the systematics uncertainties are propagated with a random variation thrown in the opportune PDF. The procedure to produce MC toys is the same discussed in the previous section for the TPC proton PID systematic, but with all the systematic errors propagated at the same time to take into account correlations between them. The width of the fitted distribution of $f_{\bar{\nu}_\mu}$ will then give the effect of the systematics on the fit. Also the likelihood fit applied on the corrected MC will be shown since it will be used to estimate flux and cross section systematics.

4.5.1 Fit results obtained for the corrected MC

The kinematic spectra of data and corrected MC and the data/MC ratios before the fit are shown in Figure 4.23.

The corrected MC composition is detailed in Table 4.3. It is worth noting that the data/MC ratio

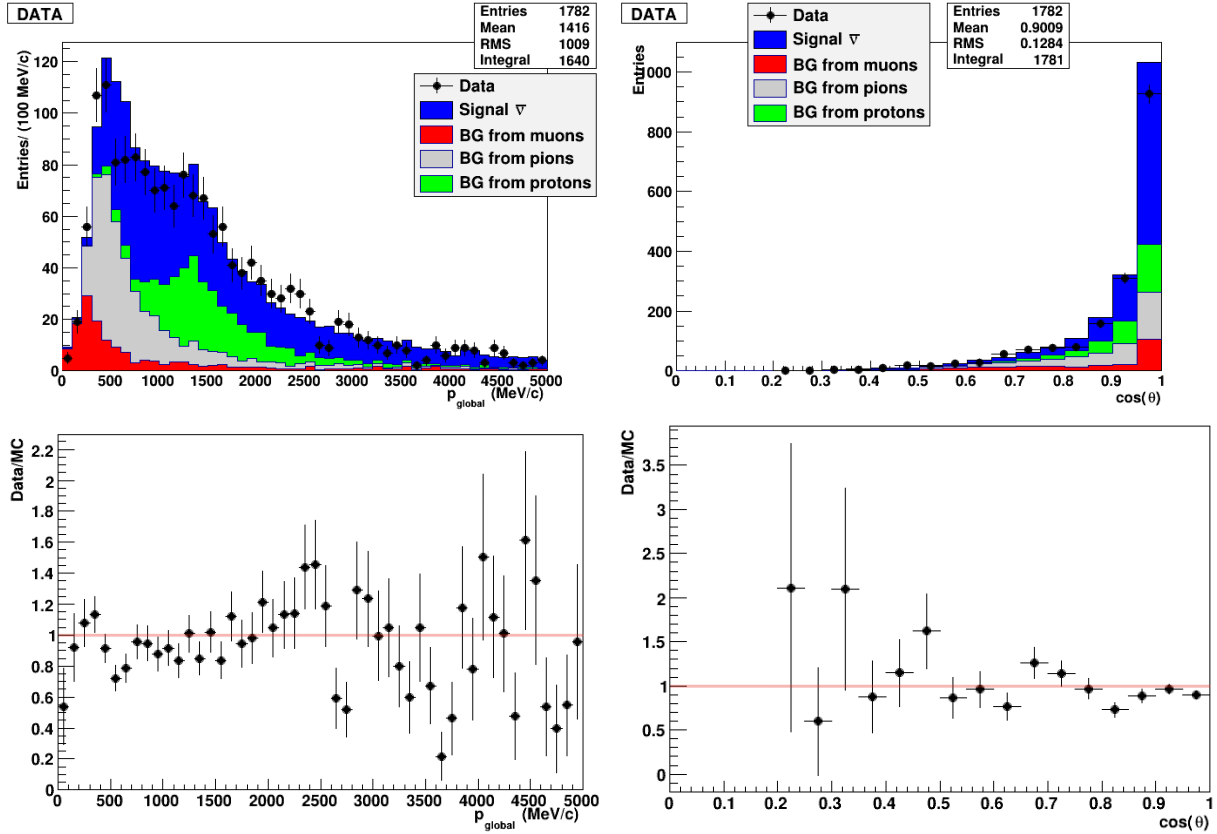


Figure 4.23: Top: Data and corrected MC kinematic spectra before the fit. The MC is broken down by signal and background sources. Bottom: Data/MC ratios for kinematic spectra before the fit.

Table 4.3: Composition of the final selected sample broken down by input to the fit.

Category	Composition (%)	corrected MC expected events
Signal $\bar{\nu}_\mu$	50	946
Background from μ	11	209.2
Background from π	21	394.2
Background from p	18	339.8

of the momentum spectrum obtained with the corrected MC is closer to one respect to the data/MC ratio obtained with the nominal MC (Figure 3.24), especially in the momentum region of the proton background. For this reason a rescaling factor f_{BG_p} closer to one is expected. Using the likelihood defined in Section 3.9.1 I obtained the results shown in Table 4.4. The number of the $\bar{\nu}_\mu$ and p

Table 4.4: Value of the parameters for best fit for the corrected MC. The rescaling factor and absolute number of events are indicated for each component.

	f	N_{events}
$f_{\bar{\nu}_\mu}$	0.95 ± 0.07	896 ± 64.6
f_{BG_μ}	1.31 ± 0.17	275.3 ± 35.6
f_{BG_π}	0.67 ± 0.12	263.8 ± 46.5
f_{BG_p}	0.95 ± 0.13	324 ± 64.6

background events are in agreement within one σ with the corrected MC predictions. However the π and μ background are still not well reproduced by the corrected MC as can be see from the difference between the number of the expected events and the fit results for these two categories. The overall effect of the fit on the kinematics distributions and the data/MC ratios after the fit is shown in Figure 4.24. Finally, also in this case the global minimum of the likelihood and the f contours are shown in Figure 4.25.

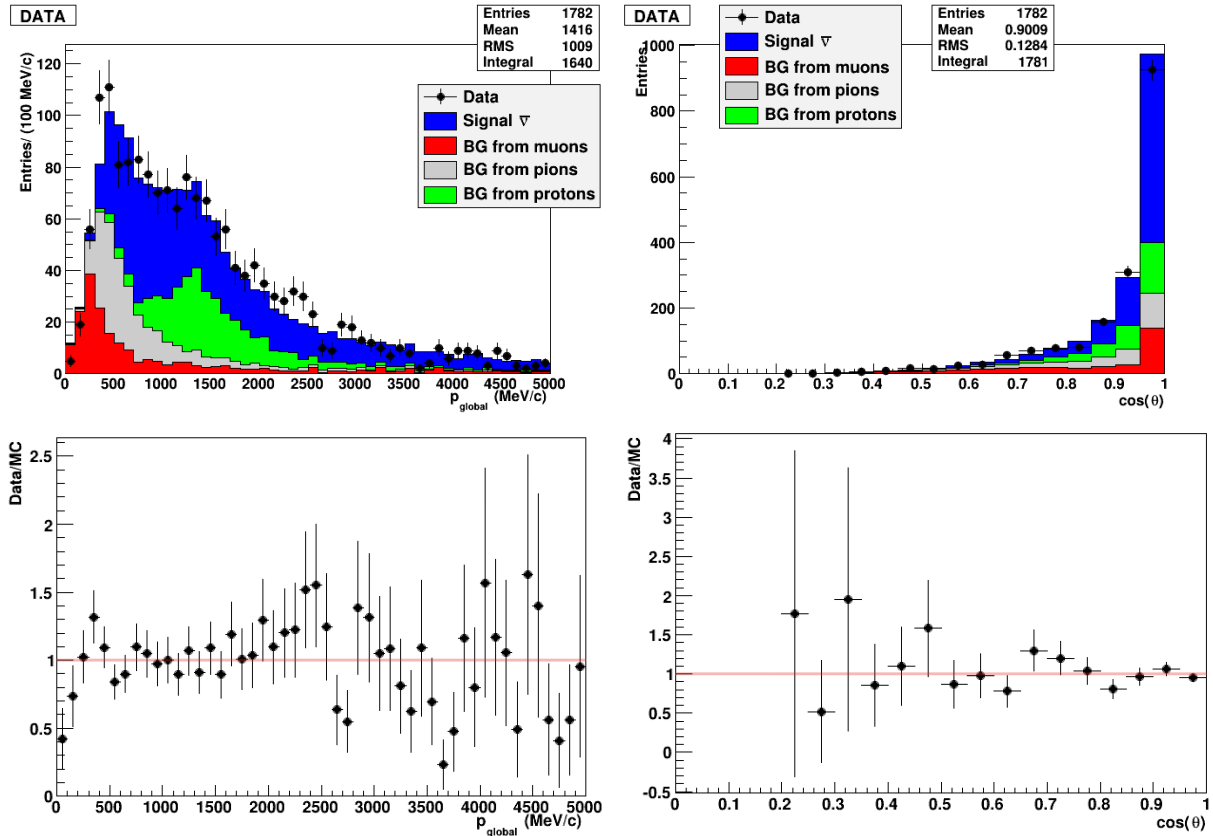


Figure 4.24: Top: Data and corrected MC kinematic spectra after the fit. The MC is broken down by signal and background sources. Bottom: Data/MC ratios for kinematic spectra after the fit.

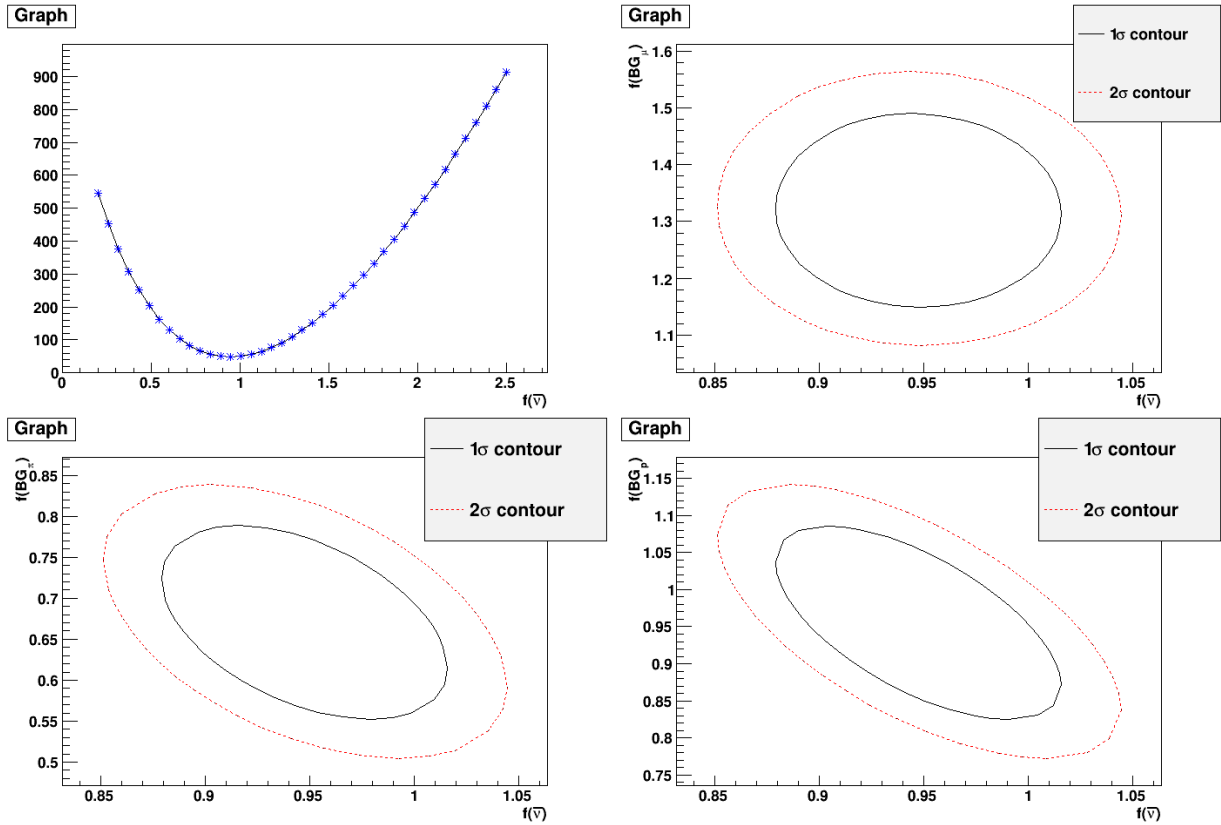


Figure 4.25: Likelihood minimum and f contours for each background component versus signal.

4.5.2 Effect of detector systematics in the likelihood fit

The kinematic spectra of data, corrected MC and one hundred MC toys are shown in Figure 4.26. As expected the larger uncertainty, mainly due to the TPC proton PID systematic, lies in the region $0.8 < p < 1.3$ GeV/c. The result obtained applying the likelihood fit on one thousand MC toys is shown in Figure 4.27 where it can be seen that the mean value of the fitted distribution differs from the value of $f_{\bar{\nu}_\mu}$ shown in Table 4.4. This occurs because systematic uncertainties are not gaussian and since the corrected MC is used to evaluate the effect of flux and cross section systematics, the difference between the mean value of the distribution in Figure 4.27 and the $f_{\bar{\nu}_\mu}$ in Table 4.4 is included as additional systematic source. The summary of the detector systematic uncertainty is shown in Table 4.5. Before the estimation of flux and cross section uncertainties, the

Table 4.5: Summary of the effect of detector systematics in the fit.

Systematic source	detector syst. err. on $f_{\bar{\nu}_\mu}$
width of syst. throws	0.045
difference from corrected MC	0.025

rescaling factor $f_{\bar{\nu}_\mu}$ is then estimated to be:

$$f_{\bar{\nu}_\mu} = 0.97 \pm 0.07 \text{ (stat.)} \pm 0.05 \text{ (det. syst.)} \quad (4.13)$$

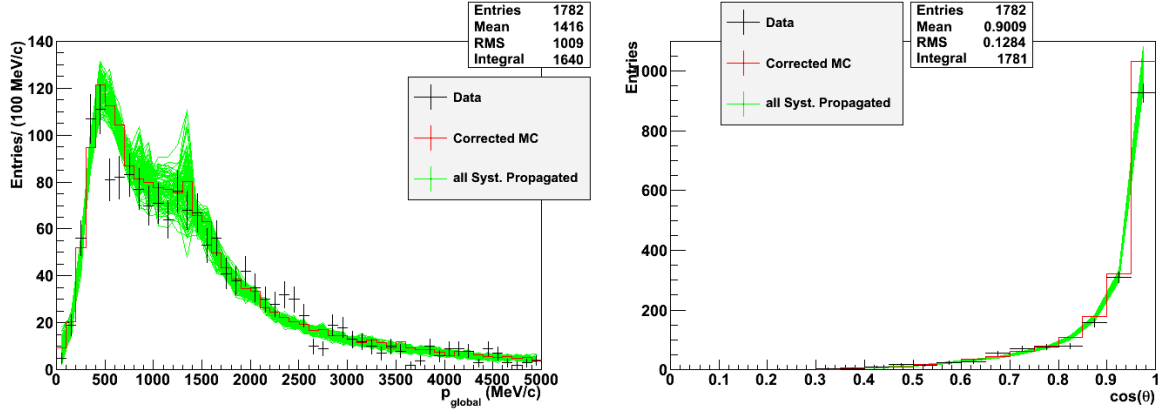


Figure 4.26: Kinematic spectra of data (black), corrected MC (red) and MC toys (green).

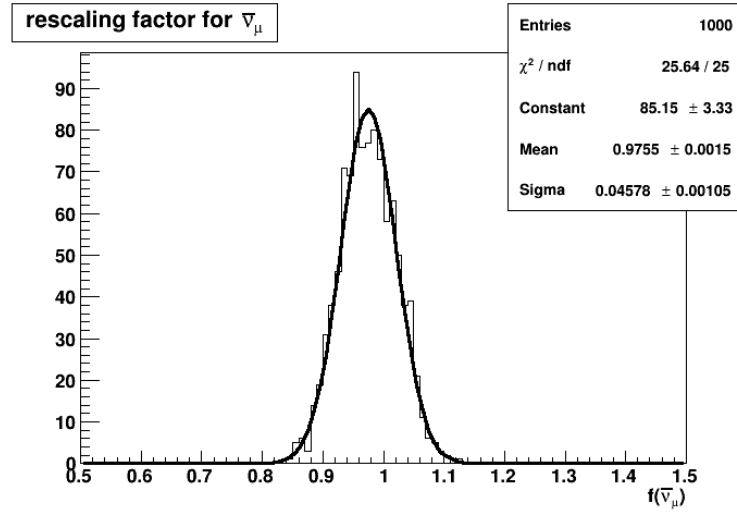


Figure 4.27: Fitted value for $f_{\bar{\nu}_\mu}$ when all systematics are enabled.

4.6 Flux and cross section systematics

In Section 3.1 I discussed how the MC sample is produced. The neutrino generator (NEUT/GENIE) cross section models and the flux predictions coming from JNUBEAM have their own systematic uncertainties which affect all the T2K analyses. In T2K, these systematics are reduced using the constraint provided by ND280 which uses a series of external and in-situ measurements:

- Flux:
 - proton beam monitors measurements;
 - NA61 hadron production measurements.
- Cross sections:
 - neutrino interaction cross sections measurements coming from external neutrino experiments such as MiniBooNE, SciBooNE and NOMAD.
- ND280 data:
 - measurements from the ND280 off-axis detector.

The ND280 constraint is based on a likelihood fit of MC to ND280 data, where the informations from external experiments or measurements are used as prior constraints for flux and cross section in the fit. The binned likelihood ratio is defined as follow:

$$\mathcal{L}_{\text{ND280}}^r = \frac{\pi(\vec{b})\pi(\vec{x})\pi(\vec{d}) \prod_i [N_i^p(\vec{b}, \vec{x}, \vec{d})]^{N_i^d} e^{-N_i^p(\vec{b}, \vec{x}, \vec{d})} / N_i^d!}{\pi(b_{\text{nom}})\pi(x_{\text{nom}})\pi(d_{\text{nom}}) \prod_i [N_i^d]^{N_i^d} e^{-N_i^d} / N_i^d!}, \quad (4.14)$$

where N_i^d and N_i^p are the binned number of events in the data and MC prediction respectively, $\pi(\vec{b})$, $\pi(\vec{x})$ and $\pi(\vec{d})$ are the prior probability density functions (multivariate normal distributions) of flux, cross sections and ND280 detector systematics respectively. The denominator is the likelihood in the numerator evaluated for $N_i^p = N_i^d$ and the nuisance parameters at their nominal values, corresponding to the maximum value of the likelihood in the numerator.

Reducing flux and cross sections systematics is crucial for the oscillation analyses because these are the largest uncertainties that affect the measurements at SK. The constraint provided by ND280 has been called the “**BANFF fit**”, as it was developed by the *Beam And ND280 Flux extrapolation task Force (BANFF)* [135]. Currently only ND280 ν_μ sample is used in the BANFF fit [136]. In 2014 also the $\bar{\nu}_\mu$ sample selected with my analysis and the ND280 ν_e sample will be added to the BANFF fit to better constraint $\bar{\nu}_\mu$ and ν_e fluxes and cross sections uncertainties at SK. In Figure 4.28 the flux and cross sections parameters correlations prior and after the BANFF fit are shown. The BANFF output can be used to:

- test the compatibility of the BANFF fit with the $\bar{\nu}_\mu$ beam data at ND280;
- include the systematic errors due to the flux and cross-sections uncertainties in the $\bar{\nu}_\mu$ analysis;
- test how much the BANFF fit results reduce flux and cross sections uncertainties in the $\bar{\nu}_\mu$ analysis.

4.6.1 Compatibility of BANFF fit with the $\bar{\nu}_\mu$ beam data at ND280

Testing the compatibility of BANFF fit with my analysis is important in order to understand if the ND280 constraint gives a good estimation of the $\bar{\nu}_\mu$ flux component to the oscillation analyses. To do that, the corrected MC must be re-weighted event by event for the central values of the BANFF fit output, shown in Table 4.6. The resulting new MC sample is called BANFF MC. The effect of this re-weight is shown in Figure 4.29 and leads to a reduction of all the four components input

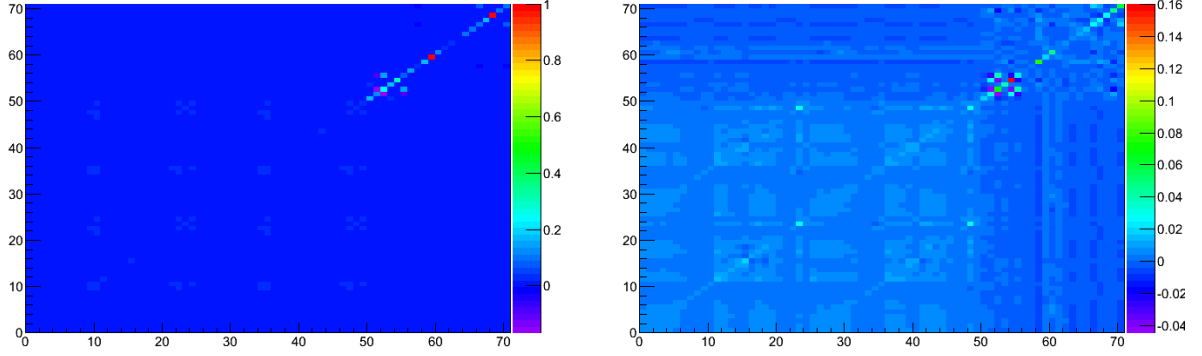


Figure 4.28: The parameter correlations prior to (left) and after (right) the BANFF fit. The parameters are numbered: 0-24 ND280 flux parameters, 25-49 SK flux parameters and the rest are cross section parameters: 50-55 FSI (Final State Interactions) parameters, 56 M_A^{QE} , 57 M_A^{RES} , 58 CC Other Shape, 59 spectral function, 60 binding energy, 61 fermi momentum, 62 pion-less Δ decay, 63-65 CCQE normalization, 66-67 CC1 π normalization, 68 CC Coh. normalization, 69 NC Other normalization, 70 NC1 π^0 normalization [136].

Table 4.6: Post-BANFF fit flux and cross section systematics central values [136].

Systematic	BANFF central values	parameters
ν_μ flux	$\sim 0.9-1.00$	11
$\bar{\nu}_\mu$ flux	$\sim 0.98-1.01$	5
ν_e flux	$\sim 0.9-1.01$	7
$\bar{\nu}_e$ flux	$\sim 0.9-1.0$	2
FSI	$\sim -0.52-0.38$	6
M_A^{QE} [GeV]	1.22	1
M_A^{RES} [GeV]	0.96	1
CC Other Shape [GeV]	0.3	1
Spectral Function (^{12}C & ^{16}O)	0.28	1
E_b (^{12}C & ^{16}O) [MeV/c]	28.885	1
P_F (^{12}C & ^{16}O) [MeV/c]	269.37	1
π -less Δ decay	0.17	1
CCQE norm.	0.96, 0.90, 0.87	3
CC1 π norm.	1.20, 1.07	2
CC Coh. norm.	0.47	1
NC Other norm.	1.32	1
NC1 π^0 norm.	1.08	1

to the fit as it can be seen from Figure 4.30. The expected number of events predicted from the BANFF MC are detailed in Table 4.7.

Fitting the BANFF MC on data, I obtained the result shown in Table 4.8. As can be seen the best fit value of $f_{\bar{\nu}_\mu}$ is closer to one with respect to the value shown in Table 4.4 obtained with the

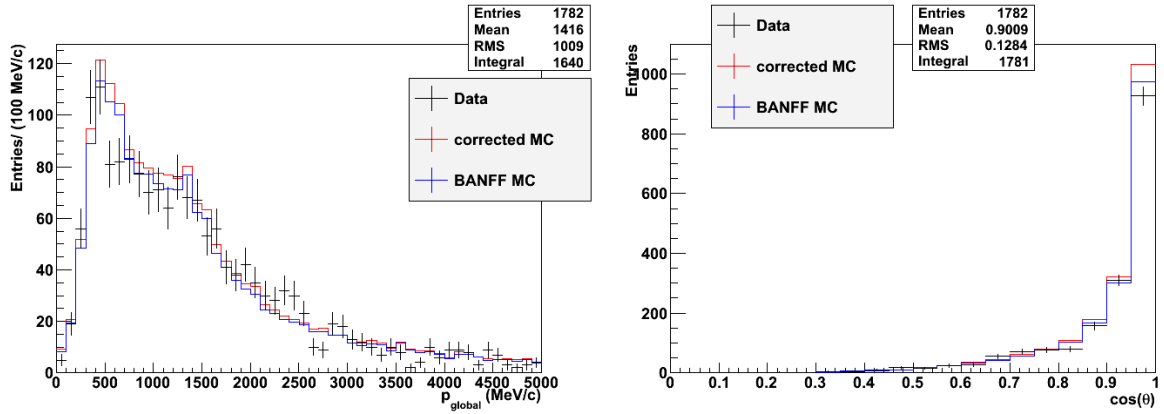


Figure 4.29: Kinematic spectra of data (black), corrected MC (red) and BANFF MC (blue).

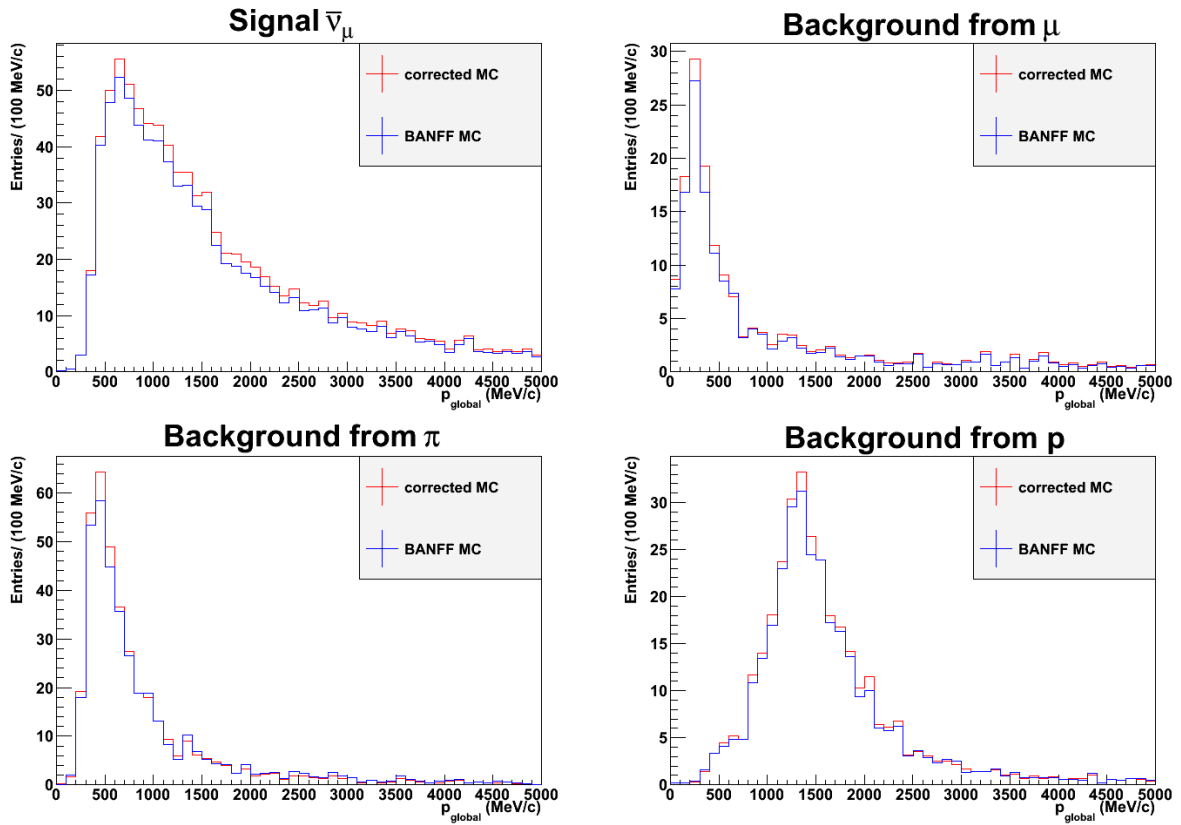


Figure 4.30: Momentum spectra of inputs to the fit corrected MC (red) and BANFF MC (blue).

corrected MC. This means that even if the BANFF fit currently uses only the ND280 ν_μ sample, is however able to give a good estimation of $\bar{\nu}_\mu$ flux to the oscillation analyses. In Figure 4.31 the obtained kinematic spectra after the fit and their data/MC ratios are shown, while in Figure 4.32 there are the global minimum of the likelihood and the contours.

Table 4.7: Composition of the final selected sample broken down by input to the fit.

Category	Composition (%)	corrected MC expected events
Signal $\bar{\nu}_\mu$	49	873.6
Background from μ	11	190.5
Background from π	22	390.3
Background from p	18	325.8

Table 4.8: Value of the parameters for best fit for the corrected MC. The rescaling factor and absolute number of events are indicated for each component.

	f	N_{events}
$f_{\bar{\nu}_\mu}$	1.01 ± 0.08	879.6 ± 68
f_{BG_μ}	1.43 ± 0.19	273 ± 36.5
f_{BG_π}	0.69 ± 0.13	271.3 ± 52.3
f_{BG_p}	1.02 ± 0.14	335 ± 45

4.6.2 Inclusion of flux and cross sections systematic errors

The inclusion of flux and cross sections systematics in the $\bar{\nu}_\mu$ analysis is done in a similar way to what was done for detector systematics. One thousand MC toys are produced with both flux and cross sections systematics propagated. These uncertainties are propagated by re-weighting event by event the corrected MC by a random value thrown in the post BANFF fit fractional covariance matrix in Figure 4.28 on the right. Finally one thousand likelihood fit are performed on these one thousand toy MC.

The extraction of a random value from the BANFF post-fit covariance matrix is done using the Cholesky decomposition. The Cholesky decomposed matrix u of the matrix v is given by:

$$v = uu^*, \quad (4.15)$$

where $u^* = \bar{u}^T$ is the conjugate transpose of u . The existence of u is guaranteed for positive definite matrices. All covariance matrices are positive definite. If the matrix u is multiplied by a Gaussian multivariate vector, i.e. a vector where each entry g_i is a Gaussian random variable, it can provide weights (w_i) to each bin i as defined below:

$$w_i = 1 + \sum_j u_{ij} g_j. \quad (4.16)$$

This weight w_i will be then applied to the event. The output of this procedure is shown in Figure 4.33. The result obtained applying the likelihood fit on one thousand MC toys is shown in the Figure 4.34. Taking into account the value of $f_{\bar{\nu}_\mu}$ obtained from the likelihood fit of the BANFF MC and the width of the distribution 4.34 as flux and cross section uncertainties to be consistent with the T2K oscillation analyses, the final result is:

$$f_{\bar{\nu}_\mu} = 1.01 \pm 0.08 \text{ (stat.)} \pm 0.05 \text{ (det. syst.)} \pm 0.09 \text{ (flux and x-sec syst.)} \quad (4.17)$$

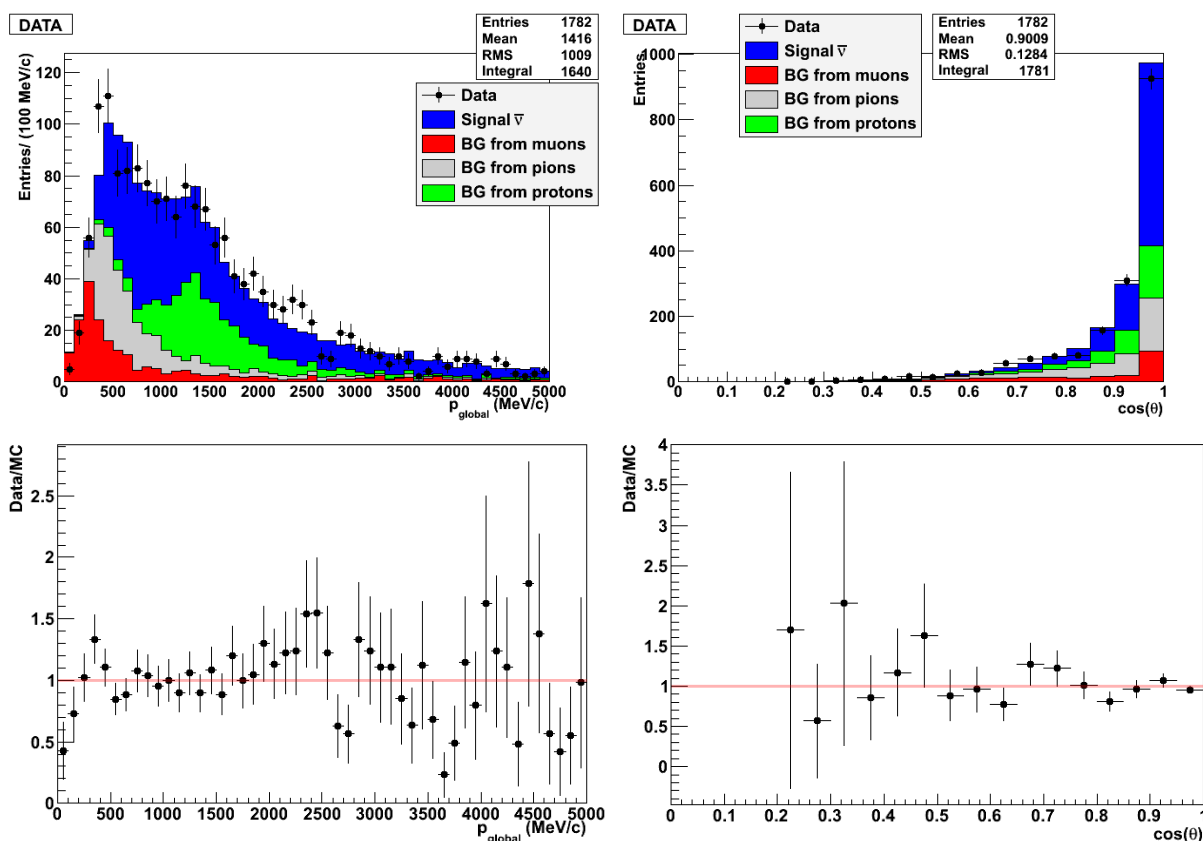


Figure 4.31: Top: Data and BANFF MC kinematic spectra after the fit. The MC is broken down by signal and background sources. Bottom: Data/MC ratios for kinematic spectra after the fit.

The power of the BANFF fit in the reduction of flux and cross sections uncertainty in the $\bar{\nu}_\mu$ analysis can be checked using the pre-BANFF fit covariance matrix shown in Figure 4.28 on the left. The procedure is the same and the result is shown in Figure 4.35. As can be seen, the BANFF fit reduce the flux and cross section uncertainties of a 50%.

4.7 Summary and outlook

As anticipated at the begin of Chapter 3 the $\bar{\nu}_\mu$ sample selected with this analysis will be used to improve the the ND280 constraints on $\bar{\nu}_\mu$ flux and cross section systematics in the oscillation analyses from 2014. At present, the BANFF fit is able to constrain the systematic uncertainties listed in Table 4.6. The $\bar{\nu}_\mu$ flux is predicted using the correlations between the ν_μ and $\bar{\nu}_\mu$ components of the beam. However the ratio $\sigma_{\bar{\nu}}/\sigma_\nu$ (that is an important systematic error source in the disappearance analysis) is not constrained at all. At the moment the uncertainty for the $\bar{\nu}_\mu$ flux is $\sim 9\text{-}14\%$ [136], whereas for $\sigma_{\bar{\nu}}/\sigma_\nu$ is $\sim 40\%$ [117].

The result (4.17) will allow the reduction of both these uncertainties. The quantitative effect will be precisely evaluated only in Spring 2014, when this result will become an official input of the BANFF fit, however a raw estimation can be done already now. The $\bar{\nu}_\mu$ flux uncertainty can be reduced down to $\sim 9\%$ for the whole energy spectra (combining statistic and detector systematic

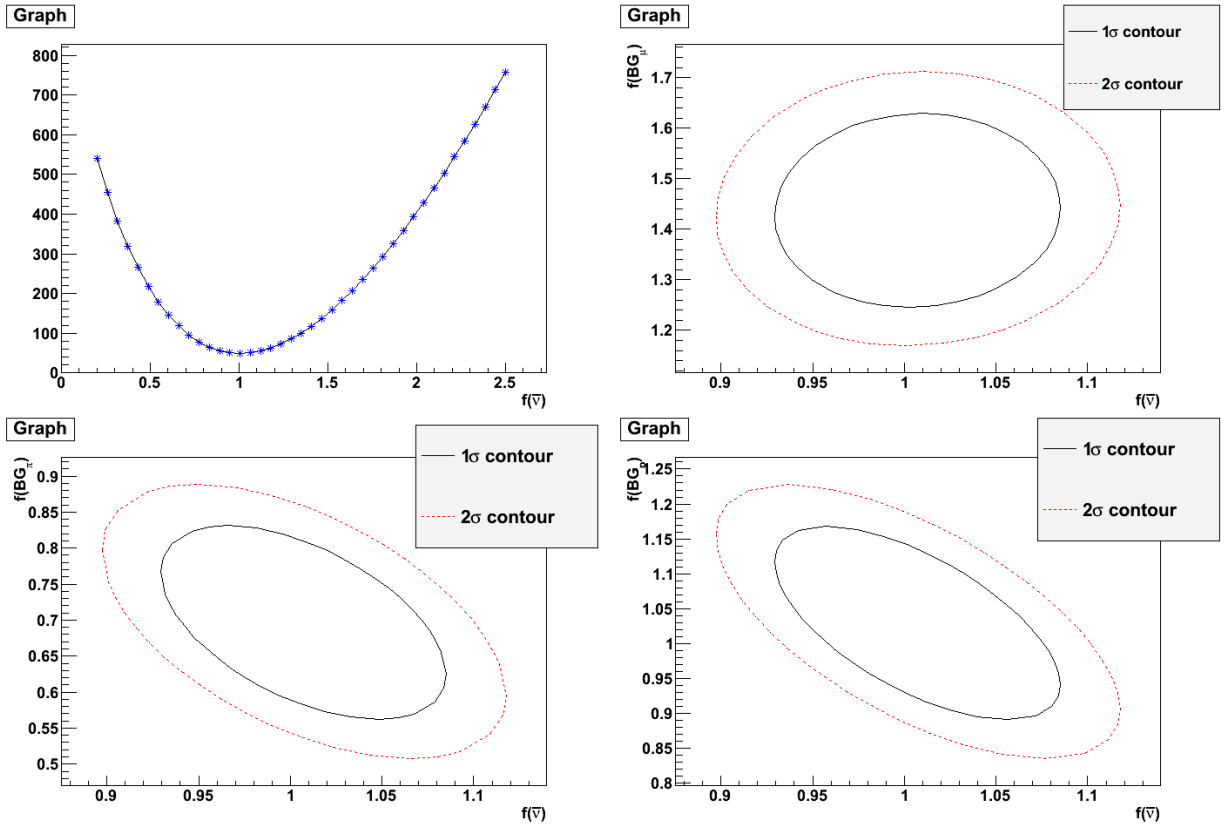


Figure 4.32: Likelihood minimum and f contours for each backgrounds component versus signal.

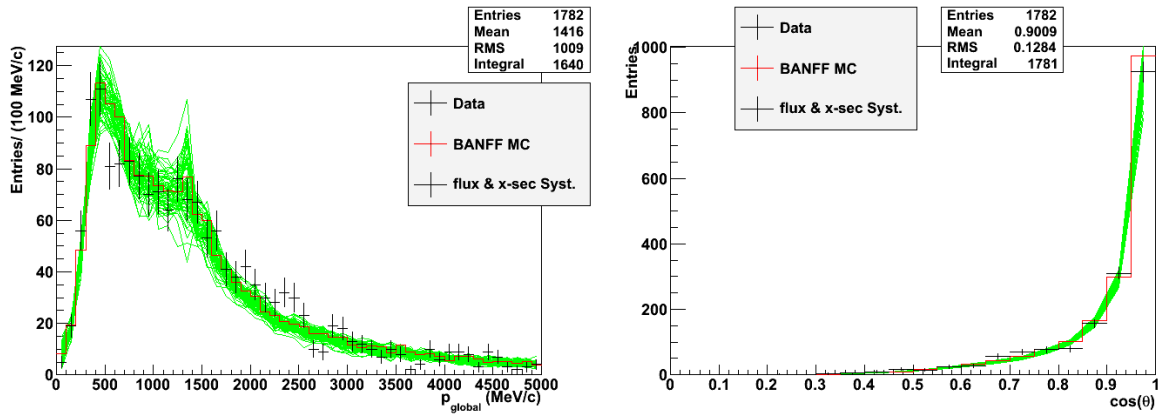


Figure 4.33: Kinematic spectra of data (black), BANFF MC (red) and MC toys (green).

errors). Much more interesting is the impact on $\sigma_{\bar{\nu}}/\sigma_{\nu}$ systematic error. In this case it is possible to obtain:

$$f_{\bar{\nu}\mu} = 1.01 \pm 0.08 \text{ (stat.)} \pm 0.1 \text{ (syst.)} = 1.01 \pm 0.13 \text{ (total)} \quad (4.18)$$

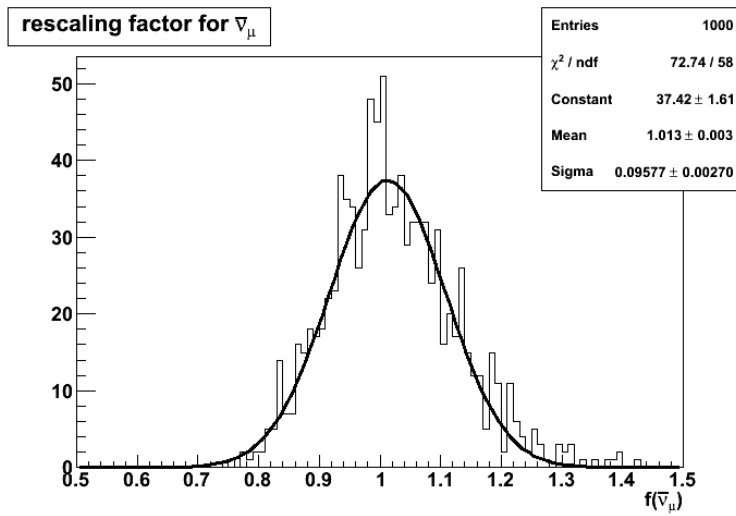


Figure 4.34: Fitted value for $f_{\bar{\nu}_\mu}$ based on flux and cross-section systematics after the BANFF fit.

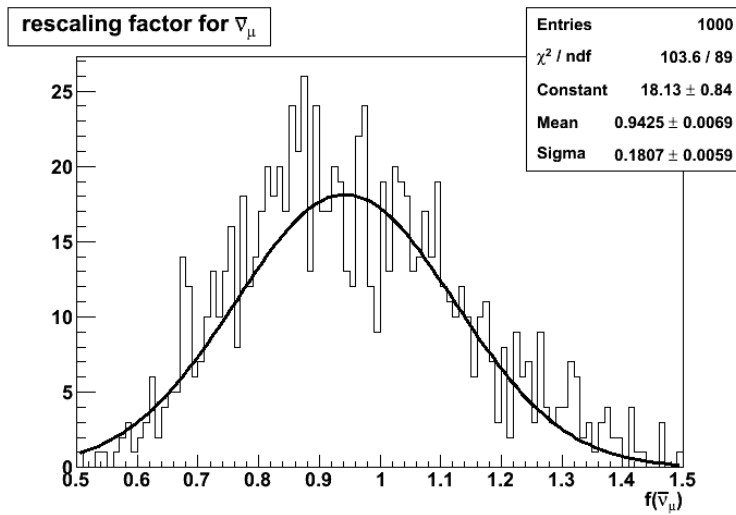


Figure 4.35: Fitted value for $f_{\bar{\nu}_\mu}$ based on flux and cross-section systematics before the BANFF fit.

allowing a reduction from $\sim 40\%$ to $\sim 13\%$ of this uncertainty.

Chapter 5

Conclusions

In T2K oscillation analyses the largest uncertainties are due to flux and cross section systematics in the measurements at SK. These uncertainties are reduced by exploiting the data collected from the close detector ND280. Through the fit of the MC on data (BANFF fit), ND280 provides constraints on flux and cross section uncertainties that are then used in the oscillation analyses. However, since only the information related to the ν_μ component of the beam is used in the BANFF fit, the systematic on the $\bar{\nu}_\mu$ flux is only slightly reduced, while the uncertainty on the $\sigma_{\bar{\nu}}/\sigma_\nu$ ratio does not get any benefit from the BANFF fit.

In this thesis I present the measurement of the $\bar{\nu}_\mu$ component in the T2K beam and it is worth noting that the determination of the $\bar{\nu}_\mu$ component allows a substantial reduction of the above mentioned $\bar{\nu}_\mu$ flux systematic as well as the $\sigma_{\bar{\nu}}/\sigma_\nu$ ratio one. The study has been performed using all the data collected until now (from run 1 to run 4) for a total of 6.63×10^{20} POT.

Since at the energy peak (~ 600 MeV) of T2K beam and in $\bar{\nu}_\mu$ CC interactions, the μ^+ is, in 95% of the cases, the positive reconstructed track with the highest momentum in the ND280 tracker, my analysis is based on the selection of such tracks by combining FGD, TPC and ECal informations. By doing so, I was able to: i) remove the huge background coming from protons generated in the ν_μ CC inclusive interactions; ii) reject the low energy electromagnetic background (e^+ and e^- pairs coming from γ conversions); and iii) decrease as much as possible the background coming from pions generated in the CCnonQE interactions. The PID selection criteria have been optimized to maximize efficiency and purity, while the ν_μ CCnonQE background was reduced by accepting that only one (positive) track crossing the TPC per event. After the selection I performed a likelihood fit on the kinematics distributions, extracting the rescaling factor used to correct the expected $\bar{\nu}_\mu$ rate obtained by MC in order to better match the data (see Section 3.9 for more details). Finally I have also discussed and evaluated the systematic uncertainties affecting my analysis as well as the perspective integration in the BANFF fit.

The final result of my analysis for the rescaling factor $f_{\bar{\nu}_\mu}$ is:

$$f_{\bar{\nu}_\mu} = 1.01 \pm 0.08 \text{ (stat.)}, \quad (5.1)$$

which, including the systematic errors shown in Table 5.1, becomes:

$$f_{\bar{\nu}_\mu} = 1.01 \pm 0.08 \text{ (stat.)} \pm 0.1 \text{ (syst.)} = 1.01 \pm 0.13 \text{ (total)}. \quad (5.2)$$

As it is evident, my result is in good agreement with the MC expectations and actually increases the effectiveness of the estimated $\bar{\nu}_\mu$ background at SK in the oscillation analyses.

The precision achieved in the knowledge of the ratio data/MC, while slightly decreasing the current

Table 5.1: Summary of the systematic errors in the $\bar{\nu}_\mu$ analysis.

Systematic source	Error on $f_{\bar{\nu}_\mu}$
Detector systematic errors	0.05
Flux and cross section	0.09
Total	0.1

systematic uncertainty on the $\bar{\nu}_\mu$ flux at SK, strongly reduces (from $\sim 40\%$ to $\sim 13\%$) the systematic uncertainty on $\sigma_{\bar{\nu}}/\sigma_\nu$ in the oscillation analyses.

The T2K collaboration is planning to swap the beam polarity (i.e. in this case the flux will be mainly composed of $\bar{\nu}_\mu$) to increase the T2K sensitivity to the CP violating phase. A first run (corresponding to $\sim 10^{20}$ POT) is scheduled in Spring 2014. To obtain a first raw estimation of the ND280 performances in this conditions, I also performed a slightly modified version of my analysis to a MC data set, the results are shown in Appendix A.

Appendix A

The muon anti-neutrino analysis with an anti-neutrino beam

In the oscillation probability the terms with the CP violating phase δ_{CP} are proportional to $\sin \theta_{13}$. Now that $\theta_{13} \neq 0$ has been measured with a significance of 7.3σ and since it is known that it is relatively large, the measurement of δ_{CP} becomes accessible. In Section 2.1.4 I presented the updated T2K physics program which include the initial measurement of δ_{CP} and determination of θ_{23} octant.

In Figures A.1 and A.2 the achievable T2K sensitivities for the δ_{CP} and θ_{23} octant are shown, considering two options: (1) data taking only in neutrino beam (figures on the left); (2) data taking shared between neutrino and anti-neutrino beam (figures on the right). As can be seen, the second option is the best solution because enhance the T2K sensitivity for the δ_{CP} and θ_{23} octant. However since T2K has never took data in anti-neutrino mode (i.e. with a flux mainly composed of $\bar{\nu}_\mu$), it is strictly necessary to understand if, as it happens with ν_μ in the standard neutrino mode, the close detector ND280 is able to extract the anti-neutrino signal with an acceptable purity and efficiency and how much it can reduce systematic errors at SK in this case. For this reason the T2K collaboration planned an anti-neutrino mode pilot run in 2014.

In this appendix I will present a MC based study of the efficiency and purity achievable by ND280 in the selection of $\bar{\nu}_\mu$ CC interactions and a preliminary estimation of the detector systematic errors in view of the anti-neutrino mode pilot run. The MC simulation of the anti-neutrino beam ($\bar{\nu}$ MC) used to perform this study, which counts $\sim 1.1 \times 10^{21}$ POT, is produced using the TIER2 in Bari and it is the first official T2K MC of this kind. The $\bar{\nu}$ MC is produced following the same procedure presented in Section 3.1. Besides the beam composition, the only difference with respect to the standard ν MC used in the analysis presented in Chapter 3 is that in the $\bar{\nu}$ MC production the interactions are simulated only in the basket of ND280¹.

The following plots and the achievable purity in the selection of $\bar{\nu}_\mu$ CC interactions have been showed on September 2013 at the JPARC PAC to point out the ND280 potentiality in anti-neutrino mode.

A.1 $\bar{\nu}_\mu$ CC event selection

As a first step, the selection criteria that I applied to the $\bar{\nu}$ MC are exactly the same presented in Section 3.5. The *pre-selection* leads to the result shown in Figure A.3.

¹ It is possible to divide ND280 in two main volumes: the *Basket* composed by P0D, tracker and DsECal and the *Magnet* composed by the *Basket* plus BrECal and magnet.

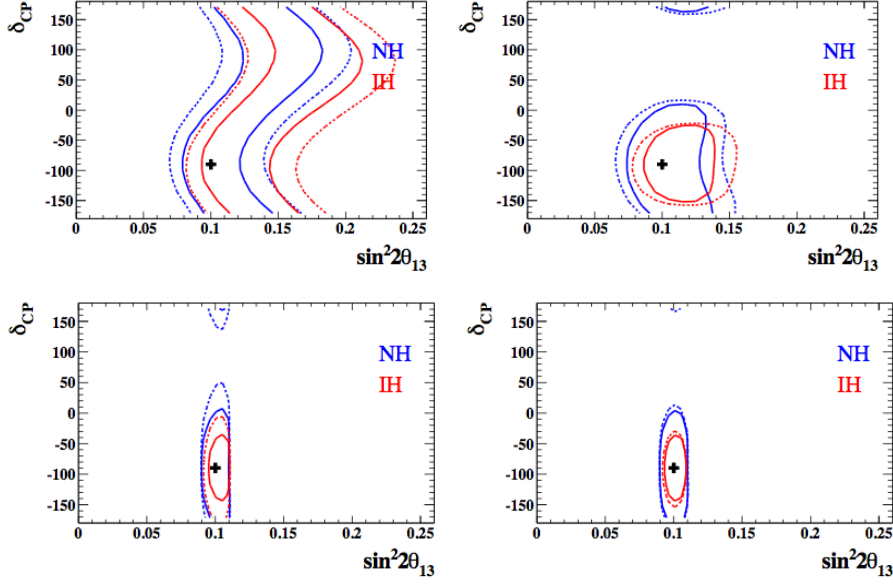


Figure A.1: δ_{CP} versus $\sin^2 2\theta_{13}$ 90% C.L. allowed regions for 7.8×10^{21} POT. Contours are plotted assuming true $\sin^2 2\theta_{13} = 0.1$, $\delta_{CP} = -90^\circ$, $\sin^2 \theta_{23} = 0.5$, $\Delta m_{23}^2 = 2.4 \times 10^{-3} \text{ eV}^2$ and normal mass hierarchy. The blue curves are fit assuming the normal mass hierarchy, while the red are fit assuming the inverted mass hierarchy. Left: 100% ν -running mode, without (top) and with (bottom) reactor constraint. Right: 50% ν – 50% $\bar{\nu}$ -running mode, without (top) and with (bottom) reactor constraint. The solid contours are with statistical error only, while the dashed contours include a conservative estimation of systematic errors.

As it can be seen, in this case the highest momentum positive tracks selected are mainly coming from $\bar{\nu}_\mu$ interactions. As expected, the momentum spectrum shows a well defined peak around 0.6 GeV/c due to the beam interactions in the detector, whereas the low energy peak is much smaller (see Figure 3.8). The main contribution to the low energy peak comes from ν_μ CC interactions with backward going negative muons which are mistakenly reconstructed as positive muons. When the beam polarity is reversed, only $\sim 27\%$ of the beam will be composed by ν_μ (see Figure A.4) and the corresponding background contribution will be thus reduced.

Applying the TPC PID (see Section 3.6.1 for more details) I obtain the result shown in Figure A.5. As it can be seen a large amount of protons, mainly coming from ν_μ CC and $\bar{\nu}_\mu$ NC interactions, is rejected in the peak region (see Figure A.6). At this stage, the $\bar{\nu}_\mu$ CC purity of the sample is $\sim 80\%$, 67% of which are CCQE interactions and 33% are CCnonQE interactions.

The remaining background coming from protons and pions produced by ν_μ CCnonQE interactions can be reduced to a value lower than 8% using the “one TPC track multiplicity” cut (see Section 3.6.1 for more details). Since this cut reject all the events with more than one track in the TPC, the $\bar{\nu}_\mu$ CCQE component will be enhanced after this cut (see Figure A.7).

Now concerning the purity, the sample is composed for 91.6% of $\bar{\nu}_\mu$ CC interactions, 71.6% of which are CCQE and 28.4% CCnonQE interactions. It is important to notice that even if the “one TPC track multiplicity” cut is crucial to reject the remaining background, also a sizeable part of $\bar{\nu}_\mu$ CCnonQE interactions will be rejected applying it (see Figure A.8).

Finally I tested the effect of the ECal on the selected sample. The ECal PID further increase the

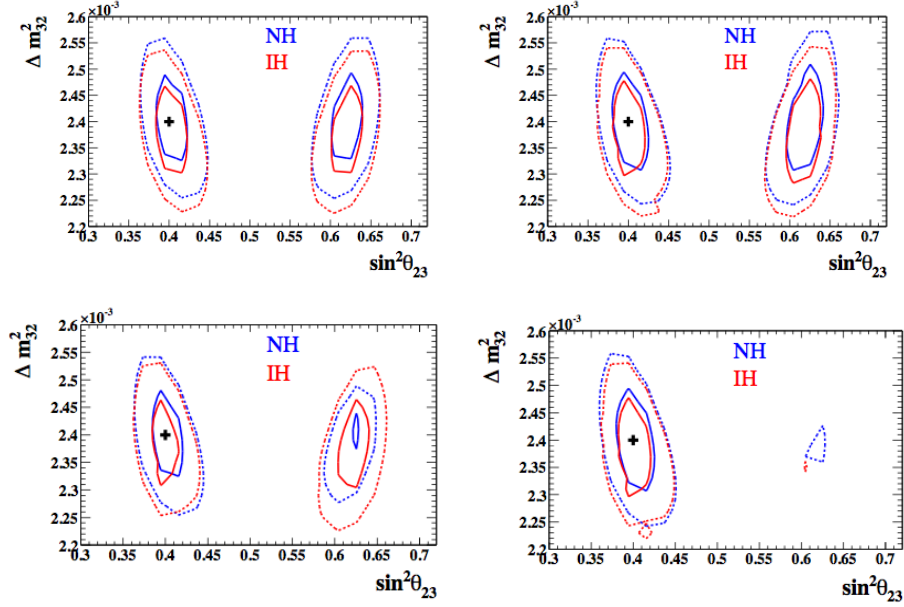


Figure A.2: Δm_{23}^2 versus $\sin^2 \theta_{23}$ 90% C.L. allowed regions for 7.8×10^{21} POT. Contours are plotted assuming true $\sin^2 2\theta_{13} = 0.1$, $\delta_{CP} = 0^\circ$, $\sin^2 \theta_{23} = 0.4$, $\Delta m_{23}^2 = 2.4 \times 10^{-3} \text{ eV}^2$ and normal mass hierarchy. The blue curves are fit assuming the normal mass hierarchy, while the red are fit assuming the inverted mass hierarchy. Left: 100% ν -running mode, without (top) and with (bottom) reactor constraint. Right: 50% $\nu - 50\%$ $\bar{\nu}$ -running mode, without (top) and with (bottom) reactor constraint. The solid contours are with statistical error only, while the dashed contours include a conservative estimation of systematic errors.

sample purity up to $\sim 96\%$, 78.5% of which are CCQE and 21.5% CCnonQE interactions (see Figure A.9). With the ECal PID is possible to obtain a “golden sample” of $\bar{\nu}_\mu$ CC interactions at the price of a significant loss of the selection efficiency, as will be detailed in Sections A.2 and A.3.

A.2 μ^+ selection efficiency and purity

Obviously in an anti-neutrino mode run, there are more μ^+ produced in $\bar{\nu}_\mu$ interactions with respect to the ones produced in a standard neutrino mode run. As a consequence the μ^+ selection described in Section 3.5 gives a much better result in terms of efficiency and purity. In fact, the sample reaches a μ^+ purity higher than 90% just by applying the selection up to the “one TPC track multiplicity” cut and either an efficiency of $\sim 70\%$ if the selection is applied up to the “one TPC track multiplicity” cut, or $\sim 50\%$ if the selection is applied up to the ECal PID (see Figure A.10 on the left). In this case, the efficiency is defined as in (3.18), thus it is relative to the μ^+ contained in the sample at the end of the *pre-selection*.

Figure A.10 on the right shows the efficiency of the μ^+ selection versus the momentum. As can be seen the efficiency in the selection of μ^+ has a peak around 600 MeV/c in correspondence to the T2K energy peak.

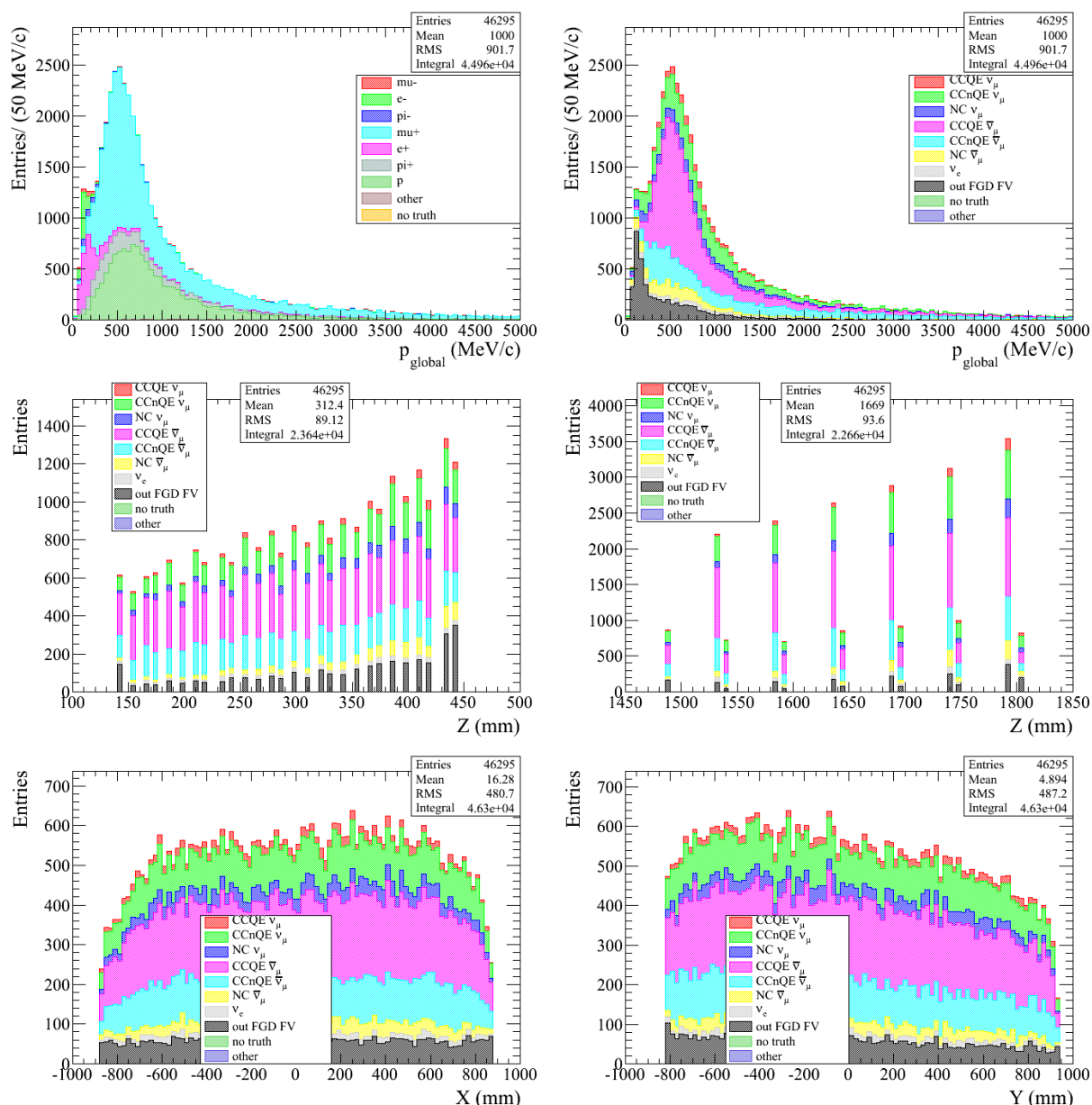


Figure A.3: Sample after the *pre-selection*. Top: the momentum spectrum of the most energetic positive tracks. The MC sample is stacked and broken down according to final state particle type (left) and kind of reaction (right). Middle: the z coordinate of the reconstructed neutrino interaction point in FGD1 (left) and FGD2 (right). Bottom: the x (left) and y (right) coordinate of the reconstructed neutrino interaction point.

A.3 Analysis results

Figure A.11 shows the overall $\bar{\nu}_\mu$ CC selection efficiency and purity achieved. In this plot, the reconstruction efficiency is taken into account too. As it can be seen, if the selection criteria are applied up to the “one TPC track multiplicity” cut, the purity is $\sim 4\%$ lower, but the efficiency is

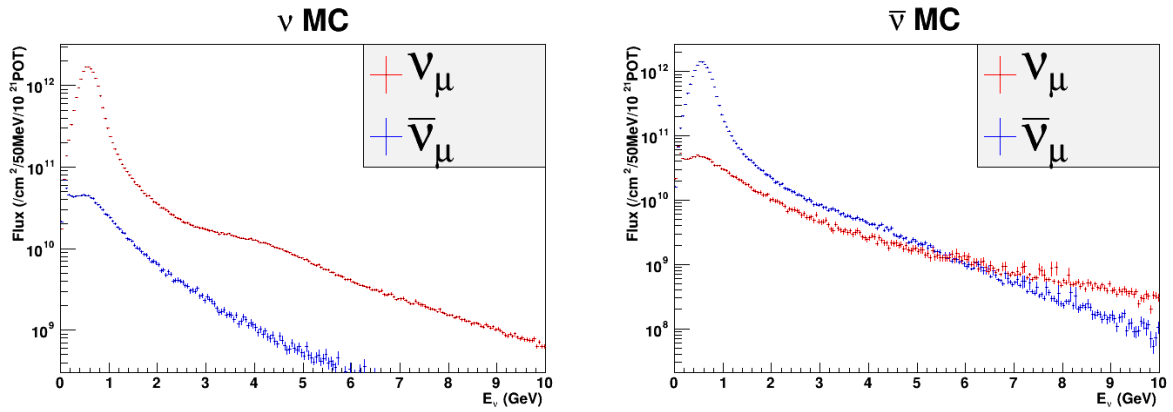


Figure A.4: Left: ν_μ and $\bar{\nu}_\mu$ composition at ND280 of the T2K ν flux in neutrino mode. Right: ν_μ and $\bar{\nu}_\mu$ composition at ND280 of the T2K $\bar{\nu}$ flux in anti-neutrino mode.

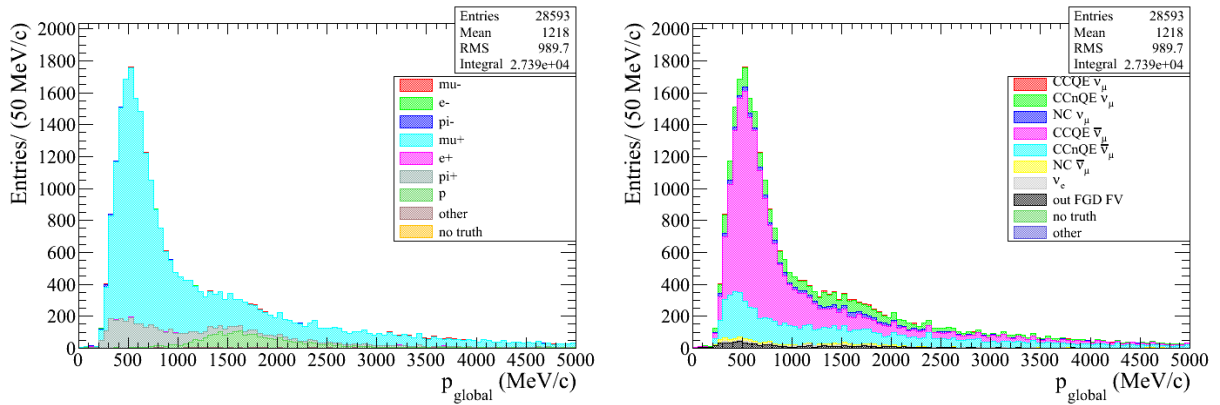


Figure A.5: Momentum spectrum of the most energetic positive tracks after the TPC PID.

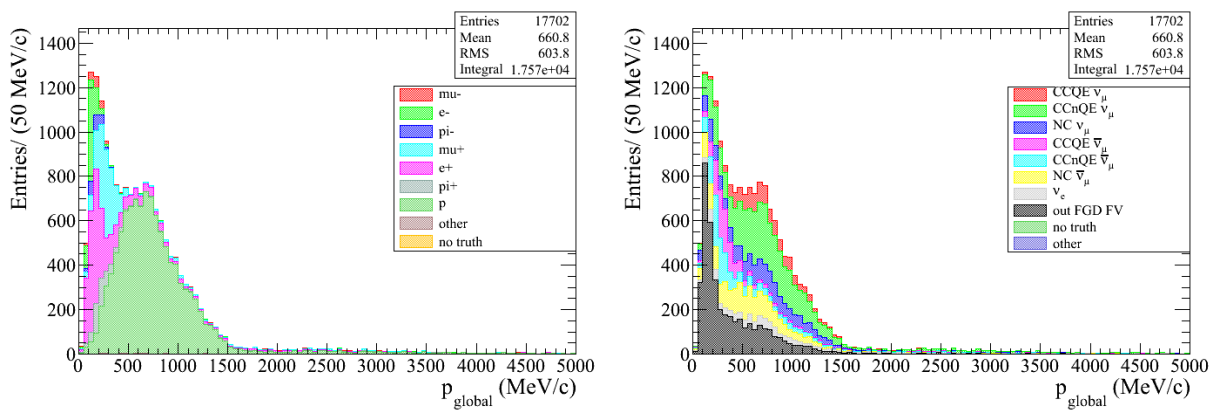


Figure A.6: Momentum spectrum of the most energetic positive tracks rejected from the TPC PID.

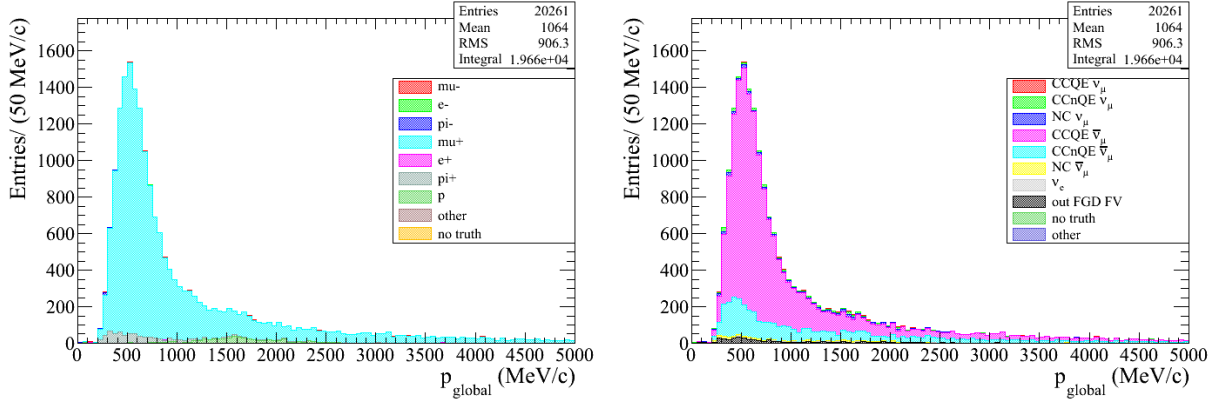


Figure A.7: Momentum spectrum of the most energetic positive tracks after the “one TPC track multiplicity” cut.

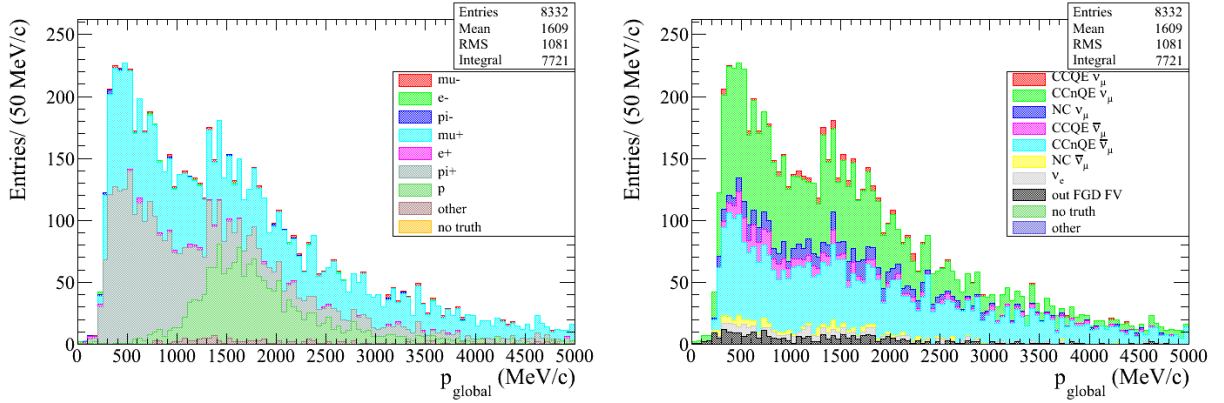


Figure A.8: Momentum spectrum of the most energetic positive tracks rejected from the “one TPC track multiplicity” cut.

$\sim 15\%$ larger with respect to the purity and the efficiency obtained when applying the selection criteria up to the end (Ecal PID). For this reason the standard selection criteria used in neutrino mode (see Section 3.5) can be modified in anti-neutrino mode, excluding the Ecal part, as follow:

- *pre-selection of the most energetic positive track in the tracker;*
- **TPC PID:** The TPC particle identification (PID) criteria are applied to the most energetic positive track that satisfies the *pre-selection*;
- **one TPC track multiplicity:** Only events with one TPC-FGD matched track are selected in order to reject as much as possible the background coming from ν_μ CCnonQE interactions.

The kinematic spectra of the final sample broken down by final state particle, neutrino interaction type and neutrino parent type are shown in Figure A.12. The composition of the final sample and the expected number of reconstructed events for 1.1×10^{21} POT are detailed in Tables A.1, A.2 and A.3.

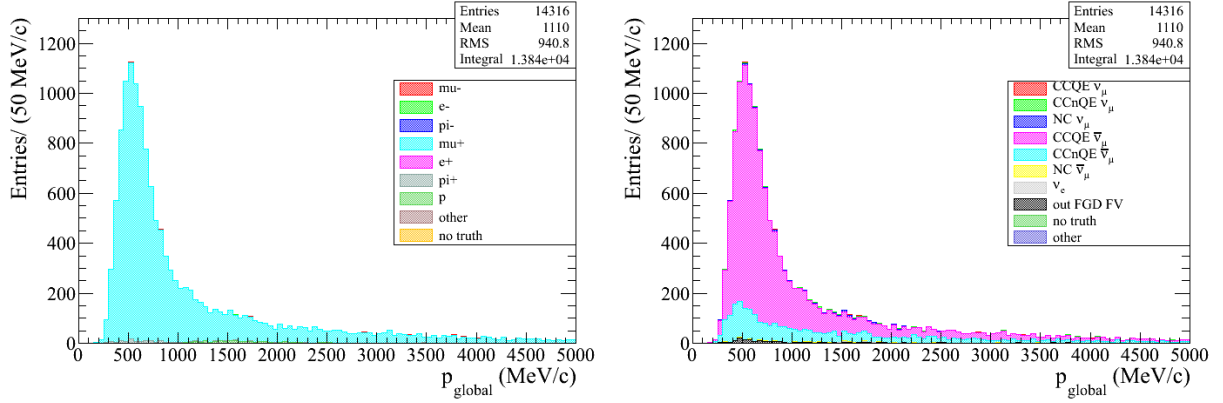


Figure A.9: Momentum spectrum of the most energetic positive tracks after the ECal PID.

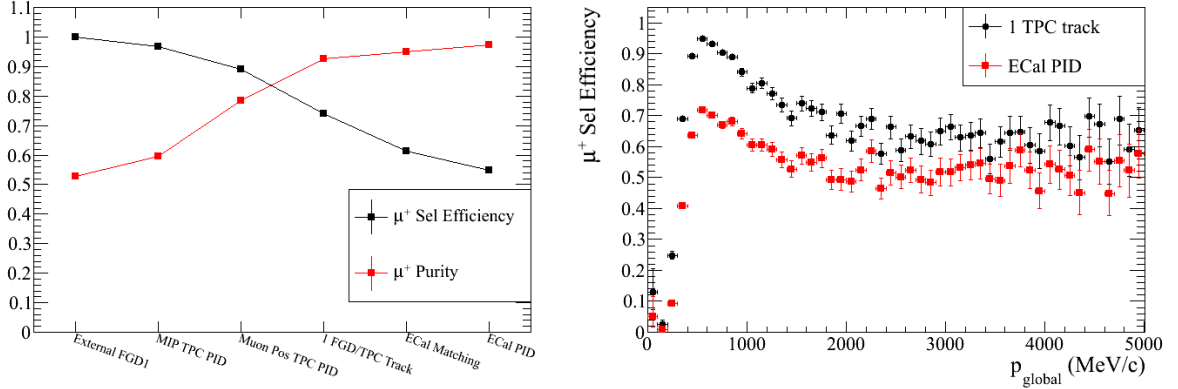


Figure A.10: Left: Efficiency and purity vs cuts applied in the μ^+ selection. Right: μ^+ selection efficiency versus momentum without using the ECal (black) and using the ECal (red).

Table A.1: Composition of the final selected sample broken down by final state particle type.

Category	Composition (%)	MC expected events
μ^-	0.55	111
e^-	0.06	13
π^-	0.22	45
μ^+	92.6	18768
e^+	0.07	15
π^+	3.61	732
p	2.75	558
other	0.09	19

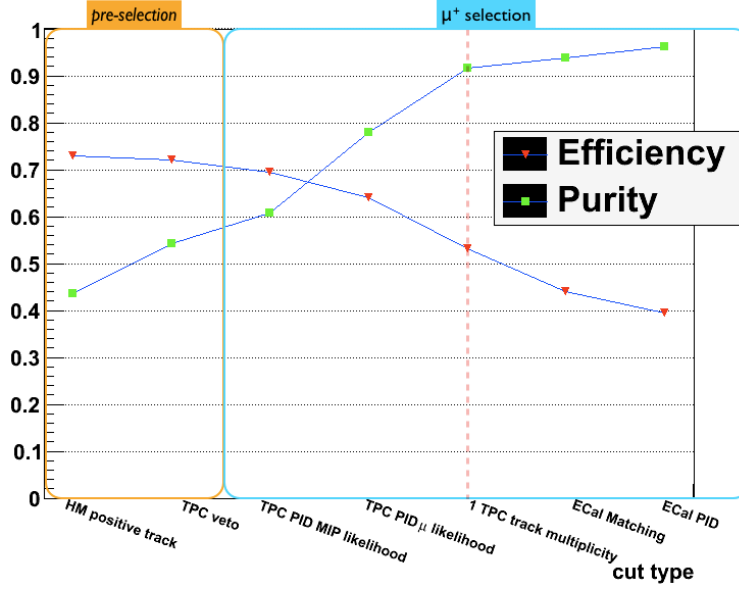


Figure A.11: $\bar{\nu}_\mu$ CC selection efficiency and purity versus the cut applied. In this plot the are distinguished the *pre-selection* and the μ^+ selection. The dashed line in red indicates the efficiency and purity obtained with the event selection applied up to the “1 TPC track multiplicity” cut.

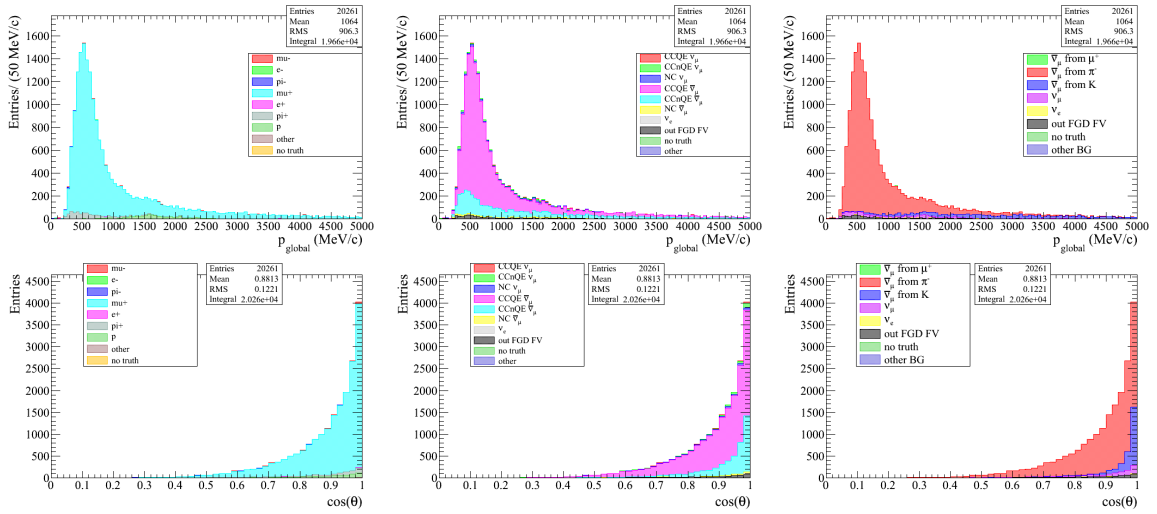


Figure A.12: Kinematic spectra of the final sample broken down by final state particle (left), neutrino interaction type (center) and neutrino parent type (right).

A.4 Detector systematic errors

This preliminary evaluation of the effect of detector systematic errors is based on the assumption that there is a perfect correlation of detector uncertainties between neutrino mode and anti-neutrino mode run. As already pointed out, the standard selection criteria are applied in anti-neutrino mode

Table A.2: Composition of the final selected sample broken down by interaction type.

Category	Composition (%)	MC expected events
$\bar{\nu}_\mu$ CCQE	71.6	14514
$\bar{\nu}_\mu$ CCnonQE	20	4068
$\bar{\nu}_\mu$ NC	1.33	271
ν_μ CCQE	0.51	104
ν_μ CCnonQE	2.01	408
ν_μ NC	1.81	368
ν_e	0.26	54
Out FGDs FV	2.34	474

Table A.3: Composition of the final selected sample. The $\bar{\nu}_\mu$ component is broken down by neutrino parent type.

Category	Composition (%)	MC expected events
$\bar{\nu}_\mu$ from μ^+	0.04	8
$\bar{\nu}_\mu$ from π^-	81.6	16532
$\bar{\nu}_\mu$ from K	11.41	2313
ν_μ	4.34	880
ν_e	0.26	54
Out FGDs FV	2.34	474

up to the “one TPC track multiplicity” cut, therefore all the systematics shown in Table 4.2 are taken into account, except the ECal Matching and the ECal PID systematics.

Using the same procedure seen in Section 4.3, it is possible to produce the corrected $\bar{\nu}$ MC sample. The kinematic spectra of the nominal and corrected MC at the end of the event selection are shown Figure A.13. Differently from that shown for the standard neutrino mode (see Section 4.3), In this case the changes in shape of kinematic spectra are just due to the momentum resolution systematic. In fact in anti-neutrino mode it is expected that the TPC proton PID systematic has not a big impact since the amount of protons coming from ν_μ interactions contained in the final sample is smaller with respect to that one observed in neutrino mode.

The effect of the systematic error propagation can be evaluated as done in Section 4.4. Also in this case I evaluated the impact of the main detector systematics sources (momentum resolution, the TPC proton PID and the TPC proton PID bias) varying them of $\pm\sigma$ in the momentum region where the largest amount of data are expected ($0 < p < 2.5$ GeV/c). As it can be seen from Figures A.15 and A.16, the impact of TPC proton PID and TPC proton PID bias systematics is very low in comparison with that shown for the standard analysis (see Section 4.4). On the other hand, also in the anti-neutrino mode case, the momentum resolution systematic has still a large impact as can be seen from Figure A.17. Finally, the effect of the systematic error propagation varying all the systematic uncertainties at the same time is shown in Figure A.18.

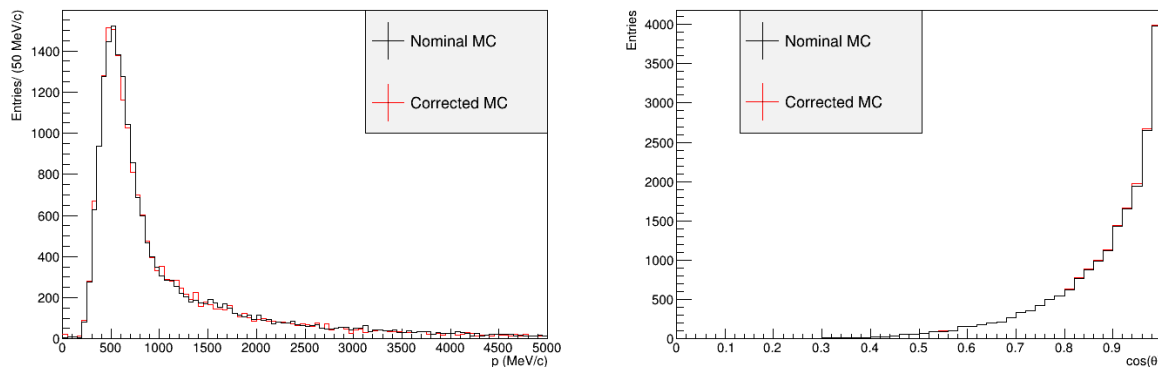


Figure A.13: Comparison between nominal and corrected MC kinematic spectra.

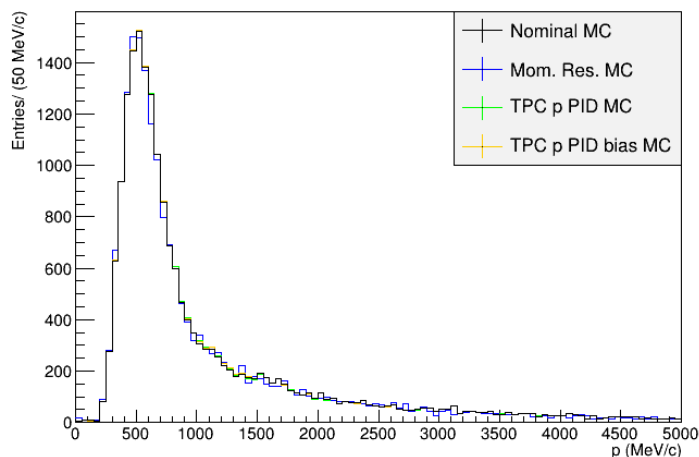


Figure A.14: Comparison between nominal (black) and corrected MC kinematic spectra. In the corrected MC are propagated only: momentum resolution systematic (blue), TPC proton PID systematic (green) and TPC proton PID bias systematic (orange).

A.5 Summary and outlook

The results that I obtained from this first MC based study of the ND280 potentiality in the case of an anti-neutrino mode run are very promising. The event selection developed indicates that differently from the standard neutrino mode run it is possible to avoid the use of the ECal to achieve a $\bar{\nu}_\mu$ sample with a sufficient purity. The final sample is $\sim 92\%$ pure of $\bar{\nu}_\mu$ CC interactions and it is selected with an efficiency of $\sim 55\%$. Moreover I estimate the effect of detector systematic errors assuming a perfect correlation of detector uncertainties between neutrino mode and anti-neutrino mode run. From this preliminary study it seems that the largest detector uncertainty is due to the momentum resolution ($\sim 5\%$ around the T2K energy peak). It is possible to conclude that, as it happens with ν_μ in the standard neutrino beam, ND280 is able to extract the $\bar{\nu}_\mu$ signal in an anti-neutrino mode run with a purity sufficient to provide constraints on flux and cross section

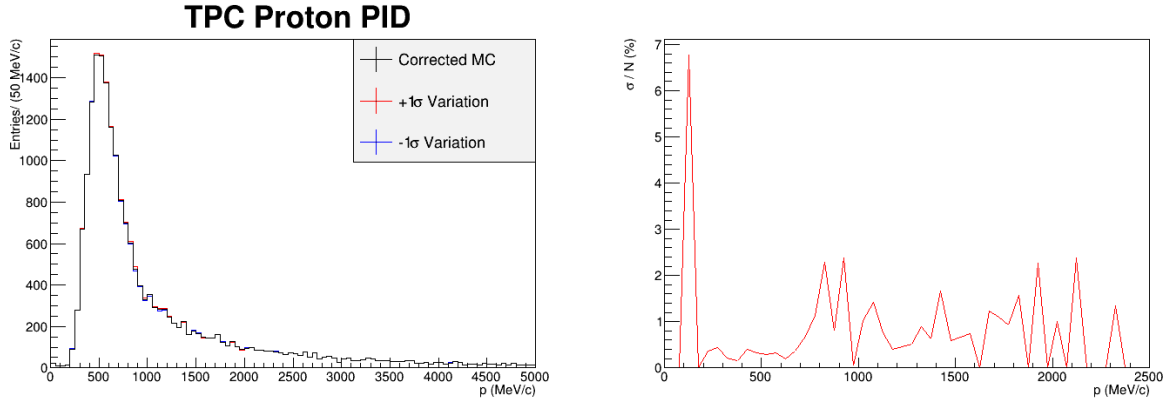


Figure A.15: Left: Effect on the momentum spectrum of the TPC proton PID systematic propagation with a variation of $\pm\sigma$ respect to the nominal value of the pull δ_p in the corrected MC. Right: relative systematic error introduced in the analysis.

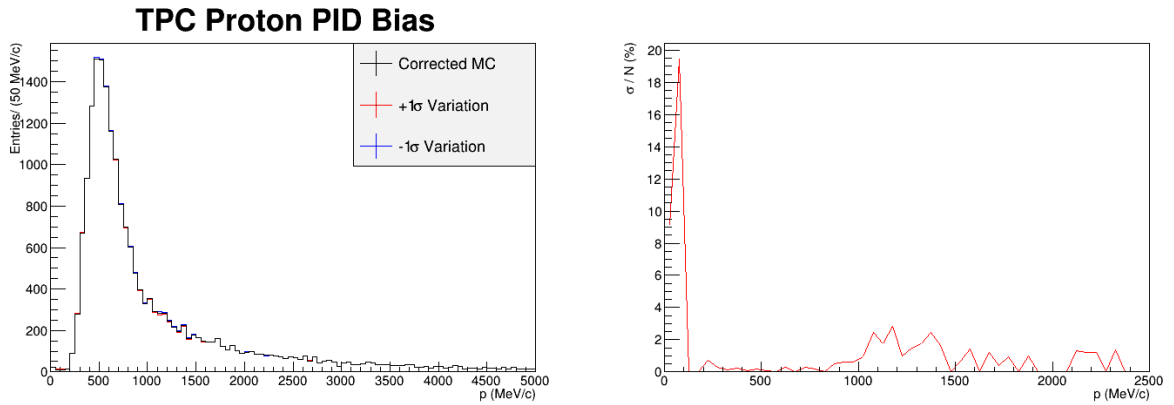


Figure A.16: Left: Effect on the momentum spectrum of the TPC proton PID bias systematic propagation with a variation of $\pm\sigma$ respect to the nominal value of the pull δ_p in the corrected MC. Right: relative systematic error introduced in the analysis.

systematics for the oscillation analyses. As a consequence T2K can share the data taking between neutrino and anti-neutrino mode runs to achieve a good sensitivity for the measures of δ_{CP} and the θ_{23} octant. The analysis presented in this appendix will be used already from the anti-neutrino pilot run planned in 2014 to figure out how much ND280 can reduce flux and cross section systematics when T2K is running in anti-neutrino mode.

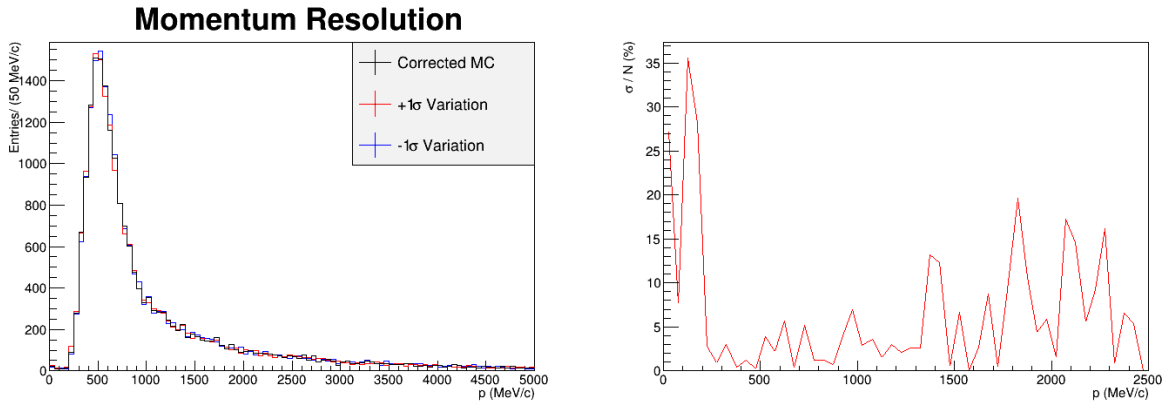


Figure A.17: Left: Effect on the momentum spectrum of the momentum resolution systematic propagation with a variation of $\pm\sigma$ respect to the nominal value of the momentum in the corrected MC. Right: relative systematic error introduced in the analysis.

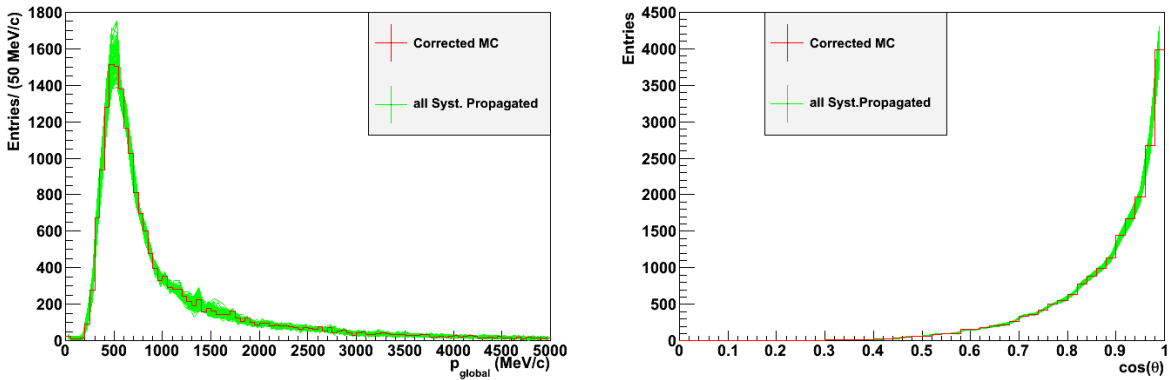


Figure A.18: Kinematic spectra of data corrected MC (red) and MC toys (green).

Bibliography

- [1] E. Fermi, *Zeitschr. f. Phys.* **88** (1934) 161.
- [2] J. Chadwick, *Nature* **193** (1932) 312.
- [3] F. Reines and C.L. Cowan, *Phys. Rev.* **92** (1953) 830; F. Reines and C. L. Cowan, *Nature* **178** (1956) 446; F. Reines and C. L. Cowan, *Phys. Rev.* **113** (1959) 273.
- [4] G. Danby, J.-M. Gaillard, K. Goulianos, L.M. Lederman, N. Mistry, M. Schwartz and J. Steinberger, *Phys. Rev. Lett.* **9** (1962) 36.
- [5] M. L. Perl et al., *Phys. Rev. Lett.* **35**, 1489 (1975).
- [6] K. Kodama et al. (DONUT Collaboration), *Physics Letters B* **504** (2001) 218.
- [7] ALEPH Collaboration (D. Decamp (Annecy, LAPP) et al.). “A Precise Determination of the Number of Families With Light Neutrinos and of the Z Boson Partial Widths ”, *Phys. Lett. B* **235** (1990) 399.
- [8] C. S. Wu *et al.*, *Phys. Rev.* **105** (1957) 1413.
- [9] R. L. Garwin, L. M. Lederman and W. Weinrich, *Phys. Rev.* **105** (1957) 1415.
- [10] S. L. Glashow, *Nucl. Phys.*, **22**, 579–588, 1961.
- [11] A. Salam, 1969, Proc. of the 8th Nobel Symposium on ‘Elementary Particle Theory, Relativistic Groups and Analyticity’, Stockholm, Sweden, 1968, edited by N. Svartholm, p. 367-377.
- [12] S. Weinberg, *Phys. Rev. Lett.* **19**, 1264–1266, 1967.
- [13] L. Landau, *Nucl. Phys.*, **3**, 127, 1957.
- [14] P. W. Higgs, *Phys. Rev. Lett.*, **13**, 508?509, 1964.
- [15] P. W. Higgs, *Phys. Lett.*, **12**, 132?133, 1964.
- [16] P. W. Higgs, *Phys. Rev.*, **145**, 1156?1163, 1966.
- [17] B. Pontecorvo, *Sov. Phys. JETP*, **26**, 984–988, 1968.
- [18] B. Pontecorvo, *Sov. Phys. JETP*, **6**, 429, 1957.
- [19] B. Pontecorvo, *Sov. Phys. JETP*, **7**, 172–173, 1958.
- [20] Z. Maki, M. Nakagawa, and S. Sakata, *Prog. Theor. Phys.*, **28**, 870, 1962.

-
- [21] L. Wolfenstein, Phys. Rev. D **17**, 2369 (1978).
- [22] S.P. Mikheev and A. Yu. Smirnov, Sov. J. Nucl. Phys. **42**, 913 (1985).
- [23] P. Langacker, J. Leveille, and J. Sheiman, Phys. Rev. **D27**, 1228 (1983);
- [24] G. L. Fogli, E. Lisi, and D. Montanino, Phys. Rev. **D54**, 2048 (1996); A. de Gouvêa, A. Friedland, and H. Murayama, Phys. Lett. **B490**, 125 (2000).
- [25] A more quantitative analysis has shown that this is true to better than 90% probability. See H. Nunokawa, S. Parke, and R. Zukanovich Funchal, Phys. Rev. **D74**, 013006 (2006).
- [26] S. Parke, Phys. Rev. Lett. **57**, 1275 (1986).
- [27] We thank J. Beacom and A. Smirnov for invaluable conversations on how LMA-MSW works. For an early description, see S. Mikheyev and A. Smirnov, Ref. 7 (first paper).
- [28] R. J. Davis, D. S. Hamer and K. C. Hoffman, Phys. Rev. Lett. **20**, 1205 (1968).
- [29] Hampel, W. et al. (GALLEX), Phys. Lett. **B420** (1998) 114-126.
- [30] Abdurashitov, J. N. et al., Astropart. Phys. **25** (2006) 349-354.
- [31] M. Altmann et al. (GNO), Phys. Lett. **B616** (2005) 174.
- [32] K. S. Hirata et al. [KAMIOKANDE-II Collaboration], Phys. Rev. Lett. **63**, 16 (1989).
- [33] S. Fukuda et al. [SuperKamiokande Collaboration], Phys. Rev. Lett. **86**, 5651 (2001).
- [34] Q. R. Ahmad et al. [SNO Collaboration], Phys. Rev. Lett. **87**, 071301 (2001).
- [35] J.N. Bahcall, A.M. Serenelli, and S. Basu, Astrophys. J. **621**, L85 (2005).
- [36] B. Aharmim et al., [SNO Collab.], Phys. Rev. **C72**, 055502 (2005).
- [37] J.N. Bahcall, A.M. Serenelli, and S. Basu, Astrophys. J. **621**, L85 (2005).
- [38] Y. Fukuda et al., [Super-Kamiokande Collab.], "Evidence for oscillation of atmospheric neutrinos." Phys. Rev. Lett. **81**, 1562 (1998).
- [39] Y. Ashie et al., [Super-Kamiokande Collab.], Phys. Rev. **D71**, 112005 (2005).
- [40] K. Eguchi et al. [KamLAND Collaboration], Phys. Rev. Lett. **90**, 021802 (2003).
- [41] G. L. Fogli et al., Phys. Rev. **D67**, 073002 (2003); M. Maltoni, T. Schwetz, and J.W. Valle, Phys. Rev. **D67**, 093003 (2003); A. Bandyopadhyay et al., Phys. Lett. **B559**, 121 (2003); J.N. Bahcall, M.C. Gonzalez-Garcia, and C. Peña-Garay, JHEP **0302**, 009 (2003); P.C. de Holanda and A.Y. Smirnov, JCAP **0302**, 001 (2003).
- [42] M. Apollonio et al. [CHOOZ Collaboration] Phys.Lett. **B466** (1999) 415-430.
- [43] F.P. An et al. "Observation of electron-antineutrino disappearance at Daya Bay". Phys. Rev. Lett. **108** (2012), p. 171803.
- [44] J.K. Ahn et al. "Observation of Reactor Electron Antineutrino Disappearance in the RENO Experiment". Phys. Rev. Lett. **108** (2012), p. 191802.

-
- [45] Y. Abe et al. “Indication for the disappearance of reactor electron antineutrinos in the Double Chooz experiment”. *Phys. Rev. Lett.* **108** (2012), p. 131801.
- [46] E. Eskut et al., *Phys. Lett.* **B497**, 8–22, 2001.
- [47] P. Astier et al., *Phys. Lett.* **B570**, 19–31, 2003, hep-ex/0306037.
- [48] A. Aguilar et al., *Phys. Rev.* **D64**, 112007, 2001, hep-ex/0104049.
- [49] B. Armbruster et al., *Phys. Rev.* **D65**, 112001, 2002, hep-ex/0203021.
- [50] P. Fritze et al., *Phys. Lett.* **B96**, 427, 1980.
- [51] H. Grassler et al., *Nucl. Phys.* **B273**, 253, 1986.
- [52] J. Dorenbosch et al., *Z. Phys.* **C40**, 497, 1988.
- [53] Aguilar, A. et al. (LSND), “Evidence for neutrino oscillations from the observation of $\bar{\nu}_e$ appearance in a $\bar{\nu}_\mu$ beam”, *Phys. Rev.* **D64** (2001) 112007.
- [54] Athanassopoulos, C. et al. (LSND), “Evidence for $\nu_\mu \rightarrow \nu_e$ neutrino oscillations from LSND”, *Phys. Rev. Lett.* **81** (1998) 1774-1777.
- [55] The CHORUS Collaboration, Final results on $\nu_\mu \rightarrow \nu_\tau$ oscillation from the CHORUS experiment, *Nucl. Phys.* **B793**, 326-343, 2008.
- [56] NOMAD Collaboration (P. Astier et al.), Final NOMAD results on $\nu_\mu \rightarrow \nu_\tau$ and $\nu_e \rightarrow \nu_\tau$ oscillations including a new search for ν_τ appearance using hadronic τ decays, *Nucl. Phys.* **B611**, 3-39, 2001.
- [57] P. Astier et al., *Nucl. Phys.* **B611**, 3–39, 2001, hep-ex/0106102.
- [58] E. Aliu et al. [K2K Collaboration] *Phys. Rev. Lett.* **94**, 081802 (2005).
- [59] T2K Collaboration (K. Abe (Tokyo U., ICRP) et al.), “Measurement of Neutrino Oscillation Parameters from Muon Neutrino Disappearance with an Off-axis Beam”, Aug 2, 2013. 8 pp., e-Print: arXiv:1308.0465 [hep-ex].
- [60] P. Adamson et al. [Minos Collaboration] *Phys. Rev. Lett.* **97**, 191801 (2006).
- [61] Guler, M. et al. (OPERA), CERN-SPSC-2000-028, 2000.
- [62] K. Abe et al. (The T2K Collaboration), *Phys. Rev.* **D85**, 031103 (2012).
- [63] Y. Itow, Nuclear Physics B, Proceedings Supplements **235**, 79 (2013) the XXV International Conference on Neutrino Physics and Astrophysics
- [64] P. Adamson et al. (MINOS Collaboration), (2013), arXiv:1304.6335 [hep-ex].
- [65] K. Abe et al., “Indication of Electron Neutrino Appearance from an Accelerator-produced Off-Axis Muon Neutrino Beam”, *Phys. Rev. Lett.* **107:041801**, 2011; July 2011.
- [66] T2K Collaboration (K. Abe et al.), Observation of Electron Neutrino Appearance in a Muon Neutrino Beam, Nov 19, 2013, e-Print: arXiv:1311.4750 [hep-ex].

-
- [67] J. Beringer et al. (Particle Data Group), *Phys.Rev.* **D86**, 010001 (2012).
- [68] Concha Gonzalez-Garcia, “Global Analyses of Neutrino Experiments”, TAUP 2013 conference, plenary talk on Neutrino Parameters, 12 September 2013, https://commons.lbl.gov/download/attachments/88868578/gonzalez-garcia_global_analysis.pdf?version=1&modificationDate=1379032388369.
- [69] F. Capozzi et al., “Status of three-neutrino oscillation parameters, circa 2013”, Dec 10, 2013 - 11 pages, e-Print: arXiv:1312.2878 [hep-ph].
- [70] D.S. Ayres et al. “NO ν A: Proposal to build a 30 kiloton off-axis detector to study $\nu_{\mu} \rightarrow \nu_e$ oscillations in the NuMI beamline”. In: (2004). arXiv:hep-ex/0503053 [hep-ex].
- [71] A. Stahl et al., Expression of Interest for a very long baseline neutrino oscillation experiment (LBNO), CERN-SPSC-2012-021, SPSC-EOI-007.
- [72] LBNE Collaboration (M. Bass (Colorado State U.) et al.), Baseline optimization for the measurement of CP violation and mass hierarchy in a long-baseline neutrino oscillation experiment, FERMILAB-PUB-13-506-E, e-Print: arXiv:1311.0212 [hep-ex] .
- [73] Hyper-Kamiokande working Collaboration (T. Ishida for the collaboration), T2HK: J-PARC upgrade plan for future and beyond T2K, Conference: C13-08-19 KEK-PREPRINT-2013-55 e-Print: arXiv:1311.5287 [hep-ex].
- [74] K. Abe et al. “Letter of Intent: The Hyper-Kamiokande Experiment — Detector Design and Physics Potential —”. In: (2011). arXiv:1109.3262 [hep-ex].
- [75] Ettore Majorana. “Theory of the Symmetry of Electrons and Positrons”. In: *Nuovo Cim.* 14 (1937), pp. 171–184. doi: 10.1007/BF02961314.
- [76] GERDA collaboration. “The GERmanium Detector Array (GERDA)”. <http://www.mpi-hd.mpg.de/gerda/>.
- [77] CUORE collaboration. “The Cryogenic Underground Observatory for Rare Events (CUORE)”. <http://cuore.lbl.gov/>.
- [78] EXO collaboration. “Enriched Xenon Observatory (EXO)”. <http://www-project.slac.stanford.edu/exo/about.html>.
- [79] NEXT collaboration, NEXT-100 Technical Design Report (TDR). Executive Summary, arXiv:1202.0721.
- [80] A. Gando. “First result from KamLAND-Zen : Double beta decay with ^{136}Xe ”. In: (2012). arXiv:1205.6130 [hep-ex].
- [81] Emilio Ciuffoli, Jarah Evsln, and Hong Li. “The Reactor Anomaly after Daya Bay and RENO”. In: (2012). arXiv:1205.5499 [hep-ph].
- [82] T2K letter of Intent <http://jnusrv01.kek.jp/public/t2k/loi/loi.v2.030528.pdf>
- [83] D. Beavis, A. Carroll, I. Chiang, et al., Long Baseline Neutrino Oscillation Experiment at the AGS (Proposal E889), 1995. Physics Design Report, BNL 52459.

-
- [84] T2K Collaboration (K. Abe (Kamioka Observ.) et al.), “The T2K Experiment”, Nucl. Instrum. Meth. **A659** (2011) 106-135.
- [85] T2K Collaboration, “Physics Potential and Sensitivities of T2K”, Report to J-PARC PAC, <http://www.t2k.org/comm/ec/pacreport2013/pacreportsubfinal/view>.
- [86] K. T. McDonald. hep:ex/0111033v1 (2001).
- [87] S. Bhadra et al. “Optical Transition Radiation Monitor for the T2K Experiment (2012)”. <http://arxiv.org/abs/arXiv:1201.1922>.
- [88] K. Matsuoka, et al., Nucl. Instrum. Meth. **A623** (2010) 385–387.
- [89] K. Matsuoka, et al., Nucl. Instrum. Meth. **A624** (2010) 591–600.
- [90] G. De Lellis et al. “Momentum measurement by the angular method in the Emulsion Cloud Chamber”. In: Nucl. Instrum. Meth. **A512** (2003), pp. 539–545. doi: 10.1016/S0168-9002(03)02016-3.
- [91] Magali Besnier. “Reconstruction and analysis of neutrino interactions in OPERA target emulsion blocks and discrimination of charm background from the channel $\tau \rightarrow 3h$ ”. (Advisor: Dominique Duchesneau). PhD thesis. Laboratoire d’Annecy le vieux de physique des particules, 2008.
- [92] N. Antoniou et al. “Study of hadron production in hadron nucleus and nucleus nucleus collisions at the CERN SPS”. In: CERN-SPSC-2006-034 (2006).
- [93] N. Abgrall et al. “Report from the NA61/SHINE experiment at the CERN SPS”. In: Technical Report CERN-SPSC-2010-025. SPSC-SR-066 (2010).
- [94] N. Abgrall et al. “Measurements of Cross Sections and Charged Pion Spectra in Proton- Carbon Interactions at 31 GeV/c”. In: Phys.Rev.C (2011).
- [95] FLUKA, version 2008.3c. 2008. <http://www.fluka.org/fluka.php>.
- [96] GEANT : Detector Description and Simulation Tool. CERN Programming Library Long Writeup W5013, GEANT version 3.21.
- [97] GEANT3, A detector description and simulation tool. 1993.
- [98] N. Abgrall et al. Neutrino flux prediction. T2K-TN-038. 2011.
- [99] V. Galymov et al. Neutrino Flux Uncertainty for 10a data analysis. T2K-TN-039. 2011.
- [100] A. Vacheret et al. “Characterization and Simulation of the Response of Multi Pixel Photon Counters to Low Light Levels”. In: Nucl. Instrum. Meth. **A656** (2011).
- [101] G. Arnison et al. Experimental Observation of Lepton Pairs of Invariant Mass Around 95 GeV/c² at the CERN SPS Collider. Phys. Lett. **B126** 398– 410 (1983).
- [102] J. Altegoer et al. The NOMAD experiment at the CERN SPS. Nucl. Instrum. Meth. **A404** 96–128 (1998).
- [103] I. Giomataris et al. Micromegas in a bulk. Nucl. Instrum. Meth. **A560** 405– 408 (2006).

-
- [104] T2K ND280 TPC Collaboration, Time Projection Chambers for the T2K Near Detectors, Nucl. Instrum. Meth. **A637** 25–46 (2011).
- [105] S. Ahn et al. Detection of accelerator produced neutrinos at a distance of 250-km. Phys. Lett. **B511** 178–184 (2001).
- [106] Y. Fukuda et al. Measurement of the solar neutrino energy spectrum using neutrino electron scattering. Phys. Rev. Lett. **82** 2430–2434 (1999).
- [107] M. Ahn et al. Measurement of Neutrino Oscillation by the K2K Experiment. Phys.Rev. D74 072003 (2006).
- [108] Y. Ashie et al. A Measurement of atmospheric neutrino oscillation parameters by SUPER-KAMIOKANDE I. Phys.Rev. **D71** 112005 (2005).
- [109] J. Hosaka et al. Three flavor neutrino oscillation analysis of atmospheric neutrinos in Super-Kamiokande. Phys.Rev. D74 032002 (2006).
- [110] M. Shiozawa et al. Search for proton decay via $p \rightarrow e^+\pi^0$ in a large water Cherenkov detector. Phys. Rev. Lett. **81** 3319–3323 (1998).
- [111] Y. Hayato et al. Search for proton decay through $p \rightarrow \bar{\nu}K^+$ in a large water Cherenkov detector. Phys. Rev. Lett. **83** 1529–1533 (1999).
- [112] H. Nishino et al. Search for Proton Decay via $p \rightarrow e^+\pi^0$ and $p \rightarrow \mu^+\pi^0$ in a Large Water Cherenkov Detector. Phys. Rev. Lett. **102** 141801 (2009).
- [113] T2K Collaboration (K. Abe (Tokyo U., ICRR) et al.), “Evidence of Electron Neutrino Appearance in a Muon Neutrino Beam”, Phys. Rev. **D88** (2013) 032002 (2013-08-05).
- [114] Y. Fukuda et al. The Super-Kamiokande detector. Nucl. Instrum. Meth. A501 418–462 (2003).
- [115] H. Nishino, et al., Nuclear Science Symposium Conference Record, 2007. NSS’07. IEEE 1 (2008) 127–132.
- [116] S. Yamada, et al., 2009 16th IEEE-NPSS Real Time Conference Proceedings (2009) 201–205.
- [117] C. Andreopoulos et al., T2K 3.010×10^{20} POT Joint 3-Flavour Oscillation Analysis, T2K-TN-154, <http://www.t2k.org/docs/technotes/154/T2KTN154v4/view>.
- [118] Clark McGrew Thomas Lindner. oaEvent Manual.
- [119] Hayato. A Neutrino Interaction Simulation Program Library NEUT.
- [120] C. Andreopoulos et al. “The GENIE Neutrino Monte Carlo Generator”. In: Nucl. Instrum. Meth. **A614** (2010), pp. 87–104.
- [121] GEANT4. <http://geant4.web.cern.ch/geant4/>.
- [122] ROOT | A Data Analysis Framework - CERN, <http://root.cern.ch/drupal/>
- [123] The ND280 Software Working Group. Conceptual Design of the ND280 Off-line Physics and Analysis Software Infrastructure.

- [124] A. Hillairet et al. ND280 Reconstruction. Tech. rep. T2K-TN-072, <http://www.t2k.org/docs/technotes/072>.
- [125] C. Giganti, M. Zito, Particle Identification with the T2K TPC, T2K-TN-001 <http://www.t2k.org/docs/technotes/001>.
- [126] C. Giganti, The TPC beam test: PID studies, T2K-TN-003, <http://www.t2k.org/docs/technotes/003>.
- [127] J. Caravaca et al. Measurement of the electron neutrino beam component in the ND280 Tracker for 2013 analyses, T2K-TN-149, <http://www.t2k.org/docs/technotes/149>.
- [128] Gary Barker et al., Second Generation Particle ID with the ND280 Tracker ECALs, T2K-TN-111, <http://www.t2k.org/docs/technotes/111>.
- [129] C. Bojecho et al., CC-multiple-pion ν_μ event selections in the ND280 tracker using Run 1+2+3+4 data, T2K-TN-152, <http://www.t2k.org/docs/technotes/152/t2ktn152v4.2/view>.
- [130] E. Frank, A. Marchionni, B-field calibration and systematic errors, T2K-TN-081, <http://www.t2k.org/docs/technotes/081>.
- [131] C. Bojecho et al., Measurement and Correction of Magnetic Field Distortions in the TPCs, T2K-TN-061, <http://www.t2k.org/docs/technotes/061/v2/view>.
- [132] S. Oser, Elemental composition and masses of FGD XY modules, T2K-TN-091, <http://www.t2k.org/docs/technotes/091/xy-chemcomp-v1.2.pdf/view>.
- [133] K. Kowalik and J. Lagoda, “The Simulation of Beam Neutrino Interactions Outside the ND280 Detector”, T2K-TN-077, http://www.t2k.org/docs/technotes/077/v2.1_sand_note/view.
- [134] J. Lagoda, Estimation of the Cosmic Muon Background, T2K-TN-112, http://www.t2k.org/docs/technotes/112/cosmic_background_note_v2.0.pdf/view.
- [135] P. de Peiro et al., Constraining the Flux and Cross Section Models with Data from the ND280 Detector for the 2012a Oscillation Analysis, T2K-TN-106, <http://www.t2k.org/docs/technotes/106/banffnotev8/view>.
- [136] M. Hartz et al., Constraining the Flux and Cross Section Models with Data from the ND280 Detector for the 2013 Oscillation Analysis, T2K-TN-166, <http://www.t2k.org/docs/technotes/166/banff2013v5/view>.